SAPIENZA
UNIVERSITÀ DI ROMA

Analysis and modelling of microalgae growth and production of high added-value metabolites

Faculty of Civil and Industrial Engineering

Department of Chemical Engineering Materials and Environment

PhD Course in Chemical Engineering – XXXII Cycle

PhD Candidate
Alessio Mazzelli
1392477

Academic Tutor: Prof. Francesca Pagnanelli

Company Tutor: Eng. Gaetano Iaquaniello

Academic Year 2019-2020

The entire project of this PhD work fell within the research agreement concluded between:

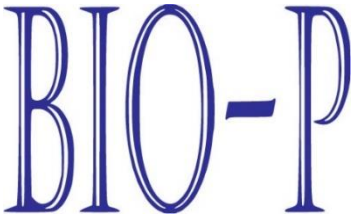

Alla mia Famiglia

Summary

Scientific Production

Papers published in international scientific journals

1. Mazzelli A., Cicci A., Franceschini G., Di Caprio F., Iaquaniello G., Altimari P., Pagnanelli F., Toro L., 2018, **Investigation of effects of nutrients and external parameters on kinetic growth of outdoor microalgal cultivation**, *Chemical Engineering Transactions*, 64, 691-696, DOI: 10.3303/CET1864116
2. Mazzelli A., Cicci A., Di Caprio F., Altimari P., Toro L., Iaquaniello G., Pagnanelli F., 2019, *Algal Research,* **Multivariate modeling for microalgae growth in outdoor photobioreactors**, DOI: 10.1016/j.algal.2019.101663
3. Mazzelli A., Cicci A., Sed G., Bravi M., 2018, **Development of semi-theoretical light radiation and photosynthetic growth model for the optimal exploitation of wastewaters by microalgae**, Chemical Engineering Transactions, 64, 685-690. DOI: 10.3303/CET1864115
4. Mazzelli A., Buonanno G., Luzzi D. M., Cicci A., Piemonte V., Iaquaniello G., 2019, **Multi-component extraction process of high added value compounds from microalgae with supercritical CO_2: A technical and economic study**, Chemical Engineering Research and Design, 150, 65–73. DOI: 10.1016/j.cherd.2019.07.023
5. Mazzelli A., Luzzi D.M., Buonanno G., Cicci A., Piemonte V., Iaquaniello G., 2019, **An optimized separation process of microalgal lipidic products by molecular distillation: Techno-economic analysis.** Chemical Engineering Science, 207, 1187–1195., DOI: /10.1016/j.ces.2019.07.043
6. Mazzelli A., Cicci A., Di Caprio F., Altimari P., Toro L., Iaquaniello G., Pagnanelli F. (*Submitted*). **A simplified structured model for the estimation of microalgal metabolites accumulation.**

List of Symbols

Statistical and Compartmental Models

- **μ**: Specific Growth Rate [d^{-1}]
- **x**: Microalgal concentration [g L^{-1}]
- **C_{init}**: Microalgal Inoculum Concentration [g L^{-1}]
- **C_{max}**: Microalgal maximum Concentration observed in the experiment [g L^{-1}]
- **t_{max}**: Time at which the maximum biomass concentration is observed [d]
- **t_{min}**: Experiment start time (time zero) [d]
- **P_{max}**: Productivity calculated at C_{max} [g L^{-1} d^{-1}]
- **$NaNO_{3init}$**: $NaNO_3$ Initial Concentration [g L^{-1}]
- **$T_{imax\ avg}$**: Maximum Internal Temperature Averaged [°C]
- **$T_{emax\ avg}$**: Maximum External Temperature Averaged [°C]
- **$T_{imin\ avg}$**: Minimum Internal Temperature Averaged [°C]
- **$T_{emin\ avg}$**: Minimum External Temperature Averaged [°C]
- **PPFD**: Photosynthetic Photon Flux Density [µE m^{-2} s^{-1}]
- **q_g**: Internal starch quota [g[C] g[C]$^{-1}$]
- **q_l**: Internal TAG quota [g[C] g[C]$^{-1}$]
- **q_n**: Internal nitrogen quota [g[N] g[C]$^{-1}$]
- **α, β**: carbon partitioning coefficient [g[C] g[C]$^{-1}$]
- **I_0**: Incident Light Intensity [W m^{-2}]
- μ_m: Theoretical maximum growth rate [d^{-1}]
- **q_{nmin}**: Minimum nitrogen quota allowing microalgal growth [g[N] g[C]$^{-1}$]
- $\bar{I}$: Light irradiance averaged over the geometry of the reactor used [W m^{-2}]
- **K_I**: Half saturation parameter for the light distribution model [W m^{-2}]
- **σ**: Mass extinction coefficient [m^2 kg^{-1}]
- **y:** Characteristic dimension of the considered reactor [m]

Supercritical CO_2 Model

- **e**: Extraction yield [$g_{extracted\ product}$ $g_{microalgae}^{-1}$]
- **q**: Specific sCO_2 flow rate per kg of microalgae [min^{-1}]
- **t_1**: Extraction time at the end of the first extraction period [min]
- **θ_f** : External mass transfer resistance
- **t_i**: Characteristic time of mass transfer in the solid phase [min]
- **t_r**: Residence time [min]
- **c_u**: Asymptotic value of extraction yield [$g_{extracted\ product}$ $g_{microalgae}^{-1}$]
- **y_s**: Solubility of each component in sCO_2 [$g_{product}$ g_{sCO2}^{-1}]
- **k,a,b**: Thermodynamic parameters for y_s equation
- **G**: Initial fraction of solute in open cells
- **ρ_s**: Microalgal solid density [kg m^{-3}]
- **ρ_f**: sCO_2 density [kg m^{-3}]
- **μ_v**: sCO_2 viscosity [Pa s]

- $\mathbf{k_f}$: External mass transfer coefficient [kg m^{-3}]
- $\mathbf{D_{12}}$: Lipids' diffusivity in sCO_2 [$m^2\ s^{-1}$]
- **Sh, Re, Sc**: Adimensional Numbers (Sherwood, Reynolds, Schmidt)
- $\mathbf{d_p}$: Microalgal diameter assumed spherical [m]
- $\mathbf{d_R}$: Extractor's diameter [m]
- $\mathbf{v_f}$: Fluid velocity [m s^{-1}]
- $\boldsymbol{\varepsilon}$: Bed's void fraction inside the extractor
- **SSR**: Solvent to Solid Ratio [kg h^{-1}_{sCO2} $kg^{-1}_{microalgae}$]

Molecular Distillation Process

- $\mathbf{C_i^0}$: Molar inlet concentration for the i-component [mol L^{-1}]
- $\mathbf{C_i}$: Molar outlet concentration for the i-component [mol L^{-1}]
- $\mathbf{C_O^0}$: Molar inlet concentration of oleic acid [mol L^{-1}]
- $\mathbf{C_E^0}$: Molar inlet concentration of ethanol [mol L^{-1}]
- $\mathbf{C_W^0}$: Molar inlet concentration of water [mol L^{-1}]
- $\mathbf{C_O}$: Molar outlet concentration of oleic acid [mol L^{-1}]
- $\mathbf{C_E}$: Molar outlet concentration of ethanol [mol L^{-1}]
- $\mathbf{C_W}$: Molar outlet concentration of water [mol L^{-1}]
- $\mathbf{C_{OE}}$: Molar outlet concentration of ethyl oleate [mol L^{-1}]
- **R**: Universal gas constant [J mol^{-1} K^{-1}]
- **Q**: Volumetric reactor flow rate [L min^{-1}]
- **Q'**: Volumetric flow rate of the liquid phase in the adsorption column [$m^3\ s^{-1}$]
- $\mathbf{k_{dir}}$: Reaction rate coefficient of the direct esterification reaction [L $mol^{-1}min^{-1}$]
- $\mathbf{k_{rev}}$: Reaction rate coefficient of the revers esterification reaction [L $mol^{-1}min^{-1}$]
- $\mathbf{E^a_{dir}}$: Activation energy for the direct reaction [kJ mol^{-1}]
- $\mathbf{E^a_{rev}}$: Activation energy for the revers reaction [kJ mol^{-1}]
- $\mathbf{n_W}$: Moles of adsorbed water per kg of adsorbent solid [mol_{water} kg^{-1}_{solid}]:
- $\mathbf{q_0}$: Adsorption capacity [mol m^{-3}]
- $\mathbf{K_L}$: Langmuir constant [m^{-3} mol^{-1}]
- $\mathbf{C_W^L}$: Water concentration in the liquid phase in the adsorption column [mol m^{-3}]
- $\mathbf{C_W^S}$: Water concentration in the solid phase in the adsorption column [mol m^{-3}]
- **R**: Adsorption column radius [m]
- $\mathbf{K_{OL}}$: Overall mass transfer coefficient in the adsorption balance [m s^{-1}]
- **a**: Specific area of the adsorbent solid [m^{-1}]
- $\boldsymbol{\rho_S}$: Solid phase density in the adsorption balance [kg m^{-3}]
- $\boldsymbol{\nu_i}, \boldsymbol{\nu_O}$: Stoichiometric coefficients for the i-component and for oleic acid
- $\mathbf{X_O}$: Oleic acid conversion
- $\mathbf{t_{SAT}}, \mathbf{t_{REG}}, \mathbf{t_{COOL}}$: Saturation, Regeneration and Cooling time [h]
- $\mathbf{W_L^{IN}}$: Lutein mass flow rate entering inside the molecular distiller [kg h^{-1}]
- $\mathbf{W_A^{IN}}$: Astaxanthin mass flow rate entering inside the molecular distiller [kg h^{-1}]
- $\mathbf{W_L^R}$: Lutein mass flow rate coming out from the molecular distiller [kg h^{-1}]
- $\mathbf{W_A^R}$: Astaxanthin mass flow rate coming out from the molecular distiller [kg h^{-1}]

Abstract

Microalgae are a very versatile microorganism that have the ability to modify their biomass composition under controlled condition in order to accumulate products having applications in several sectors. The aim of this thesis work is the analysis and modelling of both microalgal growth and production of high added-value metabolites, focusing also on their extraction and purification. An outdoor 10 bubble column photobioreactors (PBRs) pilot plant for the cultivation of two microalgae named *Tetradesmus obliquus* and *Graesiella emersonii*, covering a 9 months cultivation period (March 2017-December 2017), has been installed and operated. All collected data (as microalgal growth rate, outdoor parameters and initial cultivation's conditions) have been used to develop an empirical model for prediction of microalgal growth in photobioreactors at specific outdoor conditions, using Principal Component Analysis and Partial Least Squares regression method, obtaining acceptable outcomes for both responses: microalgal specific growth rate (μ) and maximum productivity (P_{max}). Concerning microalgal metabolism, also a new mathematical model able to represent in a simple way the accumulation of metabolites inside microalgae, focusing on the carbon partitioning process between triacylglycerides (TAG) and starch during nitrogen starvation in phototrophy, has been developed, obtaining high R-Squared values as index of model's goodness of fitting. A future application of these models can be found in the MEWLIFE European project, in which Bio-P has a role as partner, since this project has as aim the production of microalgal biomass in an integrated phototrophic and heterotrophic cultivation system using preconcentrated olive oil wastewaters (OMWW) as carbon source. As a completion of the microalgal process treatment, a study of the downstream processes for the extraction (using supercritical CO_2) and purification of the high added value metabolites (with molecular distillation) has been carried out, developing a feasibility study also from the economical point of view. As regard the supercritical CO_2 the best extraction conditions in terms of operative variables have been: T = 60°C, P = 250 bar and SSR = 5 h^{-1} with a daily amount of the desired products equal to 147 kg and OPEX = 561.7 k€/year and CAPEX = 2717.9 k€/year. Regarding the molecultar distillation process, the best operating conditions have been found at T = 128 °C and P = 0.33 Pa, obtaining OPEX = 498.23 k€/year and CAPEX = 2387.4 k€/year.

Chapter 1. Introduction

1.1 Microalgae: An overview

Microalgae are photosynthetic organisms able to grow in a wide watery environments such as oceans, pounds, rivers, lakes and also inside wastewaters. They can live and grow in a wide range of pH, temperature, salinity and light intensities, alone or in symbiosis with other organisms. (Khan et al., 2018)
Microalgae, according to their characteristics, are divided into Groups, Classes and Orders, the main examples of which are given in the Figure below (Fig. 1).

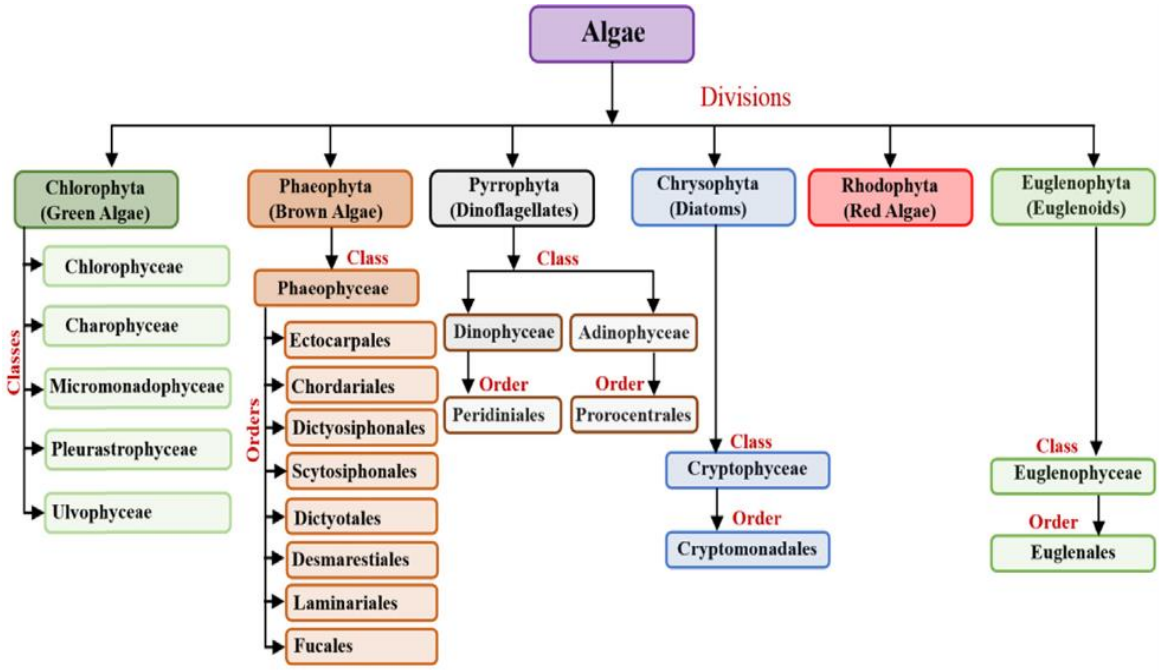

Fig. 1 Simplified algae classification (Enamala et al., 2018).

Microalgae can modify their internal composition only changing their cultivation conditions (Mazzelli et al., 2018a), accumulating thus different kind of metabolites in form of lipids, carbohydrates, proteins, etc. These products have different applications, from biofuel and energy production (Bahadar and Khan, 2013; Raheem et al., 2018) to pharmaceutical (Panis and Carreon, 2016), nutraceutical (Patel et al., 2019) and animal dietary ones (Díaz et al., 2017). In order to maximize the economic aspects of microalgal cultivation and metabolites' production a biorefinery approach must be adopted. This biorefinery concept is similar to the traditional petroleum one, the principal difference is in terms of raw materials (biomass or crude oil) and technology employed. These designs usually attempt to obtain the maximum product output (in terms of quality and profit) from a single raw material source (Chew et al., 2017). The main bottleneck of a biorefinery

approach is the separation of different fractions without causing harm to the other fractions; this can be overcome through the use of simple, low energy consumption, cost effective and scalable separation processes (see paragraph 1.7). Nowadays, the increasingly presence of this model in industrial scale allows the biorefineries to increase the development of new processes, putting on market new products having microalgae as raw material. Focusing on the principal high-added value metabolites discussed in this work, PUFA fatty acids (DHA & EPA) have a global market value of over 700 Million US$/annum followed by β-carotene with 261 Million US$/annum, then comes astaxanthin with a market value of 240 Million US$/annum, closely followed by lutein with a market value of 233 Million US$/annum and finally phyco-biliproteins with a value of just over 60 Million US$/annum. The global demand for carotenoids is still expected to in-crease further to 1.8 billion US$ by the end of 2019 (Bhalamurugan et al., 2018). As regards the process scalability, in addition to technical issues, the main objective to be achieved for microalgal cultivation in order to make the process competitive, is the reduction of production cost.

Generally, for any reduction in production cost, it is necessary to reduce labor by implementing extensive automation while reducing the depreciation cost by simplifying the equipment used and increasing the production capacity. Indeed, increasing production capacity to 200 t/year by means of an adequate scale-up of the process with a reduction in manpower to 1 person/ha and avoiding the use of expensive equipment such as freeze dryers and sterilization units, the production cost could be reduced to $16/kg vs $89/kg at the small scale (Acién et al., 2017a).

In Fig. 2 the analysis of production costs related to the production of *Scenedesmus almeriensis* using tubular reactors scaled up to 3.8 t/year., is shown.

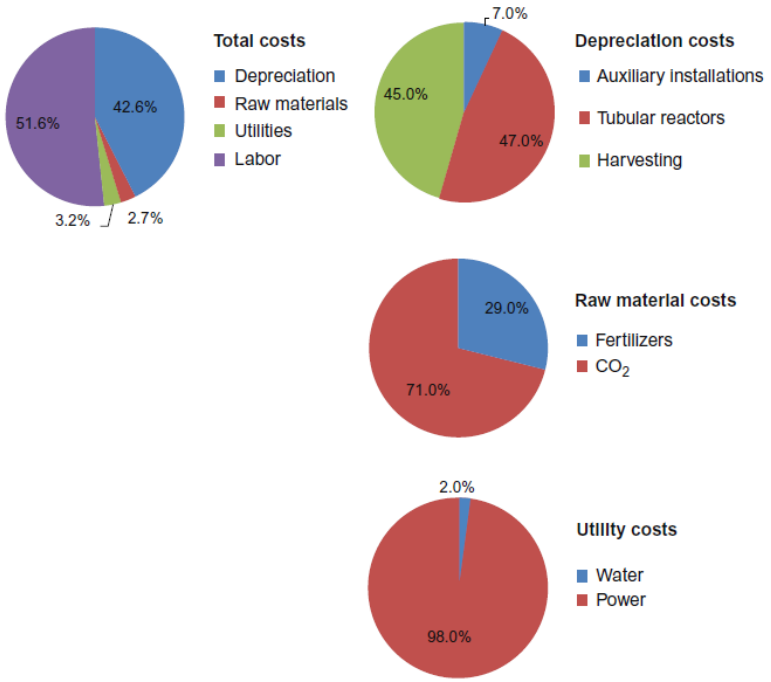

Fig. 2 Analysis of production costs related to the production of *Scenedesmus almeriensis* using tubular reactors scaled up to 3.8 t/year (Acién et al., 2017a).

It’s visible that, for a production capacity of 3.8 t/year, the main contributory factors to production cost are depreciation and labor accounting for 94% of the total production cost. All of these issues bring to the necessity of studying in an accurate way all the phases occurring in the microalgal treatments, as it has been done in this study, trying to optimize them in order to reduce costs. In addition to the process engineering solutions related to find the best conditions (in terms of operative variables, equipments’ size and type and energy/mass balances) for microalgae cultivations, a focusing on their metabolism has to be carried out in order to maximize the desired outputs with less waste of resources. In this work all of these themes will be discussed, starting from the optimization of microalgal cultivation, thanks to the development of two different models having as aim the estimation of both microalgal growth and metabolites production, and ending with a feasibility study of a downstream process able to extract and purify the desired high-added value products.

1.2 Microalgal metabolisms

Nowadays, since all microalgae are photosynthetic organism and most of them are very efficient in conversion of solar energy into biomass and useful products (i.e. lipids for biofuels), the most common way of microalgal cultivation is the photoautotrophic one. During photosynthesis microalgae are able to fix inorganic carbon (under CO_2 form) by the usage of light as energy vector that is converted into ATP and NADPH used in turn to feed Calvin cycle, which is responsible for CO_2 fixation. However, in this complex carbon metabolism there is a common denominator, the C3 pool, composed by 3-phosphoglycerate (3PG) and glyceraldehyde 3-phosphate (GAP) (see Fig. 3). This fixed carbon can be converted into reserve products, which can be grouped into the four major microalgal constituents: microalgal biomass (is the biomass produced during nitrogen replete conditions), free fatty acids and triacylglycerols (TAG), starch and other functional products (proteins and nucleic acids and also glycolipids and phospholipids that constitute the structural materials). Since without the addition of external carbon source in the culture medium photosynthesis is the only mechanism that manage the algal metabolism, a tight control of the reactions involved is necessary to understand the downstream metabolic pathways in the chloroplast (Johnson and Alric, 2013).

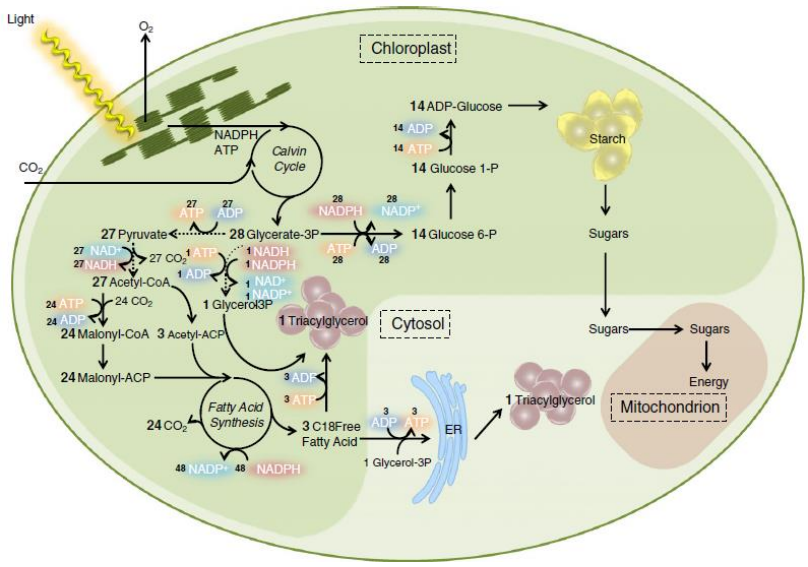

Fig. 3 A simplified phototrophic metabolism in green microalga (Jaeger et al., 2014).

A feasible alternative for phototrophic cultures, restricted to a few microalgal species, is the use of heterotrophic cultivation in the absence of light (dark fermentation), replacing the atmospheric CO_2 fixation with organic carbon sources dissolved in the culture media. The basic composition of the heterotrophic cultures medium is similar to the autotrophic one, with the only exception of organic carbon addition (Tsavalos and Day, 1994).

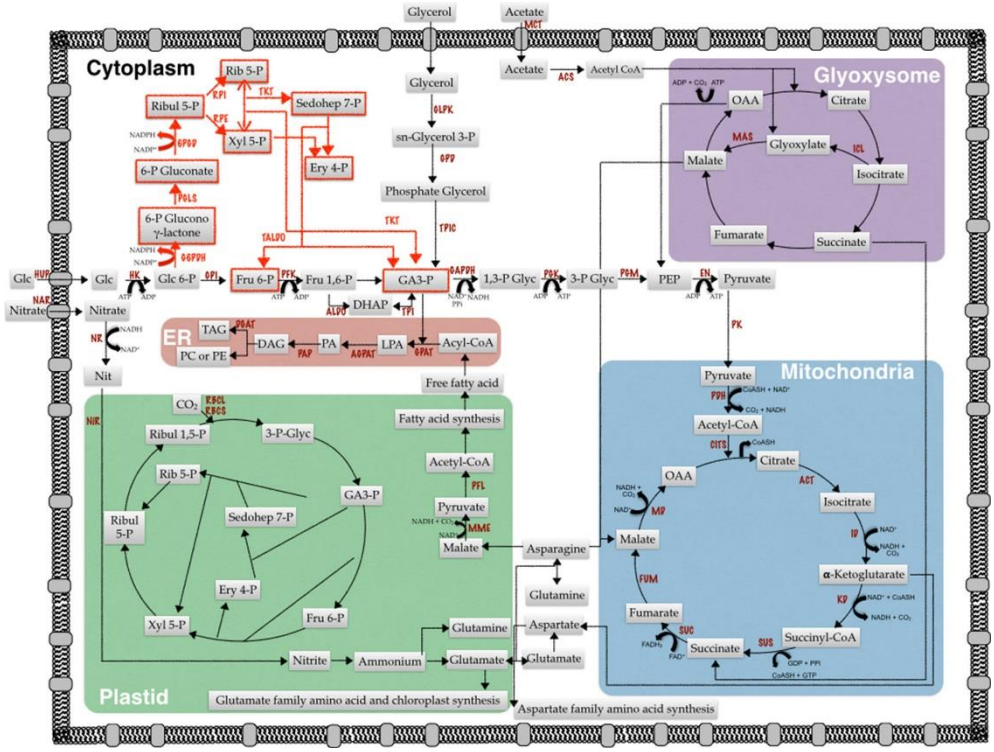

Fig. 4 Heterotrophic metabolism in a microalgal cell (Morales-sa et al., 2014).

The use of carbon sources, including acetate, glucose, lactate and glycerol, requires several enzymatic systems for the execution of several actions inside the cell (transport, activation

trough phosphorylation, energy generation through substrate-level and/or respiration, etc. (Fig. 4). The heterotrophic approach, differently from autotrophic, uses only one kind of bioreactor (fermentor), such as those used for pharmaceutical industry or beverages. Furthermore, the heterotrophic cultivation brings to significant reduction in costs of operations and daily maintenance. Another significant benefit of heterotrophy is the possibility to obtain high densities of microalgae cells, providing an economic feasibility for large scale cultivation (Perez-Garcia et al., 2011). Mixotrophic growth regime is a variant of the heterotrophic growth regime, where CO_2 and organic carbon are simultaneously assimilated and both respiratory and photosynthetic metabolism operates concurrently (Pagnanelli et al., 2014).

1.2.1 High-added value products

Even if the microalgal biomass application for biofuel production is seen as an attracting alternative to conventional sources, today this application seems to be economically not feasible (Enamala et al., 2018; Markou and Nerantzis, 2013). Microalgae, as said before, have the ability to modify their biomass composition under controlled conditions, accumulating metabolites having applications in several sectors (Borowitzka, 2013).

Microalgal species	Astaxanthin	β-Carotene	Lutein	Carbohydrates	Lipids
Chlorella zofingiensis	1.5%, high light intensity [1] >4%, 0.2 M NaCl [1]	–	–	–	65.1%, N deficiency [2] 47.7%, P-deficiency [2]
Chlorococcum sp.	0.71%, addition of H_2O_2 [3]	–	–	39.8–41%, N deficiency [4]	–
Haematococcus pluvialis	4%, nutrient starvation [5] 10%, high light intensity and non-aerated mixotrophic cultivation [6]	–	–	74%, N-starvation [7] 48%, P-starvation [7] 48%, 0.8% NaCl [7]	43%, P-starvation [8]
Muriellopsis sp.	–	–	4.3% [9]	–	–
Scenedesmus almeriensis	–	–	4.5% [9]	–	–
Chlorella protothecoides	–	–	4.6%, high temperature (35 °C) [10]	–	50%, heterotrophy [11] 43.4%, 20 g/l NaCl [17]
Dunaliella salina		12% [9] 3.1%, high light intensity [12] 2.7%, N-starvation [13]		>55%, N-starvation [14]	
Eustigmatos cf. *polyphem*		>5%, N-deficieny [15]			
Vischeria stellata		5.9% [16]			

Fig. 5 Content of different metabolites in relation to various stress factors in selected microalgal species (Markou and Nerantzis, 2013).

The main microalgal compounds that might be of particular interest are lipids, carbohydrates, proteins and pigments (carotenoids, etc.). In Fig. 5 the content of the main carotenoids, lipids or carbohydrates in relation to various stress factors in selected microalgal species are shown. As regards microalgal lipids, the industrial interest is focused on mainly to fatty acids as eicosapentaenoic acid (EPA) and docosahexaenoic acid (DHA), and some other high-value fatty acids (omega-3, omega-6, γ-linolenic acid etc.). These lipids, respect to those used for biodiesel production (neutral lipids including triacylglycerides (TAGs)) (Kim et al., 2013), have a different target market (Tocher et al., 2019). Beside lipids, also carbohydrates are a very interesting source for several application, moving from bio-plastics
(mainly in the form of starch) (Zeller et al., 2013) to bioethanol production (Ho et al., 2013). The major form of carbohydrates that is accumulated is starch, and it can be defined as transitory energy storage (TES) metabolite produced both phototrophically or

heterotrophically; it is degraded by glycolysis process after stressful conditions (or during night) in order to produce energy to carry out specific microalgal metabolic pathways (see subparagraph 1.2.2) (León-Saiki et al., 2017). A strain of *Tetraselmis suecica* was reported to accumulate between 11% and 47% of its dry weight (DW) as starch in nutrient replete vs deplete conditions (Barkia et al., 2019). Furthermore, besides lipids and carbohydrates, when microalgae are cultivated under stress conditions can accumulate specific secondary metabolites (such as carotenoids, vitamins etc.), which are high-added value products for cosmetic, food or pharmaceutical sector (Borowitzka, 2013; Panis and Carreon, 2016; Varela et al., 2015). Secondary metabolites do not play a role in growth and cellular division, like primary metabolites do, and are typically formed during the end or near the stationary growth phase.

1.2.2 Central Carbon Metabolism: a focus on Carbon Partitioning between lipids (TAG) and carbohydrates (starch)

Microalgal metabolism is so flexible and complex that it is not easy to carry out a complete description of the interconnections between the metabolic pathways. There are, however, example of constraints that govern central carbon metabolism in *Chlamydomonas reinhardtii*, revealed by compartmentalization and regulation of the pathways and their relation to key cellular processes such as cell motility, division, carbon uptake and partitioning (Johnson and Alric, 2013). In this thesis the study and modelling are based on metabolic pathways common between microalgal species in phototrophic cultivation, focusing the attention to the carbon partitioning process between TAG and starch. Notably, TAGs are produced mainly under conditions of physiological stress and in particular under nitrogen starvation (Breuer et al., 2012). During nitrogen starvation, not only TAG accumulation is induced, indeed other biomass constituents, such as starch, are produced simultaneously in a continuously changing ratio; this equilibrium between starch and TAG production is controlled by carbon partitioning mechanism (Breuer et al., 2014). Starch serves as a primary storage
compound, since the electrons required per unit of biomass are lower compared to TAG and proteins, which are more reduced than carbohydrates.

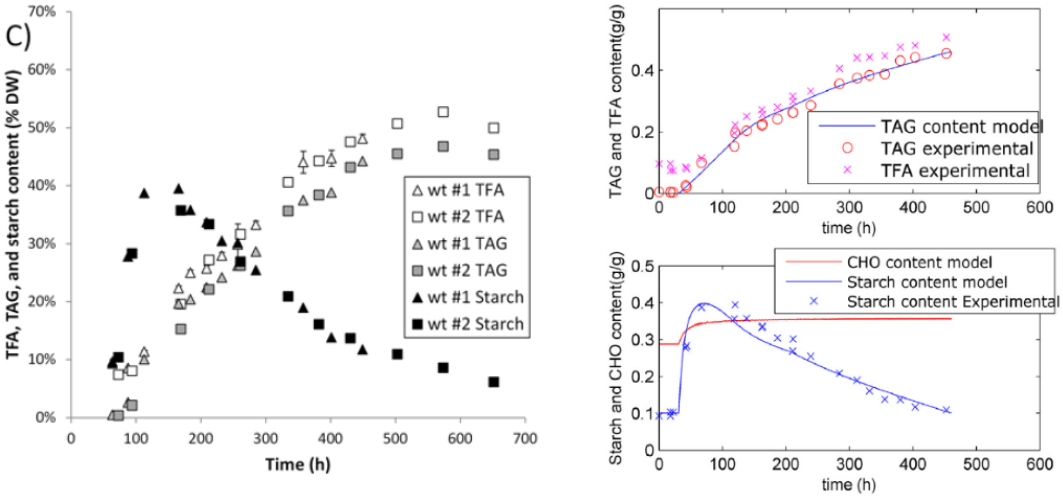

(a) (b)

Fig. 6 Experimental trends of TAG and starch content found in literature, showing the non-monotonous behavior of starch and the monotonous behavior of TAG justified by carbon partitioning between these two metabolites. (a) (Breuer et al., 2014) (b) (Breuer et al., 2015a).

Generally, starch is accumulated at the beginning of starvation with a higher rate than TAG (Adesanya et al., 2014; Breuer et al., 2015b, 2014; Zhu et al., 2014), showing a first increase until it reaches a maximum value and, after a certain period depending on cultivation conditions, decreases on the contrary of TAG that shows a monotonous trend (see Fig. 6). As regards TAGs, they are produced in order to protect the cell against the damage induced by adverse growth conditions, serving as an electron sink and avoiding the formation of reactive oxygen species (ROSs), such as H_2O_2 or superoxides, that can cause damage to the cell (Breuer et al., 2014). The main factor that regulate TAG and starch accumulation is the presence of nitrogen inside culture medium; indeed, only during nitrogen starvation microalgae stop to duplicate, moving their metabolism to accumulation of the aforesaid reserve compounds (Droop, 1968), reaching TAGs content up to 50% (% DW or g/g) and about 40% for starch (see Fig. 6). Indeed, during nitrogen starvation photosynthesis and carbon assimilation continue for a certain period, but the photosynthetic efficiency progressively decreases and the microalgae shift their metabolism on the production of nitrogen-free storage molecules such as TAG and starch, degrading them afterwards in order to obtain the necessary energy to carry out the metabolic pathways for their survival.

1.3 Microalgal cultivation methods

Microalgae cultivation reflects the versatility and complexity of these microorganisms, showing a wide variety of solutions always keeping as common goal the optimization of biomass or metabolites production. In order to carry out the microalgal phototrophic cultivation, several kinds of reactors have been studied until today. On large scale, algae can be cultured in open ponds, presenting low investment and operating costs and can be constructed on nonagricultural lands but they can be easily contaminated (Acién Fernández et al., 1999).

Cultivation system	S/V ratio	Mixing	Temperature control	Gas exchange	Advantages	Limitations
Open ponds[a]	High	Paddle wheel	None	Poor, only achieved through surface aeration	Cost effective Simple and flexible design Beneficial for mass cultivation	Lower biomass productivity Less control over culturing conditions, Susceptible to contamination, Occupy large land space, lower mass transfer Water and CO_2 loss due to evaporation
Stirred tank PBR[b]	Low	Mechanical agitator	Heat exchanger	Injection through sparger	Good heat and mass transfer Good light dispersion Lower contamination issues Simple design Moderate biomass productivity	Low surface to volume ratio Heating issue due to agitation Mechanical agitation require extra energy, expensive, not scalable
Vertical column PBR[b,d]	Low	Airlift/bubble	–	Open gas exchange at head space	High mass transfer No internal structure Lack of moving parts Good mixing with low shear stress Lower photo inhibition	Low surface area for illumination Expensive construction material Limited scale up due to design constrains, shading effect issues
Horizontal tubular PBR[b,d]	High	Recirculation via pumps	Shading, overlapping, water spraying	Injection into feed, dedicated degassing unit	High surface to volume ratio Low hydrodynamic stress Suitable for outdoor cultivation, good biomass productivity, cost effective Low mutual shading effect	Dissolve Oxygen build up Susceptible to photo inhibition Fouling due to algal growth Large space requirement Poor temperature regulation
Flat panel PBR[b,c,d]	High	Airlift/bubble from bottoms or side	Heat exchange coils	Open gas exchange at head space	High surface to volume ratio Low space requirement High photosynthetic efficiency, cheap and economic, low oxygen buildup	Short light penetration depth Not scalable, requires many components, frequent fouling and clean up issues, poor temperature regulation

Fig. 7 Advantages and limitations of microalgal phototrophic cultivation system (Gupta et al., 2015).

To overcome the disadvantages of using open cultivations, numerous closed photo-bioreactors (PBRs) of various volumes and shapes have been designed (Abiusi et al., 2014; Cicci et al., 2015; García Camacho et al., 1999). To sum up these considerations, in Fig. 7 a comparison between the various phototrophic solutions is showed. Microalgae can growth and accumulate useful products also without light, working in so-called dark fermentation (heterotrophy), employing thus the ability of some of them to grow using organic carbon source (sugar). The production of microalgae in fermenters has proven to be a very successful route to commercialization (see Fig. 8).

Fig. 8 Commercial fermentation plant for microalgae production. (Barclay et al., 2013).

Fermentation represents a long-established type of production process, both in equipment design and operation, with a high level of control on the process that make simple the optimization of the cultivation conditions and therefore also of the cell growth and metabolites production. The closed nature of fermentor also makes it easier to maintain a monoculture of the desired strain, particularly under axenic conditions, which facilitate the use of the algae in food sector. In addition to classical axenic conditions also studies about

fed-batch strategy to produce microalgal biomass under non-axenic conditions have been proposed (Di Caprio et al., 2019). Another advantage of fermentation is the achievement of higher cell densities (>100 g L^{-1}) respect to phototrophic one, reducing many of the problems related to recovering cells from the dilute cell concentrations (0.5-2 g L^{-1}), which are generally found in outdoor ponds.

1.3.1 Outdoor Cultivation: parameters affecting microalgal growth

In this subparagraph a focus on the phototrophic cultivation, and in particular on the outdoor systems, is carried out. As said before, microalgal autotrophic cultivation can be performed in indoor or outdoor systems; the outdoor cultivations are nowadays carried out in open ponds or in closed photobioreactors with different geometries and dimensions, making possible to choose the best solution individually. Each attempt to cultivate algal biomass in this way has to face principally with problems of light amount and distribution, but also with temperature variations and contaminations from competitive microorganisms (Acién et al., 2017b). Contaminations can be reduced using closed reactors that give the possibility of maintaining a strict control of operating variables, reaching generally higher productivities. Light intensity and duration are two of the major limiting factors in microalgae cultivation, directly affecting microalgal photosynthesis mechanism, influencing thus biomass yield and their intracellular composition (Krzemińska et al., 2014). Light amount varies inside the culture, reducing its value with the increase of reactor's light path (diameter, width, etc.) or culture density. Indeed, the main objective and also limiting factor of a phototrophic cultivation is the introduction of sufficient light amount (artificial or natural) in order to allow microalgal growth up to dense populations (Mata et al., 2010). At very low and very high light intensities microalgae cannot grow efficiently, indeed at very high light intensities photoinhibition effects occur, meanwhile at low light intensities problems of photolimitation arise (Sforza et al., 2014).
Thus, optimal light intensity needs to be determined experimentally in each case in order to maximize CO_2 assimilation and to reduce the photoinhibition as much as possible. In addition to light, temperature is also an important limiting factor for growing algae in both indoor or outdoor systems. Many microalgae can tolerate temperature increases or decreases, but diverging the optimum temperature by only 2 or 4 °C may lead to culture loss (Steyer, 2013). Moreover, overheating problems may occur in outdoor systems, making it necessary to use cooling systems to keep temperatures below 28-30 °C (Mazzelli et al., 2018a). Generally, temperature in microalgae cultures mainly increases due to the absorption of heat by radiation from the sunlight source; the optimal temperature for microalgae growth ranges from 20°C to 35°C, although some mesophilic species can tolerate up to 40°C (Acién et al., 2017b). Furthermore, also pH, mixing and nutrients' supply have to be controlled in order to optimize the microalgal outdoor cultivation. The optimal pH ranges from 7.5 to 8.5, since the biomass productivity strongly decreases at pH above 9.0 (Acién et al., 2017b). For mixing optimization, a sufficient turbulence of microalgae cultures reduces the gradient of nutrients in the culture broth, avoiding thus cell sedimentation in the system and forcing cells to move between dark to light zones,

enhancing photosynthesis. As regards nutrients, their correct dosage and supply avoids that the cultivation works at limiting conditions in which cell productivity decreases. On the contrary, as already described in the previous paragraph 1.2, working under nutrient stressful conditions (i.e. nutrient starvation) allows the accumulation of the desired metabolites (starch and lipids). Consequently, the correct nutrient amount and supply procedure have to be carefully chosen in accordance with the purpose of the cultivation that will be carried out.

1.4 Microalgal growth modeling

In last two decades an increasing number of scientists have tried to predict microalgal growth and metabolites production under transient conditions of light intensity and temperature using empirical models (Blanken et al., 2016; Katsuda et al., 2000) or semi-empirical models (Bernardi et al., 2017; Klok et al., 2013). The classification of these various types of models is very difficult and depends on what is necessary to be investigated. With respect to light modeling and its connection to microalgal growth, there is a differentiation based on the models' ability to take into account light gradients (Acién Fernández et al., 1997), light cycles (Quinn et al., 2011; Solimeno et al., 2017) and also physical phenomena (as scattering) that occur in outdoor cultures.
Indeed, this differentiation brought to formation of three macro groups for photosynthesis models:

- **Type I models:** They are able to predict the growth rate as a function of the incident light and the average light intensity, considering cultures inside the reactor in a well-mixed condition.
- **Type II models:** They calculate the overall productivity as the sum of local productivity inside the reactor volume, without considering short light cycles.
- **Type III models:** They consider the rate of photosynthesis as sum of the individual algae cell rates of photosynthesis that are function of their ‘light story’ (i.e. the light intensity experienced by an algae cell over time as it moves in the system).

In the compartmental model developed in this thesis (paragraph 2.4) only Type I models are considered, assuming thus well-mixed conditions inside the reactor with the growth rate depending on the averaged light intensity inside the culture volume. As regards temperature, the modeling approaches can be divided into coupled and uncoupled, depending on whether the models take into account or not the potential interdependence of light and temperature on growth (Béchet et al., 2013). Predictive power of such models is usually achieved with the usage of large number of parameters that are hardly relatable to physical or chemical phenomena (Baroukh et al., 2017; Figueroa-Torres et al., 2017; Marsullo et al., 2015; Ryu et al., 2018; Solimeno et al., 2017). These problems inevitably affect the model validation for an end user that want to apply it to different outdoor

conditions respect to those used in the model development. For these reasons, there is a need to develop models that an end user would be easily able to handle and adapt, without losing accuracy (A. Mazzelli et al., 2019a).
Another models' classification, based on the cultivation limiting factors is resumed below:

One limiting factor

Light saturating conditions:

- Balance growth approximation
- Monod-like models
- Droop like model

Light depending growth (unsaturated light conditions):

- Empirical models
- Mechanistic models

More limiting factors

- Structured models or compartmental models (also called in this work as "metabolic models")
- Mechanistic models (River Water Quality Model)

This latter classification will be used as reference in this paragraph and in the following one (paragraph 1.5). In particular in these two paragraphs only models related to those developed in this study will be discussed.

1.4.1 Monod-like and Droop-like models

Generally, the Monod-like methods are widely used to model nutrient limitation and primary productivity in water bodies, offering a straight-forward approach to simulate the main processes governing eutrophication and allowing the proper representation of many aquatic systems. The Monod approach is simpler because it directly relates growth with available nitrogen and phosphorus in the culture medium. However, it ignores the phenomenon of luxury uptake, where nutrients are acquired and stored at levels well beyond the immediate demand for growth (see Fig. 9). By drawing on internal nutrient reserves, microalgae can grow at nearly maximum rates during periods of nutrient depletion. The Droop method relates algae and plant growth to their internal nutrient levels, or cell quotas, and the minimum cell quotas, which are the internal nutrient concentrations below which growth ceases (see Fig. 10). This method allows nutrient luxury uptake to be taken into account, but it is more complex from a computational standpoint. The Droop method requires the mass balance of the internal nutrient pool to be calculated, considering the contributions from nutrient uptake from the water column, and the losses through demand and growth. The relative computational complexity required by the Droop method delayed its implementation in compartmented and dynamic water quality (see subparagraph 1.4.2).

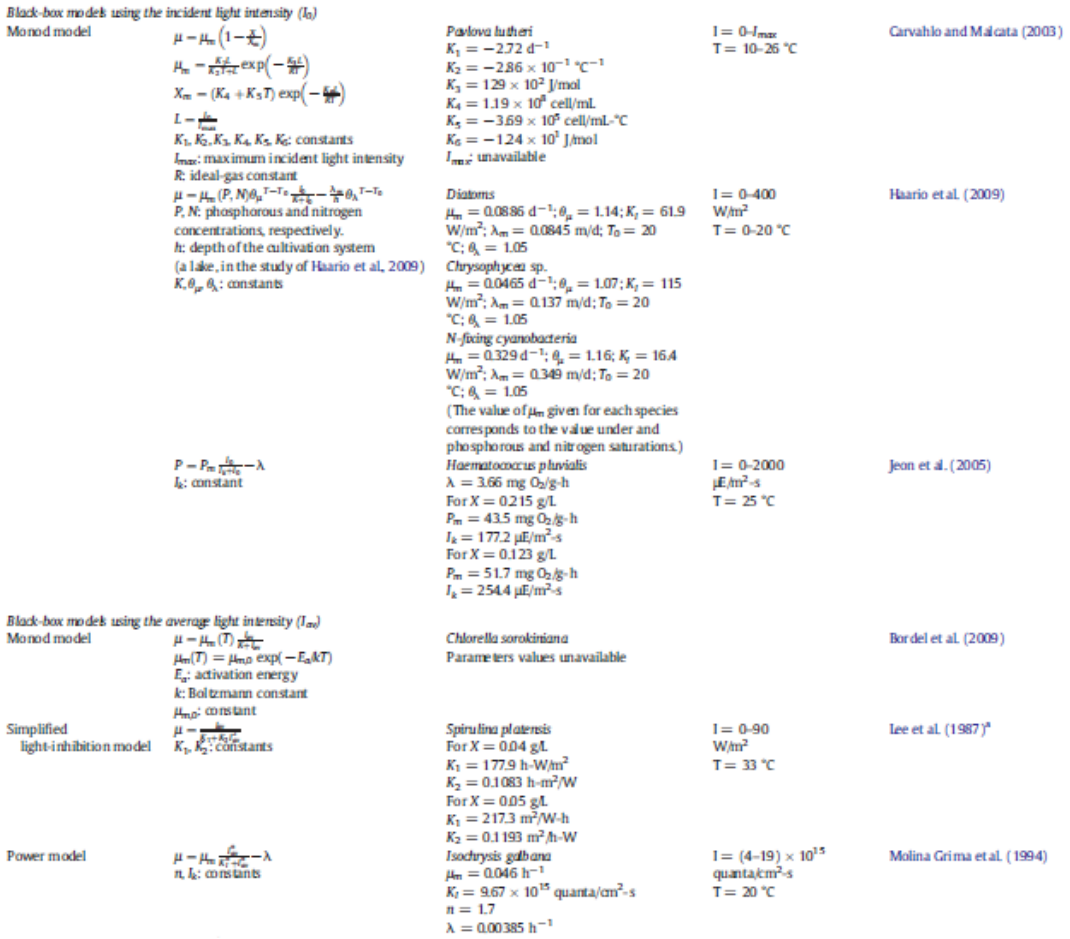

Black-box models using the incident light intensity (I_0)				
Monod model	$\mu = \mu_m\left(1-\frac{X}{X_m}\right)$ $\mu_m = \frac{K_2 L}{K_3 T - L}\exp\left(-\frac{K_4 L}{RT}\right)$ $X_m = (K_4 + K_5 T)\exp\left(-\frac{K_6}{RT}\right)$ $L = \frac{I_0}{I_{max}}$ $K_1, K_2, K_3, K_4, K_5, K_6$: constants I_{max}: maximum incident light intensity R: ideal-gas constant	*Pavlova lutheri* $K_1 = -2.72\ d^{-1}$ $K_2 = -2.86 \times 10^{-1}\ °C^{-1}$ $K_3 = 1.29 \times 10^2$ J/mol $K_4 = 1.19 \times 10^8$ cell/mL $K_5 = -3.69 \times 10^6$ cell/mL·°C $K_6 = -1.24 \times 10^3$ J/mol I_{max}: unavailable	I = 0–I_{max} T = 10–26 °C	Carvahlo and Malcata (2003)
	$\mu = \mu_m(P,N)\theta_\mu^{T-T_0}\frac{I_0}{K+I_0}-\frac{\lambda_w}{h}\theta_\lambda^{T-T_0}$ P, N: phosphorous and nitrogen concentrations, respectively. h: depth of the cultivation system (a lake, in the study of Haario et al., 2009) $K, \theta_\mu, \theta_\lambda$: constants	*Diatoms* $\mu_m = 0.0886\ d^{-1}$; $\theta_\mu = 1.14$; $K_I = 61.9$ W/m^2; $\lambda_w = 0.0845$ m/d; $T_0 = 20$ °C; $\theta_\lambda = 1.05$ *Chrysophyceen sp.* $\mu_m = 0.0465\ d^{-1}$; $\theta_\mu = 1.07$; $K_I = 115$ W/m^2; $\lambda_w = 0.137$ m/d; $T_0 = 20$ °C; $\theta_\lambda = 1.05$ *N-fixing cyanobacteria* $\mu_m = 0.329\ d^{-1}$; $\theta_\mu = 1.16$; $K_I = 16.4$ W/m^2; $\lambda_w = 0.349$ m/d; $T_0 = 20$ °C; $\theta_\lambda = 1.05$ (The value of μ_m given for each species corresponds to the value under and phosphorous and nitrogen saturations.)	I = 0–400 W/m^2 T = 0–20 °C	Haario et al. (2009)
	$P = P_m\frac{I_0}{I_k+I_0}-\lambda$ I_k: constant	*Haematococcus pluvialis* $\lambda = 3.66$ mg O_2/g-h For $X = 0.215$ g/L $P_m = 43.5$ mg O_2/g-h $I_k = 177.2$ µE/m^2-s For $X = 0.123$ g/L $P_m = 51.7$ mg O_2/g-h $I_k = 254.4$ µE/m^2-s	I = 0–2000 µE/m^2-s T = 25 °C	Jeon et al. (2005)
Black-box models using the average light intensity (I_m)				
Monod model	$\mu = \mu_m(T)\frac{I_m}{K+I_m}$ $\mu_m(T) = \mu_{m,0}\exp(-E_a/kT)$ E_a: activation energy k: Boltzmann constant $\mu_{m,0}$: constant	*Chlorella sorokiniana* Parameters values unavailable		Bordel et al. (2009)
Simplified light-inhibition model	$\mu = \frac{I_m}{K_1 + K_2 I_m}$ K_1, K_2: constants	*Spirulina platensis* For $X = 0.04$ g/L $K_1 = 177.9$ h-W/m^2 $K_2 = 0.1083$ h-m^2/W For $X = 0.05$ g/L $K_1 = 217.3$ m^2/W-h $K_2 = 0.1193$ m^2/h-W	I = 0–90 W/m^2 T = 33 °C	Lee et al. (1987)[a]
Power model	$\mu = \mu_m\frac{I_m^n}{K_I^n + I_m^n}-\lambda$ n, I_k: constants	*Isochrysis galbana* $\mu_m = 0.046\ h^{-1}$ $K_I = 9.67 \times 10^{15}$ quanta/cm^2-s $n = 1.7$ $\lambda = 0.00385\ h^{-1}$	I = (4–19) × 10^{15} quanta/cm^2-s T = 20 °C	Molina Grima et al. (1994)

Fig. 9 Examples of Monod-like models used to estimate the specific growth rate in different conditions (Béchet et al., 2013).

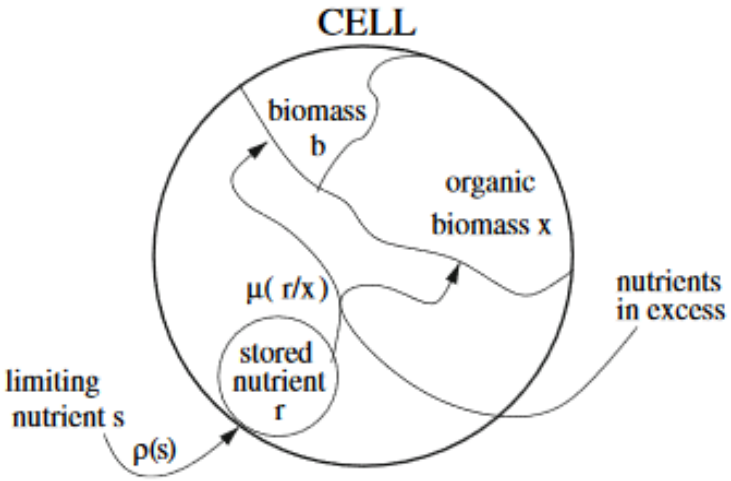

Fig. 10 Examples of a Droop-like model used to estimate cell growth and luxury uptake(Lemesle and Mailleret, 2008).

1.4.2 Compartmental Models (Metabolic Models)

As described in previous subparagraph 1.4.1, physiological models try to describe the dynamic behavior of photosynthetic cells, trying to simulate the actual mechanisms that is involved in the cells' growth. One promising modeling framework is based on Dynamic Flux Balance Analysis (DFBA) (see subparagraph 1.5.2). A DFBA model formulation is the integration of genome-scale metabolic models with mass conservation laws applied to the extracellular environment (Mahadevan et al., 2002). Indeed, this sort of models are used not only to model the photosynthetic mechanisms inside microalgae, but also to model the metabolic pathways occurring inside the cells in all kinds of cultivations (phototrophy, heterotrophy, mixotrophy), in order to simulate the metabolites accumulation. In the simple Flux Balance Analysis (FBA), models are based on the assumption that the intracellular reaction network has reached a quasi-steady state (balanced-growth assumption). Initially in the DFBA development was assumed that the intracellular dynamics were faster than extracellular dynamics such that the quasi-steady state approximation for the FBA model remained valid. For organisms that undergo to fluctuations of cultivation conditions (e.g. nutrient depletion or repletion), this assumption is not justifiable because dynamic intracellular accumulation and consumption are essential in the metabolism of the cells.

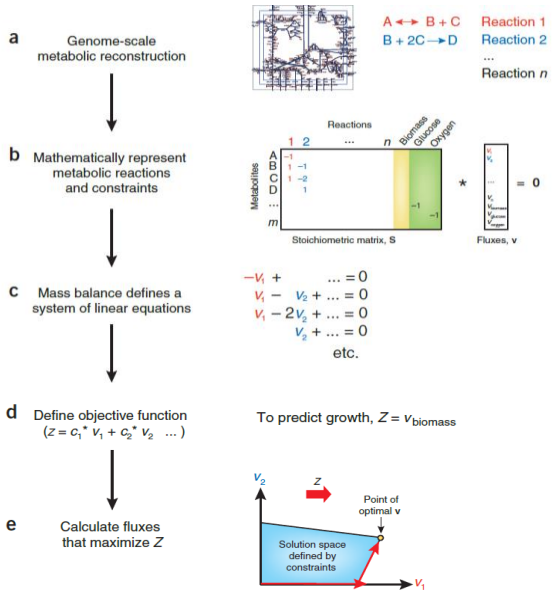

Fig. 11 Formulation of a FBA problem (Orth et al., 2010).

For this reason, the DFBA formulation was modified with the addition of intracellular dynamic states. In Fig. 11, for a better clarity, a schematic formulation of a generic FBA problem is shown. Initially in the FBA studies only *Chlamydomonas reinhardtii* was generally chosen as a representative of algal species, due to its versatile and complete metabolism. Afterwards, other species have been used as reference for this method: e.g *Synechocystis* (Shastri and Morgan, 2005) or *Chlorella sorokiniana* (Baroukh et al., 2017). The reconstructed metabolic network of *C. reinhardtii* consists of 458 metabolites and 484 metabolic reactions. Almost half of the metabolites included in the network are present in the chloroplast, which is a result of the large number of reactions localized to the chloroplast (212 out of 484). The cytosol acts as the 'hub' of transport for metabolites as well as the polymerization location for most macromolecules; as a result, roughly one third of the metabolites in the model are localized there. Another significant portion of reactions in the model function as intracellular transporters, which indicates the high interconnectivity between the compartments. As example of FBA, the Baroukh et. al work (Baroukh et al., 2017) based on the dynamic metabolic modeling of heterotrophic and mixotrophic microalgal growth on fermentative wastes, is presented. Indeed, in Baroukh work, not only photosynthesis mechanism is studied, but also the uptake of an external organic carbon source is investigated for a more complete analysis. In Fig. 12 the central carbon metabolic network, reconstructed by Baroukh, is shown. In particular, the central carbon metabolic network is composed of photosynthesis, the glyoxysome, citric acid cycle, glycolysis, carbohydrate synthesis, pentose phosphate pathway, lipid synthesis, oxidative phosphorylation, protein, DNA, RNA, chlorophyll and biomass synthesis.

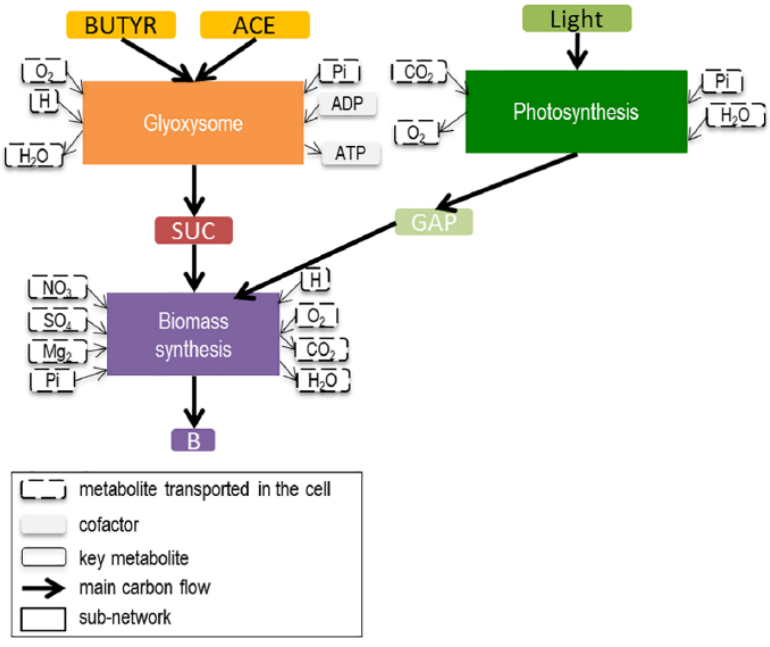

Fig. 12 Central carbon metabolic network of a unicellular microalga decomposed into three sub-networks presented in Baroukh's model (Baroukh et al., 2017).

During photosynthesis, inorganic carbon (CO_2) is assimilated using light energy to produce a 3-carbon sugar glyceraldehyde 3-phosphate (GAP). In the glyoxysome, the acetate and

butyrate are degraded to Acetyl-CoA, which is then transformed to succinate (SUC) thanks to the glyoxylate cycle. SUC and GAP are then used as primary precursors to produce precursor metabolites and energy via the Tricarboxylic Acid (TCA) cycle for protein, DNA, RNA, carbohydrate and lipid synthesis. The metabolic model described by Baroukh is based on the Dynamic Reduction of Unbalanced Metabolism (DRUM) previously developed by the same author (Baroukh et al., 2016). DRUM approach defines the sub-networks (visible in Fig. 12) as metabolic functions and take into account cellular compartments; indeed, the metabolites situated at the junction between the sub-networks, can therefore have dynamics of accumulation and depletion. Each sub-network is then reduced to macroscopic reactions (MRs) using Elementary Flux Mode analysis (EFM). In Fig. 13 the Elementary Flux Mode (EFM) applied to the schematization of Fig. 12, listing also the macroscopic reactions with their rates (kinetics), is figured.

Sub-network	Macroscopic reactions	Kinetics
Acetate & Butyrate assimilation	3.5 H + 2 ACE + 0.5 O2 —> SUC + 1.5 H2O (MR1)	$\gamma_{MR1} = k_{MR1} * \frac{ACE}{Ks_{MR1}+ACE}$
	7 H + 1.5 O2 + 1 BUTYR —> 1 SUC + 5 H2O (MR2)	$\gamma_{MR2} = \frac{k_{MR2}*BUTYR}{BUTYR+\frac{k_{MR2}}{\beta_{MR2}}*\left(\frac{BUTYR}{Sopt_{MR2}}-1\right)^2} * \frac{k_D}{ACE+k_D}$
Photosynthesis	24 Light + 3 CO2 + 2 H2O + 1 Pi—> 1 GAP + 3 O2 (MR3)	$\gamma_{MR3} = \frac{\gamma_{MR3}(1-e^{\beta_{MR1}B})}{\beta_{MR1}B}$
Biomass synthesis	7.30239 H + 4.61237 O2 + 4.14597 SUC + 0.984915 NH4 + 0.1216 Pi + 0.02169 SO4 + 0.0101 Mg2 —> 1 Biomass + 7.04167 H2O + 8.06249 CO2 (MR4)	$\alpha_{MR4} = k_{MR4} * SUC$
	4.14597 GAP + 2.53938 O2 + 0.984916 NH4 + 0.02169 SO4 + 0.0101 Mg2 —> 0.989545 H + 1 Biomass + 2.8957 H2O + 3.91652 CO2 + 4.02437 Pi (MR5)	$\alpha_{MR5} = k_{MR5} * GAP$

Fig. 13 Definition and reduction of sub-networks formed from metabolic reactions of *Chlorella sorokiniana* for heterotrophic and mixotrophic growth presented in Baroukh's model (Baroukh et al., 2017).

Finally, for the model's resolution, the dynamics of the 172 fluxes in the metabolism can be derived from a system of 14 differential equations comprising 14 metabolites and 5 macroscopic reactions representing 3 compartments. The dynamic model has 10 degrees of freedom, and each degree is represented by a parameter that needs to be calibrated. In order to estimate the parameters reducing the risk of local minima, several optimizations were performed with random initial parameters.

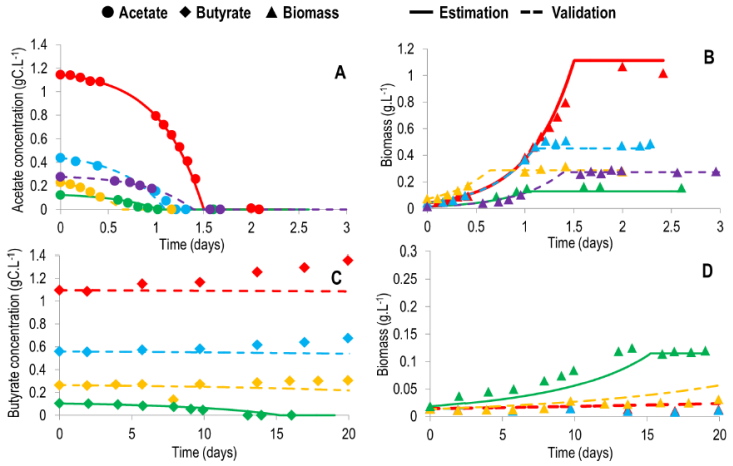

Fig. 14 Comparison between the model and experimental data for *Chlorella* presented in Baroukh work (Baroukh et al., 2017)

Even if the results obtained from the model are very similar to experimental data (see Fig. 14), this approach remains always too complex and not handy for a final user.

1.4.3 Mechanistic models

Since in this thesis work, a model for prediction of microalgal growth in photobioreactors at specific outdoor conditions using multivariate statistic has been developed, some examples of models available in literature with the same aim are presented in this subparagraph. In particular, these examples are the newest representatives of other similar or older models available in literature. Mathematical models give the opportunity to study simultaneous effects of several factors affecting microalgal growth in outdoor cultivation (see subparagraph 1.3.1) and allow prediction of microalgal production. As previously described, in order to optimize one factor influencing the microalgal cultivation, the other factors are kept at optimal conditions in order to avoid limiting or inhibitory effects. In this way the developed model will depend only on single factor such as light intensity (Darvehei et al., 2017), temperature (Béchet et al., 2017), nitrogen (Tiwari et al., 2019) and photoinhibition effects (Bernardi et al., 2017), without considering also factors' interactions. In literature, models of increasing complexity with two or more factors are few (Béchet et al., 2013; Breuer et al., 2013). As recent example of microalgal growth prediction model in outdoor cultivation, the Solimeno et. al work is presented (Solimeno et al., 2017). The model is applied to a similar raceway pond system and is based on the River Water Quality Model 1 (RWQM1) of the International Water Association (Vanrolleghem et al., 2001), selected because considers microalgal activity. The conceptual schematization of the model is shown in Fig. 15.

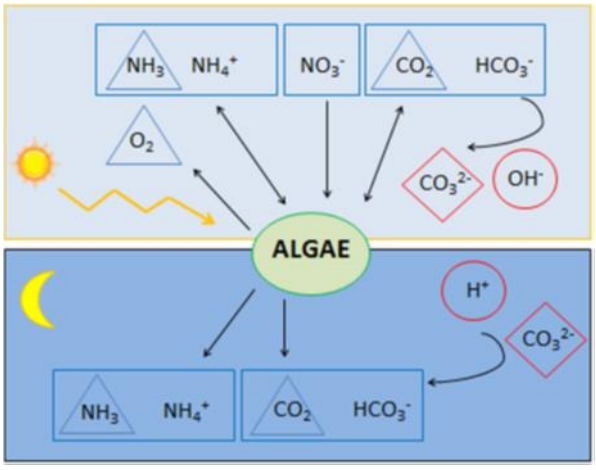

Fig. 15 Schematization of Solimeno et al. model (Solimeno et al., 2015). Microalgae are represented by green ellipse, substrates by rectangles, gaseous species by triangles and species depending on algal activity by diamonds and circles. Other nutrients (e.g. phosphorus) and micronutrients are not limiting factors.

This figure shows that microalgae grow with light, consume substrates (i.e. carbon and nitrogen) and release oxygen; in particular the model considers microalgae growing inside wastewaters. For this reason, the other nutrients (e.g. phosphorus) and micronutrients are not considered as limiting factors because they are usually highly available in wastewater.

Ass result of microalgal activity, hydroxide ions concentration and pH increase. Increasing pH displaces the equilibrium of the carbon species towards the formation of carbonates. In darkness, endogenous respiration and inactivation of microalgae release carbon dioxide, the concentration of hydrogen ions increases and pH decreases. By decreasing pH, the carbon equilibrium shifts and carbonate turns into bicarbonate, which can be used as substrate again in the presence of light. Furthermore, in Fig. 16 the mathematical description of the model's processes, in terms of process rate, is resumed. It is visible in Fig. 16 that the increase of microalgae biomass (processes 1a and 1b) per unit of time (growth rate) is expressed as the product of their maximum specific growth rate (μ_{ALG}) by their concentration at that point (X_{ALG}), by substrate functions (in the form of Monod functions) that limit or inhibit their growth and by two corrective factors (η_{PS} and $f_{T,FS}$), that are respectively the photosynthetic and the thermic-photosynthetic factor.
These latter factors are used to model the temperature and light effects on photosynthesis and consequently on growth.

Processes	Process rate $[M \cdot L^{-3} \cdot T^{-1}]$
1a. Microalgae growth on ammonia	$\rho_{1a} = \mu_{ALG} * f_{T,FS}(T) * \eta_{PS}(I, S_{O2}) * \frac{S_{CO2}+S_{HCO3}}{K_{C,ALG}+S_{CO2}+S_{HCO3}+\frac{S_{CO2}^2}{K_{CO2,ALG}}} * \frac{S_{NH3}+S_{NH4}}{K_{N,ALG}+S_{NH3}+S_{NH4}} * X_{ALG}$
1b. Microalgae growth on nitrate	$\rho_{1b} = \mu_{ALG} * f_{T,FS}(T) * \eta_{PS}(I, S_{O2}) * \frac{S_{CO2}+S_{HCO3}}{K_{C,ALG}+S_{CO2}+S_{HCO3}+\frac{S_{CO2}^2}{K_{CO2,ALG}}} * \frac{S_{NO3}}{K_{N,ALG}+S_{NO3}} * \frac{K_{N,ALG}}{K_{N,ALG}+S_{NH3}+S_{NH4}} * X_{ALG}$
2. Microalgae endogenous respiration	$\rho_2 = k_{resp,ALG} * f_{T,FS}(T) * \frac{S_{O2}}{K_{O2,ALG}+S_{O2}} * X_{ALG}$
3. Microalgae inactivation	$\rho_3 = k_{death,ALG} * f_{T,FS}(T) * X_{ALG}$
4. Chemical equilibrium $CO_2 \leftrightarrow HCO_3^-$	$\rho_4 = k_{eq,1} * (S_{CO2} - \frac{S_H S_{HCO3}}{K_{eq1}})$
5. Chemical equilibrium $HCO_3^- \leftrightarrow CO_3^{2-}$	$\rho_5 = k_{eq,2} * (S_{HCO3} - \frac{S_H S_{CO3}}{K_{eq,2}})$
6. Chemical equilibrium $NH_4^+ \leftrightarrow NH_3$	$\rho_6 = k_{eq,3} * (S_{NH4} - \frac{S_H S_{NH3}}{K_{eq,3}})$
7. Chemical equilibrium $H^+ \leftrightarrow OH^-$	$\rho_7 = k_{eq,w} * (1 - \frac{S_H S_{OH}}{K_{eq,w}})$
8.Oxygen transfer to the atmosphere	$\rho_{O2} = Ka,O_2 * (S_{O2}^{WAT} - S_{O2})$
9.Carbon dioxide transfer to the atmosphere	$\rho_{O2} = Ka,CO_2 * (S_{CO2}^{WAT} - S_{CO2})$
10. Ammonia transfer to the atmosphere	$\rho_{NH3} = Ka,NH_3 * (S_{NH3}^{WAT} - S_{NH3})$

Fig. 16 Mathematical description of the processes used in Solimeno et al. model (in terms of processes rates) (Solimeno et al., 2017).

In Fig. 17 the equations related to $f_{T,FS}$ and η_{PS} are shown; in particular the photosynthetic factor (η_{PS}) takes into account the effects of light intensity (I) and excess of oxygen (S_{O2}) on photosynthesis and therefore on microalgal growth (f_L is the light factor and f_{PR} the photorespiration factor). The photosynthetic reactions follow the state model described in Wu model (Wu and Merchuk, 2001) in which PSUs inside microalgae are present in three different states: resting (x_1), activated (x_2), and inhibited (x_3) (see subparagraph 1.4.1).

$$f_{T,FS}(T) = e^{-\left(\frac{T-Topt}{s}\right)^2} \qquad \eta_{PS}(I, S_{O2}) = f_L(I) \cdot f_{PR}(S_{O2}) \qquad f_L(I) = x_2$$

$$f_{PR}(S_{O2}) = \begin{cases} 1 - \tanh\left(\dfrac{K_{PR} \cdot \dfrac{S_{O2}}{\tau \cdot S_{O2}^{SAT}}}{1 - \dfrac{S_{O2}}{\tau \cdot S_{O2}^{SAT}}}\right), & S_{O2} \le \tau \cdot S_{O2}^{SAT} \\ 0, & S_{O2} > \tau \cdot S_{O2}^{SAT} \end{cases}$$

Fig. 17 Equations used to describe temperature and light effects in the model introduced by Solimeno et al. (Solimeno et al., 2017).

The state in which microalgae can grow is x_2, indeed in Fig. 17 is visible that $f_L=x_2$. As regards temperature, the thermic photosynthetic factor ($f_{T,FS}$) takes into account the effects of temperature on microalgae growth and also on endogenous respiration and inactivation processes (see Fig. 17). In order to solve this model, in Fig. 18 the calculation of the reaction rate for each component of the model (r_i) is showed in the red-bordered sum, where **i** is the number of components and **j** is the number of processes, ρ_j is the reaction rate for each process j and $v_{i,j}$ is the stoichiometric coefficient.

$r_i = \sum_j v_{j,i} * \rho_j$ — State variables → *i* / Processes ↓ *j*		S_{NH4} gN m^{-3}	S_{NH3} gN m^{-3}	S_{NO3} gN m^{-3}	S_{O2} gO$_2$ m^{-3}	S_{CO2} gC m^{-3}	S_{HCO3} gC m^{-3}	S_{CO3} gC m^{-3}	S_H gH m^{-3}	S_{OH} gH m^{-3}	X_{ALG} gCOD·m^{-3}
1a. Microalgae growth on ammonia	ρ_{1a}	$v_{1,1a}$			$v_{4,1a}$	$v_{5,1a}$			$v_{8,1a}$		$v_{10,1a}$
1b. Microalgae growth on nitrate	ρ_{1b}			$v_{3,1b}$	$v_{4,1b}$	$v_{5,1b}$			$v_{8,1b}$		$v_{10,1b}$
2. Microalgae endogenous respiration	ρ_2	$v_{1,2}$			$v_{4,2}$	$v_{5,2}$			$v_{8,2}$		$v_{10,2}$
3. Microalgae inactivation	ρ_3	$v_{1,3}$			$v_{4,3}$	$v_{5,3}$			$v_{8,3}$		$v_{10,3}$
4. Chemical equilibrium $CO_2 \leftrightarrow HCO_3^-$	ρ_4					$v_{5,4}$	$v_{6,4}$		$v_{8,4}$		
5. Chemical equilibrium $HCO_3^- \leftrightarrow CO_3^{2-}$	ρ_5						$v_{6,5}$	$v_{7,5}$	$v_{8,5}$		
6. Chemical equilibrium $NH_4^+ \leftrightarrow NH_3$	ρ_6	$v_{1,6}$	$v_{2,6}$						$v_{8,6}$		
7. Chemical equilibrium $H^+ \leftrightarrow OH^-$	ρ_7								$v_{8,7}$	$v_{9,7}$	
8. Oxygen transfer to the atmosphere	ρ_{O2}				$v_{4,02}$						
9. Carbon dioxide transfer to the atmosphere	ρ_{CO2}					$v_{5,CO2}$					
10. Ammonia transfer to the atmosphere	ρ_{NH3}		$v_{2,NH3}$								

Fig. 18 Matrix of stoichiometric parameters that relates processes and components through stoichiometric coefficients (Solimeno et al., 2015).

Note that microalgae grow with both carbon dioxide (S_{CO2}) and bicarbonate (S_{HCO3}) (ρ_{1a} and ρ_{1b}) and in the matrix of stoichiometric parameters (Fig. 18) only the reaction rate of carbon dioxide is affected by microalgae growth because the concentration of bicarbonate is already in chemical equilibrium with it.
Another example, completely different from the previous one, of microalgal growth prediction model in outdoor cultivation is represented by Huesemann et al. model (Huesemann et al., 2016), applied to an open pond system. The conceptual scheme of this model is shown in Fig. 19.

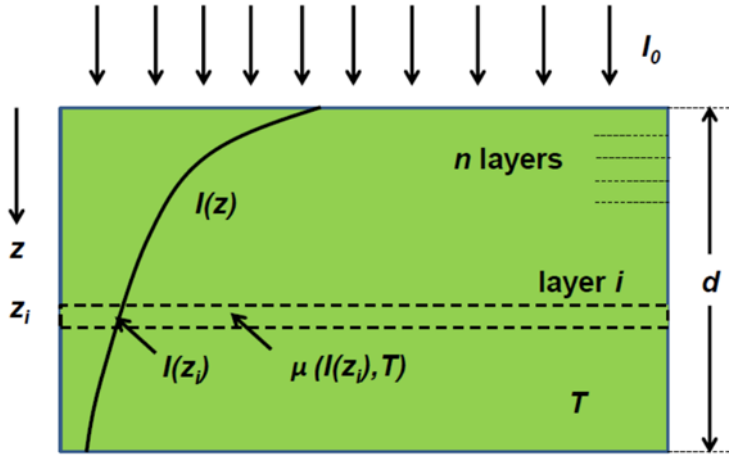

Fig. 19 Conceptual scheme of the microalgal growth prediction model introduced by Huesemann et al. (Huesemann et al., 2016).

Particularly, in this model light and temperature are assumed to be as key and instantaneous determinants of microalgae growth and productivity, and that no other factor (such as nutrients, CO_2, and mixing) limits or inhibits growth. Furthermore, also pH remains constant via feed-back controlled CO_2 addition. In Fig. 20 the principal equations used to develop this model are resumed.

$$\mu = f(T, I) \qquad I(z) = I_0 \cdot e^{-k_{sca} B \cdot z}$$

$$k_{sca} = k_a \cdot \frac{K_B}{K_B + B} \cdot \frac{K_z}{K_z + z} \qquad B(t + \Delta t) = B(t) \cdot e^{\mu \cdot \Delta t}$$

$$\mu_{dark} = f(T, I_{avg}) \quad I_{avg} = I_0 \cdot \frac{1 - e^{-k_a \cdot OD_{750} \cdot d}}{k_a \cdot OD_{750} \cdot d}$$

Fig. 20 Equations used to describe microalgal growth in outdoor open-pond cultivation in the model introduced by Huesemann et al. (Huesemann et al., 2016).

It is visible that the specific growth rate depends only on two factors: light and temperature. As regards light (I) a simple Beer–Lambert's law, for a given biomass concentration (B), is used to describe light penetration inside the culture volume at each defined height (z). Particularly, the culture volume is discretized into n equal volume layers orthogonal to the incident light and the biomass concentration in each layer is assumed to increase exponentially from B(t) to B(t + Δt), as visible in Fig. 20. In particular, this light model falls within the Tipe I definifition described in paragraph 1.4. It is assumed that individual cells respond instantaneously to the new light conditions as they enter each successive volume layer and that they exhibit the corresponding experimentally determined specific growth rate for that particular light intensity. In this model also the scattering phenomena is taken into account, since in Beer–Lambert's law the light attenuation coefficient (k_{sca}) is used. Since overnight biomass loss due to dark respiration can have a significant and negative effect on biomass productivity, in this model also the biomass loss rate (μ_{dark}), in the absence of light, is calculated as a function of temperature (T) and of averaged light intensity (I_{avg}) to which the cells are exposed in the mixed pond culture. Moreover, since both μ and $\mu_{dark,}$, in addition to light (I or I_{avg}), are influenced from temperature, in this model the dependence f(T,I) is added and considered strain-specific and to be determined experimentally prior to running the model. In particular the measurements of the specific growth rate (μ) as a function of incident light intensity and temperature were determined as a function of temperature in dilute, light-sufficient, exponentially growing shaker flask batch cultures placed on a thermal gradient incubator (8 temperatures, ranging from ca. 13 to 45 °C).
As last example a dynamic model, developed by Marsullo et al. (Marsullo et al., 2015), of microalgae outdoor cultivation in flat panel photobioreactors is presented.

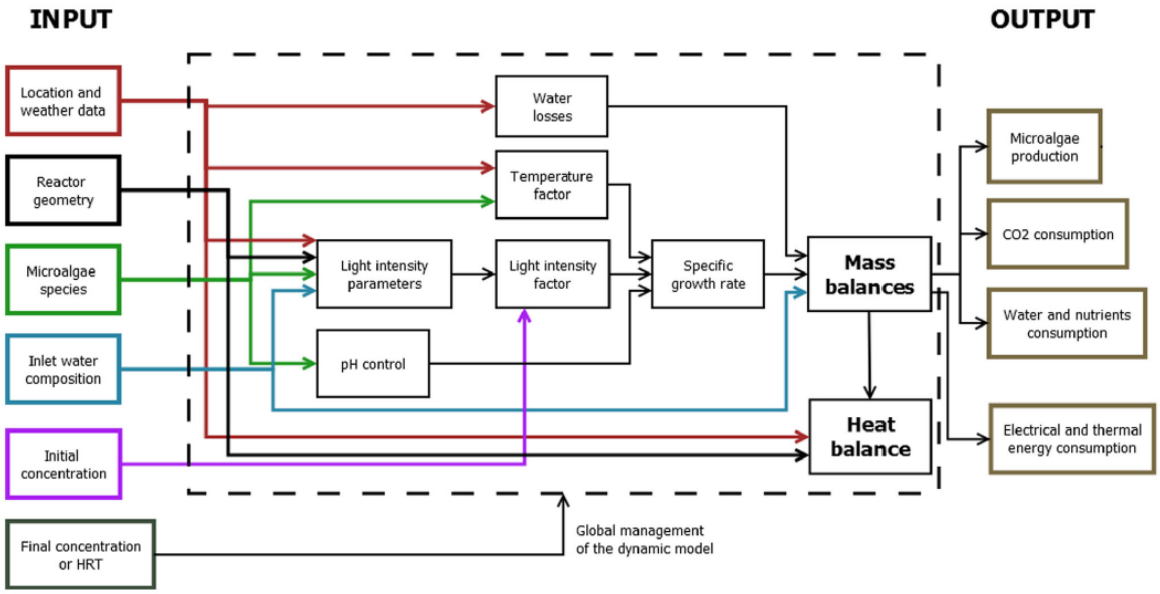

Fig. 21 Model structure presented by Marsullo et al. (Marsullo et al., 2015).

Even this model is completely different from the previous and includes all physical and chemical quantities that mostly affect microalgal growth. The equation of the microalgal specific growth rate is influenced by: CO_2 and nutrients concentration in the water, light intensity, temperature of the water in the reactor and by considered microalgal species. The schematization of this model can be found in Fig. 21. The mass and energy produced by this cultivation system are calculated by the mathematical model through time-dependent mass and energy balances as visible in Fig. 21, where the inputs and outputs of the model are indicated. In this model a dynamic approach for the resolution of energy and mass balances was preferred to a steady state analysis since the laws describing the outdoor microalgal growth are time dependent and a dynamic model gives a deeper and more accurate evaluation of microalgae production and energy consumption over the time period. Mathematically the model is constituted by a differential algebraic equations system, converted into a set of algebraic equations by finite differences (backward) approximation. Some of the differential equations depend on one another, making impossible to solve them in a sequential logic: it is, therefore, necessary to solve them altogether as a system. A peculiar characteristic of this model is its application to two different microalgae species, considering thus the species as input parameter to add in the model. Differently from other models that consider only weather or position's conditions for the outdoor model's development, in Marsullo model also the "composition of the inlet water" and the "operating strategy" are added as input. In particular this latter parameter is divided in two different strategies: if the objective consists in searching the hydraulic retention time (HRT) required to reach a certain microalgae concentration in the reactor, the initial and the final microalgae concentrations are to be supplied as input information to the model. If the HRT is fixed along the whole time period, then the input data will be the initial concentration and the HRT, leaving the final concentration in the reactor free to change.

In Fig. 22 the equations for growth rate (r_{gA}) are resumed. In particular X_A is the mass concentration of microalgae and μ_A is the specific growth rate depeding, in addition to nutrients, also on light intensity factor (f_I) and on temperature factor (f_T). In this model, only nitrogen is taken into as limiting factor and the presence of micro nutrients have not been introduced. For all parameters' definition see the corresponding reference (Marsullo et al., 2015).

$$r_{gA} = \mu_A X_A \qquad \mu_A = \hat{\mu}_A \left(\frac{CO_{2D}}{K_C + CO_{2D}} \right) \left(\frac{N_T}{K_{NA} + N_T} \right) f_I f_T$$

$$f_I = \frac{I_a}{I_s} \exp\left(1 - \frac{I_a}{I_s} \right) \qquad f_T = \left(\frac{T_{let} - T_w}{T_{let} - T_{opt}} \right)^{\beta_{algae}} \exp\left(-\beta_{algae} \left(\frac{T_{let} - T_w}{T_{let} - T_{opt}} - 1 \right) \right)$$

Fig. 22 Equations used to describe microalgal growth in outdoor flat panel cultivation in the model introduced by Marsullo et al. (Marsullo et al., 2015).

Focusing only light modeling, in Marsullo's model a detailed description of light influence on microalgae growth in outdoor cultivation is reported, as visible in Fig. 23 where the equations used to model light's effects are shown.

$$I_i(t) = I_0(t)(1 - R_1' R_2')T_m \qquad I_0(y,t) = G_{direct}(t) I_{direct}(t) + G_{diffuse}(y) I_{diffuse}(t)$$

$$I(y,z,t) = I_{front} e^{-(K_{e1} + K_{e2} X_A) z} + I_{back} e^{-(K_{e1} + K_{e2} X_A)(s - z)}$$

$$G_{direct}(t) = \frac{\cos\theta}{\cos\theta_z} \qquad G_{diffuse} = \frac{1 + \cos(\beta)}{2} \qquad R' = \frac{R_s + R_p}{2}$$

$$R_s = \left[\frac{\eta_i \cos(\theta_i) - \eta_t \sqrt{1 - \left(\frac{\eta_i}{\eta_t} \sin(\theta_i) \right)^2}}{\eta_i \cos(\theta_i) + \eta_t \sqrt{1 - \left(\frac{\eta_i}{\eta_t} \sin(\theta_i) \right)^2}} \right]^2 \qquad R_p = \left[\frac{\eta_i \sqrt{1 - \left(\frac{\eta_i}{\eta_i} \sin(\theta_i) \right)^2} - \eta_t \cos(\theta_i)}{\eta_i \sqrt{1 - \left(\frac{\eta_i}{\eta_i} \sin(\theta_i) \right)^2} + \eta_t \cos(\theta_i)} \right]^2$$

Fig. 23 Equations used to describe light behavior in outdoor flat panel cultivation in the model introduced by Marsullo et al. (Marsullo et al., 2015).

Also in Marsullo model the Lambert–Beer's law is used to model the overall light gradient in the culture volume (I (y,z,t)), integrating it in order to find a mean value of irradiation for whole culture inside the reactor at a given time t. In this model, also the dependence on sunlight changing position during the day is considered, using a geometrical parameter for

direct radiation (G_{direct}), depending on solar incidence angle (θ) and on solar zenith angle (θ_z). Furthermore, also the dependence on light scattering ($G_{diffuse}$), and light reflection (R_s and R_p) are considered in the model.
As last point, in Fig. 24 the mass and energy balance equations used in the model are represented. Even in this case, for all parameters' definition see the corresponding reference (Marsullo et al., 2015).

$$\frac{dX_A}{dt} = \mu_A X_A - k_{dA} X_A \qquad \frac{dCO_2}{dt} = \mu_A X_A Y_{ACO_2} + f_{CO_2} - k_{Lg}\alpha\left(CO_2 - CO_2^*\right)$$

$$\frac{dM}{dt} = \mu_A X_A Y_{AM} - k_{Lg}\alpha\left(M - M^*\right) \qquad V_R cp_w \rho_w \frac{dT_w}{dt} = Q_{irr} - Q_{algae} - Q_{exch} - Q_{conv+cond}$$

Fig. 24 Mass and energy balance equations used in the model introduced by Marsullo et al. (Marsullo et al., 2015).

In Fig. 24 both nutrient and microalgal mass balances are included, indeed M is the concentration of the respective component in the bioreactor and M* is the saturation concentration of the associated dissolved element.

1.5 Models for prediction of metabolites accumulation

For the same reason of subparagraph 1.4.3, since in this thesis work a model for prediction of metabolites accumulation inside microalgal cells in phototrophy has been developed, some examples of models available in literature with the same aim are presented in this subparagraph. The common feature of these models is the intent to understand and simulate the influence of factors (nutrients inside culture medium, light, temperature, etc.) on microalgal growth and on metabolites accumulation, in order to optimize a specific feature of the cultivation process (trying for example to maximize the starch production respect to lipids). In order to achieve these goals the developed models available in literature show different levels of complexity and accuracy, moving from empirical (Bekirogullari et al., 2017; Bernard et al., 2016; Kumar et al., 2016; Olivieri et al., 2014; Ryu et al., 2018), that with a proper parameters' fitting give good results and are more easy to handle, to structured models based on more complex but accurate metabolic flux balance analysis (MFBA) (Baroukh et al., 2017; Breuer et al., 2015a; Fachet et al., 2014; Flassig et al., 2016). Generally, as basis of the metabolites' accumulation empirical modeling, during stress conditions due to nitrogen starvation, the equations based on Droop model are used (Droop, 1968; Mairet et al., 2011). In particular, amongst all models of this type available in literature, there is a lack in simulation (in handy but also accurate way) of the entire starch trend, describing also the decrease phase of its intracellular quota (see Fig. 6). Moreover, focusing of empirical models, they are developed mainly for phototrophic cultivations with few applications to mixotrophy, (Deschênes et al., 2015; Figueroa-Torres et al., 2017) but none of them is applied or switchable to heterotrophy (dark fermentation). On the opposite side, even if rigorous models can be applied to all cultivations type, they are not handy and require high computational costs for a final user with a large number of parameters to estimate.

One aim of this thesis work, well described in the following sections, is thus the development of a model easy to handle and to adapt to the specific cultivation condition, having at the same time a firm metabolic structure that guarantees good results in terms of predictive accuracy.

1.5.1 Empirical models

In this subparagraph an overview on empirical and semiempirical models used to model products' accumulation inside microalgae is resumed. As has been done in subparagraphs (1.4.1-1.4.3) some representative examples of what is available in literature is presented, focusing only on metabolites' modeling without considering the other cultivation's parameters (light, temperature, pH, etc.) as done in previous paragraph. As first example, the Bernard et al. (Bernard et al., 2016) work is presented. In particular, the cited article is not the last and only work available in literature, since other studies have been done by this author on this topic (Baroukh et al., 2017; Béchet et al., 2017; Bernard, 2011; Bougaran et al., 2010; Mairet et al., 2011).
In Fig. 25 the schematization of the metabolic pathways developed in the Mairet et al. work (Mairet et al., 2011), used also in the cited Bernard work (Bernard et al., 2016), is shown.

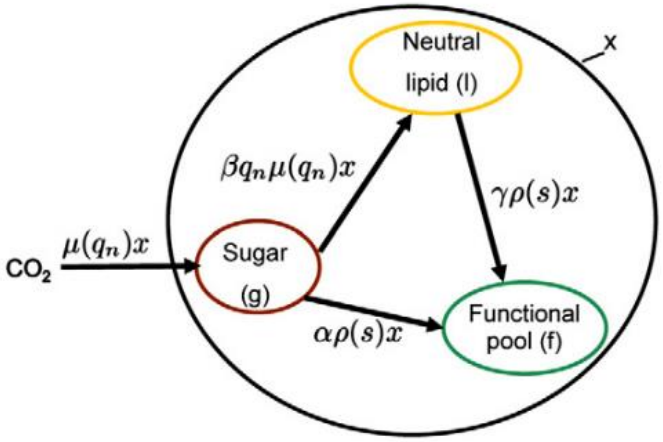

Fig. 25 Representation of the carbon flows used in Bernard et. al model (Bernard et al., 2016).

In particular the functional compartment (f) includes the biosynthetic apparatus (proteins and nucleic acids) and the structural material (mem- branes mainly made of glycolipids and phospholipids). Furthermore, the storage pool is divided into a sugar reserve compartment (g) and a neutral lipid reserve compartment (l). In Fig. 25 the model's carbon flows start with the carbon (CO_2) uptake that is first transformed in sugars and after in functional products and lipids. This behavior is different from the assumption of the compartmental model presented in this thesis work (paragraph 2.4) and from results available in literature (Fig. 6), in which the simultaneous starch and lipids production with different rate is showed. In Fig. 26 the principal equations used to model the desired metabolites' accumulation/production in Bernard model, as intracellular quotas, are represented.

$$\rho(s) = \rho_{\mathrm{m}} \frac{s}{s + k_{\mathrm{s}}} \qquad \dot{\theta} = \delta' \mu(q_n, \cdot)\,[\gamma(I)\, q_n - \theta]$$

$$\dot{q}_{\mathrm{n}} = \rho(s, \cdot) - \mu(q_{\mathrm{n}}, \cdot) q_{\mathrm{n}}$$

$$\gamma(I_0) := \gamma_{\mathrm{m}} \frac{k_{I_0}}{I_0 + k_{I_0}}$$

$$\dot{q}_{\mathrm{f}} = -q_{\mathrm{f}}\, \mu(q_{\mathrm{n}}, \cdot) + (k_1 + k_3)\rho(s, \cdot)$$

$$\dot{q}_l = [k_2\, q_{\mathrm{n}} - q_{\mathrm{l}}]\, \mu(q_{\mathrm{n}}, \cdot) - k_3\, \rho(s, \cdot) \qquad \dot{I}_0 = \delta\, \mu(q_n, \cdot)\,[I - I_0]$$

$$q_{\mathrm{f}} + q_{\mathrm{s}} + q_{\mathrm{l}} = 1,$$

$$\mu(I, \theta, q_{\mathrm{n}}) = \mu_{\max}(q_{\mathrm{n}}) \frac{I}{I + \frac{\mu_{\max}(q_{\mathrm{n}})}{\alpha\theta} \left(\frac{I}{I_{\mathrm{opt}}} - 1\right)^2}$$

$$\mu(q_{\mathrm{n}}) = \mu_\infty \left(1 - \frac{Q_0}{q_{\mathrm{n}}}\right)$$

Fig. 26 Equations used in Bernard et. al model for the representation of metabolites' accumulation inside microalgal cells(Bernard et al., 2016).

Similarly, to the compartmental model of this thesis (paragraph 2.4), in Bernard work the nutrient uptake and biomass growth are uncoupled processes and the nutrient are taken up by the microalgae to make cellular nitrogen (n) with a rate ρ(s), where s is the nitrogen available in the culture medium. Furthermore, is visible in Fig. 26 that the specific growth rate $\mu(q_n)$ is in line with the Droop modelling approach (Droop, 1968), where μ_∞ and Q_0 represent respectively the theoretical maximum growth rate and the minimum nitrogen quota allowing growth. In addition to Droop, the specific growth rate defined in Bernard model $\mu(q_n, I, \theta)$ depends also on light (I) and on pigments' amount(θ); the dynamics of this latter ($\dot{\theta}$) are visible in the equations of Fig. 26 (for the definition of all parameters and equations used in Bernard model, see the cited work (Bernard et al., 2016)). Since this model is applied on chemostat cultivation conditions, the starch trends are not taken into account since they are not comparable with conditions used in the model described in paragraph 2.4.

Another example of empirical compartmental modeling is constituted by Figueroa-Torres work (Figueroa-Torres et al., 2017) applied to a mixotrophic cultivation. In Fig. 27 the model scheme is represented. This work, differently from Bernard is focused on kinetic modelling of starch and lipid formation during mixotrophic, nutrient limited microalgal growth. Furthermore, differently from the model developed in this thesis, the

interconversion between starch and lipid is not present in Figueroa-Torres model. Indeed, the model is not able to simulate the non-monotonous starch trend, occurring inside microalgae after a certain period of nitrogen starvation.

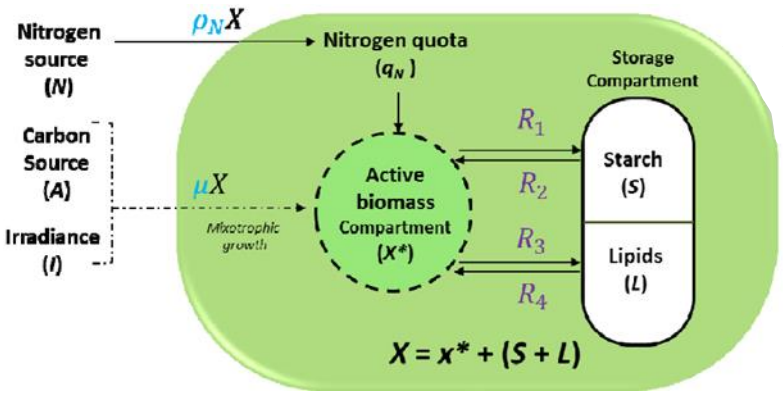

Fig. 27 Model schematization proposed by Figueroa-Torres et. al (Figueroa-Torres et al., 2017)

The reason of this behavior is also due to the model structure that don't calculate the products' dynamics as quotas (with exception of nitrogen quota q_n) but as concentration (g L^{-1}), as visible in Fig. 28 where the model equations are resumed (for the definition of all parameters and equations used in Figueroa model, see the cited work (Figueroa-Torres et al., 2017)).

$$\frac{dx^*}{dt} = \mu \cdot X + R_2 + R_4 - (R_1 + R_3) \qquad R_1 = r_1 \cdot \frac{N_i^{n_s}}{N_i^{n_s} + K_{s,S}^{n_s} + \left(N_i^2/k_{i,S}\right)^{n_s}} \cdot \frac{k_1}{k_1 + N/N_o} \cdot \left[1 + \frac{1}{\mu} \cdot e^{\phi_S \cdot A_{int}}\right] \cdot \mu \cdot x^*$$

$$\frac{dX}{dt} = \mu \cdot X \qquad \mu = \bar{\mu}_{max} \cdot \left(1 - \frac{q_{N,0}}{q_N}\right) \qquad R_3 = r_3 \cdot \frac{N_i^{n_L}}{N_i^{n_L} + K_{s,L}^{n_L} + \left(N_i^2/k_{i,L}\right)^{n_L}} \cdot \frac{k_2}{k_2 + N/N_0} \cdot \left[1 + \frac{1}{\mu} \cdot e^{\phi_L \cdot A_{int}}\right] \cdot \mu \cdot x^*$$

$$\frac{dN}{dt} = -\rho_N \cdot X \qquad \bar{\mu}_{M,max}(A,I) = \mu_{max}\left[w_H \cdot \frac{A}{A + K_{s,A} + A^2/k_{i,A}} + w_I \cdot \frac{I}{I + K_{s,I} + I^2/k_{i,I}}\right] \qquad R_2 = \frac{r_2}{q_N} \cdot X;\ R_4 = \frac{r_4}{q_N} \cdot X$$

$$\frac{dL}{dt} = R_3 - R_4 \qquad w_H = \frac{A/K_{s,A}}{A/K_{s,A} + I/K_{s,I}};\ w_I = \frac{I/K_{s,I}}{A/K_{s,A} + I/K_{s,I}}$$

$$\frac{dA}{dt} = -\frac{1}{Y_{X/A}} \cdot \frac{\mu_H(A)}{\mu_H(A) + \mu_I(I)} \cdot \frac{dX}{dt} \qquad \rho_N = \bar{\rho}_{N,max}(N_o, X) \cdot \frac{N}{N + K_{s,N} + N^2/k_{i,N}} \cdot \frac{A}{A + K_{s,A:N} + A^2/k_{i,A:N}}$$

$$\frac{dH}{dt} = K_H \cdot \frac{dx^*}{dt}$$

$$\bar{\rho}_{N,max}(N_0, X) = \rho_{N,max} \cdot \frac{{N_o}^n}{N_o^n + K_*^n} \cdot e^{-\phi_N \cdot X}$$

$$\frac{dS}{dt} = R_1 - R_2$$

Fig. 28 Principal equations used in Figueroa-Torres et. al model for the representation of metabolites' accumulation inside microalgal cells (Figueroa-Torres et al., 2017).

In Fig. 27-28 can be seen that, due to the mixotrophic metabolism, the specific growth rate depends on nitrogen (as Droop model), on light (I) but also on substrate's (Acetate=A) concentration inside the culture medium. Furthermore, starch concentration is not influenced by lipids but only by the amount of active biomass (x^*); also the nitrogen uptake inside the cell depends on both extracellular nitrogen and acetate concentrations. In general, in this model a significative number of parameters (31) and equations are used to simulate the microalgal mixotrophic metabolism and products' accumulation, requiring

first a sensitivity analysis, that reduced to 27 the parameters used in the model, and after a double optimization step with Simulated Annealing (SA) algorithm and Successive Quadratic Programming (SQP) method. All these steps make the model cumbersome and complex.
As last example, the model introduced by Ryu et. al (Ryu et al., 2018) is described.
In Fig. 29 a summary of the metabolic pathways described in the model is shown.

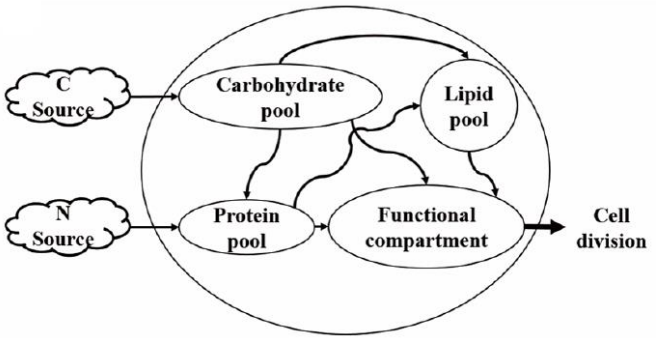

Fig. 29 Model schematization proposed by Ryu et. al (Ryu et al., 2018).

Fig. 29 is similar to that presented by Bernard with but with some differences.
Indeed, in this model is assumed that the nutrients' uptake from bulk to cellular phase via cell membrane is splitted in two: one is connected to the carbon source (CO_2) with an uptake rate of ρ_C and the other depends on nitrogen concentration uptake with a rate ρ_n.
This division is visible also in the equations represented in Fig. 30, in which a new variable μ_C, constituted by the carbon partitioning rate, is added to the classical μ_n of Droop. This variable depends in turn on carbon partition rate due to membrane lipids (m) and to storage lipids (s).

$$\frac{dN}{dt} = (\mu_N - R_N)N \qquad \frac{ds_n}{dt} = -\rho_n N \qquad \frac{dQ_C}{dt} = \rho''_{c,\max}\left(1-\frac{q_C}{q_{C,\max}}\right)N - \alpha_C\mu_N N - Y_{C2P}\rho_n N - \mu_C Q_C$$

$$\frac{dQ_P}{dt} = Y'_{n2P}\rho_n N - R_N Q_P - \alpha_P\mu_N N - \gamma\mu_{C,s}Q_P \qquad \frac{dQ_L}{dt} = Y_{C2L}\mu_C Q_C + Y_{P2L}\gamma\mu_{C,s}Q_P - \alpha_L\mu_N N$$

$$X = (1+k_{Chl})Q_P + Q_C + Q_L + \beta N \qquad \rho_n = \rho_{n,\max}\frac{s_n}{s_n + K_{s_n}}\left(1-\frac{q_P}{q_{P,\max}}\right) \qquad \mu_N = \mu_{N,\max}\left(1-\frac{q_{P,\min}}{q_P}\right)$$

$$\mu_C = \mu_{C,m} + \mu_{C,s} \qquad \mu_{C,s} = \mu_{C,s,\max}\left(1-\frac{\mu_N}{\mu_{N,\max}}\right)\left(1-\frac{q_L}{q_{L,\max}}\right) \qquad \mu_{C,m} = \mu_{C,m,\max}\left(\frac{\mu_N}{\mu_{N,\max}}\right)\left(1-\frac{q_L}{q_{L,\max}}\right)$$

Fig. 30 Principal equations used in Ryu et. al model for the representation of metabolites' accumulation inside microalgal cells (Ryu et al., 2018).

Differently from Figueroa-Torres' model, in this case the metabolites dynamics are calculated considering intracellular quota but without succeeding in representation of non-monotonous starch trend (see Fig. 31), even in presence of a large number of parameters used to make the model more accurate.

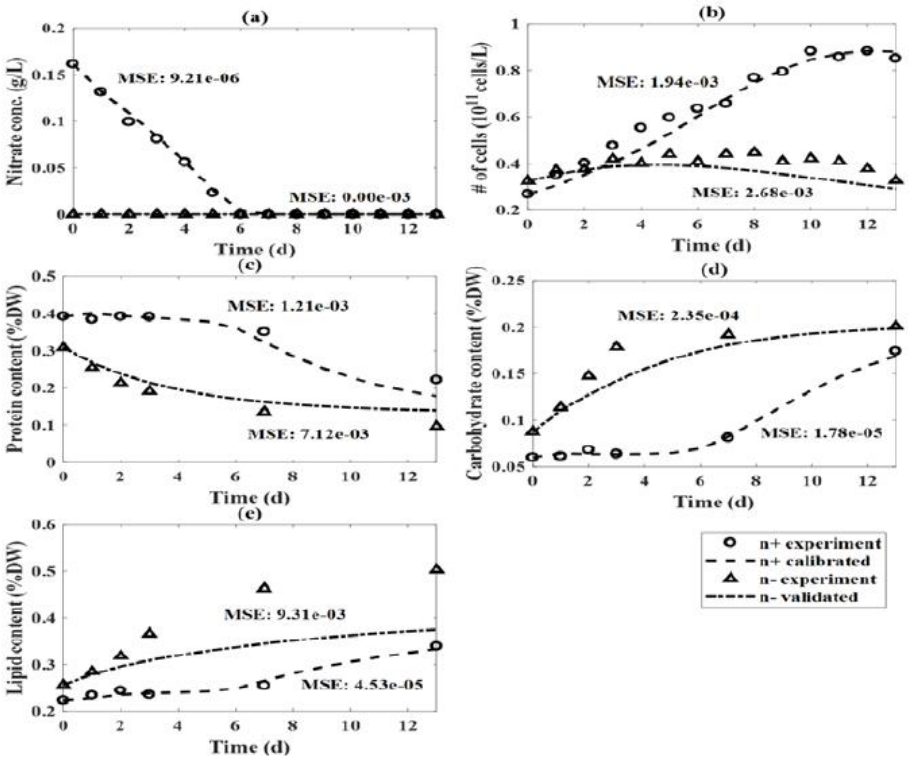

Fig. 31 Ryu model's results in terms of metabolites quota dynamics. (Ryu et al., 2018).

1.5.2 Structured models (Metabolic Flux Balance Analysis)

In this subparagraph an application of rigorous modeling for the representation of metabolites accumulation inside microalgal cells is presented. As anticipated in subparagraph 1.4.2, the Flux Balance Analysis and its improvement Dynamic Flux Balance Analysis (DFBA) are a powerful and complex techniques able to simulate the metabolic pathways inside microalgal cells in all types of cultivations, focusing on both growth and metabolites accumulation. As application of DFBA in a phototrophic cultivation, aimed to model the high added value products storage, the Flassig et al. model (Flassig et al., 2016) is presented. The DFBA model developed in that work consists of two main components, a metabolic model of the microalga (*Dunaliella salina*) and a dynamic model of the photobioreactor environment. The simulated dynamic state variables are: the biomass concentration on dry weight basis X, the extracellular nitrate concentration C_{NO3} and the intracellular metabolites, which are the chlorophyll fraction of total biomass ω_{Chl}, the β-carotene fraction of total biomass ω_{Car}, and the nitrogen cell quota ω_N. In this model since a genome-scale metabolic network reconstruction for *D. salina* was not available, the metabolic network reconstruction of the green fresh water alga *Chlamydomonas reinhardtii* is used as model basis. As first consideration, the light energy available for photosynthesis ($\bar{E}_x$) is assumed to depend on chlorophyll fraction with an efficiency η visible in Fig. 32, where the principal equations used to define the main metabolic fluxes are shown.

$$\eta = \theta_{\text{eff}}(\eta_1 \omega_{\text{chl}} + \eta_0) \quad \bar{E}_x = \frac{\theta_{\dim \eta}}{\rho_A} \bar{E} \quad \nu^{LB}_{\text{NO}_3,\text{met}} = -\nu_{\text{NO}_3,\text{met,max}} \left(1 - \frac{\omega_{\text{N,min}}}{\omega_{\text{N}}}\right)$$

$$\nu^{\text{LB}}_{\text{Car}} = \nu_{\text{Car,gen}} \Psi(\alpha_1 \bar{E}_{\text{x}} + \alpha_0 - \omega_{\text{N}}) \quad \nu^{\text{LB}}_{\text{Car,gen}} = \nu_{\text{Car,max}} \frac{\bar{E}_x^{n_{\text{Car}}}}{\bar{E}_{\text{x,A}}^{n_{\text{Car}}} + \bar{E}_x^{n_{\text{Car}}}}$$

$$\nu^{\text{LB}}_{\text{Chl}} = \left(\gamma(\bar{E}) - \frac{\omega_{\text{Chl}}}{\omega_{\text{N}}}\right)$$

Fig. 32 Principal equations representing the exchange fluxes proposed in Flassig et al. model (Flassig et al., 2016).

As representative of the exchange fluxes' equations shown in Fig. 32, a quick explanation for the nitrate metabolization flux is carried out. The rate at which the internal nitrate storage is metabolized, is denoted by $\nu_{NO3,met}$; as with all other exchange fluxes, the sign convention implies that a negative value indicates a consumption of nitrate. The lower bound on nitrate metabolization rate is given by $\nu^{LB}_{NO3,met}$, visible in Fig. 32 and the maximal flux value $\nu_{NO3,met,max}$ is considered as a model parameter. The metabolization is inhibited as the nitrogen cell quota ω_N reaches its minimal value $\omega_{N,min}$. Furthermore, it is assumed that no nitrate is synthesized through this flux and therefore the upper bound of the nitrate metabolization flux is set to zero. The other boundaries are referred to chlorophyll and carotenoids accumulation's fluxes (for additional information, see the reference work (Flassig et al., 2016)).
In Fig. 33 the equations used to model the photobioreactor's dynamic are resumed.

$$\dot{x} = \mu x,$$

$$\dot{c}_{\text{NO}_3} = -\nu_{\text{NO}_3} x, \qquad \nu_{\text{NO}_3} = \nu_{\text{NO}_3,\text{max}} \frac{c_{\text{NO}_3}}{K_{\text{m}} + c_{\text{NO}_3}} \left(1 - \frac{\omega_{\text{N}}}{\omega_{\text{N,max}}}\right)$$

$$\dot{\omega}_{\text{Chl}} = m_{\text{Chl}} \nu_{\text{Chl}} - \mu \omega_{\text{Chl}},$$

$$\dot{\omega}_{\text{Car}} = m_{\text{Car}} \nu_{\text{Car}} - \mu \omega_{\text{Car}},$$

$$\dot{\omega}_{\text{N}} = \frac{m_{\text{N}}}{m_{\text{NO}_3}} \nu_{\text{NO}_3} - \mu \omega_{\text{N}},$$

Fig. 33 Equations representing the dynamic of a flat-plate photobioreactor proposed in Flassig et al. model (Flassig et al., 2016).

It is visible in Fig. 33 that Droop model is used to represent limitation of nitrogen due to internal accumulation. The model, as the one developed in this thesis work (see paragraph 2.4), promotes the idea that growth depends on the stored intracellular pool of nutrients (mainly on nitrogen) and not directly on the extracellular concentration. On the other side,

respect to the model of paragraph 2.4, it requires high computational cost (due to the high number of reactions/fluxes considered) and a large number of parameters to be optimized.

1.6 Multivariate models

Since in this work an empirical model to predict microalgae growth in outdoor cultivation system, using multivariate statistics, is implemented to overcome the problems of complex mathematical models (see further paragraphs), a brief introduction to these methods used for similar applications is carried out. In particular, the multivariate statistical projection methods PCA (Principal Component Analysis) and PLS (Partial Least Square) are used for this purpose. PCA and PLS were initially used in process control for their ability to compress multidimensional data, extracting from them useful informations by projecting these data into a low-dimensional space having as new reference system the principal components (Härdle and Simar, 2015). In particular, for algae production both techniques have been used to analyze the water chemistry conditions in three wastewater stabilization ponds with excessive algae growth and fluctuating pH, finding correlations between variables (pH, temperature, light, dissolved oxygen, etc.) and developing a multivariate regression model for pH as a dependent variable (Wallace et al., 2016). Other similar applications were used to study and identify correlations between different algal species present in Lake Wingra (Allen and Koonce, 1973) and also to illustrate the influence of environmental variables on phytoplankton composition in the Vaal River (van Vuuren and Pieterse, 2005). Unlike previous works, in this paper an innovative use of PCA and PLS methods is developed, not only to reduce data redundancy but also to predict microalgal growth in a specific period of the year with defined weather and cultivation conditions. Further informations about these two methods are reported in the Materials and Methods section (paragraph 2.3).

1.7 Microalgal downstream processes

Nowadays, as anticipated in subparagraph 1.2.1, the interest in molecules with high added value arising from bio-sources is constantly growing. In this context microalgae can represent a valid alternative for their various interesting compounds, moving from lipids to starch and pigments, depending on cultivation conditions. The presence of these high-added value compounds has increased the need of implementation of new microalgal growth models (A. Mazzelli et al., 2019a; Mazzelli et al., 2018b), reactor configurations, but also simulations of the subsequent extraction processes (A Mazzelli et al., 2019; A. Mazzelli et al., 2019b). These high added value compounds are extracted by classic (Cartens et al., 1996; Ferrell and Sarisky-Reed, 2010) or innovative solvents (Cicci et al., 2018), that in the most cases are toxic and need to work with high temperatures, causing thus thermal degradation of the extracted biomolecules (Mercer and Armenta, 2011). For these reasons the scientists' attention is moving toward the use of green solvents and between them supercritical CO_2 (sCO_2) is catching on ever more. sCO_2 is the most used supercritical fluid because of its skill to reach the supercritical state (31.1°C at 73.8 bar) at

temperature close to the Standard Ambient(25 °C), allowing to extract heat-sensitive compounds without degrading them (Sapkale et al., 2010). In order to sell the extracted molecules, such as fatty acids and carotenoids, from the oily phase it is necessary to carry out a fractionation of the microalgal oil coming out from the extraction step. The most used separation technology in the chemical industry doing this is represented by distillation (Liu and Jobson, 1999; Ponce et al., 2015) including also the vacuum distillation (Andrzej Gòrak and Zarko Olujic, 2014; Treybal R.E., 1980). The main problem of this technology is that the column's bottom will work at temperature too high for the preservation of the thermosensitive molecules such as those found in microalgal extracted oil (Ketenoglu and Tekin, 2015). Moreover, at each stage of the column, the vapor liquid equilibrium is reached, and this implies too high residence times. Due to these reasons, conventional distillation techniques are not suitable for fractionation of the oil extracted from microalgae. Molecular distillation, or short path distillation, is generally accepted as the safest method to separate and purify thermally unstable compounds (Fregolente et al., 2010; Wang et al., 2009). Specifically it is a special type of very high vacuum distillation (between 0.001 and 0.01 mbar), where the distance between evaporation and condensation's surface that the molecules have to cross is smaller than their mean free path (defined as the average distance traveled by a particle between two successive collisions) (Lutisan and Cvengros, 1995). In this work, in addition to models for prediction of microalgal growth and metabolites accumulation, a study of the downstream processes for the extraction (using sCO_2) and purification of the high added value metabolites (with molecular distillation) has been carried out. For this reason, in the following subparagraphs a focus on the methodologies investigated for microalgal downstream treatment is resumed.

1.7.1 Supercritical CO_2 extraction

The supercritical fluids' extraction is a process that allows the extraction of one or more components (such as lipids), from a matrix (such as a microalgae) with the usage of supercritical fluid as solvent. Generally, a component is in a supercritical state when it has higher pressure and temperature than the critical point (P_c, T_c). In Fig. 34 the regions of temperature and pressure in which a given substance (in this case CO_2) is present as solid, liquid and gas, are depicted.

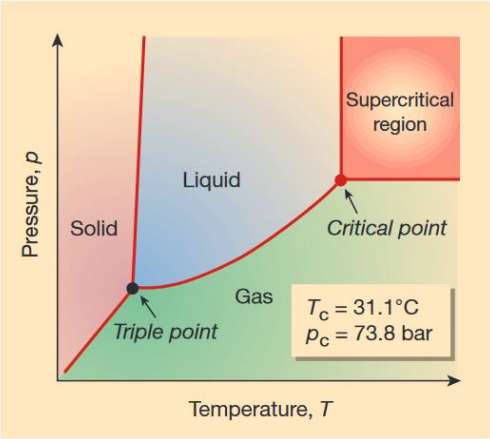

Fig. 34 Phase diagram for carbon dioxide. Beyond the critical point carbon dioxide becomes a supercritical fluid, with a state having properties of both gas and liquid (Leitner, 2000).

It can be noticed, that the balance between the gas and the liquid starts at the triple point, a in which the gaseous and liquid phases are no longer distinguishable.
The transition from these two different phases (gas and liquid) to a single phase (supercritical) is even more evident in the figure below (Fig. 35), always referred to CO_2. It is clear that initially the two phases are separated from a meniscus. With the increase in temperature and pressure the difference between these two phases, however, is less evident, and the meniscus, although still visible, is always less defined. Finally, when supercritical conditions are reached there is no distinction between two phases and the separation meniscus is no longer visible. The main characteristic of supercritical fluids is that they have properties specific to gases and other liquids. They have, for example, a density similar to that of liquids, while viscosity and diffusivity are closer to those of gases. Due to its lower viscosity, a supercritical fluid is able to penetrate more deeply in the microalgal matrix containing the desired substances. This, in addition to the high diffusion, typical of gases, allows these fluids to spread more easily through solids than conventional organic solvents (Herrero et al., 2006).

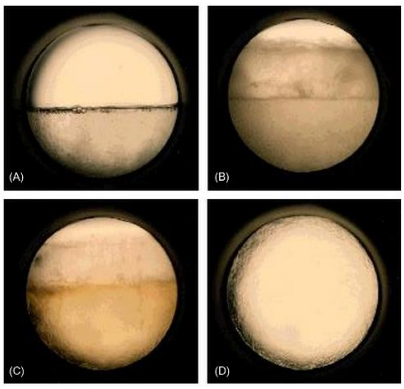

Fig. 35 Pictures of a variable volume view-cell with a transparent sapphire window showing the phase transfer of CO_2. (A) vapor-liquid phase equilibrium; (B) vapor-liquid phase equilibrium with an increased temperature; (C) the densities of the liquid and vapor phases are more and more similar and finally (D) the Critical Point is reached and the two phases are no longer distinguishable. In D the CO_2 reached the supercritical state (Cunico and Turner, 2017).

However, since supercritical fluids' density is similar to that of liquid, their activity as solvent is very similar and can be adjusted by controlling pressure and temperature. Indeed, one of the main feature of a supercritical fluid is the possibility to modify appreciably its density by changing pressure and/or temperature, changing consequently also its solubility.
Focusing on CO_2, it has several interesting features that are listed below:

- It is not toxic for human health, differently from most of the organic solvents (for example chloroform)
- It is not flammable
- It is odorless
- From the chemical point of view it is an inert, so extracted components' isomerization, oxidation or hydrolysis are avoided
- Being a gas is in normal condition, it is easily separable from the solute when the extraction process is finished (Abbas et al., 2008).
- Has a highly competitive cost compared to normal organic solvents
- It can be recycled, resulting in cost savings for both solvent and energy
- CO_2 recirculation applied to the industrial processes do not alter the environmental balance
- It is generally recognized as harmless and classified as a GRAS product (Generally Recognized As Safe) by American Food and Drug Administration (FDA) and European Food Safety Authority (EFSA)
- CO_2-based processes do not contribute directly to the greenhouse effects and therefore global warming. Indeed, CO_2 generated by other industrial processes, such as production of ethanol, ammonia, and hydrogen can be used as solvent, thus respecting the principles of green chemistry (design of products and processes that minimize the use and generation of hazardous substances to man and the environment) (Desimone and Desimone, 2014).
- Due to its not-polar nature, sCO_2 cannot be used by itself for polar molecules' extraction.

Regarding the last point of the list, in order to increase process selectivity and solubility of polar compounds in CO_2, small amounts of other solvents, usually co-solvents or modifiers, may be added. The modifier selection, as well as the proportion with which it is used, usually 5-10 %, should be carefully selected in order to optimize the extraction (Sanchez-Camargo et al., 2017). Surely the addition of a modifier, such as ethanol, improves the solvation characteristics of supercritical CO_2 but, nevertheless, part of the co-solvent tends to remain in trace in the product, removing the advantage of supercritical CO_2 by extracting completely solvent-free products (Sapkale et al., 2010). In addition to the extraction of high-added value products, sCO_2 finds numerous applications, such as (Manjare and Dhingra, 2019):

- Extraction of essential oils from plants
- Extraction of aromas and fragrances from natural products
- Caffeine extraction from coffee and tea
- Extraction of nicotine from tobacco
- Fractionation of crude oil
- Removal of solvent residues from waste and decontamination of soils
- Removal of impurities from powders of pharmaceutical excipients

As practical example, in Fig. 36 a sCO_2 extraction pilot plant is showed. For a more detailed description of the process used in the work see paragraph 2.5.

Fig. 36 Example of a sCO_2 extraction pilot plant (www.separeco.it)

.

1.7.2 Molecular distillation separation

As anticipated before, for highly thermolabile components separation, such as those studied in this work, it is necessary to resort to distillation methods that use very high vacuum. Typically for very high vacuum distillations are used two types of evaporators:

- Thin film evaporators or Thin Film Evaporator (TFE)
- Evaporator Short Path (SPE) (is the molecular distiller considered in this study)

These devices, although they have a similar design, are differentiated by specific characteristics that distinguish them.

Thin film evaporators (Fig. 37) are equipment used for separation of compounds requiring an operating pressure between 1 and 100 mbar (Ketenoglu and Tekin, 2015). Consists of a cylindrical or conical evaporator coated with a heating jacket fed with a warm fluid, such as oil thermal or condensing steam. The feed is shaken by a rotor, forming on the walls of

the heating surface a thin film with a typical thickness equal 0.5 mm. The action of the rotor blades creates in the interface with the surface heating a region of turbulence that improves both the heat and mass transfer.

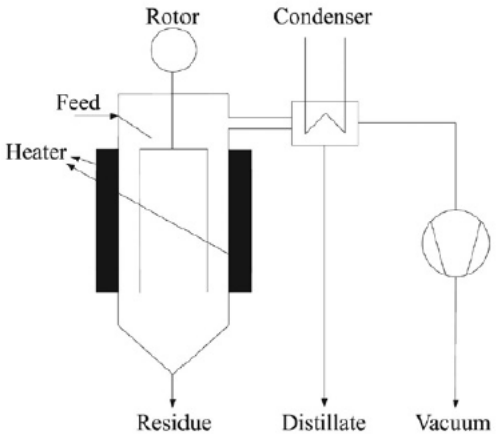

Fig. 37 Scheme of a Thin Film Evaporator (TFE) (Ketenoglu and Tekin, 2015).

It can be seen from the figure above (Fig. 37), that between the condenser and the vacuum machine, which can be represented both by a steam ejector or by a vacuum pump, there is no other element. Indeed, in TFE the fundamental role is covered by the rotor, having the task of stabilizing the liquid film on the evaporating surface in order to obtain high vaporization rates. The action of the rotor must therefore prevent breakages in the film. Moreover, the action of the centrifugal force induced by the rotor itself, which presses the film on the heating surface, prevents the phenomenon of reverse evaporation. Reverse evaporation is constituted by formation of a vapor film between the heating surface and the evaporating film, which could lead to undesirable thermal insulation effects (Komori et al., 1988).
On the other side, the Short-path evaporators (SPE) are equipment used for separation of compounds requiring an operating pressure which can reach 0.001 mbar. Unlike TFE, the condenser is located inside the cylinder surrounded by the heating shirt, as can be seen in Fig. 38.

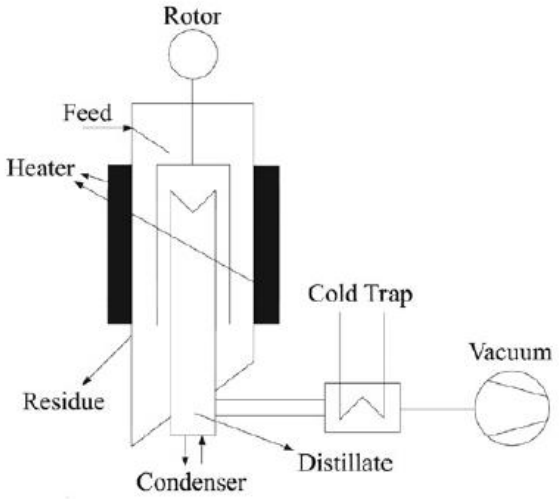

Fig. 38 Scheme of a Short Path Evaporator (SPE) (Ketenoglu and Tekin, 2015).

Pursuant to this configuration, SPE is also known as a Molecular Distiller. Molecular distillation is a distillation process in which the distance between the evaporator surface and the condenser surface is less than the mean free path of molecules (defined as the average distance traveled by a particle between two successive collisions) (Lutisan and Cvengros, 1995; Shi et al., 2007). Molecular distillation is recognized as the safest method for the separation of components with low relative volatility and high boiling points (Lutisan and Cvengros, 1995). This technique works in fact with variable operating pressures, typically, between 0.1 Pa and 1 Pa. Pressure less than 0,1 Pa would not allow the formation of a condensed phase, while pressures above 1 Pa would not allow good evaporation and thus a good separation (Stephan, 1992). The feed is fed at the top of the equipment and is distributed, thanks to the action of a rotor, in a thin film along the entire surface of the evaporator, equipped with a heating jacket. The film thickness is function, as well as the feed flow rate and the speed of the rotor, also of the viscosity of the fluid. Due to heat provided by the jacket, the more volatile components leave the film surface and reach the cooling surface, condensing. The liquid is then enriched with less volatile components and is collected on the bottom of the evaporator. In particular, the residue is collected in an inclined ring at the bottom of the cylinder and discharged through the bottom nozzle. Similarly, the distillate is collected at the bottom of the condenser. Since the distance between evaporating surface and condensing surface is less of the average free path of molecules, the more volatile components have to make a very short path, reaching the condenser without any delay. This condition is not verified in the
in the case of traditional distillation processes, where vapor-liquid equilibrium is reached. This feature of short path evaporators make the residence times very short in the order of few seconds and suitable for separation of highly thermolabile components (Hickman, 1947). In general, the free mean path (λ) is defined as:

$$\lambda = \frac{RT}{\sqrt{2}\pi d^2 N_A P} \qquad \text{(Eq. 1)}$$

The parameters appearing in the previous report have the following meaning:

- R is the universal gas constant
- T is the operating temperature in K
- d indicates the diameter of the molecule
- N_A is the Avogadro number
- P is the operating pressure in Pa

By placing the condensation surface at a distance from the evaporation surface less than λ, the collision of molecules, rising from the liquid film before reaching the condensing surface, is avoided. If particles collided, a certain percentage of molecules would fall into the liquid film, thus decreasing the evaporation rate and efficiency of the separation. At pressures of the order of 0.001 mbar, the average free path of molecules is about 5 cm. Even if in every distillation process the driving force of separation is represented relative volatility between the components of the feed mixture, in molecular distillation process a second phenomenon occurs. In fact, when lighter molecules leave the liquid film and are condensed on the cooling surface, the liquid film gets depleted of more volatile components. This mechanism triggers a diffusion driving force, determined by a gradient of concentration between hot and cold zones that improves the separation.

1.8 MEWLIFE (LIFE17 ENV IT/000180) European Project

A real application of the models developed in this thesis work, described in the following paragraphs 2.3 and 2.4, can be found in the European Project named MEWLIFE in which Bio-P has a role as partner. In this paragraph a description of the project is carried out. The MEWLIFE (acronim that stands for MicroalgaE biomass from phototrophic-heterotrophic cultivation using olive oil Wastewaters) is a LIFE project that aims to demonstrate the environmental benefit and economic feasibility of an innovative approach to produce microalgal biomass in an integrated phototrophic and heterotrophic cultivation system using preconcentrated olive oil wastewaters (OMWW) as carbon source for growing algae, thus contributing to waste reuse and valorization. The duration of the project is 36 months (01/07/2018 start date – 30/06/2021 end date).

Fig. 39 MEWLIFE logo.

The project has three main objectives:

1) **Re-using and valorizing wastewaters from olive oil production:** wastewaters from olive oil plants are used as carbon source for algae cultivation, thus increasing biomass productivity, limiting the costs associated with nutrients input, and at the same time treating wastewaters by reducing the initial organic load of recalcitrant compounds (polyphenols) (PPs). These wastewaters, largely diffuse in the whole Mediterranean Basin, cannot be treated in conventional biological depuration plants due to the toxic effect of antioxidants (PPs) on active sludge. In order to overcome the limit of seasonal availability of olive oil waste, a pretreatment of these wastewaters is included giving an organic-rich concentrate to be used in microalgae cultivation during the whole year.
2) **Producing microalgal biomass**: dried microalgae suitable for applications in nutraceutics but also exploitable in bio-plastic field. Microalgae formulations are already in the market in different countries (Japan, China, USA, Germany) for feed and food applications with an annual turnover of 80 million of US$. The biomass produced in the MEWLIFE project will be tested for nutraceutical applications by potential stakeholders evaluating the benefit due to cultivation using antioxidant-rich medium. In addition, samples of fractions extracted from the biomass (starch and other carbohydrates and lipid fraction) will be tested for the production of biopolymers, as alternative source to crops.
3) **Reduce cost associated with algae cultivation:** the proposed integrated cultivation system (small phototrophic section for inoculum production + extended heterotrophic section for biomass production) will allow reducing at minimum level the costs associated with the algae cultivation in large scale applications, which is mainly due to the high investment costs for photobioreactors. By limiting the first step of algae cultivation in the phototrophic system just to the production of the inoculum needed for the next heterotrophic section, a reduction of the capital costs associated with large scale photobioreactors system will be achieved.

A simplified scheme of the entire process is presented in Fig. 40

The prototype related to microalgal treatments is composed of the following units (that will be discussed in paragraph 2.7):

- Upstream unit: phototrophic growth (photobioreactor volume: 600 L) and dark fermentation (reactor volume: 6 m^3 divided in two fermenters of 3m^3).
- Downstream unit: algal biomass harvesting, dewatering and packaging.

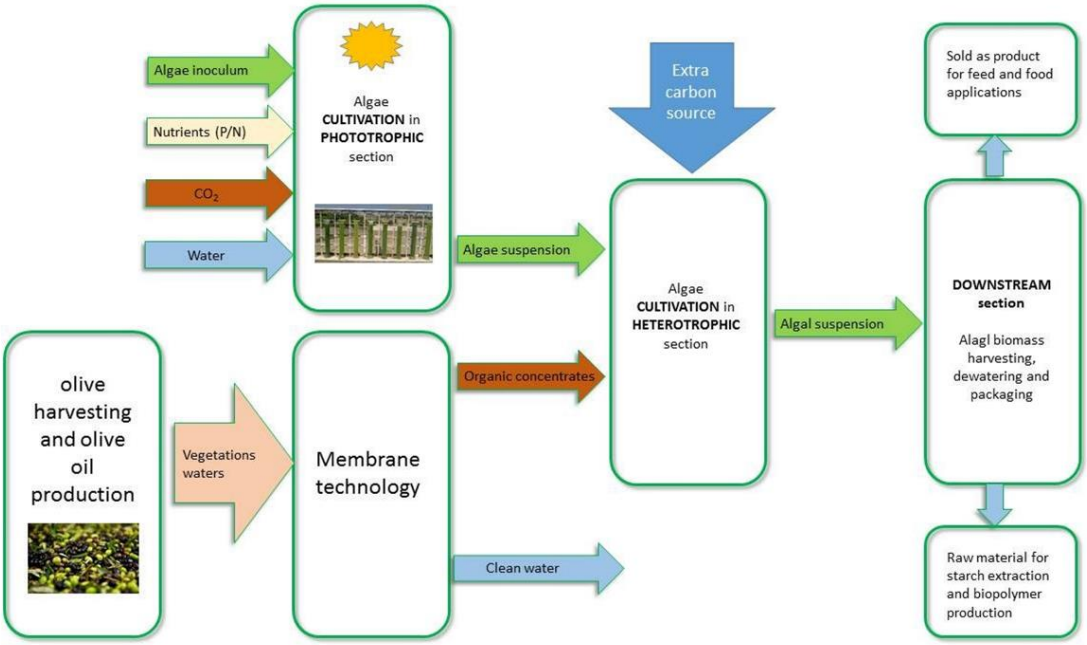

Fig. 40 MEWLIFE simplified process scheme.

Action #	Action Description	As responsible	Timetable	Status
B1	Design and construction of the prototypes		M4-M14	**Started**
B1.1	Basic Process Design of new prototype units		M4-M6	**Concluded**
B1.3	Construction of the new prototype units and start up		M10-M15	**Started**
B2	Upstream treatment of vegetation waters		M13-30	**Started**
B3	Photo-heterotrophic cultivation and downstream	X	M16-M30	**Started**
C1	Technical Monitoring and evaluation of prototype units	X	M4-M36	**Started**
C2	Socio-economic impact study	X	M25-36	Not started
D1	Dissemination&Exploitation Planning and execution	X	M1-M36	**Started**

Fig. 41 B3 action in which Bio-P is leader and in which the models developed in this work can find an application.

As can be seen in Fig. 41, the main action in which Bio-P is responsible is B3, dedicated to both microalgal cultivation (in phototrophy and heterotrophy) and downstream processes. Its precisely in action B3 in which the models developed in this work (see paragraph 2.3 and 2.4) can be applied and validated with the experimental data coming out from the running pilot (see subparagraphs 2.7.1 and 2.7.2). Indeed in this action, all of three main objective described above have to be reached and to help this achievement the models described in the following paragraphs could be used. The multivariate model could be applied to phototrophic cultivation, knowing thus how much time would be necessary to reach the desired concentration in a specif part of the year. The multivariate study could be

also applied to heterotrophic cultivation in order to analyze the principal factor influencing microalgal dark fermentation, finding also useful correlations between them. On the other side, the compartmental model applied to heterotrophy will permit to reach two important results, prediction of time needed to reach a fixed output concentration (at a certain glucose or OOMWW and Nitrate concentration; see paragraph 2.7) but also the estimation of the desidered metabolites quotas, accumulated during nitrogen starved conditions.
Furthermore, it could be useful to analyze the effect of changing OOMWW composition or concentration on microalgal growth. With few modifications it could be applied also for the estimation of starch accumulation inside microalgae, showing when to stop cultivation in order to maximize its quota depending on OOMWW concentration. Moreover, Bio-P (represented by myself) collaborated to the design of the entire prototype, supporting the partners responsible of Basic Process Design (Technosind) and Detailed Engineering (NextChem). In particular, Bio-P designed the 3 m^3 fermentors in all of their parts, supporting NextChem in the procurement and relations with suppliers (see subparagraph 3.9.1); this design collided with some technical issues related to the available space for pilot installation (see Fig. 42). Furthermore, also for the packages related to phototrophic cultivation and downstream (centrifuge and spray dryer), Bio-P gave to Technosind and NextChem all the parameters needed to define the equipments' design to be provided for the chosen suppliers, supporting also in this case the procurement phase on the technical point of view.

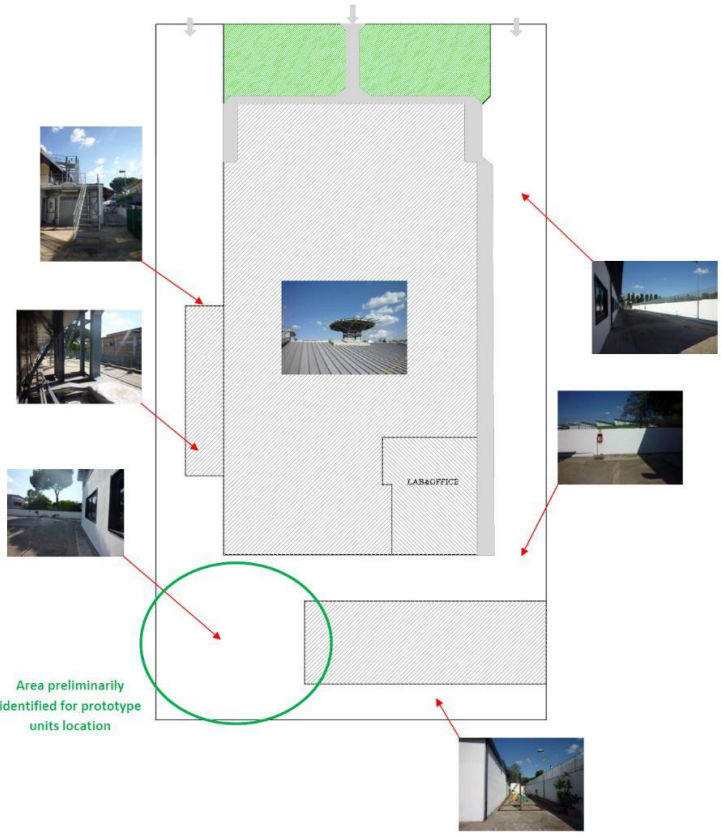

Fig. 42 Area identified in Bio-P/NextChem site for the installation and operation of both phototrophic and heterotrophic pilot plant.

Chapter 2. Materials and Methods

2.1 Outdoor cultivation in the pilot plant

In this work two different algal strains named *Tetradesmus obliquus* and *Graesiella emersonii* were selected and cultivated in an outdoor photobioreactors (PBRs) pilot plant (Di Caprio et al., 2016; Mazzelli et al., 2018a) during 1 year of operation. Each inoculum was prepared using local tap water (ACEA, 2017) in place of distilled water (Di Caprio et al., 2017, 2015). The pilot plant was installed in Rome (Italy) at the Bio-P s.r.l. site (N 41°55' 5" E 12°35' 35"); it was fitted with 10 bubble column photobioreactors (divided into two parallel lines called *line 1* and *line 2*) with an operative volume of 21 L each (internal diameter = 14 cm, height = 150 cm), anchored to a metal support structure and equipped with three sampling points placed approximately 40, 80 and 120 cm from the ground (Fig. 43).

Fig. 43 Working pilot plant installed in Bio-P srl site (N 41°55' 5" E 12°35' 35").

They were spaced from each other approximately 30 cm and the lines were placed at a distance of 1.5 m each other with an orientation of 140° respect to the magnetic north (SE direction), minimizing thus the shading effects caused by the near building. Each reactor was connected to air (for mixing purposes) and to CO_2 lines (for pH control). The air flux was generated by a membrane compressor (AIRMAC 40W) (see further paragraphs for more detailes). Furthermore, when foaming problems occurred, 1-2 ml of antifoam were added in order to avoid self-diluition process due to the superficial adhesion on the reactors' top.

2.1.1 Aeration & Mixing

A membrane compressor (AIRMAC 40W), having a nominal flowrate of 120 L min^{-1} at a pressure of 0.2 Kgf cm^{-2}, was used to ensure proper aeration and suspension mixing. In order to dehumidify the air fed into the circuit, a glass column (Ø 3.5 cm, h 30 cm) containing silica gel was placed after the compressor, thus limiting humidity condensation in the line. 10 rotameters (FLOW METER), equipped each with a control valve, were installed to regulate the flowrate of air sent to each reactor; each flowmeter had a flow range between 0 and 5 NL min^{-1}.

A toroidal sparger (Ø 13 cm) was designed and manufactured *ad hoc* and positioned at the bottom of each reactor, connected to the aeration system with non-return valves (Ø 6x4 mm) in order to prevent backflow of water. The sparger has been designed with holes (Ø 0.5 mm) spaced from each other about 1-2 cm, ensuring a better mixing and diffusion of oxygen and CO_2 inside the reactor (Fig. 44).

Fig. 44 Toroidal sparger designed and manufactured *ad hoc* for culture aeration and mixing.

The choice to make this system was forced, because the porous stones initially used inside the reactors were subjected to clogging problems due to the microalgal adhesive deposits. Furthermore, even the toroidal spargers showed this problem, but they needed less frequent maintenance, indeed their unclog was carried out only with the usage of pressurized water.

2.1.2 Control system

In order to ensure the monitoring of PBRs' process parameters such as pH and internal/external temperature, the installation of probes connected to a feedback control system with a PC graphical interface, was provided. The computer program LABVIEW

red in input temperature and pH signals coming from the two temperature's probes WE711-42-IM / PT 100 and two pH probes WQ420 (made by SIM INSTRUMENTS) and, based on the desired set-points, controlled the opening of the on/off valves placed at the battery limit of the pilot plant. Both pH and temperature were controlled only for their high values. Indeed, pH was controlled with injection of pure CO_2 when it exceeded pH=8 in order to moderate the basicity of microalgal cultures, whereas the temperature was controlled with a water spray cooling system during hot days in order to avoid the overcoming of its set-point T=30° C. In particular, only one of the two temperature probes was connected to the cooling system, controlling thus the internal reactor temperature, while the other probe was positioned outside the reactor in order to monitor the external temperature; a justification of this set-up is resumed in paragraph 3.2. A schematic representation of the control system used in the pilot plant is resumed in Fig. 45.

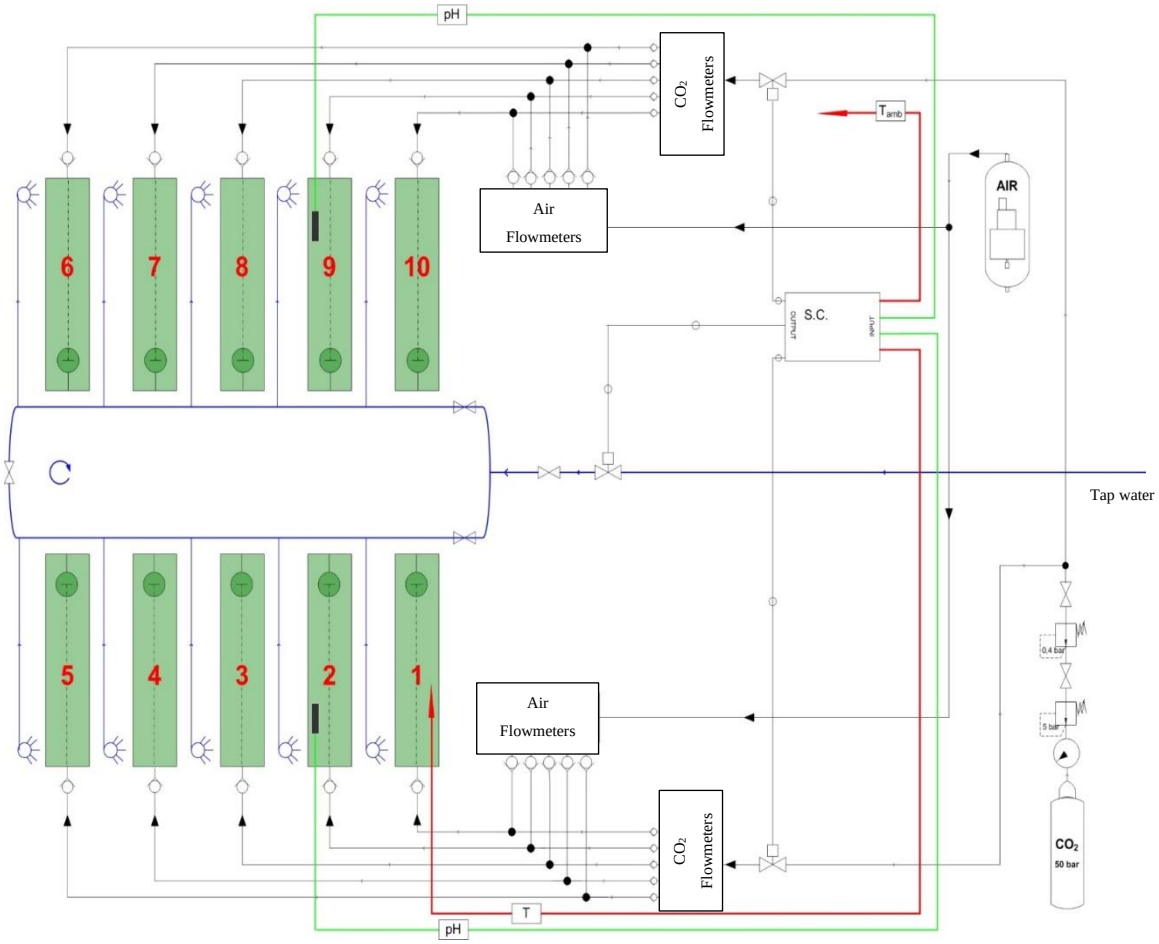

Fig. 45 Schematic representation of the pilot plant with the control system used during the experiments.

2.1.3 Cooling system

In order to control the maximum temperature reached in the PBRs during summer period, as anticipated in the previous subparagraph, a cooling circuit with tap water was designed and installed in the pilot plant. It consisted of a Polyethylene (PE) collector pipe (PN6, Ø 16 mm) placed above the supporting structure with as many outputs as the number of the

reactor. From each outputs of the collector a perforated ring (Ø 17 cm), with the same design of the spargers, was connected and positioned at the top of each reactor. These perforated rings worked as water spray cooling system that, with evaporation of the falling water film along the reactor surface, cooled the culture volume and kept the temperature at set point (Fig. 46). A normally closed remote controlled solenoid valve ensured the water supply for the cooling circuit, while a manual valve allowed the adjustment of the water flow. At the lowest point of the circuit a ball tap, acting as emergency release valve, was placed: in case of high pressure in the loop its connection would jumped out, reducing thus the system pressure.

Fig. 46 Active water spray cooling system.

2.1.4 CO_2 injection system

As regards pH and the maintaining at its set-point (pH=8), an automatic system for the supply of pure CO_2 through cylinders pressurized at 50 bar was set up, optimizing thus the growth conditions. The cylinders were placed in a security cage with a steel platform raised from the ground and protected from weathering. To obtain a pressure suitable for being injected in the line, a BEHRINGER pressure reduction panel with double gauge and manual releasing device, able to reduce the pressure up to 5 bar, was installed at the cylinders' output. This first decrease in pressure was followed by an additional disc reducer, placed before the CO_2 injection into the reactors, reducing the pressure to 1.4 bar. Once CO_2 was passed through the second reducer, at 0.4 barg, it was conveyed into two normally closed solenoid valves connected to a feedback control system (subparagraph 2.1.2), and mixed into the air by Y-connections, measuring also its flow rate with dedicated flow-meters.

2.1.5 Culture medium preparation

Application of microalgal cultivation in large-scale requires the reduction of expensive resources. It is therefore necessary to use tap water, for the formulation of culture media, instead of distilled water used in laboratory-scale cultivations. This choice can lead to reduction of growth efficiency due, for example, to the higher concentration of Ca^{++} ions in tap water (Di Caprio et al., 2017). The culture medium was prepared according to the quantities listed in Tab. 1 for the macronutrients and in Tab. 2 for the micronutrients. Once prepared a 1 L solution for each nutrient, an amount of that (210 mL) was inserted inside each reactor with also a volume of microalgal inoculum (the amount of this will be specified in the following subparagraphs) and made up to the PBR mark (21 L) with tap water.

Chemical compound	**Amount needed (g) for preparation of 1 L of stock solution**	**Amount (mL) to be added in each 21 L reactor**	**Nutrient's concentration (g L^{-1}) reached inside each 21 L reactor**
$NaNO_3$	35	210	0.35
K_2HPO_4	3.05	210	0.031
$MgSO_4 \cdot 7\ H_2O$	7.5	210	0.075
$CaCl_2 \cdot 2\ H_2O$	3.6	210	0.036
Citric Acid	0.6	210	0.006
Ammonium ferric citrate	0.6	210	0.006
EDTA	0.1	210	0.001
Na_2CO_3	2	210	0.02

Tab. 1 Macro-nutrient used for culture medium preparation.

Chemical compound	**Amount needed (mg) for preparation of 1 L of Stock solution**
H_3BO_3	61.0
$MnSO_4 \cdot 5H_2O$	169.0
$ZnSO_4 \cdot 7H_2O$	287.0
$CuSO_4 \cdot 5H_2O$	2.5
$(NH_4)_6Mo_7O_{24} \cdot 4H_2O$	12.5

Tab. 2 Micro-nutrient used for culture medium preparation.

2.1.6 Growth monitoring

During each experiment, when a certain concentration was reached (1-3 g L^{-1}), the microalgal suspension was collected and sent to a 95 L h^{-1} bucket centrifuge (Raw Power Centrifuge). An aliquot of the concentrated suspension was used for the subsequent inoculum. In order to monitor the microalgal growth trends, knowing thus when to stop the cultivation, two different methodologies were used:

- Direct cell count by optical microscope
- Dry weight measurement

The cell count was performed using the Thoma-Zeiss chamber (Fig. 47).

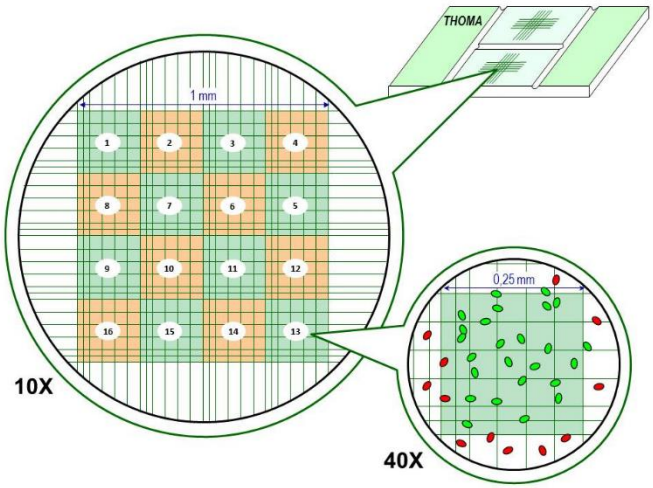

Fig. 47 Thoma cell counting chamber (http://insilico.ehu.eus/counting_chamber/thoma.php).

This counting chamber has a large central square (with a 1 mm^2 area) that can be seen entirely with an optical microscope at 10x (in our experiments a MOTIC EF-NPLAN model was used). This central square, in turn, is divided into 16 medium squares (visible with a 40x objective), each of them composed by 25 small squares (9 of them are divided in half). Once the sample is put under the coverslip, the cell suspension reaches a height of 0.1 mm.

Considering these data related to one of the large squares, the volume will be:

$$1 \times 1 \times 0.1 = 0.1\ mm^3 = 10^{-4}\ mL.$$

The count was done by counting the number of cells that fall within the 16 squares present in the four larger squares along the diagonal; the number of cells obtained was multiplied by four, indicating the number of cells that were stochastically positioned in the entire area. The following formula was used to obtain the concentration (10^6cells mL^{-1}):

$$N = \frac{\sum n_i}{V} * 10^6 \qquad (Eq.\ 2)$$

Where: n_i are the number of cells counted inside the squares and V is the total volume of the squares considered in the count.

As regards dry weight measurement, it was done by filtration of a known volume (10 mL) of the microalgal sample (as aqueous suspension) through a glass microfiber filter having pores with a diameter of 0.70 μm (VWR), by means of a vacuum pump (Vacuubrand MZ 1C). The sampled algal suspension had to be pre-treated in order to remove any precipitated salts. Pretreatment was carried out with 1 mL of sodium acetate buffer solution (at 40 g L^{-1}) and hydrochloric acid 37% (w/w) added drop by drop until reaching pH=4.7.
The filter was weighed on the analytical balance in this order:

- Before filtration, after a preliminary drying phase (10 minutes) at 105°C
- After filtration (Fig. 48), always preceded by a drying phase (40 - 60 minutes) at 105°C

Finally, the difference between the two weight measurements gave the biomass dry weight (g) that divided by the volume of the sample (10 mL) gave the concentration in g L^{-1}.

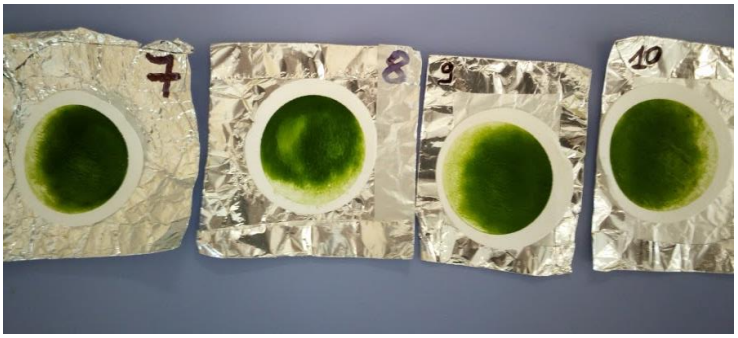

Fig. 48 Dry weighed samples obtained after the drying phase (40 - 60 minutes) at 105°C.

2.1.7 Outdoor factors' monitoring

Temperature and light were the two principal outdoor factors considered and monitored in this work. Temperature's monitoring and control has been explained before (subparagraph 2.1.2 and 2.1.3), the collection of temperature data was easily carried out extracting them directly from LABVIEW software during each experiment both for internal and external temperature. As regards light, the illuminance (Lux) was measured every day (at 10 am, at 2 pm and at 5.30 pm) by using a luxmeter (LM-8000, LT-Lutron) and transformed to the corresponding value of Photosynthetic Photon Flux Density (PPFD) (μE m^{-2} s^{-1}) through multiplication with the conversion factor (0.0185) for sunlight light source (A. Instrument, 2019). Every measure was taken at three points of each reactor, at different heights from the ground: at the bottom (20 cm), at a middle height (80 cm) and at the top (140 cm). Light measurements at the bottom and middle were normalized with respect to light on the top, being always lower than this value. This procedure was justified by a preliminar statistical study (see paragraph 2.2) carried out in order to understand how to collect data. Futhermore, as reference of light fluctuations, light was also measured at a fixed point not affected by any shadowing (named as "unshaded reference point").

2.1.8 Effect of nutrients and inocolum concentration

In addition to the external factors described above, also the effect of $NaNO_3$ ($NaNO_{3init}$ in g L^{-1}) and initial inoculum concentration (C_{init} in g L^{-1}) on biomass growth were studied. In particular, these initial conditions were varied during the first experiments in order to know which was the best initial condition to use (subparagraph 3.1.6). The C_{init} values investigated in the experiment were 0.1 g L^{-1} and 0.3 g L^{-1}. As regards the nitrate concentrations, assumed as main nutrient to be monitored for the reasons described in paragraph 1.5, the values investigated in the experiments were: 0.175 g L^{-1}, 0.35 g L^{-1} and 0.7 g L^{-1} (see Results and Discussion section).

2.2 Preliminary Statistical Studies

In order to define a clear data collection protocol to follow during all the experiments, a preliminar statistic analysis of the effects of several factors which could have influenced temperature and light's measurements was investigated.
In particular, for light studies two ANOVA tests were carried out, considering for each one two factors with replicates:

1) The analyzed factors were: "position along the axis of each reactor" and "reactors' position inside the plant". Measures taken at different days were considered as replicates.
2) The analyzed factors were: "time of measurements' uptake (part of the day)" and "time of measurements' uptake (different days)". Measures taken on different reactors were considered as replicates.

Considered Factor	Data collection's procedure
Position along the axis of each reactor	Measurements were taken at three positions (Top, Medium, Bottom)
Reactors' position inside the plant	Measurements were taken on each reactor of the pilot plant
Time of measurements' uptake (during the day)	Measurements were taken three times (10 a.m., 2 p.m. and 5:30 p.m.) for each working day
Time of measurements' uptake (different days)	Measurements were taken at different days

Tab. 3 Light factors vs. Data collection.

In Tab. 3 factors hypothesized to influence the measures are resumed, together with the explanaitions of how measures were taken.
For temperature, a paired t-test analysis was conducted comparing thus internal and external temperatures in time. Data were divided in three time intervals: temperature increment, internal temperature constant (system control active) and temperature decrement. For all analyses a value of α=0.05 was choosen and Microsoft Office Excel software was used for calculation.

2.3 Multivariate Statistical Model

In the present study two multivariate methods, PCA and PLS respectively, were used, firstly to investigate the effects of variables on microalgal growth, and then to develop an empirical model for growth estimation using MINITAB and OriginPro (OriginLab Corporation) software. In this paragraph a short resume of PCA and PLS methods is carried out. Considering a data matrix X with m rows and n columns, where the rows correspond to samples (or replicates) and column correspond to variables (Eq. 3), PCA will project the X matrix, by means of the projection matrix P, on an smaller dimensional subspace with new object coordinates contained in the matrix T (Eq. 4).

Variables $\longrightarrow$

Sample (replicates) $\downarrow$

$$X_{m,n} = \begin{pmatrix} x_{1,1} & x_{1,2} & \cdots & x_{1,n} \\ x_{2,1} & x_{2,2} & \cdots & x_{2,n} \\ \vdots & \vdots & \ddots & \vdots \\ x_{m,1} & x_{m,2} & \cdots & x_{m,n} \end{pmatrix} \quad \text{(Eq. 3)}$$

$$T = XP \quad \text{(Eq. 4)}$$

$$E = X - TP' \quad \text{(Eq. 5)}$$

The columns in T, t, are called score vectors and the rows in P, p, are called loadings vectors. Vectors t, and p are orthonormal, and the deviations between projections and the original coordinates constitute the residuals' matrix E (Eq. 5) (Härdle and Simar, 2015). PCA, thereby, is able to find a new basis (new directions) that best express data set, as linear combination of the original basis, overcoming the data varability and making visible informations that weren't visible before (correlation between variables, observation clustering, outliers, etc.). Generally, with variable dimensions higher than 2 it is necessary to use the Covariance matrix (Eq. 6) to identify variable redundancy, i.e. when a variable gives similar information of another variable causing some distortions and anomalies in the results.

$$C_X \equiv \frac{1}{n-1} XX^T \quad \text{(Eq. 6)}$$

Mostly, the Correlation matrix (Eq. 7) is preferred to the Covariance one (Eq. 6), because each variable (especially those with different units of measures) is scaled to a null average and to unit variance.

$$R_{i,j} \equiv \frac{C_{i,j}}{\sqrt{C_{i,i}\, C_{j,j}}} \qquad \text{with } i, j = 1, \ldots, p \qquad (\text{Eq. } 7)$$

Mathematically, PCA is based on a diagonalizazion of C_X, minimizing thus the redundancy measured by covariance and yielding score and loading vectors corresponding to eigenvalues in descending order. The eigenvalue order represents the information contained in them, meaning that the first eigenvalue (related to Principal Component 1) is the most important because contains the most useful informations relating to the specific problem, being thus the most important. The other Principal Components contain less informations compared to PC1 and the latest mainly comprises noise.
The Partial Least Square (PLS) is insead a regression method that can be considered an evolution of PCR (Principal Component Regression), because the principal components used are derived not only from the predictor set (X) but also from the responses (Y).
PLS is different from PCR because it uses actively the response data during the statistical analysis, balancing in a better way, the informations inside both Y and X, avoiding those big predictor variations for PCA that are, however, useless for prediction. It also gives more exhaustive answers even in the presence of less detailed data in which PCR can fail. The PLS model can be considered to consist of outer relations (X and Y considered individually) and an inner relation (linking X to Y). The first (outer) relation for X coming from PCA (Eq. 8) is applied to the Y calculation (Eq. 9).

$$X = TP' + E = \sum t_h p_h' + E \qquad (\text{Eq. } 8)$$

$$Y = UQ' + F = \sum u_h q_h' + F \qquad (\text{Eq. } 9)$$

Notably, U, Q and F in Eq. 9 have respectively the same meaning of T, P and E in Eq. 8. The model's intention is to describe Y as well as is possible and hence to make $\|F\|$ as small as possible and, at the same time, get a useful relation between X and Y. The second relation (inner) can be seen at Eq. 10 and symbolizes the relationship between Y and X with their corresponding scores:

$$u_h = b_h t_h \qquad (\text{Eq. } 10)$$

where b_h is the regression coefficient vector.

2.3.1 Multivariate input and output model values

Unlike previous works, in this paper an innovative use of PCA and PLS methods was developed, not only to reduce data redundancy but also to predict microalgal growth in a specific period of the year with defined weather and outdoor cultivation conditions. Inputs (variables for PCA and predictors for PLS) and required outputs (responses for PLS) are summarized in Tab. 4. Internal and External terms refer to the positions of the probes relatively to the reactors; furthermore the "averaged" terms are referred to the variables' collected data, averaged over all their values for each experiment.
The values of specific growth rates were obtained as:

$$\mu = \frac{1}{x}\frac{dx}{dt} \qquad (Eq.\,11)$$

Where x is the microalgal concentration values (g L^{-1}) obtained during the exponential growth phase. The productivity calculated at C_{max}, was obtained as:

$$P_{max} = \frac{C_{max} - C_{init}}{t_{max} - t_{init}} \qquad (Eq.\,12)$$

Input Values	Output Values
Daily Illumination Time (h)	Specic Growth Rate: μ (d^{-1})
Microalgal Inoculum Concentration: C_{init} (g L^{-1})	
$NaNO_3$ Initial Concentration: $NaNO_{3init}$ (g L^{-1})	
Maximum Internal Temperature Averaged: $T_{imax\ avg}$(°C)	
Maximum External Temperature Averaged: $T_{emax\ avg}$(°C)	Productivity calculated at C_{max}: P_{max} (g $L^{-1}d^{-1}$)
Minimum Internal Temperature Averaged: $T_{imin\ avg}$(°C)	
Minimum External Temperature Averaged: $T_{emin\ avg}$(°C)	
Photosynthetic Photon Flux Density: PPFD (μE m^{-2} s^{-1})	

Tab. 4 Input and Output values of the model.

Where C_{max} and C_{init} are respectively the maximum observed biomass concentration (g L^{-1}) reached in each experiment and the biomass concentration (g L^{-1}) at the beginning of each experiment; likewise t_{max} and t_{init} are respectively the time at which the maximum observed biomass concentration was reached and the experiment start time (time zero). Consequently, P_{max} is not referred to the final/total productivity that is actually related to the batch duration.

Experiment	Period of 2017	Notation
A	02-March/14-March	March I
B	21-March/31-March	March II
C	4-April/14-April	April
D	19-April/10-May	April-May
E	15-May/22-May	May
F	20-June/07-July	June-July
G	10-July/27-July	July
H	22-September/17-October	Sep-Oct
I	27-October/22-November	October-November
L	24-November/22-December	Nov-Dec

Tab. 5 Experiments' Periods during 2017.

The experimental data, collected from the installed outdoor pilot plant (see paragraph 2.1), covered a 9 months period (March 2017-December 2017) and to each experiment (totally 10) was assigned a label (A-L) for a better clarity. In Tab. 5 the experiments with the corresponding label and the period in which were conducted are resumed. All the cultivations periods were ended when the microalgae showed a decrease of their growth rate due to nutrients depletion.

2.4 Model for the estimation of metabolites accumulation

One the aims of this thesis is the development of a new mathematical model able to represent in a simple way the microalgal metabolites accumulation, focusing on carbon partitioning process between TAG and starch (see subparagraph 1.2.2). As basis of the metabolites accumulation during stress conditions due to nitrogen starvation, the equations based on Droop model were used (Droop, 1968; Mairet et al., 2011). In order to reduce the model complexity, the number of the equations and parameters were kept at a minimum value without losing the rigor of a structured model. Indeed, the equations used were based on the metabolism pathways typical of microalgae (see paragraph 1.2), without having to resort to complex methods requiring high computational costs and low usability for a final user. Indeed, the model presented in this work, assumes that growth rate and metabolites' accumulation depend on nitrogen concentration uptaked by microalgal cells. Differently from other works presented in literature, the model of this thesis was applied only to nitrogen starvation phase, focusing on interconversion between TAGs and starch molecules, without considering molecules produced during nitrogen replete conditions(Bernard et al., 2016; Mairet et al., 2011). The main feature of this model, differently from what is present in literature (Bekirogullari et al., 2017; Bernard et al., 2016; Figueroa-Torres et al., 2017; Ryu et al., 2018), is the simulation of starch conversion in TAG after a certain period of nitrogen starved cultivation. Furthermore, the model

presented in the following subparagraphs was applied to phototrophy but was built to be easy to handle and also easy re-usable for other cultivations conditions (such as heterotrophy) with only few changings to do, without the need to use complex models specific to phototrophy and not easy editable (Breuer et al., 2015a).

2.4.1 Data used for model design

Before starting to describe the model's structure, an introduction to data used for the model development is carried out in this subparagraph. As said before, the aim of this work is to model the carbon partitioning between starch and TAG molecules and also starch transformation in TAG after a certain period of nitrogen starvation in order to simulate its non monotonous trend. In order to do that, several experimental data found in literature were used for the validation of the new developed model related to phototrophic conditions (Adesanya et al., 2014; Breuer et al., 2015b, 2014; Zhu et al., 2014). In Tab. 6 the informations extracted from the cited article, with the corresponding authors, were resumed. From all the extracted data from the articles presented in Tab. 6, only those referred to the nitrogen starvation period were used in the new developed model, using as time zero the beginning of nitrogen starvation phase (See Results and Discussion section).

Corresponding Author	**Microalgae Used**	**Cultivation Conditions**	**Reactor Configuration and Geometrical Dimensions**	**Incident Light Intensity (I_0)**
Adesanya et al., 2014	*Chlorella vulgaris*	Phototrophy (Indoor Cultivation)	Glass flask assumed planar Reactor depth z=0.3 m	17.44 W m^{-2} (Fluorescent Lamp)
Breuer et al., 2014	*Scenedesmus obliquus*	Phototrophy (Indoor Cultivation)	Flat Panel Photobioreactor Reactor depth z=0.02 m	109 W m^{-2} (White Cool Fluorescent LED)
Breuer et al., 2015b	*Scenedesmus obliquus*	Phototrophy (Indoor Cultivation)	Flat Panel Photobioreactor Reactor depth z=0.02 m	218 W m^{-2} (White Cool Fluorescent LED)
Zhu et al., 2014	*Chlorella zonfingiensis*	Phototrophy (Indoor Cultivation)	Cylindrical Photobioreactor Diameter d=0.05 m	32.7 W m^{-2} (White Cool Fluorescent Lamp)

Tab. 6 Informations obtained from articles available in literature whose data are used for validation of the developed metabolic model.

As additional information, the units of measure of the Incident Light Intensity (I_0) in W m^{-2} shown in Tab. 6 were calculated multiplying the values obtained (from the cited research articles) in Photosynthetic Photon Flux Density (PPFD) in µE m^{-2} s^{-1} with the correction factor related to cool white fluorescent lamp source (0.218) (Environmental Growth Chambers, 2014). Furthermore, considering only nitrogen starved condition, the biomass was assumed to be constituted by the sum of lipids (in forms of TAG), carbohydrates (in form of starch) and proteins; those last were assumed to remain constant at value that had at the starting of the nitrogen deplete cultivation without nitrogen release from cells to the culture medium. The initial protein content (g L^{-1}) was calculated based on considerations of Breuer et. al (Breuer et al., 2012), multiplying the initial biomass concentration (g L^{-1}) by the average protein content of functional biomass; this latter was estimated by dividing the average nitrogen content of functional biomass (0.09 g g^{-1}) by an average nitrogen content in protein assumed equal to 0.16 g g^{-1}, obtaining an initial protein averaged content per unit of biomass of about 0.5625 g g^{-1}. With this consideration was possible to calculate the nitrogen quota in terms of N multiplying the average nitrogen content of functional biomass per the $NaNO_3$ concentration extracted from the plots in the reference articles. Furthermore, for the calculation of starch and TAG quotas in terms of C, the total C content per unit of biomass was calculated; in order to that the C content for starch (0.45), for lipids (0.76) and for proteins (0.4) were estimated and multiplied with the quotas of these components experimentally measured and plotted in the works listed in Tab. 6. These modified data, in terms of units of measure, were used for the model validation.

2.4.2 Model Structure

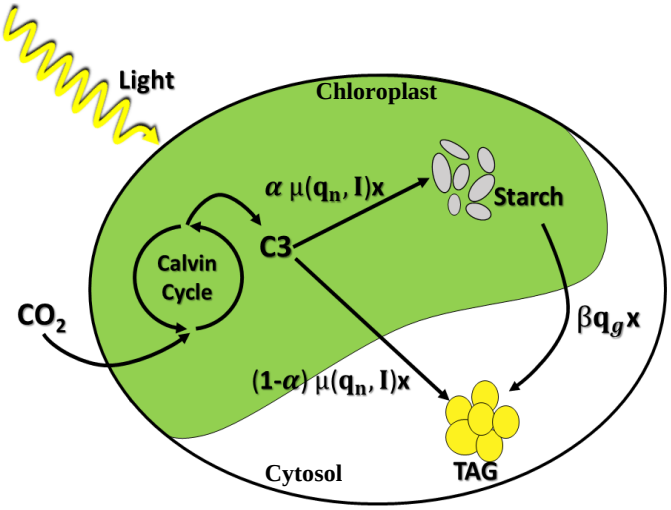

Fig. 49 Schematic representation of the model's carbon pathways used to describe the accumulation of the desired products during nitrogen starvation inside a microalgal cell.

In Fig. 49 the schematization of the developed model is represented, showing the carbon pathways used to simulate the accumulation of starch and TAG during nitrogen starvation inside a microalgal cell. It is visible that the reactions regarding the passage from Free Fatty Acids (FFA) to TAG, both due to conversion of C3 molecules and to starch degradation, were not included in the model because were assumed faster respect to other

reactions (Mairet et al., 2011); furthermore, FFA quota were considered too small to analyze their variations (Guschina and Harwood, 2009). In this model the reactions related to starch and TAG production, due to carbon partitioning of the fixed carbon molecules (C3) from CO_2, were assumed to start simoultaneasly in parallel but with a different rate represented by the partitioning coefficient **α** (g[C] g[C]$^{-1}$) between 0 and 1. Moreover, in this model also the interconversion of starch to TAG was represented, simulating thus the phenomenon that occurs inside microalgae after a certain period of nitrogen starvation and making it dependent on the internal starch quota q_g (g[C] g[C]$^{-1}$) and on the partitioning coefficient β (g[C] g[C]$^{-1}$). In general, the quota for a generic component *i* presented in the model is defined as:

$$q_i = \frac{i}{x} \qquad (Eq.\,13)$$

Where *i* is the concentration (in terms of g[C] L^{-1} or g[N] L^{-1}) of the generic component and *x* is the concentration (in terms of g[C] L^{-1}) of the biomass.
With this definition the quota of nitrogen (q_n), starch (q_g) and TAG (q_l) were introduced in the model in order to analyze their intracellular content variation. Furthermore, in order to pass from the concentration (g L^{-1}) to the elemental concentration (g[C] L^{-1} or g[N] L^{-1}), all the data were modified consequently (see the subparagraph 2.4.1). In accordance with the kinetic equations showed in Fig. 49, the variation of the biomass and of the desired components can be resumed by the following equations:

$$\frac{dx}{dt} = \mu x \qquad (Eq.\,14)$$

$$\frac{dn}{dt} = 0 \qquad (Eq.\,15)$$

$$\frac{dg}{dt} = \alpha\mu x - \beta q_g x \qquad (Eq.\,16)$$

$$\frac{dl}{dt} = (1-\alpha)\mu x + \beta q_g x \qquad (Eq.\,17)$$

Based on Eq. 13, the quota dynamics for a generic component can be written as:

$$\frac{dq_i}{dt} = \frac{d(i/x)}{dt} = \frac{1}{x^2} x \frac{di}{dt} - \frac{1}{x^2} i \frac{dx}{dt} = \frac{1}{x}\frac{di}{dt} - \frac{1}{x}\mu i \qquad (Eq.\,18)$$

Following the Eq. 18, the quota dynamics of the desired components were defined in the equations below:

$$\frac{dq_n}{dt} = -\frac{1}{x}\mu n = -\mu q_n \qquad (Eq.\,19)$$

$$\frac{dq_g}{dt} = \frac{1}{x}\left(\alpha\mu x - \beta q_g x\right) - \frac{1}{x}\mu g = \mu\left(\alpha - q_g\right) - \beta q_g x \qquad (Eq.\,20)$$

$$\frac{dq_l}{dt} = \frac{1}{x}\left((1-\alpha)\mu x + \beta q_g x\right) - \frac{1}{x}\mu l = (1-\alpha-q_l)\mu + \beta q_g \qquad (Eq.\,21)$$

The implemented ODE system was thus:

$$\begin{cases} \frac{dx}{dt} = \mu x \\ \frac{dq_n}{dt} = -\mu q_n \\ \frac{dq_g}{dt} = \mu(\alpha - q_g) - \beta q_g \\ \frac{dq_l}{dt} = (1 - \alpha - q_l)\mu + \beta q_g \end{cases} \quad (Eq.\,22)$$

In particular this parametric ODE system was solved in Matlab using the ode45 function for non-stiff differential equations (for the parametric resolution technique used in the model development see subparagraph 2.4.4).

2.4.3 Specific growth rate and light modeling

As regards the specific growth rate (μ) the following mathematical expression was used:

$$\mu = \mu_m \left(1 - \frac{q_{nmin}}{q_n}\right)\left(\frac{\bar{I}}{K_I + \bar{I}}\right) \quad (Eq.\,23)$$

Where μ_m is the theoretical maximum growth rate (d^{-1}) and q_{nmin} is the minimum nitrogen quota (g[N] g[C]$^{-1}$) allowing microalgal growth. Moreover, $\bar{I}$ (W m^{-2}) is the light irradiance averaged over the geometry of the reactor used and K_I (W m^{-2}) is the half saturation parameter for the light distribution model. Indeed, in this model, besides the dependence of the specific growth rate on the intracellular nitrogen quota defined by Droop model (Droop, 1968), also the dependence on light irradiance was considered with a simple Monod-like function. The necessity of using a light model for μ definition was justified by the experimental conditions of the data used for model validation, in which light was a limiting nutrient influencing thus the specific growth rate. In order to describe the light penetration inside the culture medium, the Lambert–Beer law was used as a first approximation because it could easily estimate light attenuation in simple photobioreactor configurations like the ones used in the examined works. Furthermore, as additional simplification, the collected data were referred to diluted cultures; therefore, light scattering phenomena, that could influence the light distribution in dense culture systems, were not included in the light model. The Lambert–Beer equation is resumed below:

$$I = I_0 e^{-\sigma x y} \quad (Eq.\,24)$$

Where I_0 is the incident light intensity in W m^{-2} (the values of which can be found in Tab. 6), σ is the mass extinction coefficient (m^2 kg^{-1}), x is the biomass concentration (g[C] L^{-1}) and y is the characteristic dimension of the considered reactor (m). About σ , it is a measure, at a given wavelength, of how strongly a microalga can attenuate light; this is

thus dependent on the microalga used in the phototrophic cultivation. In our case σ was assumed to be equal to 200 $m^2\ kg^{-1}$ (Ogbonna et al., 1995) for *Graesiella* species, using the value found in literature related to *Chlorella* due to the morphological similitudes of these two microalgae. For the same reason, since for *Tetradesmus* the mass extinction coefficient values were not available in literature and since its morphology is similar to that of *Monodus subterraneus* (Liu and Lin, 2005), the σ of this last equal to 214 $m^2\ kg^{-1}$ (Bosma et al., 2008) was applied for *Tetradedesmus*. In order to calculate the specific growth rate μ, the average light irradiance had to be defined. In this work was assumed that the individual microalgal cells were exposed to the same light intensity equal to its averaged value across the culture volume (paragraph 1.4). This assumption is reasonable for well-mixed cultivation systems and for low cell density cultures; these conditions describes well those found in the works listed in Tab. 6. For a generic culture volume, the mean irradiance can be calculated as:

$$\bar{I} = \int_V \frac{I(V)}{V} dV \qquad (Eq.\ 25)$$

In particular for a simple planar geometry of thickness L, the mean irradiance is:

$$\bar{I} = \int_0^L \frac{I_0 e^{-\sigma x z}}{L} dz = \frac{I_0}{\sigma x L}(1 - e^{-\sigma x L}) \qquad (Eq.\ 26)$$

As regards a cylindrical geometry with radius R, the averaged irradiance can be found with integration by parts:

$$\bar{I} = \int_0^R \frac{I_0 e^{-\sigma x r}}{\pi R^2 H} 2\pi r H dr = \frac{2I_0}{R^2\sigma^2 x^2} - \frac{2I_0 e^{-\sigma x R}}{R\sigma x}\left(1 + \frac{1}{R\sigma x}\right) \qquad (Eq.\ 27)$$

2.1.2 Parameter Estimation

In order to solve the parametric ODE system shown in Eq. 22 it was necessary to estimate the parameters **α**, β, q_{nmin}, μ_m, K_I. In particular q_{nmin} (g[N] g[C]$^{-1}$) value was found from the q_n data plotted in the works listed in Tab. 6. Indeed, in this work the estimated parameters were only 4 (**α**, β, K_I, μ_m), differently from other models available in literature which use a large number of parameters in order to increase the accuracy, becoming too much complex and very little handy. The Simulated Annealing Constrained method was used to find the best set of parameters that fit data extracted from each reference work, using as function to optimize the Residual Sum of Squares (deviations of predicted values from experimental data); in this way the developed code will solve the parametric ODE finding at the same time the best set of parameters that minimize the difference between experimental and predicted data. The Simulated Annealing method can solve both unconstrained and bound-constrained optimization problems but in this work lower boundary were used, avoiding thus mathematically acceptable but unrealistic results. Indeed, as lower bound null values were

used for each parameter because they couldn't be physically negative; as regard upper bounds, no limitations were applied. Simulated Annealing method was chosen for the presence of several local minima in which other classical optimization algorithms available in Matlab, used to solve nonlinear curve-fitting problems in least-squares sense (e.g nlinfit, lsqnonlin, nlinfit), could be trapped.

2.5 Supercritical CO_2 extraction modeling

In this paragraph the model developed to describe the sCO_2 extraction process of high added value metabolites from microalgal matrix is explained. *Chlorella vulgaris* was the microalga chosen, differently from other literature works (Follegatti-romero et al., 2009; Taher et al., 2014), as extraction matrix and lipid source for its wide range of fatty acids (from 16 to 22 carbon atoms such as oleic acid, omega-3eicosapentaenoic acid (EPA) and docosahexaenoic acid (DHA)) and carotenoids (lutein and astaxanthin) that can accumulate in specific growth conditions (Přibyl et al., 2013). Furthermore, this microalga is morphologically very similar to *Graesiella emersonii* used in the experiments described above, both as internal composition and geometry. In particular, the Sovová simplified model (Sovová, 2005), coupled with other models used for the estimation of the principal physical properties of sCO_2 (solubility (Chrastill, 1982), density (Brunner, 1994) and viscosity (Heidaryan et al., 2011) was applied to *Chlorella* matrix and to its lipidic molecules considered singularly. Indeed, in this model the metabolites were studied and modeled singularly and not as a pseudo-component "oil", differently from other literature works, in order to analyze their affinity inside the sCO_2 (such as diffusivity) and to define the best extraction conditions in terms of operative variables (mainly pressure and temperature) that also allow the extraction and separation of carotenoids (residue stream) from fatty acids (extract stream), preserving their bioactive properties. The model's results were used to implement a simulation of the designed process, calculating the daily amount of the extracted products and estimating also Operating Expense (OPEX) and Capital Expenditure (CAPEX) (see subparagraphs 3.7.4).

2.5.1 Microalgal composition

Chlorella vulgaris, as said before, was the microalga chosen for the extraction simulation and similarly to *Graesiella*, can grow in both photoautotrophy or heterotrophy and, depending on nutrients' limitation (mainly nitrogen), it can store more a product (lipids) than another (proteins or carbohydrates). In Tab. 7 a "simplified" *Chlorella* composition on dry weightbasis (%DW) is represented; this list was based on values found in literature for the principal components of interest present in the microalga (Adamakis et al., 2018; Damergi et al., 2017; Gouveia et al., 1996).
Specifically, the palmitic acid was chosen as representative of fatty acids with 16 carbon atoms, since it is present in highest concentration. The same considerations were done for oleic acid (fatty acids with 18 carbon atoms) and for the others components representing bothomega-3 and carotenoids' classes.

Components	Mass fraction (%DW)
Palmitic acid	0.14
Oleic acid	0.15
EPA	0.06
DHA 0.13	0.13
Lutein	0.08
Astaxanthin	0.06
Carbohydrates	0.17
Proteins	0.21

Tab. 7 *Chlorella* composition on dry weight used in the extraction model.

2.5.2 Sovová's simplified model for sCO_2 extraction

In this work the simplified version of the "Broken and Intact Cell Model" developed by Sovová (Sovová, 2005) was used, describing the whole process with realistic results without requiring the knowledge of numerous parameters necessary in the complete model. Furthermore, this model is suitable for our scope because it describes exactly the structure of the microalgal particle with broken cells as a result of the pre-treatment.
According to this model, in the particle there are two distinguishable regions (see Fig. 50):

- A region where broken cells are present, located near the particle's surface
- A region where intact cells are present, located in the inner part of the particle

Cell rupture or not is the result of pre-treatment to which the natural matrix is undergone. The mass transfer, in the two previously mentioned regions, is described differently. In the region near the surface where the broken cells are present, internal resistance to mass transfer is neglected and is the resistance to mass transfer in the external film is controlling the transport. The free solute in the broken cells easily passes from the particle to the solvent. As a result, extraction at this stage is fast, with a steady rate of progress. This the first extraction period. At the end of this period, the oil, now present inside the intact cells, passes first into the broken cells and finally into the solvent. Transfer, in this case, is controlled by the resistance to internal mass transfer, such as occurs in the diffusive model; the extraction is slow and is typical of the final phase of the extraction process.

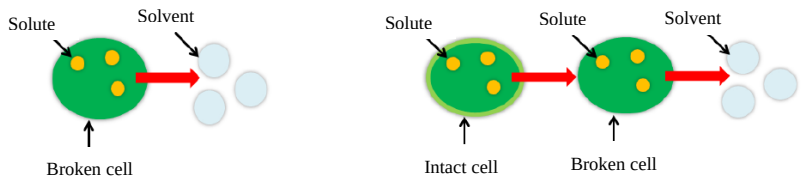

Fig. 50 Simplified representation of mass transfer from microalgal matrix using sCO_2 as solvent.

In particular, this simplified version is built on two equations describing the extraction yield (e) in two periods (a fast one and a slower one) without considering the transition phase during which the solute from the broken cells continues to be extracted while the extraction of the same begins from intact cells. The equations for both periods used in this work are:

$$e = ty_s\left[1-e^{-\frac{1}{\theta_f}}\right]q \qquad \text{for } t \leq t_1 \qquad (Eq.\,28)$$

$$e = c_u\left[1-(1-G)e^{-\frac{t-t_1}{t_i}}\right] \qquad \text{for } t > t_1 \qquad (Eq.\,29)$$

Where:

- e is the extraction yield expressed as the ratio of the extract mass and the mass of microalgae loaded into the reactor ($g_{extracted\ product}\ g_{microalgae}^{-1}$)
- q is the specific flow rate, that is the ratio between the solvent flow rate and the mass of microalgae loaded into the reactor (min^{-1})
- t_1 is the extraction time at the end of the first period defined as $e(t_1) = Gc_u$ (min)
- θ_f is the external mass transfer resistance
- t_i is the characteristic time of mass transfer in the solid phase, function of the internal diffusivity (min)
- c_u is the asymptotic value of extraction yield ($g_{extracted\ product}\ g_{microalgae}^{-1}$)
- y_s is the Solubility of each component in sCO_2 ($g_{product}\ g_{sCO2}^{-1}$)
- G is the initial fraction of solute in open cells.

In Eq. 28 and Eq. 29 reported above, the dependences of the extraction yield (e) on solubility (y_s) and on the asymptotic value of extraction yield (c_u) are reported. Among the various parameters present in the previous equations θ_f appears (Eq. 30), that is the external mass transfer resistance. This unknown parameter can be defined as the ratio of t_f (fluid phase mass transfer's characteristic time) and of the t_r (residence time).

$$\theta_f = \frac{t_f}{t_r} = \frac{d_p q \rho_s}{k_f 6 \rho_f} \qquad (Eq.\,30)$$

Where ρ_s and ρ_f are respectively the Solid and Fluid density (kg m^{-3}).
In order to calculate the external mass transfer coefficient (k_f), the dimensionless numbers Sh, Re, and Sc were used. In the case of mass transfer using sCO_2 as solvent with microalgal particles assumed spherical (with a diameter d_p), the Sherwood number (Sh) was calculated by the following expression (Taher et al., 2014):

$$Sh = 0.13Re^{1.4}Sc^{0.75} \qquad (Eq.\,31)$$

Known Reynolds (Re) and Schmidt (Sc) numbers, it was possible to calculate k_f:

$$k_f = \frac{Sc\, D_{12}}{d_p} \qquad (Eq.\,32)$$

where D_{12} is the lipids' diffusivity in sCO_2 ($m^2\,s^{-1}$).
The parameters used in these equations, and listed in Tab. 8, were obtained from calculations based on literature values (Lin, 1985) and from contact with extractor's suppliers.

Parameter	Value
d_p	$0.4*10^{-5}$ m
$\boldsymbol{\varepsilon}$	0.36
t_i	51.5 min
ρ_s	1554 kg m^{-3}
d_R	0.7 m
G	0.41

Tab. 8 Parameters used for extraction modeling.

In Tab. 9 the diffusivities values of each soluble compounds in sCO_2 at T = 60°C and P = 250 bar (see the optimized conditions obtained in the Results and Discussion paragraph 3.7) are listed; these values were obtained by a regression of literature data at P and T different from those used in the modeling (Funazukuri et al., 2003; Rezaei and Temelli, 2000).

Parameter	Diffusivity ($\times 10^{-9} m^2 s^{-1}$)
Palmitic acid	4.3
Oleic acid	4.1
EPA	6.8
DHA	6.4

Tab. 9 Diffusivities of soluble compounds in sCO_2 present in *Chlorella* at T = 60 °C and P = 250 bar.

As can be seen in Tab. 9, the carotenoids are not present because at the optimized process conditions, and without any co-solvent added to CO_2, they have a very low solubility (approximated to zero) in sCO_2 as confirmed by literature (Macìas-Sànchez et al., 2008; Mendes et al., 1995; Safi et al., 2013). The carotenoids will be thus separated from fatty acids without any further purification steps, being part of the residue stream together with proteins and carbohydrates.

2.5.3 Models for physical properties

In each sCO_2 extraction model, especially for the Sovová one, there are three physical properties that have to be taken into account in detail: the components' solubilities in sCO_2 (y_s), the density of sCO_2 phase (ρ_f) and the viscosity of sCO_2 (μ_v). These physical properties for both solvent and solute were based on literature data with experiments done in a range within which the conditions used in the modeling fall. In particular also the parameters used in each model to describe solubility, density and viscosity were related to the specific conditions used in the modeling. In this work, for solubility calculation the Chrastil model was used (Chrastll, 1982), requiring the smallest number of parameters compared to others present in literature (Adachi and C.-Y.Lu, 1983; del Valle and Aguilera, 1988) and giving similar results. According to this model, the solubility was described with the following expression (Eq. 33), where k,a,b are thermodynamic parameters.

$$y_s = \rho_f^k \exp\left(\frac{a}{T} + b\right) \qquad \text{(Eq. 33)}$$

The analysis of each target component present in the microalgal matrix, considered singularly, permitted to study their extraction yield (based on their affinity to sCO_2) and to choose the slower one for the extraction process. As regards density (influenced by pressure and temperature), it directly affects the components' solubility in sCO_2 and requires an equation able to describe its behavior in a wide range of process conditions. Simple equations of state were not able to estimate density very accurately over a large interval of pressure and temperature; indeed, to better represent the data, multi-parameter equations of state are required. Between several models present in literature, the most suitable for our case can be found in the Bender equation of state (Brunner, 1994):

$$P = RT\rho_f + B\rho_f^2 + C\rho_f^3 + D\rho_f^4 + E\rho_f^5 + F\rho_f^6 + (G + H\rho_f^2)\rho_f^3 \exp(-a_{20}\rho_f^2) \qquad \text{(Eq. 34)}$$

This equation calculates the pressure as a function of temperature and density using 20 parameters, fitted on property data, with the aim to find the constants B, C, D, E, F, G, H (Tab. 10). The Bender equation of state was considered a good compromise between simple and more elaborate equations and it has a high reliability in homogeneous fluids in supercritical state, particularly for well-known compounds as CO_2 with a low acentric factor (Ghazouani et al., 2005).

Parameter	Value	Parameter	Value
$\mathbf{a_1}$	0.22488558	a_{11}	0.12115286
$\mathbf{a_2}$	$0.13717965*10^{3}$	a_{12}	$0.10783386*10^{3}$
$\mathbf{a_3}$	$0.14430214*10^{5}$	a_{13}	$0.43962336*10^{2}$
$\mathbf{a_4}$	$0.29630491*10^{7}$	a_{14}	$-0.36505545*10^{8}$
$\mathbf{a_5}$	$0.20606039*10^{9}$	a_{15}	$0.19490511*10^{11}$
$\mathbf{a_6}$	$0.45554393*10^{-1}$	a_{16}	$-0.29186718*10^{13}$
$\mathbf{a_7}$	$0.77042840*10^{2}$	a_{17}	$0.24358627*10^{8}$
$\mathbf{a_8}$	$0.40602371*10^{5}$	a_{18}	$-0.37546530*10^{11}$
$\mathbf{a_9}$	0.40029509	a_{19}	$0.11898141*10^{14}$
$\mathbf{a_{10}}$	$-0.39436077*10^{3}$	a_{20}	$0.50*10^{-1}$

Tab. 10 Parameters used in Bender's equation.

In addition to these two variables there is the sCO_2 viscosity and for its calculation the following formula was used (Heidaryan et al., 2011):

$$\mu_v = \frac{A_1 + A_2\rho_f + A_3\rho_f^2 + A_4(\ln(T))^2 + A_6(\ln(T))^3}{1 + A_7\rho_f + A_8\ln(T) + A_9(\ln(T))^2} \qquad (\text{Eq. } 35)$$

Parameter	Value
$\mathbf{A_1}$	$-1.146067*10^{-1}$
$\mathbf{A_2}$	$6.978380*10^{-7}$
$\mathbf{A_3}$	$3.976765*10^{-10}$
$\mathbf{A_4}$	$6.336120*10^{-2}$
$\mathbf{A_5}$	$-1.166119*10^{-2}$
$\mathbf{A_6}$	$7.142596*10^{-4}$
$\mathbf{A_7}$	$6.519333*10^{-6}$
$\mathbf{A_8}$	$-3.567559*10^{-1}$
$\mathbf{A_9}$	$3.180473*10^{-2}$

Tab. 11 Parameters used in the viscosity equation.

This viscosity is a function of both sCO_2 density and the extractor temperature. Moreover, the coefficients shown in Eq. 35 were taken from the reference paper (Heidaryan et al., 2011) (Tab. 11).

2.5.4 Extraction modeling and simulation

All of the equations listed in paragraph 2.5 were used for developing a simulative extraction model using MATLAB and giving results in terms of extraction yield (against time). Furthermore, the effects of the principal operative variables (temperature, pressure and Solvent to Solid Ratio=SSR) on the extraction yield were evaluated (see paragraph 3.7). The optimization of these variables is crucial not only for the extraction from the microalgal matrix, but also for the preservation of the biological activity of the target metabolites. Working at these optimized conditions assures also to keep the carotenoids with a very low solubility (approximated to zero) in sCO_2 and to avoid further purification steps, having already done the principal separation of carotenoids (residue) from fatty acids (extract). The results obtained from the model were used to develop a simulation of the extraction process, with the help of the software Aspen Plus, calculating and optimizing the number of working cycles with aim of increasing productivity. The composition of the inlet stream to the extractor is reported in Tab. 7; in particular, carbohydrates were simulated as starch and the proteins were represented by the leucin, since it is the more synthesized in *Chlorella*. Since lutein and astaxanthin were not available in ASPEN databases, it was necessary to add them with the corresponding .mol files. Once that the molecular structure was available, the basic thermo-physical properties for both pure components were estimated using NIST (National Institute of Standards and Technology) TDE (Thermo Data Engine). For a final check, a comparison of the principal estimated properties for both pure components (vapor pressure, critical point, etc.), with those available in literature was carried out, confirming the goodness of the estimation. Since a group contribution model was used to define the molecules not present in the database, the most logical choice was then to use as thermodynamic reference a model based on group contribution method; indeed UNIFAC (UNIquac Functional-group Activity Coefficients) was chosen as thermodynamic method in the simulation.

Thermodynamic Method	**UNIFAC**	**SRK**
Property	**Value**	**Value**
Density (mol/l)	4.14	4.17
Fugacity (bar)	$5.8*10^{-10}$	$5.5*10^{-11}$
C_v (kJ/kmol-K)	950.63	1050.06
C_p (kJ/kmol-K)	693.01	1071.98
Vapor Pressure (bar)	$6.55*10^{-11}$	$6.55*10^{-11}$

Tab. 12 Comparison of the estimated principal properties in liquid phase of Lutein with two thermodynamic models at P=250 bar e T=20°C.

In order to motivate this choice, a comparison of the principal thermophysical properties for lutein (the same results were obtained for astaxanthin), estimated with two different thermodynamic models (UNIFAC and Soave-Redlich-Kwong=SRK) at P = 250 bar and T = 60°C, are reported in Tab. 12, showing very small differences between them and confirming the choice made. This simulation was necessary to calculate the energy and utilities consumption that, coupled with the design of each equipment of the facility, provided to make an estimation of Operating Expense (OPEX) and Capital Expenditure (CAPEX) (see subparagraph 3.7.4).

2.6 Simulation of molecular distillation process

In this paragraph the study of a new designed separation process with molecular distillation of oily microalgal metabolites (fatty acids esters, in part as omega-3 and carotenoids), coming out from the extraction process with sCO_2 described in paragraph 2.5, is described. To reach more realistic results, each step of the designed process was investigated and optimized in order to increase the purification of the desired outputs
with less energy and costs expenditure. In particular, for the optimization of the operating conditions (pressure and temperature) at which the molecular distiller had to work, a statistical analysis by Respone Surface Method (RSM) was performed, based on the results obtained from simulations by dedicated software (Aspen Plus). In addition to molecular distiller, also the other equipments of the facility were studied and optimized always maintaining a green approach. Indeed, for the esterification reaction ethanol as replacement of the classic methanol was used. Moreover, for the same reasons a dewatering section was necessary to recover the ethanol and reusing it in the reaction, minimizing wastes and increasing the esterification's productivity. As has been done for sCO_2 extraction (subparagraph 3.7.4), also for molecular distillation the entire optimized process was then simulated in order to calculate the energy and utilities consumption that, coupled with the design of each equipment, provided to make an estimation of Operating Expense (OPEX) and Capital Expenditure (CAPEX) (see subparagraph 3.8.6).

2.6.1 Feed characterization and process simulation

The process' feed shown in Tab. 13 was based on results obtained from a simulation, carried out in Aspen (see subparagraph 3.8.1), aimed to extract and separate carotenoids from starch and protein (with ethanol) from the residual stream of sCO_2 extraction showed in Tab. 27. In addition to traces of water and ethanol due to this pre-treatment, fatty acids and carotenoids are the most present components. The feed flow rate was equal to 3.55 kg h^{-1}.

Component	Mass frac
Palmitic Acid	0.109
Oleic Acid	0.116
Eicosapentaenoic acid (EPA)	0.048
Docosahexaenoic acid (DHA)	0.099
Lutein	0.332
Astaxanthin	0.268
Ethanol	0.023
Water	0.005

Tab. 13 Molecular distillation process' feed composition.

The Block Flow Diagram of the process, focused on the separation of the carotenoids from fatty acids (as esters) is shown in Fig. 51. The simulation of the whole process was carried out with the software Aspen Plus, including molecular distillation and water removal with adsorption/desorption column, even if they didn't have a dedicated equipment in it. Regarding the components described in Tab. 13, only lutein and astaxanthin were not present in the simulator database, so it was necessary to import the .mol files of the two molecules into the software. The .mol file contains a graphic-functional representation of the molecule thanks to which, through a group's contributions method, it was possible to estimate its physical and chemical properties. Since for the evaluation of some chemical-physical features it was necessary to use predictive estimations, also in this case UNIFAC (UNIquac Functional-group Activity Coefficients) was chosen as thermodynamic method for the simulation. This method exploits the functional groups present in the molecules to evaluate the activity coefficients.

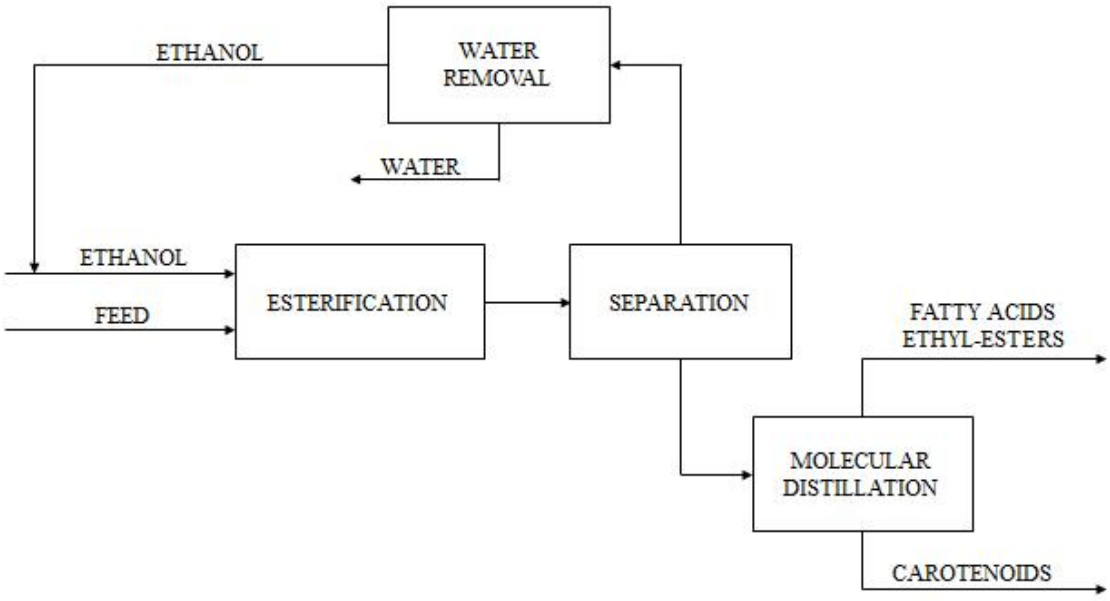

Fig. 51 Block Flow Diagram of the designed process for separation of carotenoids from fatty acids as esters.

2.6.2 Esterification and separation

The stream containing fatty acids and carotenoids described in the previous subparagraph was subjected to an esterification reaction with ethanol in order to convert the fatty acids into the respective ethyl esters. This step is generally crucial for two reasons: (1) The ethyl-esters are more stable for a physical separation (2) The ethyl-esters formation increased the fractionation efficiency, because it increases the relative volatility of carotenoids and fatty acids ethyl-esters. Indeed, the esters don't have the hydrogen bonding between molecules that carboxylic acids have, so they cannot act as hydrogen-bond donors and cannot self-associate; consequently, esters are more volatile than corresponding carboxylic acids (March, 1992). In particular, this latter consideration can be applied only to classical distillation, because for molecular distillation the partial pressure of the evaporated substance approaches the total pressure, the passage of the molecules through the distillation space is collision free and the fractionation efficiency depends on the molecular weight (dimensions) of the molecules. Anyway, for the esterification of our components, the increase of the molecular weight was very little (DHA passes from 328.488 g/mol to 356.55 g/mol respect to Astaxanthin with 596.841 g/mol), having thus negligible negative impact into the molecular distillation efficiency compared to the high benefits given by the increased stability of the esterified molecules. Ethanol was the alcohol used in this work for the reaction (in substitution of the classical methanol), having been classified as GRAS (Generally Recognized As Safe) by the FDA (U.S. Food and Drug Administration, HHS, Code of Federal Regulations, Title 21: (Subpart I: Nutrients.), 2013, 229070) and being thus suitable for the nutraceutical use of the purified products. The reaction was carried out at P = 1 bar and at T = 60 °C, in order to not damage the thermosensitive molecules. Since oleic acid is an intermediate component from the point of view of steric hindrance between the considered fatty acids, and also due to the absence of kinetic information for palmitic acid, EPA and DHA, the same conversion of oleic acid for the other components was used for a first attempt estimation. The reactors' configuration, suitable for the not catalyzed homogeneous-phase esterification reaction with a second order kinetic considered in this work, was the CSTR. Esterification is usually catalyzed in homogeneous phase by strong, corrosive and environmentally harmful acids (as sulfuric acid). In literature there are very few reports about non-catalytic kinetics for fatty acid esterification and those few work always with methanol as solvent; this latter cannot be applied in our process due to the nutraceutical usage of the purified molecules. Furthermore, the non-catalytic reaction, at the expense of slower reaction rates, overcome the problems of catalyst separation (for homogenous catalysis), purification of the feedstock in order to avoid catalyst damages and deactivation (for heterogeneous catalysis) and high costs (for enzymatic catalysis). In particular, the data chosen for the forward rate constant (E_a) was similar to the values of 2560 kJ/mol reported for sulfuric acid-catalyzed esterification of FFA with methanol (Aranda et al., 2008), underlining anyway the goodness of the application of a noncatalyzed reaction (with ethanol) in this study.

As said before, since oleic acid is an intermediate component from the point of view of steric hindrance between the considered fatty acids, and also due to the absence of kinetic informations for palmitic acid, EPA and DHA, the same conversion of oleic acid for the other components was used for a first attempt estimation. The reaction is thus structured:

$$C_{18}H_{34}O_2 + C_2H_6O \leftrightarrow C_{20}H_{38}O_2 + H_2O$$

The kinetic constants follow the Arrhenius equation and both pre-exponential factors and activation energies of both direct and indirect esterification reaction for oleic acid are reported in Tab. 14 (Pinnarat and Savage, 2010). For a better clarification of the terms used, see Fig. 52.
The material balance equation for a generic component *i* in a CSTR was written as:

$$V\frac{dC_i}{dt} = QC_i^0 - QC_i + Vr_i \qquad (Eq.\,36)$$

Where V is the reactor's liquid volume, C_i^0 and C_i are respectively the inlet/outlet molar concentration for the i-component, Q is the volumetric flowrate and r_i is the reaction rate per unit of volume for the i-component. The material balance described in Eq. 36 and applied to our esterification reaction is represented in Eq. 37, integrated using gPROMS software.

Parameter	Value	Unit of measure
$\mathbf{k_{dir}^0}$	$10^{3.5}$	L mol^{-1} min^{-1}
$\mathbf{k_{rev}^0}$	$10^{5.3}$	L mol^{-1} min^{-1}
$\mathbf{E_a^{dir}}$	56	kJ mol^{-1}
$\mathbf{E_a^{rev}}$	66	kJ mol^{-1}
$\mathbf{C_O^0}$	0.048	mol L^{-1}
$\mathbf{C_E^0}$	14.11	mol L^{-1}
$\mathbf{C_W^0}$	0.03	mol L^{-1}
Q	0.51	L min^{-1}
T	333.15	K
R	8.314	J mol^{-1} K^{-1}

Tab. 14 Parameters used for the integration of the Eq. 37 in gPROMS for the esterification reaction of oleic acid

Nomenclature

C_O^0	concentration of oleic acid in the inlet reactor stream (mol L^{-1})	k^{rev}	reaction rate coefficient of the revers esterification reaction (L mol^{-1} min^{-1})
C_E^0	concentration of ethanol in the inlet reactor stream (mol L^{-1})	q_0	adsorption capacity (mol m^{-3})
C_W^0	concentrations of water in the inlet reactor stream (mol L^{-1})	K_L	Langmuir constant (m^3 mol^{-1})
C_O	concentration of oleic acid in the output reactor stream (mol L^{-1})	C_W^L	water concentration in the liquid phase in the adsorption column (mol m^{-3})
C_E	concentration of ethanol in the output reactor stream (mol L^{-1})	C_W^S	water concentration in the solid phase in the adsorption column (mol m^{-3})
C_{OE}	concentration of ethyl oleate in the output reactor stream (mol L^{-1})	Q'	volumetric flow rate of the liquid phase in the adsorption column (m^3 s^{-1})
C_W	concentration of water in the output reactor stream (mol L^{-1})	R	adsorption column radius (m)
Q	volumetric reactor flow rate (L min^{-1})	a	specific area of the adsorbent solid (m^{-1})
V	reactor's volume (L)	K_{OL}	overall mass transfer coefficient in the adsorption balance (m s^{-1})
k^{dir}	reaction rate coefficient of the direct esterification reaction (L mol^{-1} min^{-1})	ρ_S	solid phase density in the adsorption balance (kg m^{-3})

Fig. 52 Nomenclature of the symbols used in the molecular distillation study.

$$\begin{cases} V\dfrac{dC_O}{dt} = QC_O^0 - QC_O - k^{dir}C_OC_EV + k^{rev}C_{OE}C_WV \\ V\dfrac{dC_E}{dt} = QC_E^0 - QC_E - k^{dir}C_OC_EV + k^{rev}C_{OE}C_WV \\ V\dfrac{dC_{OE}}{dt} = -QC_{OE}^0 + k^{dir}C_OC_EV - k^{rev}C_{OE}C_WV \\ V\dfrac{dC_W}{dt} = QC_W^0 - QC_W + k^{dir}C_OC_EV - k^{rev}C_{OE}C_WV \end{cases} \quad \text{(Eq. 37)}$$

The values obtained from this calculation gave an idea of the esterification's conversion and reactor volume. The stream coming out from the reactor was sent to a vacuum flash, operating at 0.01 bar and 80 °C, in order to separate the formed water and the unreacted ethanol from the rest of the stream.

In order to show the dependence of oleic acid conversion from CSTR reactor liquid volume, some mathematical passages have to be shown. Considering the acetic acid as the reference component of the abovesaid reaction, the equation that bounds components' concentration (C_O) to conversion (X_O) of oleic acid was defined as:

$$C_i = C_i^0 + \frac{\nu_i}{\nu_O}C_OX_O \quad \text{(Eq. 38)}$$

Where ν_i and ν_O are the stoichiometric coefficients for the i-component and for oleic acid respectively. Substituting the Eq. 38 into the material balance Eq. 36 for a steady state condition the following equation was obtained:

$$QC_i^0 - Q\left(C_i^0 + \frac{\nu_i}{\nu_O}C_OX_O\right) + Vr_i = 0 \quad \text{(Eq. 39)}$$

Applying the mass balance to the reference component (oleic acid) the Eq. 39 became:

$$QC_O^0X_O + Vr_O = 0 \quad \text{(Eq. 40)}$$

Furthermore, as previously specified, the reaction considered was non-catalyzed with a second order kinetic, so the r_O is:

$$r_O = -k^{dir} C_O C_E + k^{rev} C_{OE} C_W \qquad (Eq. 41)$$

Knowing the C_i for each component, on the basis of the Eq. 38:

$$\begin{aligned} C_O &= C_O^0 (1 - X_O) \\ C_E &= C_E^0 - C_O^0 X_O \\ C_{OE} &= C_{OE}^0 + C_O^0 X_O \\ C_W &= C_W^0 + C_O^0 X_O \end{aligned} \qquad (Eq. 42)$$

The Eq. 41 can be rewritten in function of X_O:

$$\begin{aligned} r_O = -k^{dir} C_O^0 C_E^0 + k^{dir} (C_O^0)^2 X_O + k^{dir} C_O^0 C_E^0 X_O - k^{dir} (C_O^0)^2 (X_O)^2 + \\ + k^{inv} C_{OE}^0 C_W^0 + k^{inv} C_{OE}^0 C_O^0 X_O + k^{inv} C_W^0 C_O^0 X_O + k^{inv} (C_O^0)^2 (X_O)^2 \end{aligned} \qquad (Eq. 43)$$

Where k_{rev} and k_{dir} were the reaction rate coefficient of the revers and direct esterification reaction following the Arrhenius law.
Finally, replacing thus the Eq. 43 into Eq. 40, the dependence of oleic acid conversion from CSTR reactor liquid volume was obtained.

2.6.3 Water removal by adsorption column

In order to recover the ethanol coming out from the flash after the esterification, it was necessary to remove the water that tend to accumulate in the closed loop circuit, undermining thus the esterification rate. A molecular sieve with a 3 Å zeolite particle, having a diameter of 3.6 mm (Simo et al., 2009) was used to do this separation and a TSA (Thermal Swing Adsorption) approach was adopted, where a hot air flow at a temperature between 140 °C and 250 °C was used to regenerate the adsorbent solid (Gabruś et al., 2015). For the sizing of the adsorption column, the water material balances both in the liquid and solid phase were written, coupling them to the water adsorption isotherm in a 3 Å zeolite (Yamamoto et al., 2012). Eq. 44 is the Langmuir isotherm, where n_W are the moles of adsorbed water per kg of adsorbent solid (mol kg_{solid}^{-1}):

$$n_W = \frac{q_0 K_L C_w^S}{1 + K_L C_w^S} \qquad (Eq. 44)$$

For the material balance calculations, a LDF (Linear Driving Force) approach was used, considering the solid as a pseudo homogeneous phase. Moreover, with this approach an overall exchange coefficient (K_{OL}), which takes into account the mass transfer resistances of the solid-liquid system, was used (Teo and Ruth van, 1986). In the solid phase it was possible to write a macroscopic balance reported in Eq. 45; likewise, the mass balance in the liquid phase along the axial coordinate of the column was done.

$$\begin{cases} \varepsilon \dfrac{\partial C_w^L}{\partial t} = -\dfrac{Q'}{\pi R^2}\dfrac{\partial C_w^L}{\partial z} - aK_{OL}(C_w^L - C_w^S) \\ (1-\varepsilon)\rho_S \dfrac{\partial n_W}{\partial t} = aK_{OL}(C_w^L - C_w^S) \\ n_W = \dfrac{q_0 K_L C_w^S}{1 + K_L C_w^S} \end{cases} \qquad (Eq.\,45)$$

In Eq. 45 ε is the bed void fraction defined as ratio of V_L and V_{TOT}, where V_L is the liquid volume inside the column with a volume V_{TOT}. The system was integrated with the software gPROMS (chosen due to its easy applicability for PDE solution), with the initial and boundary conditions:

$$\begin{cases} C_w^L|_{t=0} = 0 \\ n_W|_{t=0} = 0 \\ C_w^L|_{z=0} = C_w^{IN} \end{cases} \qquad (Eq.\,46)$$

Tab. 15 reports the values of the parameters used for the integration (Gabruś et al., 2015; Simo et al., 2009; Yamamoto et al., 2012). The aim of the column's sizing was to find its minimum dimensions and also to find a way to make the process working continuously with at least two columns in parallel. For this latter purpose, the saturation time of the solid must be greater than the sum of the regeneration and cooling times:

$$t_{SAT} > t_{REG} + t_{COOL} \qquad (Eq.\,47)$$

To evaluate the regeneration time, a simulation similar to the previous one was carried out, integrating the following system:

$$\begin{cases} \varepsilon \dfrac{\partial C_w^L}{\partial t} = -\dfrac{Q'}{\pi R^2}\dfrac{\partial C_w^L}{\partial z} + aK_{OL}(C_w^L - C_w^S) \\ (1-\varepsilon)\rho_S \dfrac{\partial n_W}{\partial t} = -aK_{OL}(C_w^L - C_w^S) \\ n_W = \dfrac{q_0 K_L C_w^S}{1 + K_L C_w^S} \end{cases} \qquad (Eq.\,48)$$

With the initial and boundary conditions:

$$\begin{cases} C_w^L|_{t=0} = 0 \\ C_w^S|_{t=0} = C_w^0 \\ C_w^L|_{z=0} = 0 \end{cases} \quad \text{(Eq. 49)}$$

The parameters used were the same as those shown in Tab. 15, with the exception of C_w^0 equal to 186.55 mol m^{-3}, and aK_{OL} equal to 9.5*10^{-4} s^{-1} (Simo et al., 2009).

Parameter	Value	Unit of measure
C_W^{IN}	186.53	mol m^{-3}
ε	0.372	-
Q'	7.55*10^{-3}	m^3 s^{-1}
aK_{OL}	2.6*10^{-3}	s^{-1}
ρ_S	838	kg m^{-3}
q_0	22.6*10^{-2}	mol kg^{-1}
K_L	0.611	m^3 mol^{-1}

Tab. 15 Parameters used for the integration of the macroscopic balance in order to size the adsorption column.

2.6.4 Molecular distillation and RSM study

The molecular distiller configuration chosen in this work and confirmed by specialist suppliers, was the "Agitated thin-film evaporator" with a falling and revolving liquid film. This distiller has a film with thickness of 0.1-1 mm, with a mean residence time ranging from 0.1 to 10 s and throughput rate of up to 1 t/h (Lutisan and Cvengros, 1995; Sattler and Feindt, 1995). The molecular distillation process was simulated in Aspen Plus software, even if there wasn't a dedicated equipment for this separator, with a flash vessel. The flash vessel was the best solution able to simulate the separation of a distilled stream from the residue with very short residence time, without requiring the development of a specific and more complex model in order to reduce the already short residence time. In order to identify the optimal operating conditions for the molecular distiller, a RSM analysis (Response Surface Method) with a CCD (Central Composite Design) was performed (Bezerra et al., 2008; Kalil et al., 2000). The selected natural (or independent) variables for the distillation process were the temperature and the pressure of the molecular distiller, which varied in the following ranges (Stephan, 1992):

$$60°C \leq T \leq 150°C$$
$$0.1\ Pa \leq P \leq 1\ Pa$$

Because of different ranges and units of measures of natural variables, it was necessary to pass to codified variables that are dimensionless variables with value between -1 and 1 Eq. 50.

$$X_i = \frac{x_i - \bar{x}_i}{0.5(x_i^H - x_i^L)} \quad (Eq.\,50)$$

Then RSM analysis with CCD needed N experiments, which in this case were replaced by as many simulations in Aspen Plus:

$$N = 2^k + 2k + n_0 \quad (Eq.\,51)$$

Where 2k indicates the number of experiments conducted with a two-level factorial design, where one of the natural variables was set to 1, while the others were kept to the central value equal to 0. In the same expression 2k indicates the number of experiments conducted in the axial points, where all the codified variables have a value equal to ±α:

$$\alpha = (2^k)^{-\frac{1}{4}} \quad (Eq.\,52)$$

Furthermore, n_0 indicates the number of experiments conducted with all the variables set to the central value, equal to 0. The parameter k indicates the number of natural variables used in the analysis equal to 2. For this reason, α was about equal to 0.707. With these calculations, the number of simulations N obtained was equal to 10.

Run	X_1	X_2	T [°C]	P [Pa]
1	0	0	105	0.55
2	0	0	105	0.55
3	1	0	150	0.55
4	0	1	105	1
5	-1	0	60	0.55
6	0	-1	105	0.1
7	0.71	0.71	137	0.87
8	0.71	-0.71	137	0.23
9	-0.71	0.71	73.2	0.87
10	-0.71	-0.71	73.2	0.23

Tab. 16 Operating conditions of temperature and pressure (also as codified variables (X_1, X_2)) at which the simulations in Aspen Plus were carried out.

Tab. 16 shows the conditions to which the simulations were carried out: X_1 is the codified variable relative to the temperature, while X_2 is the codified variable relative to the pressure. As response variables, the sum of the carotenoids' mass fractions in the residue and their recovery in the same current were chosen. Recovery was evaluated as ratio

between the sum of the lutein (W_L^R) and astaxanthin (W_A^R) mass flow rates coming out from the bottom of the evaporator and the sum of the lutein (W_L^{IN}) and astaxanthin (W_A^{IN}) flow rates entering in the molecular distiller:

$$Recovery = \frac{W_A^R + W_L^R}{W_A^{IN} + W_L^{IN}} \quad (Eq. 53)$$

In order to represent the system, a second order model with linear, quadratic and interaction terms was chosen (Ba and Boyaci, 2007):

$$y = \beta_0 + \sum_{i=1}^{k} \beta_i X_i + \sum_{i=1}^{k} \beta_{ii} {X_i}^2 + \sum_{i=1}^{k} \sum_{j=1}^{n} \beta_{ij} X_i X_j \quad (Eq. 54)$$

In Eq. 55 the model in vector terms was written. In particular y is the response vector obtained from the N simulations in Aspen Plus, X is the matrix of the codified variables, β is the vector of coefficients, and ε is the error vector given by the difference between the responses from the simulations and the fitted ones ($y_i - \bar{y}_i$).

$$y = X\beta + \varepsilon \quad (Eq. 55)$$

The least squares method was used to calculate the regression coefficients, minimizing the Sum of Square Errors (SSE) (Eq. 56).

$$SSE = \varepsilon^T \varepsilon = (y - X\beta)^T (y - X\beta) \quad (Eq. 56)$$

In order to minimize the residual errors between the simulated responses and the fitted ones, the partial derivative of the SSE respect to β was equalized to 0:

$$\frac{\partial(SSE)}{\partial \beta} = -2X^T(y - X\beta) = 0 \quad (Eq. 57)$$

The condition for which the equality at 0 is verified is y=Xβ. Multiplying the equality to both members for $X^T$to the left-hand equals, the following expression was obtained:

$$X^T X\beta = X^T y \quad (Eq. 58)$$

Finally, by multiplying both members to the left by $(X^T X)^{-1}$it was possible to obtain the equation written below:

$$\beta = (X^T X)^{-1} X^T y \quad (Eq. 59)$$

With the regression coefficients it was possible to express the responses as a function of the natural variables through some polynomials and to proceed with the optimization of the operating conditions; for this reason an objective function to be maximized was defined:

$$\mathrm{OF} = 0.7y_1 + 0.3\mathrm{y}_2 \qquad (\mathrm{Eq.}\,60)$$

In Eq. 60 y_1 is the recovery, while y_2 is the sum of carotenoids' mass fracs in the residue. The coefficients multiplying the responses (y) indicate the weight given to the responses in the optimization. In this case it was decided to give a greater weight (importance) to carotenoids' recovery in the residual current rather than the sum mass fractions of carotenoid. This solution was supported by the necessity of a compromise between the recovery of the components and the residue purity in terms of carotenoids. Once the optimal operating conditions of temperature and pressure were evaluated, the results of the simulations at those conditions were compared with those of the model, and the percentage error δ% was calculated:

$$\delta\% = \frac{|\text{Estimated value} - \text{Simulated value}|}{\text{Simulated value}} \qquad (\mathrm{Eq.}\,61)$$

2.7 MEWLIFE process description

As anticipated in paragraph 1.8, a real application of the models developed in this thesis work (see paragraph 2.3 and 2.4) can be found in the MEWLIFE project. The description of the process that will be carried out in MEWLIFE pilot plant, installed in Bio-P/NextChem site in Rome (Via di Vannina, 88), without considering the Olive Oil Mill WasteWaters (OOMWW) membrane treatments in charge of Labor partner, is described in this section for a better clarity. As previously mentioned the microalgal process was divided in two parts: the cultivation section, carried out in both photobioreactors and fermentors, and the downstream section, composed by a dewatering step by centrifugation and a drying step by a spray dryer. Bio-P supported the corresponding responsibles of Basic and Detailing Engineering phases (Technosind and NextChem) for the documents implementation. In particular, Bio-P helped partners with Heat&Material Balance of both phototrophic and heterotrophic cultivations, based considerations furnished by HTR (university partner) obtained from lab-scale data. Another important contribution of Bio-P was done in the Data Sheet implementation of the principal equipment involved in the process, designing the entire heterotrophic section and supporting partners for packages purchasing with the definition of the principal parameters to supply to vendors.

2.7.1 Phototrophic section

As regards the phototrophic section, its operation will begin with the inoculum previously prepared in the laboratory (6 L at 1-1.5 g L^{-1}) that will be inserted and diluted (1:10) into

the 600 L outdoor bags photobioreactor (see figures in subparagraph 3.9.1), beginning its start-up phase. Once reached a concentration of 1 g L^{-1} (in about 18 days) the volume will be re-diluted (1:10) in order to reach its operative volume of 600 L. The start-up phase will end when the all the photobioreator's volume will gain a concentration of 1 g L^{-1} (about 13 days). In this outdoor photobiorectors temperature and pH will be actively monitored and controlled. Indeed, in addition to nitrogen-based nutrients, a flow of carbon dioxide equal to 0.660 Sm^3 h^{-1} will be flushed in order to keep the pH at optimal values (equal 8). Futhermore, temperature will be controlled either to contrast cold weather conditions (using electric resistance inside each bag) and hot conditions during summer period (using a water spray cooling system). The growth and outdoor parameters monitoring will be performed in the same way of the experiments carried out in the bubble column photobioreactors (see paragraph 2.1). During the duration of the project, 5 batches will be performed for the start-up phase of the heterotrophic section and 20 batches in the operative phase. As specificied in paragraph 1.8, the multivariate model described in paragraph 2.3 could be applied to this cultivation, validating and reinforcing its predictive power also in this different photobioreactor configuration. Indeed, once collected enough data in this new configuration for model validation, an estimation of the specific growth rate and productivity, using the measured outdoor conditions of the bubble column experiments descibed in subparagraph 2.1.7, could be extracted. In this way it will be possible to know how much time would be necessary to reach the desired concentration (1 g L^{-1}) in a specif part of the year.

2.7.2 Heterotrophic (Dark Fermentation) section

The algal suspension obtained from each batch of the phototrophic cultivation (540 L of the 600 L) will be used as an inoculum for the heterotrophic section woking at atmospheric pressure. This cultivation, unlike the previous one, will take place in the absence of light inside two fermenters both with an operative volume of 3 m^3 (see paragraph 3.9). The start-up phase begins in the first of the two fermenters (F-101).

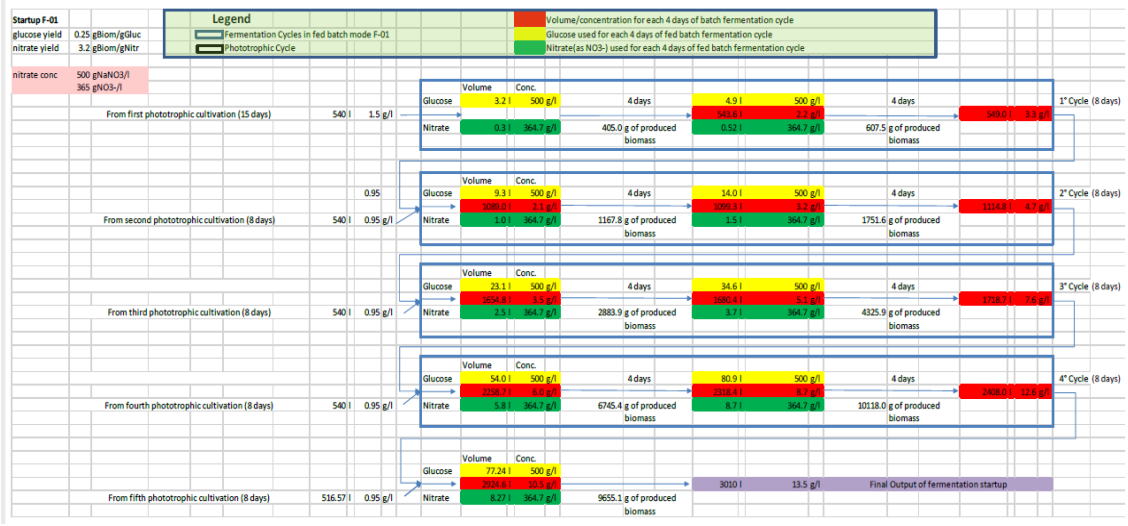

Fig. 53 Start-up schematization of F-101 fermenter.

The start-up phase will last approximately 36 days and will be divided into 4 growth cycles lasting about 8 days each in fed-batch mode (see Fig. 53). Each cycle will be performed in this way: feeding the fermenter with the product of the phototrophic growth section with the addition of a synthetic glucose-based volume.
Glucose is used to grow algal biomass until it doubles the mass. This phase will last about 2 days. Subsequently, a nutrient flow based on $NaNO_3$ will be introduced, bringing to microalgal cell duplication instead of metabolites' accumulation. Also this phase with nitrates lasts about 2 days. Within the same growth cycle these two operations will be repeated a second time before inserting the new phototrophic growth product which will determine the beginning of the next cycle. At the end of the 4 cycles (4 days each) described above, it will take another 4 days to complete the start-up operation reaching a concentration of 13.5 g L^{-1} in a volume of 3 m^3. At this point the operational phase will start: 1 m^3 of algal suspension will be inserted inside the second fermenter (F-102) together with the addition of the OOMWW concentrate which has the same function as the synthetic glucose described above, finally the volume of 3 m^3 will be reached by adding water. In about 2 days in F-102 the algal suspension, with an initial concentration in algae equal to 4.5g L^{-1}, will reach a concentration in algae equal to 9g L^{-1} determining the end of the heterotrophic growth. Once arrived at this phase, the entire volume (3 m^3) of microalgal suspension in F-102 can be sent to the downstream process. During these two days of cultivation in F-102, the first fermenter F-101, where 2 m^3 of algal suspension were left, will be fed with water and glucose and subsequently nitrates in order to bring back the algal suspension at a concentration of 13.5g L^{-1}; this operation will last in 4/5 days (2 days with glucose in parallel with F-102 and 2/3 with nitrate). During the whole project period about 40 batches of heterotrophic growth will be carried out lasting 4/5 days each. Both fermenters were designed mainly by Bio-P (represented by myself) and modified later by NextChem in accordance with suppliers' reviews and suggestions. In particolar, in each fermenter 3 main variables will be monitored and controlled: temperature, pH and level. With respect to temperature, is more a maintenance than a control because the internal temperature will be keeped at its set-point of 30 °C using cooling water inside fermenters' jacket; none hot utilities will be used because it was estimated that the only variation of temperature will be caused by the exotermicity of the fermentation reaction. Furthermore, also pH will be actively controlled, adding chemicals inside the microalgal solution both as base (NaOH) and acid (H_2SO_4) when will be necessary. As last control, the level will be monitored and manually controlled. Indeed, four level will be monitored: High Low Level, Level at 1 m^3, Normal Level (3 m^3) and High Level (see paragraph 3.9 for results of the design phase). In particular the level at 1 m^3 will be necessary to verify the correct volume transfer from F-101 to F-102. In addition to the control system, each reactor was equipped with an air sparger and a mixing system composed of a mixer with double impeller (one Rushton turbine and one 4 blade hydrofoil impeller), both designed for the scope by Bio-P. For the same reasons described in the previous subparagraph 2.7.1, also for the heterotrophic cultivation the models developed in this work can be applied. Specifically, between two models the metabolic one would find more applicability in this case, due to its easy handling and reusablility with simple and

few changes to other cultivations conditions. Indeed, in this way an experimental campaign, carried out in parallel with cultivation and aimed to quantify the metabolites of interest inside microalgal cells cultivated in dark fermentation, will permit to test the model, modified accordingly, to this new cultivation condition. This model, applied to heterotrophy will permit to reach to two important results, prediction of the time needed to reach a fixed output concentration (at a certain glucose/OOMWW and Nitrate concentration) but also the estimation of the desidered metabolites quotas, accumulated during nitrogen starved conditions.

2.7.3 Biomass harvesting, drying and packaging

In order to preserve the algal biomass obtained from the heterotrophic growth section, a downstream section was essential in the process. In this process the downstream was divided in three steps: centrifugation, drying and packaging. Indeed the microalgal suspension, after having reached the specified concentration in F-102 (9 g L^{-1}), will be sent into a disc stack centrifuge. This operation will concentrate the algal suspension by 80%, thus removing about 2400 liters of water. The remaining suspension will have a concentration of 45 g/l of algal biomass (4.5%DW). Disc stack centrifuges are able to apply a force from 4000 to 14,000 times gravitational force, thus reducing separation time. These are the most common industrial centrifuges and are widely used in commercial plants for high-value microalgal products and in microalgal biofuel pilot plants. Although several variants exist, the generic type is characterised by an imperforate bowl surrounding an inverted stack of 30–200 thin conical discs separated by 0.3–3 mm spacers. The disc spacing is dependent on the viscosity and solids content in the feed and needs to be fixed accordingly, lower viscosities and solids concentrations favour spacings below 1 mm. As the discs are spun on a common vertical axis the process suspension, which is fed centrally from the top, travels through the annular spaces between the discs. Centrifugal forces cause particles to accumulate on the underside of the discs from where they slide down towards the outer periphery of the centrifuge bowl. In batch units the thickened solids remain in the bowl until the solids handling capacity of the centrifuge is reached. At this point rotation stops and the basket containing the trapped solids is manually replaced or a discharge valve on the periphery of the bowl is manually operated to facilitate removal of the sediment. In continuous units the solids sludge, which must be flowable, is automatically discharged, sometimes intermittently, through nozzles positioned on the outer periphery of the bowl. The concentrated microalgal suspension will be sent to an accumulation vessel where it will be sent to a spray dryer. Inside the spray dryer the solid will be completely dried. Spray drying is a well-known method of particle production which comprises the transformation of a fluid material into dried particles, taking advantage of a gaseous hot drying medium. The process may be described by three major phases: atomization, droplet-to-particle conversion and particle collection. Generally, a solution is pumped into an atomizer, breaking up the liquid feed into a spray of fine droplets. Then, the droplets are ejected into a drying gas chamber where the moisture vaporization occurs, resulting in the formation of dry particles. There are different drying chamber configurations, in which the flow pattern between the hot gas and the spray of droplets is distinct: co-current flow,

counter-current flow and mixed flow. Finally, using an appropriate device, the dried particles are separated from the drying medium, being then collected in a tank.
The solid obtained from this unit will be packaged and stored before being sent to subsequent treatments covered in this project: such as starch extraction. Bio-P, also for the equipments described in this subparagraph, gave the inputs needed to complete their datasheet (input/output concentrations, separation or drying efficiency, type of spray-dryer atomizer, etc.), defining with vendors the best solution to use. Since these equiments were designed with suppliers know-how, they are defined packages and their design spefications will not be shown in Results and Discussion session, differently from fermentors.

Chapter 3. Results and Discussion

3.1 Outdoor growth results

In this paragraph the results obtained from the outdoor pilot plant cultivation, during the experiments described in Tab. 5 are resumed, both as cellular concentration (10^6 cell mL^{-1}) and dry weight (g L^{-1}). As additional informations, at the top of each plot the initial cultivation conditions in terms of inoculum (C_{init}) and sodium nitrate ($NaNO_{3init}$) concentration are specified. Furthermore, the terms displayed in each legend are referred to the microalgal species used and in which reactor were cultivated (for example t.o.1 stands for *Tetradesmus obliquus* cultivated in reactor 1, or g.e.10 stands for *Graesiella emersonii* cultivated in reactor 10).

3.1.1 Experiment A (from 02-03-17 to 14-03-17)

In this experiment only *Tetradesmus* was cultivated with a $NaNO_{3init}$=0.35 g L^{-1} and two different C_{init} (0.1 g L^{-1} and 0.3 g L^{-1}). The growths of PBRs 1, 3 and 5, inoculated with the lowest cell concentration (0.1 g L^{-1}), show an incongrous trend between the reactors. In particular, PBR-1 (t.o.1) shows the typical trend of cell growth (Fig. 54a), highlighting well the latency phase, the exponential phase and the stationary phase. On the 12^{th} day of culture, an important drift in cell concentration appears, but not in dry weight (Fig. 54b), probabily due to the metabolites accumulation phase started as result of nitrogen depletion. The other PBRs (3 and 5), on the other hand, don't reach the same final concentration, showing a slower growth and a rapid and early decay, due to the frequent clogging of the air diffusion system. Indeed only PBR-1 and PBR-2 were cultivated with the toroidal sparger as test, while for the other reactors porous stones were used (see subparagraph 2.1.1). This clogging problem brought to repetitive biomass sedimentation, limiting thus the air/CO_2 amount, with high impact to microalgal metabolism. In this case, therefore, the reactors cannot be considered as replicate. Also in the case of PBRs 2,4 and 6, inoculated with a higher concentration (0.3 g L^{-1}), the same problem is found in Fig. 54c and Fig. 54d. Indeed, the best growth trend is reached in PBR-2, for the reasons previously described, and on the 12^{th} day the cell concentration decays vertiginously, while the dry

weight tends to increase to approx 1 g L^{-1}. Also these PBRs cannot be considered as replicate for microalgal growth. As regards the outdoor temperature, similar values of both internal and external temperatures were found in this experiment. In particular the minimum internal temperature oscillated between 5.7 °C and 9.4 °C and the minumum external temperature oscillated between 3.3 °C and 7.4 °C; almost similar variations were found for maximum internal (between 21 °C and 25 °C) and external (between 23 °C and 28 °C) temperatures. Furthermore, since this experiment was carried out during spring season, also good PPFD values were found. Indeed, the minimum and maximum values obtained were 35 µE m^{-2} s^{-1} and 300 µE m^{-2} s^{-1}. The lowest value is justified by bad weather conditions occurred during few days in the experiment.

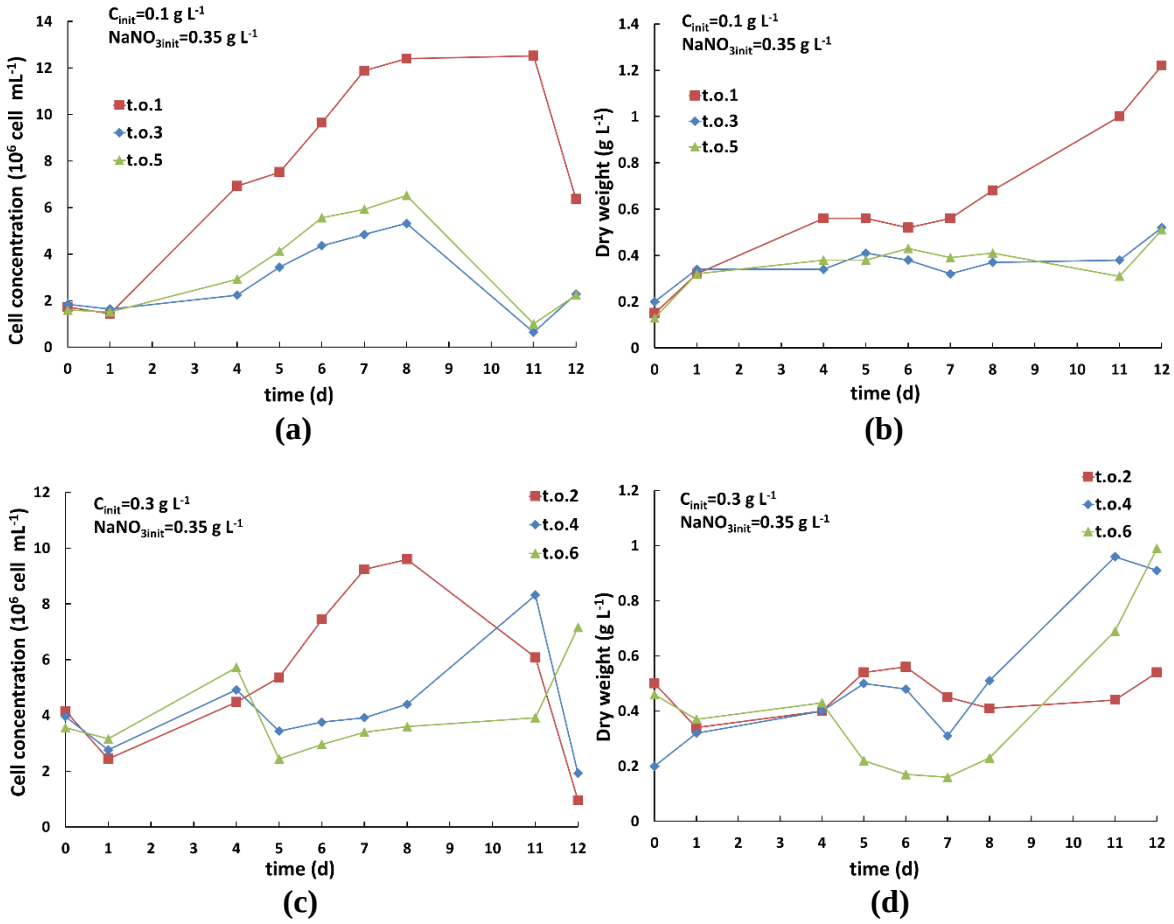

Fig. 54 Microalgal (*Tetradesmus obliquus*) growth trends as cellular concentration [with C_{init}=0.1 g L^{-1} **(a)** and C_{init}=0.3 g L^{-1} **(c)**] and dry weight [with C_{init}=0.1 g L^{-1} **(b)** and C_{init}=0.3 g L^{-1} **(d)**], obtained during the experiment A (from 02-03-17 to 14-03-17).

3.1.2 Experiment B (from 21-03-17 to 31-03-17)

In this experiment only *Tetradesmus* was cultivated with a $NaNO_{3init}$=0.35 g L^{-1} and two different C_{init} (0.1 g L^{-1} and 0.3 g L^{-1}); in particular in all PBRs porous stones were used but with a more frequent execution of cleaning and maintainance operations. In all subplots of Fig. 55 a more regular trend is shown, giving good results in terms of replicability. These results were obtained guaranteeing a good aeration performance due to a constant

monitoring and maintainance of the porous stones that continued to show clogging problems. These outcomes, compared to those in Fig. 54a and Fig.54c of using a different sparger configuration in order to obtain better results; for this reason in the subsequent experiments toroidal spargers were used.

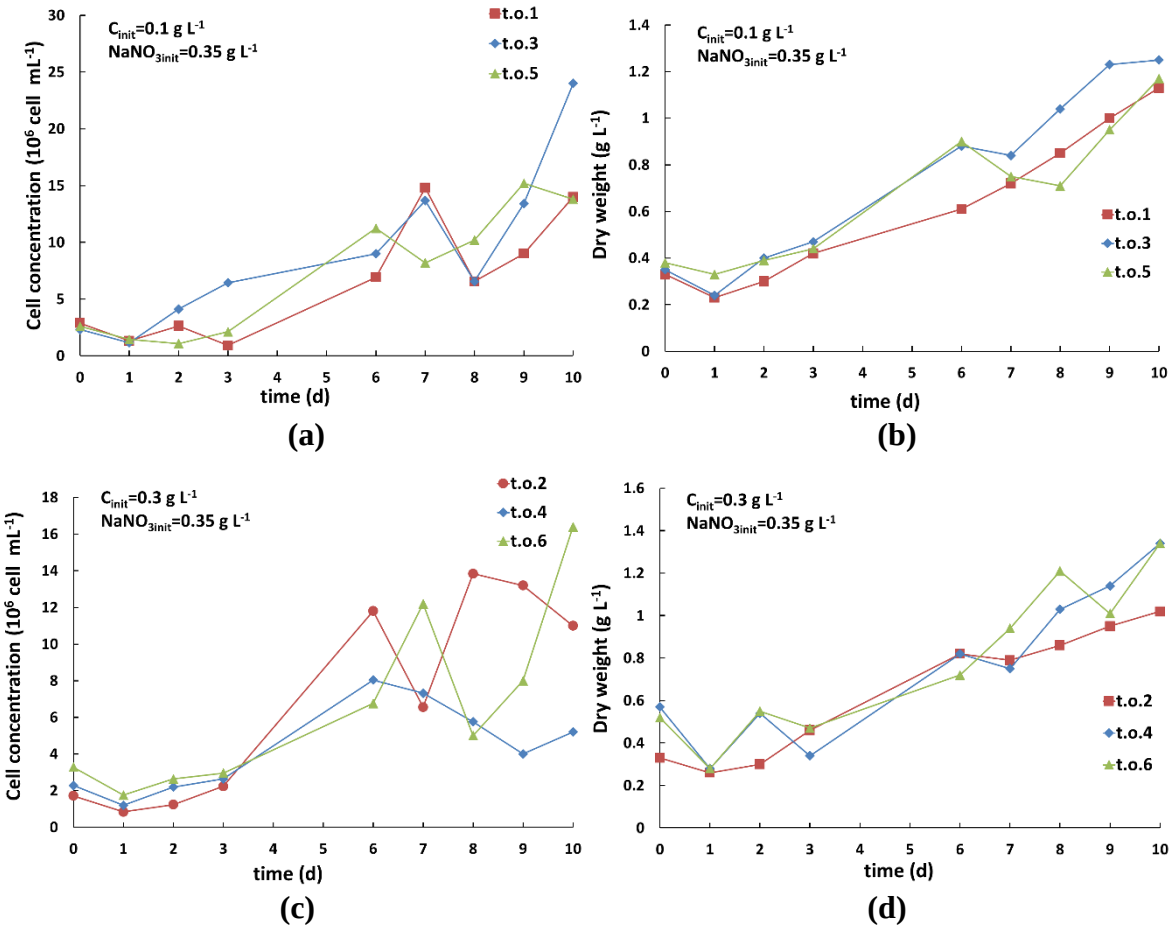

Fig. 55 Microalgal (*Tetradesmus obliquus*) growth trends as cellular concentration [with C_{init}=0.1 g L^{-1} **(a)** and C_{init}=0.3 g L^{-1} **(c)**] and dry weight [with C_{init}=0.1 g L^{-1} **(b)** and C_{init}=0.3 g L^{-1} **(d)**], obtained during the experiment B (from 21-03-17 to 31-03-17).

The fluctuating trend, in terms of cellular concentration, showed in Fig. 55a and Fig. 55c after the 6th day is due to the foaming process that occurred in this experiment. Indeed, the biomass adhesion in the top surface of the reactors brought to continous decrease/increase of the cellular concentration inside the PBR; this mechanism was named as "self-diluition process". However, it is visible in Fig.55a and Fig.55c that a higher values for the PBRs inoculated with lower C_{init} are reached, confirming what has been affirmed in subparagraph 3.1.1 about the $NaNO_3$ limitations. Indeed, a higher value of C_{init} (0.3 g L^{-1}) means a higher number of microalgal cells that need to uptake the nitrogen from the cultivation medium for their duplication, causing thus a shortening of the nitrogen replete conditions respect to those cultivated at lower C_{init} (0.1 g L^{-1}). In terms of dry weight (Fig. 55b and Fig. 55d) the two conditions show similar results and good replicability, giving slightly higher values for the PBR with a C_{init}=0.3 g L^{-1} as a consequence of the early beginning of nitrogen

starvation. Regarding the outdoor factors, similar values, respect to experiment A, of both internal and external temperatures were found. In particular the minimum internal temperature oscillated between 4.5°C and 10 °C and the minumum external temperature oscillated between 2.5 °C and 7.9 °C; almost similar variations were found for maximum internal (between 21 °C and 25 °C) and external (between 24 °C and 30 °C) temperatures. Even in this case good PPFD values were found; indeed, minimum and maximum values obtained were 37 $\mu E\ m^{-2}\ s^{-1}$ and 320 $\mu E\ m^{-2}\ s^{-1}$. These similarities to experiment A are due to the same period in which the experiments were carried out (March 2017); even in this experiment few days with bad weather conditions were found.

3.1.3 Experiment C (from 04-04-17 to 14-04-17)

In this experiment only *Tetradesmus* was cultivated with a $NaNO_{3init}$=0.35 g L^{-1} and two different C_{init} (0.1 g L^{-1} and 0.3 g L^{-1}); in particular in each PBR the new toroidal sparger was used. It should be noted that in these experiments (Fig. 56a and Fig. 56c) a clearly defined latency phase is not present, beginning immediately with exponential phase without any sign of microalgal acclimation. However, the exponential phase lasts for 5 days in PBRs with C_{init}=0.1 g L^{-1} (Fig. 56a) and only 1-2 days for PBRs with C_{init}=0.3 g L^{-1} (Fig. 56c), even if for these latter the real stationary phase begins after the 5th day. The reason of this short growth period, ending briefly after few days, can be traced back to the temperature oscillations between maximum (higher than 30 °C) (see Fig. 66) and minimum (about 5°C). These strong uncontrolled oscillations caused probably the growth inhibition shown in Fig. 56. In this case the nitrogen deficiency cannot be considered the cause of this behaviour, since also PBRs with C_{init}=0.3 g L^{-1} shows immediately low growth values and is not possible to think of a complete nitrate consumption in this brief period. However, in general a good replicability both in terms of cellular concentration and dry weight in all the subplots is shown in Fig. 56. The only ecception is represented by PBR3 (t.o.3 in Fig. 56b) where a higher value respect to others PBRs is visible. The reason of this behaviour is due to the presence of higher level of contamination in this reactor maybe caused by a not correct execution of the inoculum operation. Regarding the outdoor factors, similar values, between internal and external temperatures were found. In particular minimum internal temperature oscillated between 8 °C and 12 °C and the minumum external temperature oscillated between 5 °C and 10 °C. Very similar difference between maximum internal (oscillating from 28 °C to 33 °C) and external (oscillating from 24 °C to 35 °C) temperatures were found. In this experiment the presence of cloudy days during the most part of this experiment was observed. These cloudy days didn't impacted too much on PPFD results. Indeed, minimum and maximum values obtained were 55 $\mu E\ m^{-2}\ s^{-1}$ and 365 $\mu E\ m^{-2}\ s^{-1}$. It is visible that both PPFD values are higher than those seen in the previous experiments because even if clouds reduced a little the sunlight amount, the shift to sunnier months increased the available irradiance.

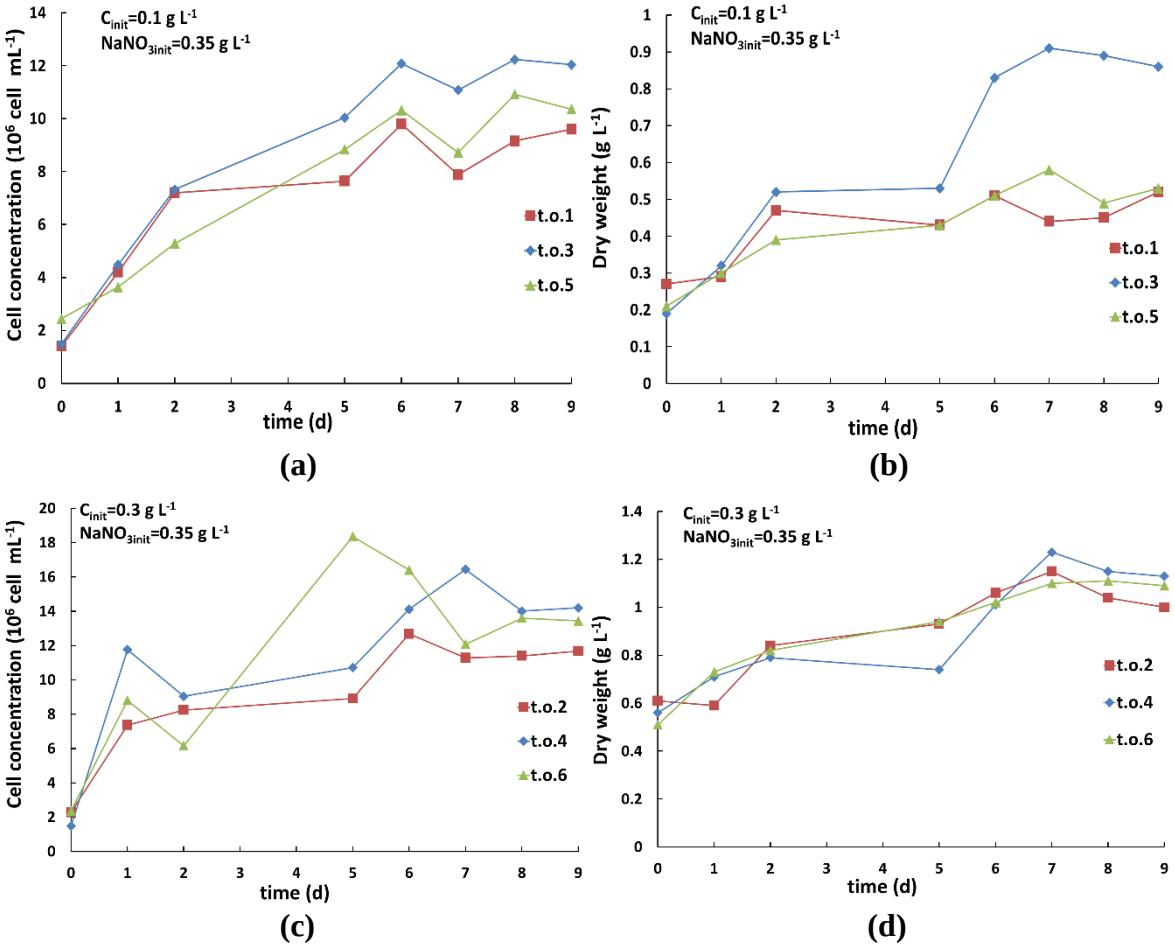

Fig. 56 Microalgal (*Tetradesmus obliquus*) growth trends as cellular concentration [with C_{init}=0.1 g L^{-1} **(a)** and C_{init}=0.3 g L^{-1} **(c)**] and dry weight [with C_{init}=0.1 g L^{-1} **(b)** and C_{init}=0.3 g L^{-1} **(d)**], obtained during the experiment C (from 04-04-17 to 14-04-17).

3.1.4 Experiment D (from 19-04-17 to 10-05-17)

In this experiment only *Tetradesmus* was cultivated with a $NaNO_{3init}$=0.70 g L^{-1} and two different C_{init} (0.1 g L^{-1} and 0.3 g L^{-1}); this new $NaNO_{3init}$ value was used to investigate the duration and the final concentrations obtained in a batch carried out with a doubled amount of nitrate. This experimental setting led to higher final concentrations (Fig. 57) respect to previous cultivations (see subparagraph 3.1.1-3.1.3). These results demonstrate that the microalgae cultivated in the experiments A-C were not affected by photolimitation, since in this experiment higher final concentrations (above 2.5 g L^{-1} as DW) are reached (Fig. 57b and Fig. 57c). Therefore, since no limitation of light distribution inside the reactors was present, the cellular concentration's lowering discussed before can be justified only by nitrogen depletion or cultivation problems (clogging, etc.), as previously written. It is visible in both Fig. 57a and Fig. 57b the presence of foaming problems in correspondence of the fluttuating trends after the 11th-12th day.

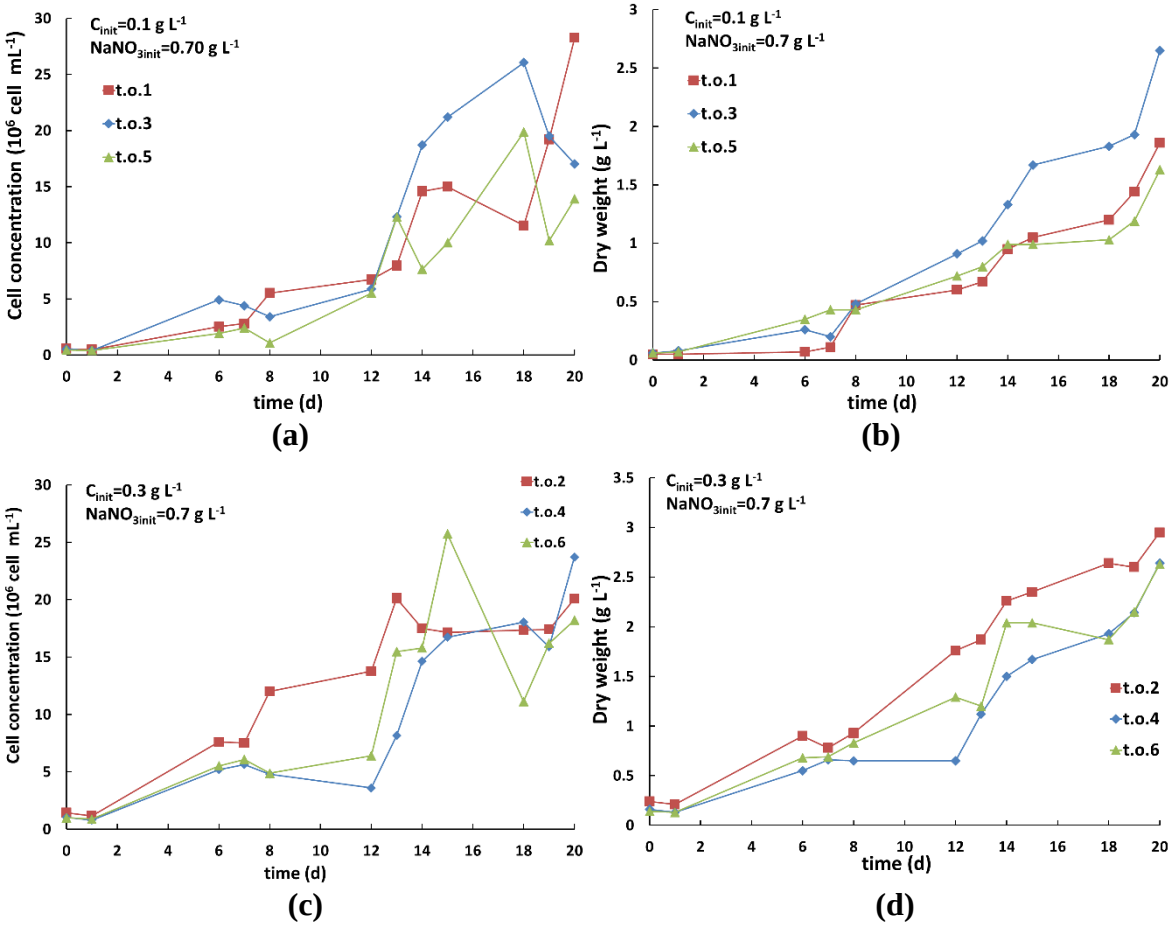

Fig. 57 Microalgal (*Tetradesmus obliquus*) growth trends as cellular concentration [with C_{init}=0.1 g L^{-1} **(a)** and C_{init}=0.3 g L^{-1} **(c)**] and dry weight [with C_{init}=0.1 g L^{-1} **(b)** and C_{init}=0.3 g L^{-1} **(d)**], obtained during the experiment D (from 19-04-17 to 10-05-17).

These fluctuations can be justified also by the high internal temperature reached even in this experiment (> 30°C) (see Fig. 66) due to the non-active cooling system. However, with this doubled $NaNO_{3init}$ concentration the cultivation don't reached the steady state at the 20th day, demonstrating the high impact that the initial nutrients amount have on the microalgal cultivation influencing cellular concentration (Fig. 57a and Fig. 57c), dry weight (Fig. 57b and Fig. 57d) and also batches' duration. Also in this case the PBRs show a good replicabilty in terms of dry weight and a little less for cellular concentration due to foaming problems. Regarding the outdoor factors, an high temperature ranges were found. Indeed the minimum internal temperature oscillated between 5.20 °C and 15 °C and the minumum external temperature oscillated between 2 °C and 12.3 °C; the same high variations were found for maximum internal (between 22 °C and 36 °C) and external (between 20 °C and 31 °C) temperatures. As mentioned before, the presence of several days with high temperatures (> 30°C) without an active cooling system stressed the microalgae, influencing their growth. Even for PPFD values an high range was found; indeed, minimum and maximum values obtained were 100 µE m^{-2} s^{-1} and 377.5 µE m^{-2} s^{-1}. These high variations are justified by a not-stable weather conditions during the day and during the days.

3.1.5 Experiment E (from 15-05-17 to 22-05-17)

In this experiment only *Tetradesmus* was cultivated with a $NaNO_{3init}$=0.175 g L^{-1} and two different C_{init} (0.1 g L^{-1} and 0.3 g L^{-1}); this new $NaNO_{3init}$ value was used to investigate the duration and the final concentrations obtained in a batch carried out with a halved nitrate amount. These results are the exact opposite of those obtained in previous experiment (see subparagraph 3.1.4), underlining thus the importance of the $NaNO_{3init}$ in a microalgal cultivations.

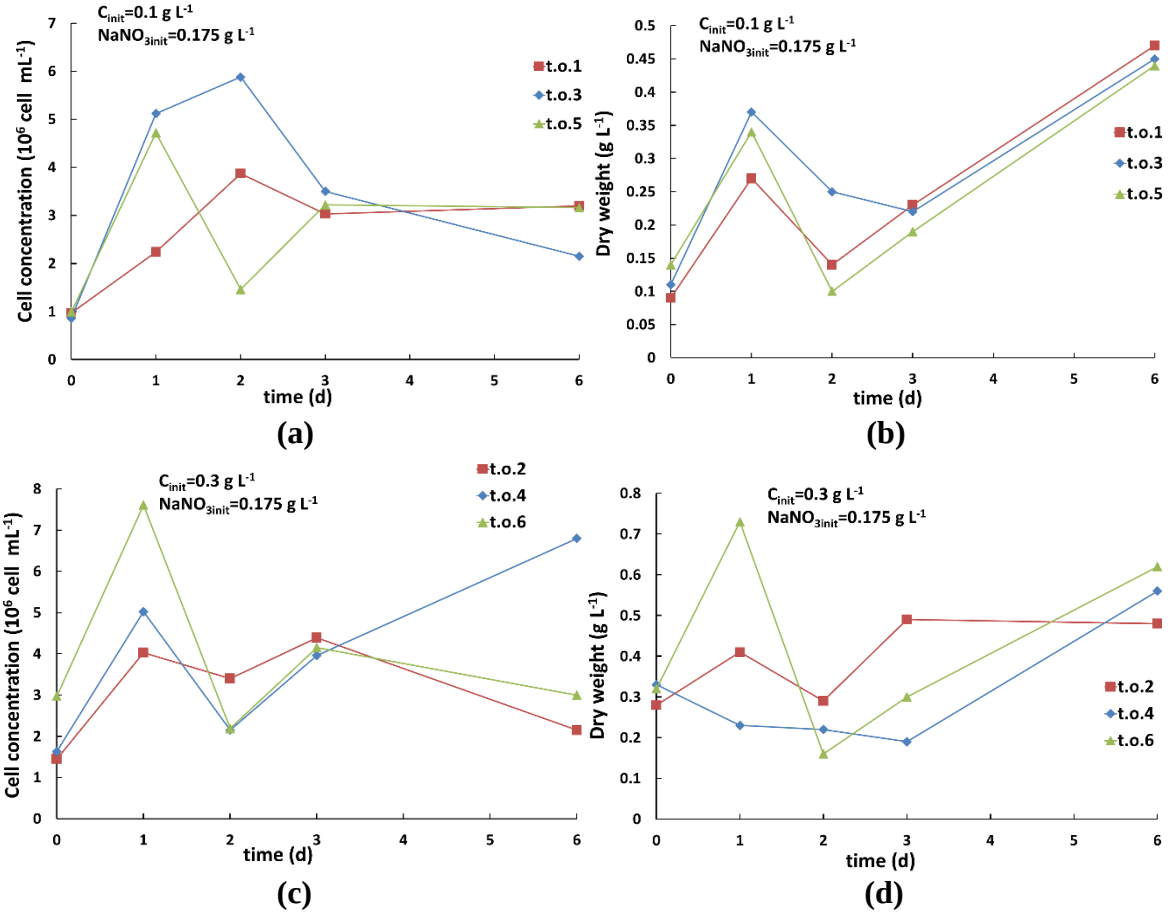

Fig. 58 Microalgal (*Tetradesmus obliquus*) growth trends as cellular concentration [with C_{init}=0.1 g L^{-1} **(a)** and C_{init}=0.3 g L^{-1} **(c)**] and dry weight [with C_{init}=0.1 g L^{-1} **(b)** and C_{init}=0.3 g L^{-1} **(d)**], obtained during the experiment E (from 15-05-17 to 22-05-17).

Indeed, in this case the metabolites' accumulation phase (nitrogen starvation) begins almost immediately (Fig. 58b and Fig. 58d) at the expense of a low cellular concentration (Fig. 58a and Fig. 58c) in which the stationary phase is reached after 2 cultivation days. Futhermore, as regards the replicability, the results visible in Fig. 58 show appreciable variability between the PRBs (in a smaller way in Fig. 58b) due to cultivations' problems occurred during this experiment. Indeed, in addition to foaming problems bounded to low $NaNO_{3init}$ that caused immediaty stress inside microalgae, also the malfunction of the solenoid valves that controlled air/CO_2 flow-rate occurred. As said before (subparagraph

3.1.4), these operational problems are very impactful on microalgal growth and have to be always actively monitored in order to keep the pilot opertive at the best working conditions. Regarding the outdoor factors the minimum internal temperature oscillated between 14 °C and 19 °C and the minumum external temperature oscillated between 13 °C and 17 °C; higher variations were found for maximum internal (between 30 °C and 40 °C) and external (between 25 °C and 32 °C) temperatures. As described in the previous subparagraph, the presence of several days with high temperatures (> 30°C) without an active cooling system stressed the microalgae, but in this case the effect of low $NaNO_{3init}$ concentration influenced more (negatively) microalgal growth. Even for PPFD values an high range was found; indeed, minimum and maximum values obtained were 105 μE m^{-2} s^{-1} and 380 μE m^{-2} s^{-1}.

3.1.6 Considerations about initial cultivation conditions

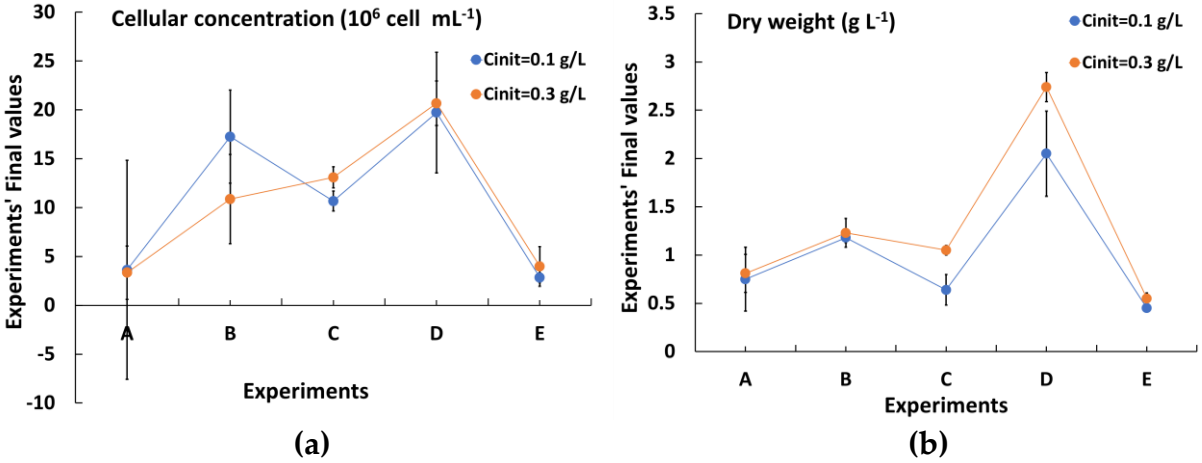

Fig. 59 Microalgal (*Tetradesmus obliquus*) final values obtained in each experiment as cellular concentration **(a)** and dry weight **(b)** both with C_{init}=0.1 g L^{-1} and C_{init}=0.3 g L^{-1}. The bars represent the Standard Deviations of the replicates in each experiment.

In this subparagraph the decisions about the initial cultivation conditions to adopt in the following experiments are summed up. As regards $NaNO_{3init}$, in previous subparagraphs (in particular from 3.1.3 to 3.1.5) the best value equal to 0.35 g L^{-1} has been shown, being that a compromise between high final concentrations (with long batch's duration) and low final concentrations (with short batch's duration). Indeed with $NaNO_{3init}$=0.35 g L^{-1}, a right balance between nitrogen repletion and starvation is guarateed. Concerning C_{init}, a comparison between two levels (0.1 g L^{-1} and 0.3 g L^{-1}), both in terms of cellular concentration and dry weight is reported in Fig. 59; in both subplots the bars represent the Standard Deviations of the replicates in each experiment. Since for cellular concentration (Fig. 59a) is difficult to define the better condition to use, due to high variability between replicates, the results in terms of dry weight (Fig. 59b) are taken as reference for the decision. It is can be seen in Fig. 59b that DW values obtained from cultivations carried out with C_{init}=0.3 g L^{-1} are higher than those cultivated with C_{init}=0.1 g L^{-1}. For this reason, for the following experiments C_{init}=0.3 g L^{-1} was adopted.

3.1.7 Experiment F (from 20-06-17 to 07-07-17)

In this experiment only *Tetradesmus* was cultivated with the optimal initial cultivation conditions ($NaNO_{3init}$=0.35 g L^{-1} and C_{init}=0.3 g L^{-1}) described before (subparagraph 3.1.6). In particular in the Experiments F-G-H the cooling system was activated and also the addition of 1-2 mL of antifoam (paragraph 2.1), in order to avoid biomass losses, began in this Experiment F. The Fig. 60a shows a good exponential phase, a stationary period from 8th to 12th day and a decay phase that occurred for all three reactors between 14th and 17th day. This decay is justified by cell death due to absence of nutrients in the culture medium. This condition is reinforced also both by antifoam addition that avoided the aforesaid "self dilution" process (due to biomass losses on the reactors' top) and by the active cooling system.

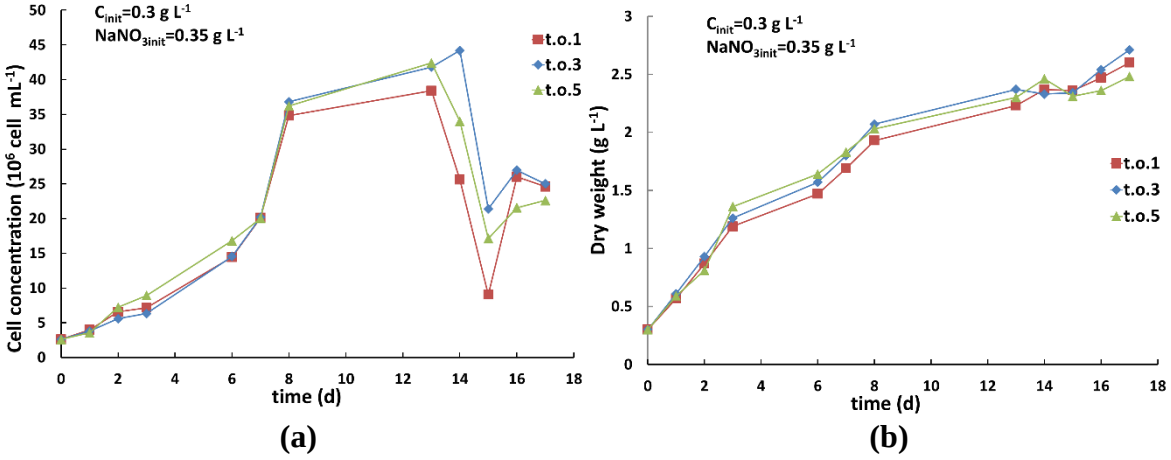

Fig. 60 Microalgal (*Tetradesmus obliquus*) growth trends as cellular concentration **(a)** and dry weight **(b)** with C_{init}=0.3 g L^{-1} $NaNO_{3init}$=0.35 g L^{-1}, obtained during the experiment F (from 20-06-17 to 07-07-17).

The interaction of this two factors improved the cultivation conditions, increasing thus the cellular concentration inside reactors and reaching the highest values obtained since the first experiment. In fact, the continue addition of antifoam (1-2 mL) didn't inhibit at all the growth, since no lag phase is visibile at the beginning of the cultivation; furthermore the antifoam guaratee a better data replicability. Also the temperature control system was necessary, demonstrating how its presence assures good growth trends, avoiding the considerable stress caused by high temperatures reaching. As regards dry weight trends, Fig. 60b shows instead a continuous increase due to the metabolites accumulation during nitrogen starvation. An additional cause of this increment is probably due to weighing of lised and dead cell during the dry weight analysis. Regarding the outdoor factors, since in this experiment the cooling system was activated, the internal temperature's trend was constrained to the high value (30 °C). The minimum internal temperature oscillated between 20 °C and 24 °C, the minumum external temperature oscillated between 18 °C and 23 °C and the maximum external temperature oscillated between 30 °C and 40 °C. The high external temperatures reached during this summer period justified the necessity

of using an active cooling system in order to keep microalgae in good cultivation conditions. Even for PPFD high values were found due to the summer period; indeed, minimum and maximum values obtained were 110 μE m^{-2} s^{-1} and 385 μE m^{-2} s^{-1}.

3.1.8 Experiment G (from 10-07-17 to 27-07-17)

In this experiment and in the following ones, both *Tetradesmus* and *Graesiella* were cultivated with the optimal initial cultivation conditions ($NaNO_{3init}$=0.35 g L^{-1} and C_{init}=0.3 g L^{-1}) described before (subparagraph 3.1.6). Both cellular growth present all the typical phases of microalgae growth trend. Differently from the initial experiments (A-E) carried out during spring, in which the cultivation phases lasted for about 30 days, in the summer period all the phases ended in about 15 days (see also Eperiment F in subparagraph 3.1.7). However, in this experiments lower final concentrations in terms of number of cells (Fig. 61a and Fig. 61c), respect to Experiment F, are reached. On the contrary, similar dry weight values (Fig. 61b and Fig. 61d) compared to those visibile in Fig. 60b, are obtained. This lower final cellular concentrations, both for *Tetradesmus* and *Graesiella* can be traced back to presence of competitive microorganisms found in the microscope analysis for cell count.

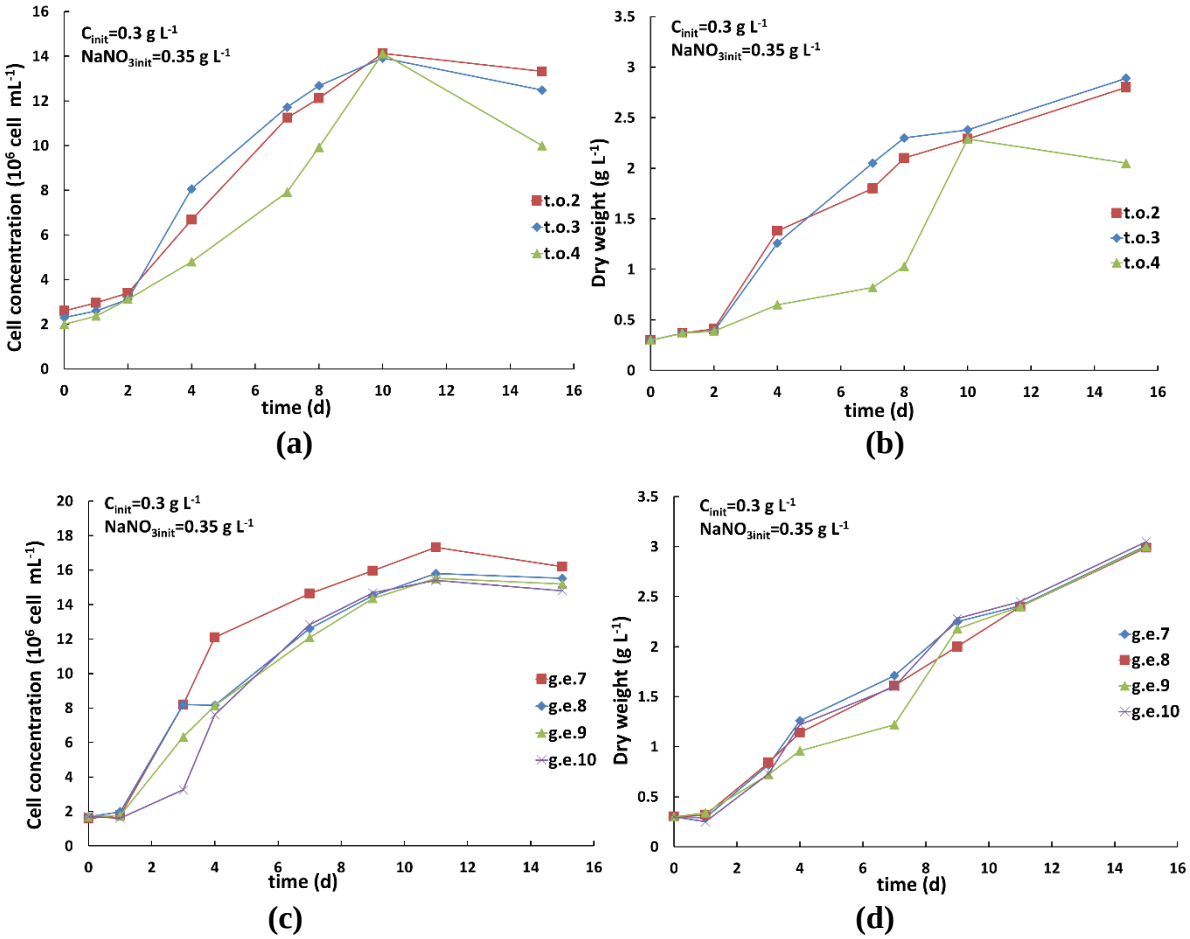

Fig. 61 Microalgae *Tetradesmus obliquus* **(a)-(b)** and *Graesiella Emersonii* **(c)-(d)** growth trends as cellular concentration and dry weight with C_{init}=0.3 g L^{-1} $NaNO_{3init}$=0.35 g L^{-1}, obtained during the experiment G (from 10-07-17 to 27-07-17).

As comparison between two species, the results obtained either as cell concentration and dry weight are very similar, not allowing the choice of the best one. Furthermore, also these results show very good replicability due to the optimized operative cultivation conditions used. Regarding the outdoor factors, even in this experiment the cooling system was activated, holding the maximum internal temperature at its set point (30 °C). Minimum internal temperature oscillated between 18 °C and 24 °C, the minumum external temperature oscillated between 17 °C and 24 °C and the maximum external temperature oscillated between 34 °C and 38 °C. Even for PPFD high values were found, slightly higher than the previous experiment; indeed, minimum and maximum values obtained were 150 μE m^{-2} s^{-1} and 380 μE m^{-2} s^{-1}.

3.1.9 Experiment H (from 22-09-17 to 17-10-17)

In this experiment both *Tetradesmus* and *Graesiella* were cultivated with the optimal initial cultivation conditions ($NaNO_{3init}$=0.35 g L^{-1} and C_{init}=0.3 g L^{-1}) described before (subparagraph 3.1.6). During August, due to company's summer vacantion, the cultivations of both species were transferred in two indoor PBRs, providing an artificial lighting system and an aeration system. This experiment started at the beginning of autumn, after several days in which microalgae were brought back to outdoor environment, trying to ensure the necessary acclimatization to the different temperatures and lighting conditions between indoor and outdoor systems. The results in Fig. 62 show a slower and less regular growth respect to those obtained during summer. The main factor that caused these behaviors is the sun irradiance, indeed a significan lowering of light amount (both as PPFD and Daily Illumination Time) was verified (see Fig. 67). In addition to this factor it must be considered that on the 11th day a CO_2 solenoid valve's failure occurred, remaining in the open position for about 3 days, continuing to supply CO_2 and keeping pH constantly to 4. This problem affected negatively the growth trends and data replicability for both species. Furthermore, as visible in Fig. 62a and Fig. 62b the cultivation carried out in the PBR1 (t.o.1) ends at 17th day due the high level of contamination detected, maybe caused by a not-complete cleaning operation of the PBR1 after the summer pause. In this case a comparison between two specied cannot be done also due to lack of replicates especially for *Tetradesmus.* Regarding the outdoor factors, this was the last experiment with the active cooling system that held the maximum internal temperature at its set point (30 °C). The minimum internal temperature oscillated between 10 °C and 15 °C, the minumum external temperature oscillated between 8°C and 12 °C and the maximum external temperature oscillated between 27 °C and 35 °C. It is visible that the temperature's values are lower than those collected in experiment F and G due to the autumn approach. This change of the season influenced also the PPFD values; indeed, minimum and maximum values obtained were 38.5 μE m^{-2} s^{-1} and 232 μE m^{-2} s^{-1}.

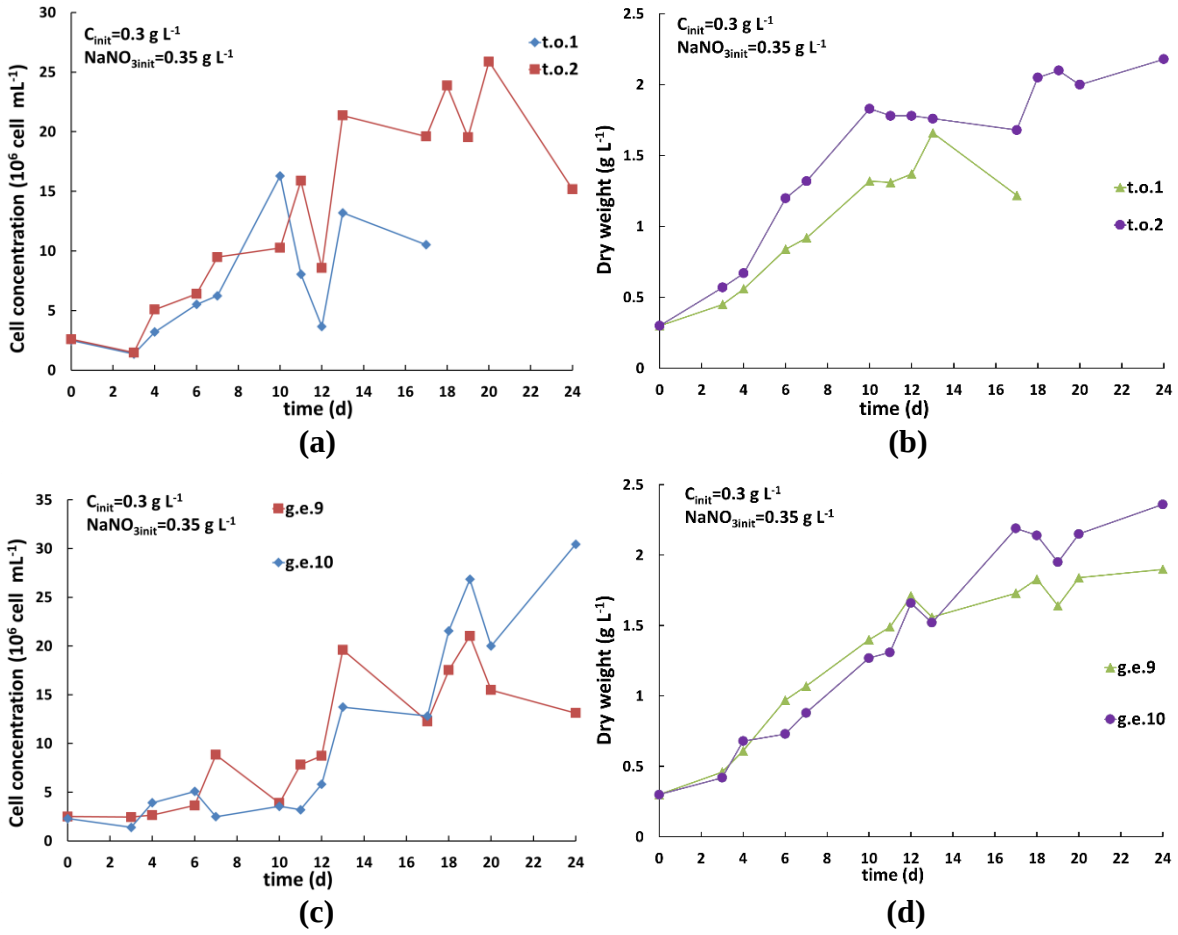

Fig. 62 Microalgae *Tetradesmus obliquus* **(a)-(b)** and *Graesiella Emersonii* **(c)-(d)** growth trends as cellular concentration and dry weight with C_{init}=0.3 g L^{-1} $NaNO_{3init}$=0.35 g L^{-1}, obtained during the experiment H (from 22-09-17 to 17-10-17).

3.1.10 Experiment I (from 27-10-17 to 22-11-17)

In this experiment both *Tetradesmus* and *Graesiella* were cultivated with the optimal initial cultivation conditions ($NaNO_{3init}$=0.35 g L^{-1} and C_{init}=0.3 g L^{-1}) described before (subparagraph 3.1.6). Even in this experiment the effect of low light amount influenced negatively the results obtained both as cellular concentration and dry weight for both species. In this experiment, in order to have more replicates, all PBR available inside the pilot plant were used; the only exception was PBR6 (g.e.6) that after two days showed leakege problems at its basis and for this reason the cultivation was stopped. *Tetradesmus* cultivation shows goood replicability in terms of cell concentration (Fig. 63a) but evident variability as dry weight is visible in Fig. 63b. Also in *Graesiella*'s dry weight results (Fig. 63d) variability is present during the period between 8^{th}-24^{th} days. These problems visible in dry weight measurements, and also in *Graesiella*'s cellular concentration (Fig. 63c), are attributable to contamination problems already found in the previous experiment (subparagraph 3.1.9) due to the restart of reactors left in standby mode during summer vacation. Anyhow *Tetradesmus* showed higher results (as cellular concentration) compared

to *Graesiella* although this latter was more influenced by other contaminating microorganisms, falsifying thus the results obtained.

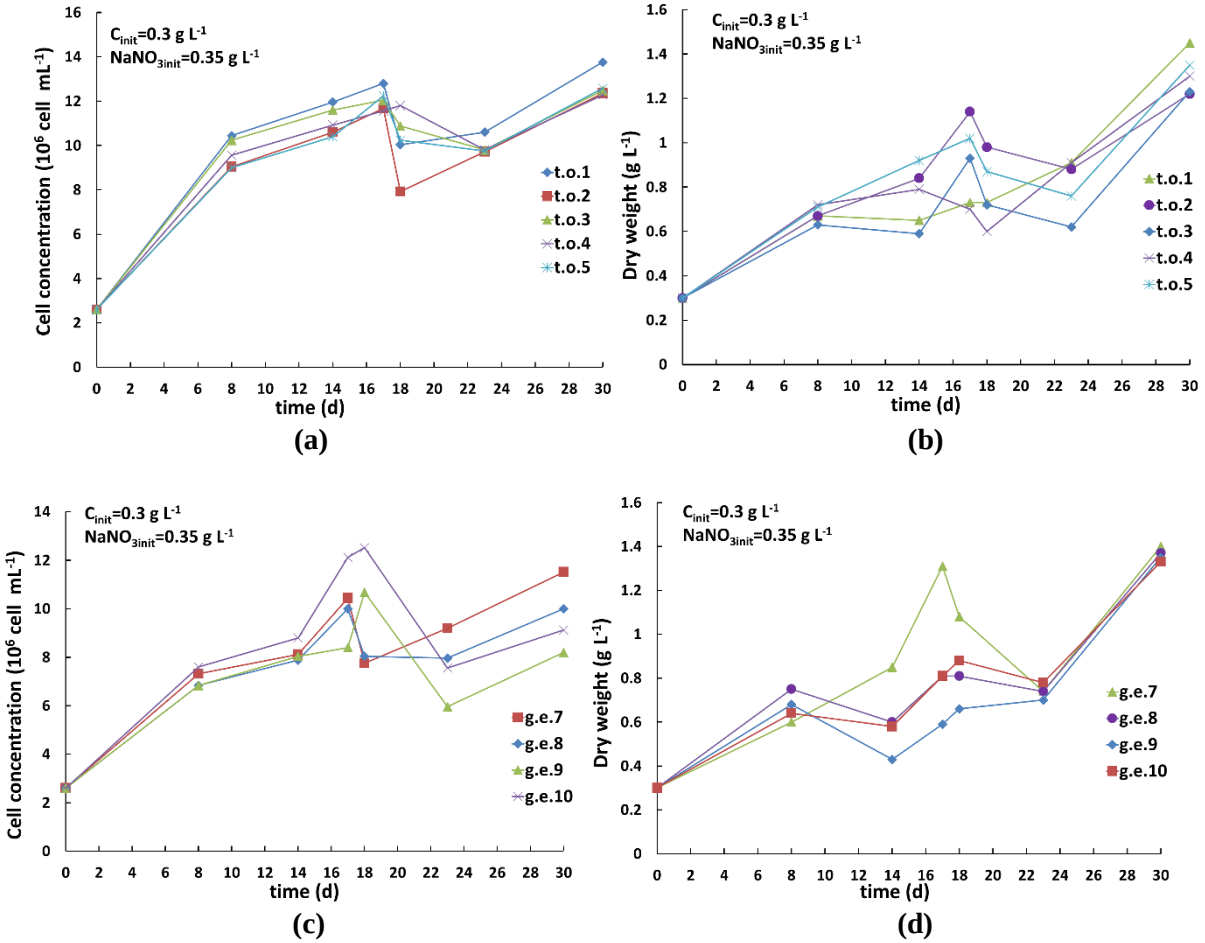

Fig. 63 Microalgae *Tetradesmus obliquus* **(a)-(b)** and *Graesiella Emersonii* **(c)-(d)** growth trends as cellular concentration and dry weight with C_{init}=0.3 g L^{-1} $NaNO_{3init}$=0.35 g L^{-1}, obtained during the experiment I (from 27-10-17 to 22-11-17).

As regards dry weight, considering also the contamination problem, both algae reached the same results, making impossible the decision on which was the best. Regarding the outdoor factors the minimum temperature was pratically the same for the internal and external probes oscillating between 5 °C and 13 °C. The maximum external temperature oscillated between 28 °C and 31 °C and the maximum internal temperature oscillated between 20 °C and 32 °C. On the other side the minimum and maximum PPFD values obtained were 28 µE m^{-2} s^{-1} and 90 µE m^{-2} s^{-1}. In this experiment an high variability of the outdoor factors occurred, indeed even if in some days the temperature overcame 30 °C the light availabilty was always low due to the short light availability typical of winter months.

3.1.11 Experiment L (from 24-11-17 to 22-12-17)

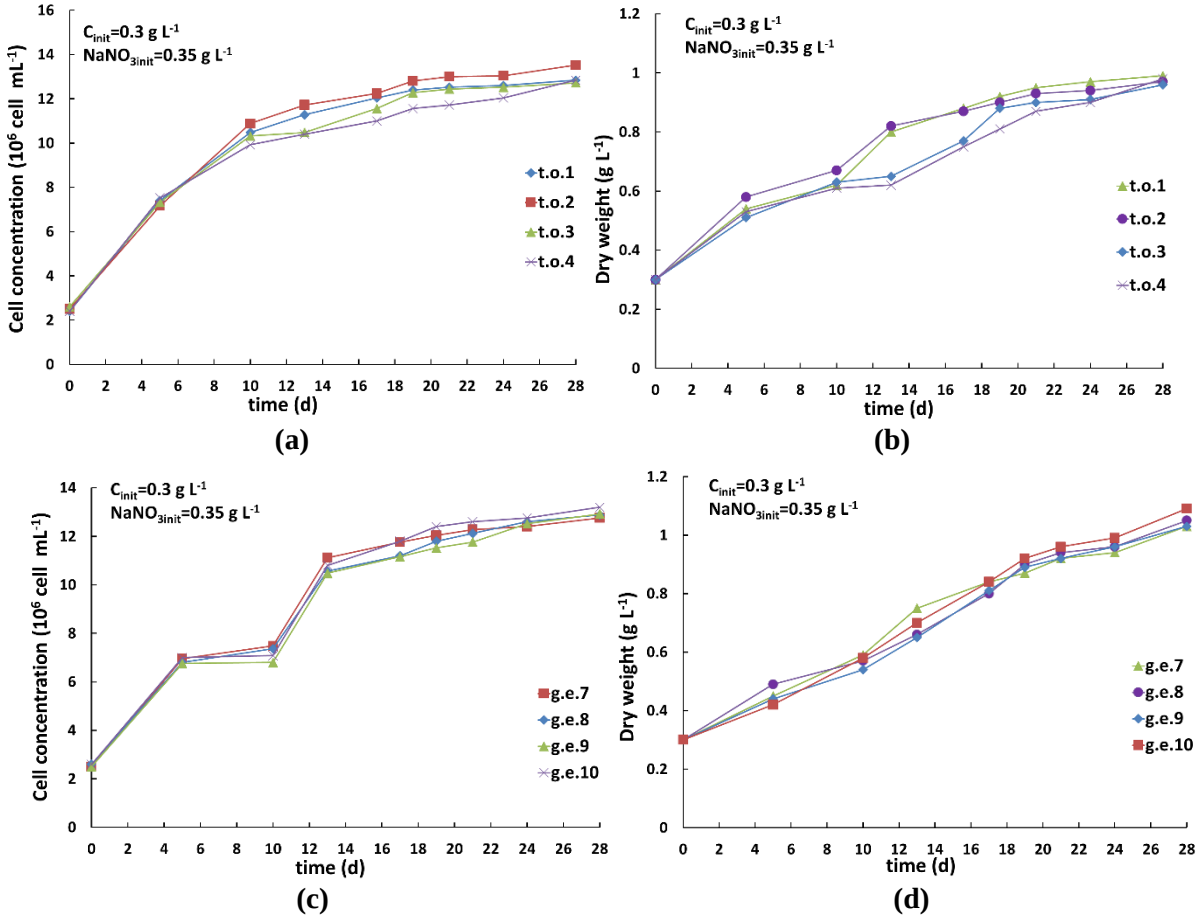

Fig. 64 Microalgae *Tetradesmus obliquus* **(a)-(b)** and *Graesiella Emersonii* **(c)-(d)** growth trends as cellular concentration and dry weight with C_{init}=0.3 g L^{-1} $NaNO_{3init}$=0.35 g L^{-1}, obtained during the experiment L (from 24-11-17 to 22-12-17).

In this experiment both *Tetradesmus* and *Graesiella* were cultivated with the optimal initial cultivation conditions ($NaNO_{3init}$=0.35 g L^{-1} and C_{init}=0.3 g L^{-1}) described before (subparagraph 3.1.6). In order to avoid the contamination problems found in the previous experiments H-I, an accurate cleaning and disinfection of the largest part of the reactors (excluding PBR5 and PRB6 for leakeages issues) was carried out. This reactors' preatreatments gave a good responses for both microalgae either as cellular concentration (Fig. 64a and Fig. 64c) and dry weight (Fig. 64b and Fig. 64d); indeed a good level of replicability is reached, even if the final values are lower than those showed in the previous experiments H and I (see subparagraph 3.1.9 and 3.1.10). These results are justified by lowering of both temperature and light amount (see Fig. 66 and Fig. 67), common effects of outdoor cultivation carried out during autumn or winter period. As comparison of two species, *Tetradesmus* shows slightly higher results in terms of cellular concentration respect to *Graesiella*, but as dry weight they reach the same final values; therefore even in this case both species can be considered equivalent. Regarding the outdoor factors, in this case both internal and external probes showed similar values, in particular the minimum temperature oscillated between -3.5 °C and 8 °C and the maximum temperature oscillated between 9 °C

and 24 °C. On the other side the minimum and maximum PPFD values obtained were 30 μE m^{-2} s^{-1} and 90 μE m^{-2} s^{-1}. In this experiment, due to winter season, very low temperature (below zero) and irradiance's values were obtained, having a negative impact on the microalgal specific growth rate and productivity.

3.1.12 Experiment M (from 19-01-18 to 22-02-18)

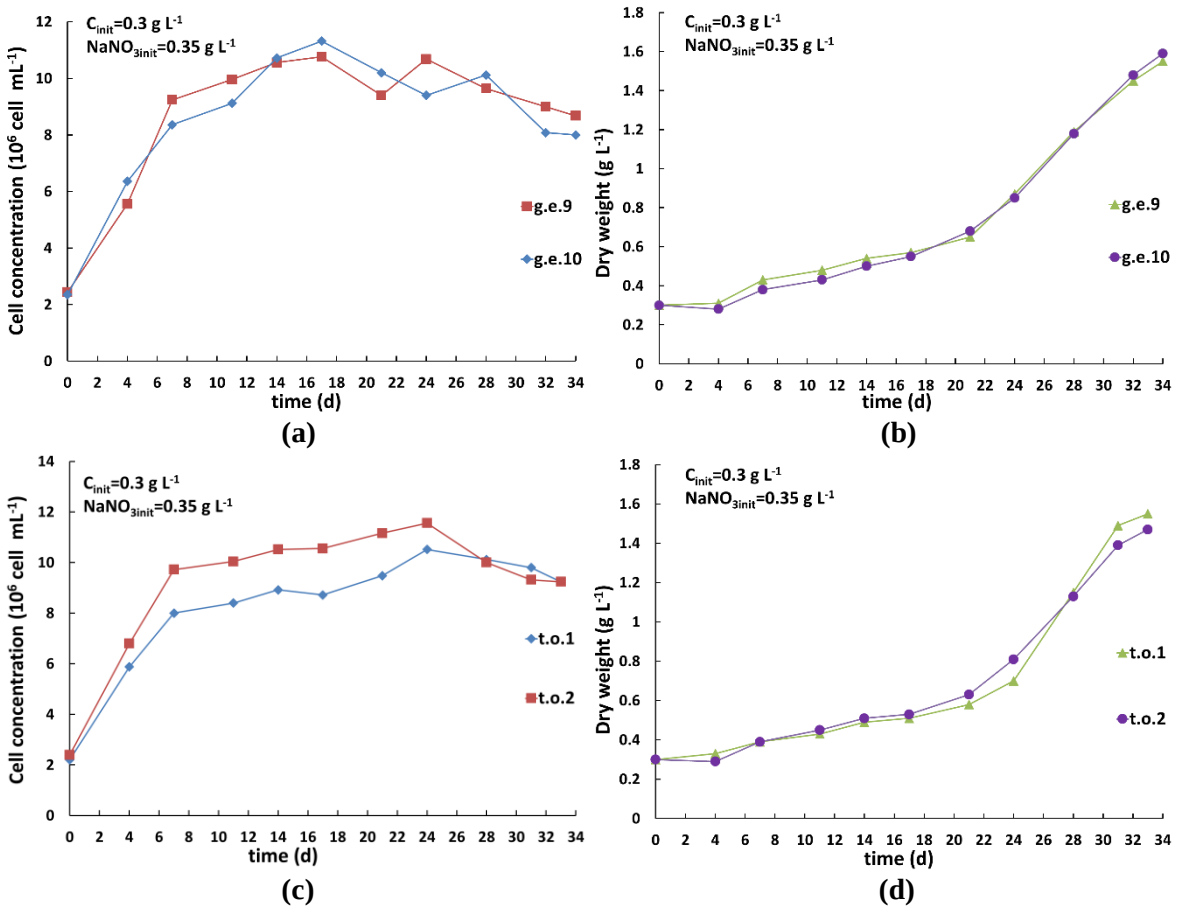

Fig. 65 Microalgae *Tetradesmus obliquus* **(a)-(b)** and *Graesiella Emersonii* **(c)-(d)** growth trends as cellular concentration and dry weight with C_{init}=0.3 g L^{-1} $NaNO_{3init}$=0.35 g L^{-1}, obtained during the experiment M (from 19-01-18 to 22-02-18).

In this experiment both *Tetradesmus* and *Graesiella* were cultivated with the optimal initial cultivation conditions ($NaNO_{3init}$=0.35 g L^{-1} and C_{init}=0.3 g L^{-1}) described before (subparagraph 3.1.6). This experiment is not present in Tab. 5 because it wasn't used to multivariate model developing, differently from previous experiments (from A to L). Indeed this experimet was used to validate the model's prediction ability, which results will be showed in the following paragraphs (see paragraph 3.6). The results are similar to those obtained in the previous experiment L, in particular for dry weight (Fig. 65b and Fig. 65d) at a first glance the results seems higher but this increase is due to the stretching of the batch duration. Indeed if the cultivation had been stopped at 28th day the results were very similar to those of experiment L. Even in this case the contamination is not visible

and the results show high level of replicability between reactors; furthermore, even in this case both species can be considered equivalent. Regarding the outdoor factors, even in this experiment both internal and external probes showed similar values, in particular the minimum temperature oscillated between 0.37 °C and 5 °C and the maximum temperature oscillated between 18 °C and 26 °C. With respect to minimum and maximum PPFD, the values obtained were 28 μE m^{-2} s^{-1} and 55.5 μE m^{-2} s^{-1}. The outdoor variables' behaviour was identical to those of the previous experiment (L).

3.2 Results of the preliminary statistical analysis

As regards the factors listed in Tab. 3, the results of ANOVA test for those are reported in Tab. 17. The only factor that didn't influence the collected data (F<Fcrit, null hypothesis accepted) is the position of the reactors inside the plant, so each reactor inside the plant could be considered as a replicate for light exposition. The other factors influenced significantly light data collection and the causes can be found in the shadow's effect between reactor-reactor and reactor-building, in the day-night cycle and also in weather and seasonal light variability. These preliminary results show that collecting light data in a casual position of the reactor would not been an accurate way to describe light exposition and could have affect the forecast growth value in a predictive empiric model.

Factor	SS	df	MS	F	P-value	Fcrit
Position along the axis of each reactor	0.586	1	0.586	49.76	$7.34*10^{-11}$	3.91
Reactors' position inside the plant	0.097	6	0.016	1.37	0.229	2.16
Time of measurements' uptake: Part of the day	$5.55*10^{8}$	2	$2.77*10^{8}$	$2.29*10^{3}$	$1.40*10^{-119}$	3.05
Time of measurements' uptake: Different days	$3.03*10^{7}$	8	$3.79*10^{5}$	31.31	$2.88*10^{-29}$	1.99

Tab. 17 Results of ANOVA test for the different factors considered to be able to influence light measures. SS=Sum of Squares; df=degree of freedom; MS=mean square; F= Fisher statistic.

As concerns temperature, the paired t-test results, comparing thus internal and external temperatures in time divided in three phases (temperature increment, constant temperature and temperature decrement), indicated a significant difference between two temperatures, showing respectively for each aforesaid phase a p-values equal to 0.01, $1 \cdot 10^{-19}$ and 0.08. This statistical analysis, confirmed the necessity of using two probes, because internal and external temperatures should had to be considered as two different input parameters influencing microalgal growth.

3.3 Input and Output values for multivariate model development

Before showing PCA and PLS results, the values of two inputs and outputs, representing the most important outdoor variables (light and temperature) influencing outdoor cultivation in closed photobioreactors, are reported in this paragraph. Both of these outdoor factors can change several folds in response to seasons, day/night cycle and weather, in a range known to affect microalgae metabolism. Besides the environmental variables, as visibile in the cultivation results (subparagraph 3.1.1.-3.1.12), also the initial biomass concentration (C_{init}) and the initial $NaNO_3$ concentration ($NaNO_{3init}$) of each test were used as input in the model. These two factors were essential to understand the experiment's duration and the biomass production. Other factors, such as CO_2 and pH, that can also influence microalgal growth, were not considered for model development. Indeed, pH was controlled by a control system which maintained it always constant around 8 (subparagraph 1.3.1). CO_2 was supplied on demand by the pH control system and thus was assumed to be sufficient, and not a limiting nutrient for microalgae growth throughout the cultivation. For such reasons these two factor were assumed to be not influent on our tests.
In Fig. 66 averaged maximum and minimum values of Internal and External Temperature measured during the experiments are shown. It is evident that the Minimum Temperatures' plots (Fig. 66b and Fig. 66d) have the same trends and similar values, in contrast to the Maximum Temperatures (Fig. 66a and Fig. 66c). This difference is due mainly to two reasons: firstly, the water contained in a closed vessel directly irradiated by sun, without an active cooling system, heats up to a temperature higher than that of the air ($T_{imax} > T_{emax}$) for physical reasons related to heat transfer efficiency and the thermal capacity of water. Moreover, these effects are improved by trigger of Non-Photochemical Quenching (NPQ) mechanism. This particular defence mechanism protects microalgae from the negative effects of high solar light absorption, dissipating the excess amount of light energy to heat and giving the appearance of an exothermic reaction. The second reason is the presence of the temperature control system with water spray cooling (see subparagraph 2.1.3), that kept during June-September period the Internal Temperature at its set point T= 30 °C. In all four subplots, anyway, the seasons' temperature trend is visible reaching maximum value at about T_{max}=38° C in July, and minimum value at about T_{min}=4° C in December.
In Fig. 67, the light trend both in terms of Daily Illumination Time (dotted) and of PPFD (yellow bars) is plotted; the Daily Illumination Time is averaged on the light hours during each experiment. The irradiance measured values can be positioned between those of Amsterdam (N 52° 22' 13" E 4° 53' 43") and Ankara (N 39° 55' 32" E 32° 51' 59") (Boxwell, 2009).

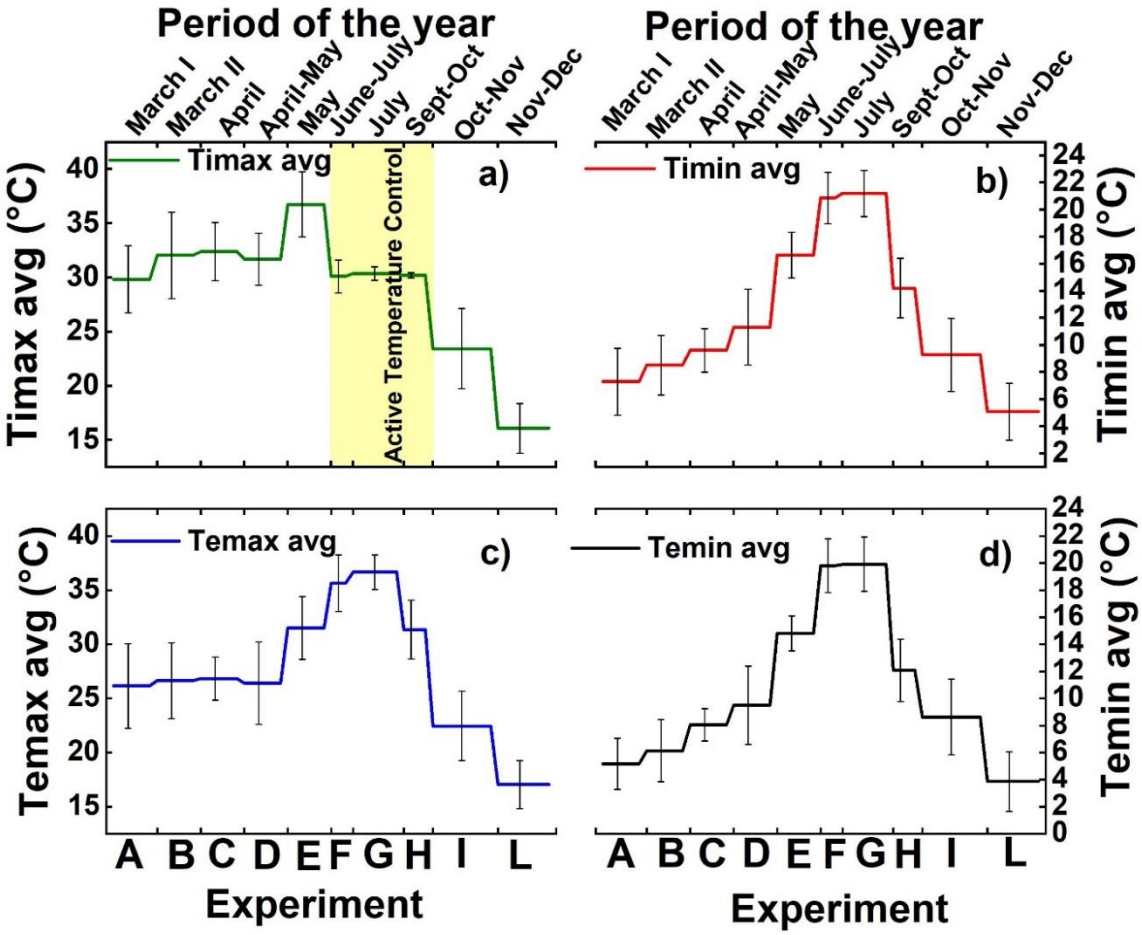

Fig. 66: Averaged maximum/minimum values of Internal (a/b) and External (c/d) Temperature during the experiments. The yellow bar indicates the cooling system activation during the summer periods. The bars represent the Standard Deviations of the replicates.

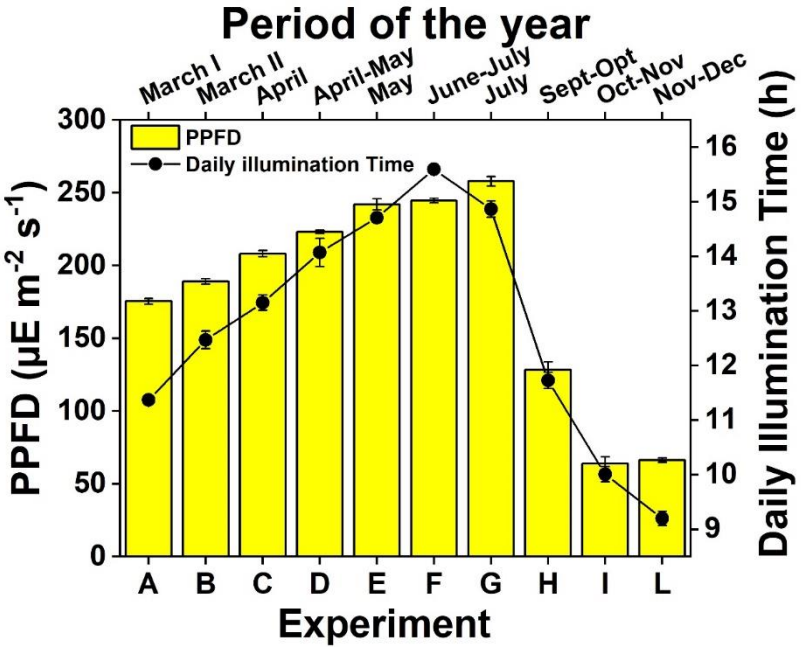

Fig. 67: Photosynthetic Photon Flux Density (PPFD) (µE m^2 s^{-1}) and Daily Illumination Time (h) averaged trends during each experiment. The higher values are obtained in summer periods, having more daylight hours and a better solar irradiance. The bars represent the Standard Deviations of the replicates.

It can be seen, as expected, that the maximum value of PPFD (260 µE m^2 s^{-1}) is reached during the summer period, as also for the Daily Illumination Time (15.6 h) that begins to decrease with autumn. In Fig. 68 the output values (subparagraph 2.3.1) during each esperiment are plotted in terms of specific growth rate (µ (d^{-1})) and productivity calculated at C_{max} (P_{max} (g L^{-1} d^{-1})), both averaged on the replicates. These values are referred to both *Tetradesmus* and *Graesiella*, which were considered as belonging to a single microalgal strain for the empiric model's development.

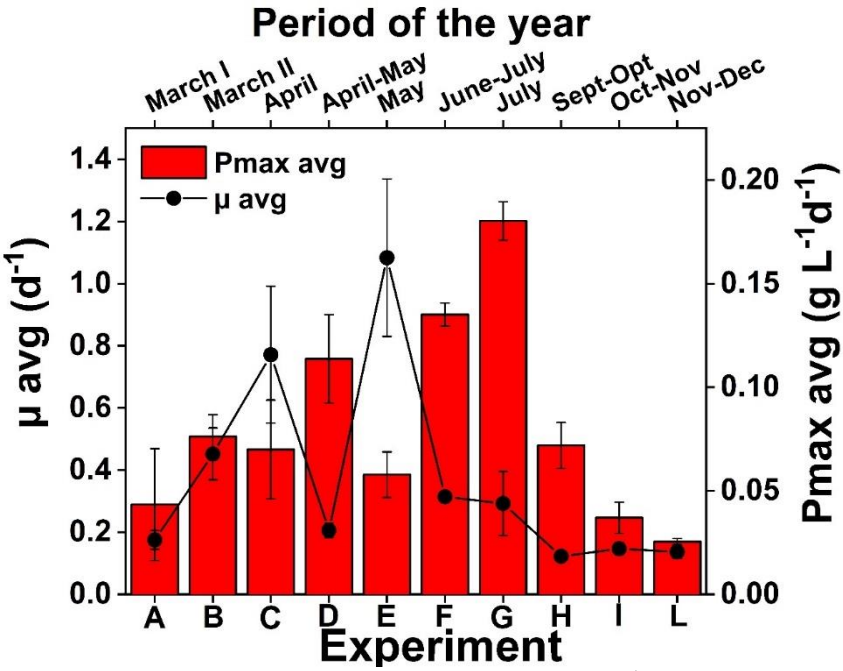

Fig. 68: Output values profiles in terms of Specific growth rate (µ (d^{-1})) and Productivity calculated at C_{max} (P_{max}(g L^{-1} d^{-1})) obtained during the experiments (March 2017-December 2017). A positive trend of P_{max} towards summer months (with the exception of E conducted at a half of normal $NaNO_3$ concentration) is shown. µ doesn't show a clear trend because of high standard deviations between the replicates (especially for C and E) due to the several factors influencing the outdoor microalgal growth. The bars represent the Standard Deviations of the replicates for both microalgae, in each experiment, considered separately.

These assumptions were verified by analyzing results obtained running PCA/PLS methods, with experimental values of each microalga considered singularly (see paragraph 3.6), highlighting thus that these slight differences, in terms of the experimental values of µ and P_{max} between *Tetradesmus* and *Graesiella*, were too small to be detectable from these multivariate statistics methods. Fig. 68 shows a positive P_{max} trend moving towards the summer period (from experiment A to G), with the highest value (0.17 g L^{-1} d^{-1}) obtained in the experiment G and a negative trend moving towards winter months (from experiment H to L). These P_{max} values are fully in line with the outdoor variables plotted in Fig. 66 and Fig. 67 showing better results with the increasing of temperature and light availability. The only exception of P_{max} increasing trend towards summer period, is shown in experiments D and E and is due to different $NaNO_3$ concentration used (see subparagraphs 3.1.4 and 3.1.5). Indeed in D a doubled concentration of $NaNO_3$, respect to others experiments, was used, leading to a biomass and productivity increase. On the other hand in E experiment

using an half of normal $NaNO_3$ concentration led to a lower productivity. These results highlight the relevance of C_{init} and $NaNO_{3init}$ factors, in order to understand the experiments duration and the biomass production; indeed, the D and E experiment show different values of P_{max} (therefore intrinsically also of duration), even if were conducted at similar environmental conditions. As regards the specific growth rate μ, in Fig. 68 there isn't a clear trend because of high standard deviations between the replicates, especially in the experiments C and E (see subparagraphs 3.1.3 and 3.1.5). This μ variability has been explained before and is caused by the several factors influencing the outdoor microalgal growth; for this reason PCA and PLS methods were chosen to isolate the different factors affecting the growth. The P_{max} and μ values in Fig. 68 are comparable with those reported in Tab. 8, obtained in similar environmental conditions in outdoor cultivations, both in Italy and in other locations of the world.

Reactor configuration	**Microalgae Used**	**Location**	**Cultivation period**	**P_{max} ($g\ L^{-1}\ d^{-1}$)**	**μ (d^{-1})**	**Corresponding Author**
Bubble Column	*Tetraselmis suecica*	Italy	August-September	0.4-0.65	0.32-0.65	Chini Zittelli, et al., 2006
Closed Bags	*Nannochloropsis gaditana*	Spain	January-December	0.02-0.13	0.1-0.5	Camacho-Rodríguez et al., 2014
Bubble Column	*Monodus subterraneus*	Netherlands	July-October	0.05-0.2	0.6-0.4	Bosma et al., 2007
Flat Panel	*Nannochloropsis sp.*	Israel	Winter-Summer	0.14-0.25	0.15-0.17	Cheng-Wu et al., 2001
Bubble Column	*Tetradesmus obliquus and Graesiella emersonii*	Italy	March-December	0.025-0.25	0.12-1.1	This work

Tab. 18: μ and P_{max} comparison with other similar environmental conditions in outdoor microalgal cultivations.

In particular during the cultivation period of work described by Camacho-Rodrìguez et al. (Camacho-Rodríguez et al., 2014) we obtained P_{max} = 0.025-0.25 $L^{-1}\ d^{-1}$ and μ = 0.12-1.1 d^{-1}, during the cultivation period of work described by Bosma et al. (Bosma et al., 2007) we obtained P_{max} = 0.04-0.135 $L^{-1}\ d^{-1}$ and μ = 0.15-0.31 d^{-1} and lastly during cultivation period of of work described by Cheng-Wu et al.(Cheng-Wu et al., 2001) we obtained P_{max} = 0.025-0.18 $L^{-1}\ d^{-1}$ and μ = 0.14-0.3 d^{-1}. Only Italy values of Chini Zittelli et al. (Chini Zittelli et al., 2006) are slightly different than our (P_{max} = 0.07-0.18 $L^{-1}\ d^{-1}$ and μ = 0.12-0.3

d^{-1}, especially for P_{max}), due to their optimized pilot plant positioning that increased the photosynthetic productivity.

3.4 Multivariate Model Results

In this paragraph the results obtained from the developed multivariate model having the aim to predict microalgal growth in specific outdoor cultivation conditions, are resumed.

3.4.1 PCA Results

As preliminar result, PCA analysis was implemented and the redundant variables were eliminated; for example variables related to light measures along reactor axis (top, medium, bottom) were deleted, leaving as light representig data, the measure taken on the “unshaded reference point". After this first modification PCA were recalculated, showing that only 2 Principal Components (PC) were needed to explain most of the data variance (88%). This result was carried out by using Cross Validation (CV) method and calculating the Predicted Residual Error Sum of Squares (PRESS) (Wold et al., 1987). The results obtained with PCA implementation, giving a PC=2, granted an easy interpretation of the variables' effects on PCs in a bidimensional plot. In particular, the Loading Plot (Fig. 69) and the Score Plot (Fig. 70) are reported.

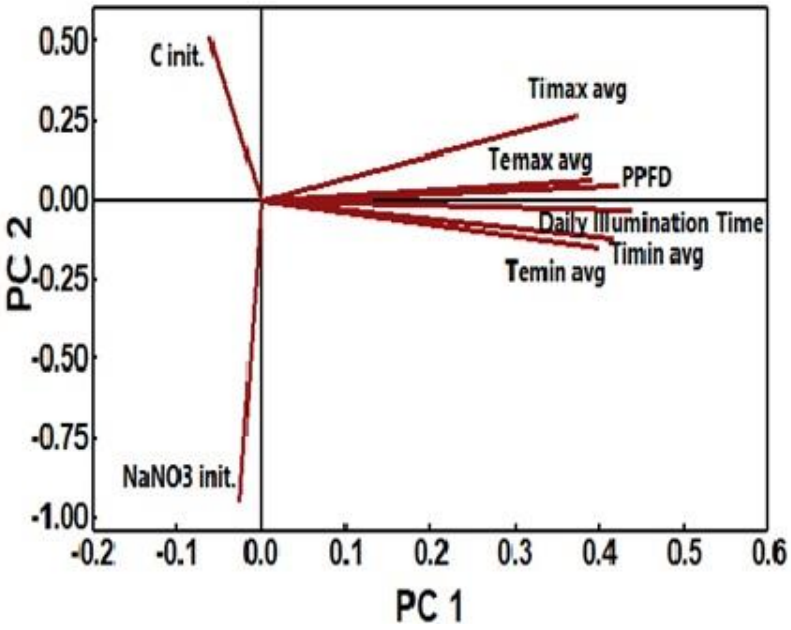

Fig. 69: Loading Plot relatively to the first two Principal Components (PC1 and PC2). The vectors with a horizontal orientation influence more PC1 (“Environmental Conditions”) and for the same reason the vectors with a vertical orientation influence more PC2 (“Cultivation Conditions”).

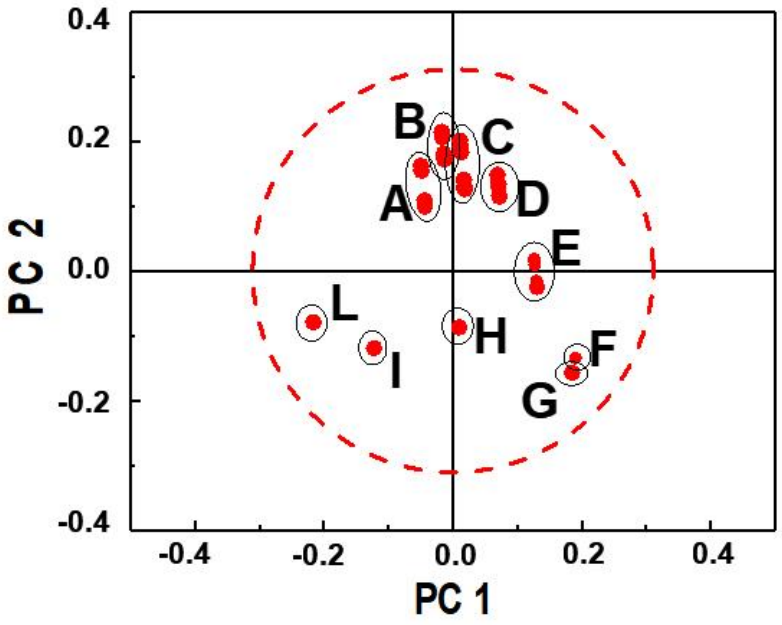

Fig. 70: Score Plot relatively to the first two Principal Components (PC1 and PC2). This plot shows the individual observations, collected during the experiments, clustered in groups having as common features to belong to the same experiment (A-L) and moved near or far from the axis depending on the influence of PC1 or PC2.

Loading Plot is an illustration of how much each variable contributes to build (or "load") each PC, showing how much each variable influence the PCs. In particular the Fig. 69 evidences that the variables with a horizontal orientation ($T_{imax\ avg}$, $T_{emax\ avg}$, $T_{imin\ avg}$, $T_{emin\ avg}$, Daily Illumination Time, PPFD) and similar lenght (which means similar influence on a PC) have a low effect on PC2 but a high effect on PC1. These variables also have good correlation to each other (verified also physically), due to the small angles between the vectors. Fig. 69 also shows that variables approaching to a vertical orientation ($NaNO_{3init}$, C_{init}) are irrilevant to PC1, but significantly influence PC2. In particular, the $NaNO_{3init}$ vector is longer than C_{init} one, being the most influent in PC2 load. Furthermore these two variables do not correlate with each other; indeed they physically represent two different conditions. Since vectors that influence more PC1 are composed by environmental variables, the PC1 can be named: "Environmental Conditions" and for the same reason the PC2 is called "Cultivation Conditions". In Fig. 70 the Score Plot is represented, showing that the observations are clustered in groups having as common feature to belong to the same experiment (A-L). Moreover, the experiments A-B-C-D are also clustered near the vertical axis and shifted from the origin, highlighting that the obeservations are more influenced by the variables with a vertical orientation ($NaNO_{3init}$ and C_{init}) that define PC2. This result is due to the changes, in terms of initial biomass concentration (C_{init}) and the initial $NaNO_3$ concentration ($NaNO_{3init}$), carried out during those experiments. Besides that, the experiments F-G-I-L are affected by both Enviromental conditions and Cultivation conditions, without either of this two Pricipal Components prevail over the other. Lastly, for the experiments H and E, there is almost no

contribution of both variables groups, indicating that the variables have values near their average level, having centered and scaled the observation matrix. In Fig. 70 a dashed circle is reported, representing the Mahalanobis distance, denoting no outlier (Härdle and Simar, 2015). Like many other multivariate statistic methods, the results obtained (in terms of plots, tables and numbers) have to be interpreted and sometimes are not univocal. Indeed, even if the first principal component (PC1) is the most important one because explains the maximum percentage of variability present in the data that can be represented in only one dimension, it is possible that the second one (PC2) is influenced by more important variables (maybe economically). In our case PC2, influenced by the Cultivation Condition variables, is less important for the explanation of data variance but is more important for the economical point of view. Indeed, the amount of nutrients ($NaNO_3$ in our study) can affect, besides the growth rate and productivity, also the Operative Expenditures (OPEX) of the process. For this reason, a correct and deeper interpretation of PCA results, without stopping to a shallow analysis, is essential.

3.4.2 PLS Results: Model Selection and Predictors' Evaluation

PCA results showed the connections between variables and their effects on PCs, grouping both observations and variables. An empiric model able to represent the variables' effect on biomass growth was developed with PLS. As first step, in Fig. 71 the PRESS (Predicted Residual Error Sum of Squares) values of each predictor (the same meaning of component for PCA) are plotted. It is shown that the minimum value of PRESS is obtained at the 6^{th} predictor and consequently the PLS model will need six predictors to describe most of the variance (84%). This is shown in Fig. 72, where the R-Squared (R^2) value for each predictor is plotted for μ response (the same trend is observed also for P_{max}). The R-Sq value provides the proportion of variation in each response that is explained by predictors, indicating how well each model fits data (the higher value obtained, the better the model fits data). In particular, in Fig. 72 both absolute R-Sq (bars) and cumulative R-Sq (dots) are plotted, denoting the same result: i.e. maximum value of R-Sq at 6th predictor (84%). As shown in Fig. 72, with the usage of Cross Validation (CV), an improvement in variability representation can be achieved. The cross-validation technique (the leave-one-out case was used in this study) works by omitting each observation one at a time, rebuilding the predictive model using remaining data and then using this model to predict the omitted data, estimating at the end with PRESS the predicted residual error.

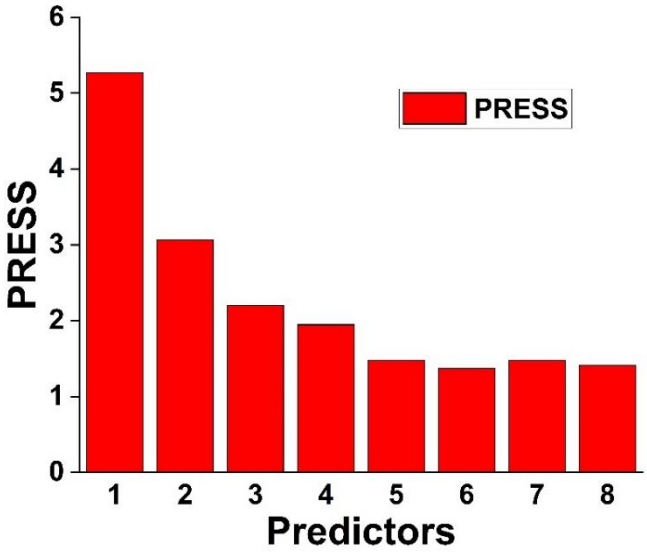

Fig. 71: PRESS (Predicted Residual Error Sum of Squares) Plot for each predictor. This plot aims to illustrate the minimum number of predictors needed to explain the most part of the system variance: in this case PLS model will need six predictors to describe most of the variance.

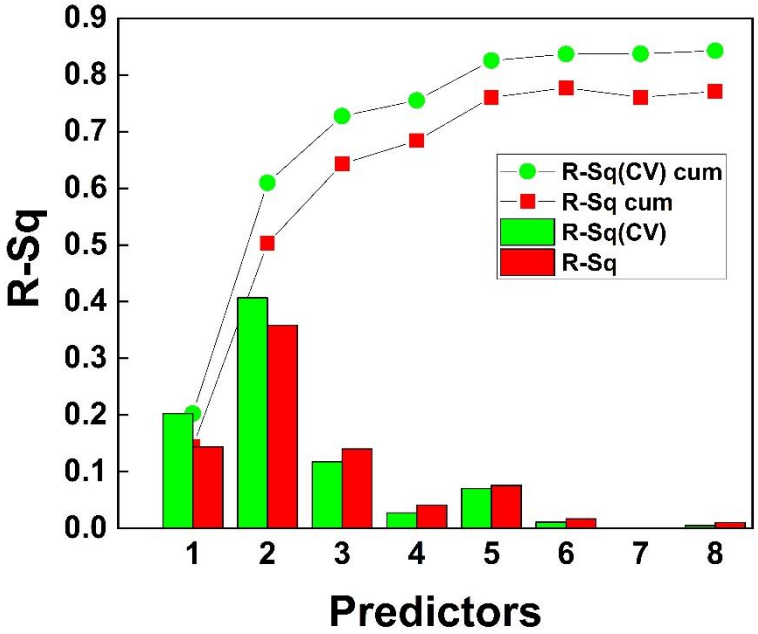

Fig. 72: Model Selection Plot representing the R-Squared trend for each predictor both with and without the Cross Validation (CV) method in absolute and cumulative values. This plot shows that PLS model will need six predictors to describe most of variance (84%) with Cross Validation method, as can be seen also in Model Selection Plot.

3.4.3 PLS Results: Response Analysis

In Fig. 73 and Fig. 74 predicted responses versus experimental data are reported for both outputs for direct fitting and CV procedure. Both plots show very little difference between the fitted and cross-validated fitted responses. Furthermore the points on both plots lie around the correlation line in a similar linear pattern, indicating that model fits data with a good level of accuracy. The analysis of residuals between fitted and experimental data can give further insight into the model goodness.

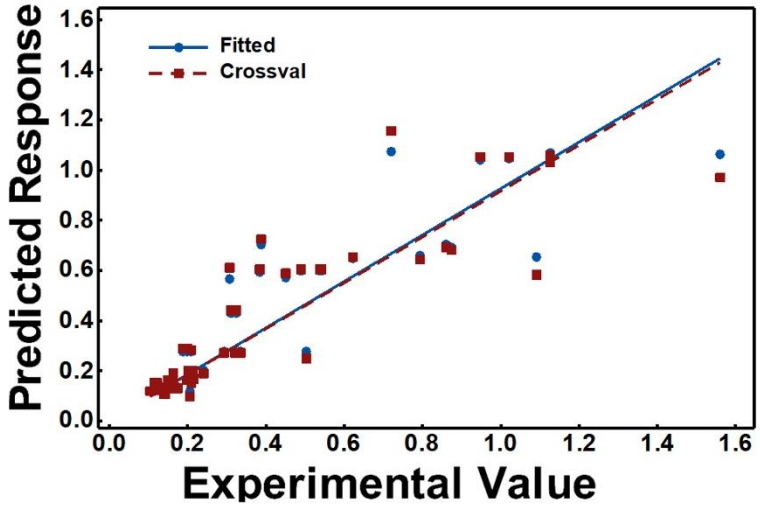

Fig. 73: Response Plot (plot of fitted and cross-validated fitted responses versus experimental values) for μ (d^{-1}). It shows very little differences between fitted and cross-validated fitted responses with points lying around the correlation line in a similar linear pattern, indicating the good level of accuracy of the model data fitting. Plotted data are referred to the individual observations collected during the experiments.

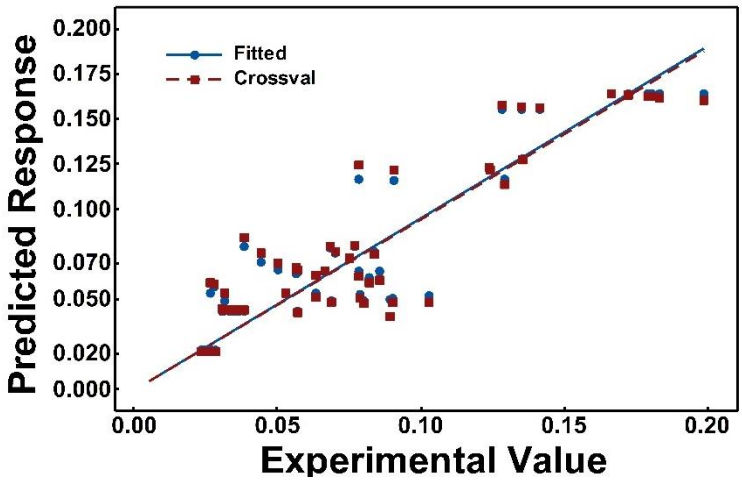

Fig. 74: Response Plot (plot of fitted and cross-validated fitted responses versus experimental values) for P_{max} ($gL^{-1}d^{-1}$). It shows very little differences between fitted and cross-validated fitted responses with points lying around the correlation line in a similar linear pattern, indicating the good level of accuracy of the model data fitting. Plotted data are referred to the individual observations collected during the experiments.

In Fig. 75, the Residual Normal Probability Plot for both outputs μ (d^{-1}) (a) and P_{max} ($gL^{-1}d^{-1}$) (b) are reported. These figures show the standardized residuals versus their expected values when the distribution is normal. The residuals appear to follow a straight line for μ values, while some distorsion can be noticed for P_{max} but always within the range of confidence intervals at 95%.

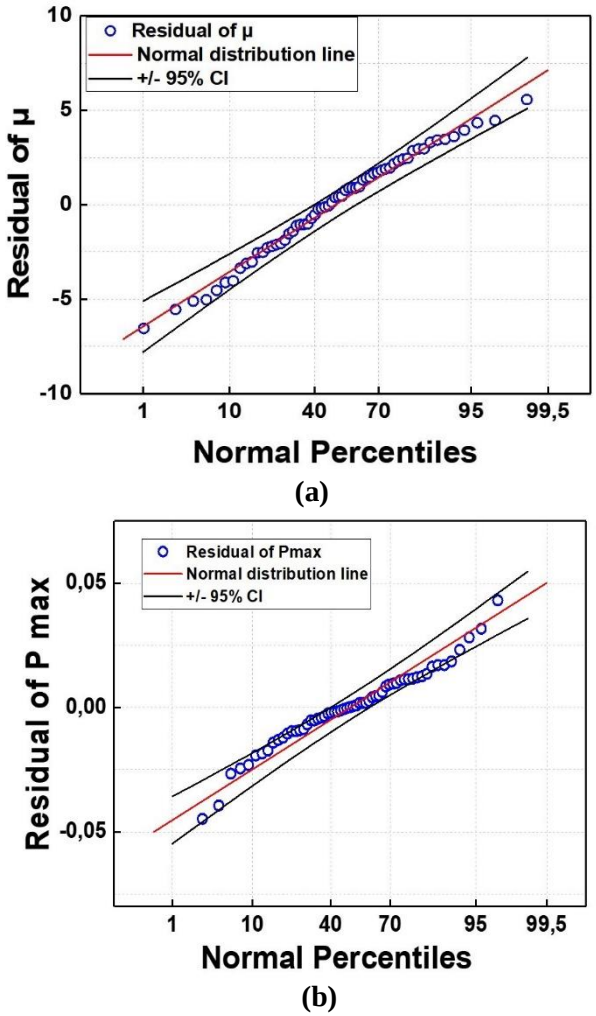

Fig. 75: Residual Normal Probability Plot (standardized residuals results versus their expected values when the distribution is normal) for μ (d^{-1}) (a) and P_{max} ($gL^{-1}d^{-1}$) (b). The residuals appear to follow a straight line for μ values, while some distortions can be noticed for P_{max} but always within the range of 95% confidence intervals. In both plots the data are referred to the individual observations collected during the experiments.

In Fig. 76 and Fig. 77 the predicted and experimental results are compared for both μ and P_{max} outputs, confirming the quality of PLS regression model for different sets of experiments. In both plots the model is able to follow the experimental trends, overcoming the variability specific of the environmental conditions and resembling the effect of changed cultivation condition. Indeed, in both plots some possible outliers, for μ (d^{-1}) in April and May and for P_{max} ($gL^{-1}d^{-1}$) during March, are present.

As regards μ, the outliers could be caused by outdoor variability and operation problems, as described in subparagraphs of paragraph 3.1. On the other hand, for P_{max} the presence of possible outliers can be explained by the different initial cultivation conditions, in terms of C_{init} and $NaNO_{3init}$ carried out in the first experiments (see the experiments results in paragraph 3.1)

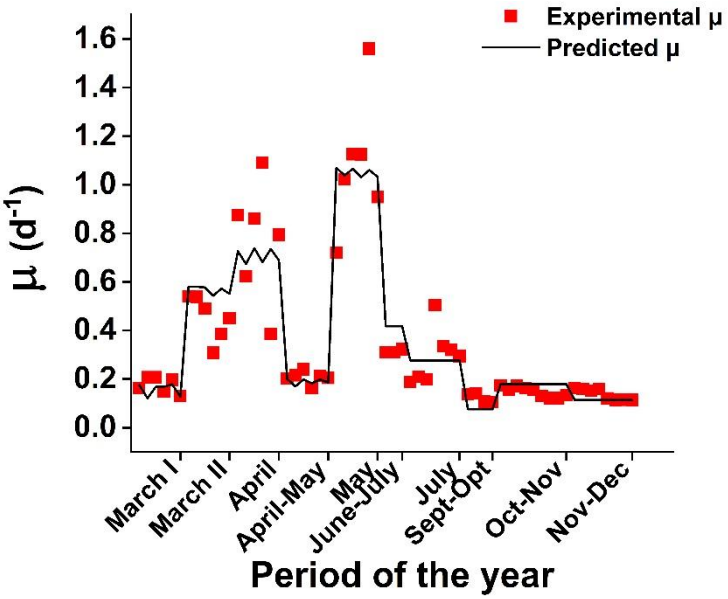

Fig. 76: Comparison between PLS predicted results and experimental ones for μ (d^{-1}). Is visible that the model is able to follow the experimental trends even with the presence of some possible outliers for in April and May (due to the outdoor variability as described in paragraph 3.1). Plotted data are referred to the individual observations collected during the experiments.

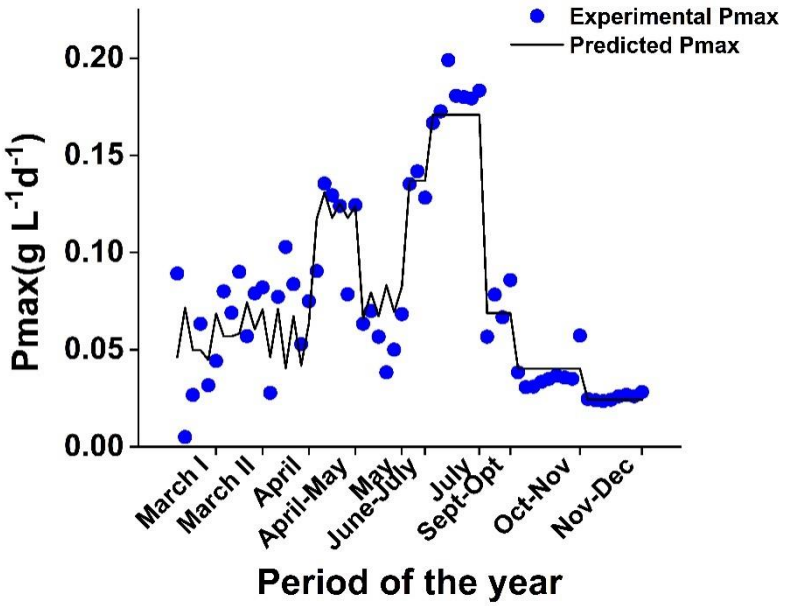

Fig. 77: Comparison between PLS predicted results and experimental ones for P_{max} (g L^{-1} d^{-1}). Is visible that the model is able to follow the experimental trends even with the presence of some possible outliers during March (due to the different initial cultivation condition carried out). Plotted data are referred to the individual observations collected during the experiments.

3.4.4 PLS Results: Empiric Model Prediction Results

In this subsection the prediction results using PLS model are shown. In particular, in Tab. 19 the experimental values obtained during period M (subparagraph 3.1.12) are listed; these values are used only for testing and validating PLS model's prediction abilities and not for its development.

	Response		Predictor							
Experiment	**μ**	**P_{max}**	**C_{init}**	**$NaNO_3$ init**	**$T_{imax\ avg}$**	**$T_{imin\ avg}$**	**$T_{emax\ avg}$**	**$T_{emin\ avg}$**	**PPFD**	**Daily illumination time**
M	0.2	0.03	0.3	0.35	19.6	5.43	18.9	4.74	4090	10.25

Tab. 19: μ and P_{max} comparison with other similar environmental conditions in outdoor microalgal cultivations experimental values obtained during M period (from 19-01-2018 to 22-02-2018), used for testing and validating model's prediction abilities. Responses: specific growth rate μ (d^{-1}) and productivity calculated at C_{max} (P_{max} ($gL^{-1}d^{-1}$)). Predictors: maximum and minimum internal and external temperatures averaged during each experiment $T_{imax\ avg}$, $T_{imin\ avg}$, $T_{emax\ avg}$, $T_{emin\ avg}$ (°C); initial inoculum concentration C_{init} (gL^{-1}) and initial nitrate concentration $NaNO_{3init}$ (gL^{-1}); photosynthetic photon flux density PPFD (μE m^2 s^{-1}); Daily Illumination Time (h).

In Tab. 20 the Predicted Responses both for μ and P_{max}, with their correspondig Standard Error (SE) of Fit and 95% Confidence Interval (CI), are listed and compared with the experimental ones. It can be seen that for both output variables, the regression values are similar but not identical to the experimental ones. This difference is mainly due to the absence of the experimental data collected during M period for PLS model development, lowering a little its prediction ability. The values obtained in Tab. 20 are still an acceptable estimation, considering the high variability that influenced outdoor microalgal growth, underlining the effective goodness of the PLS regression model.

Output variable	Experimental value	Regressed value	SE of Fit	95% CI
μ	0.2	0.28	0.037	(0.206; 0.357)
P_{max}	0.031	0.024	0.006	(0.012; 0.035)

Tab. 20: μ (d^{-1}) and P_{max} ($gL^{-1}d^{-1}$) PLS Regressed Values with relative Standard of Error (SE) and 95% Confidence Interval (CI) compared with the Experimental Values.

As a final step, in Tab. 21 the standardized regression coefficients, used with predictors in order to calculate the fitted value of both response variables, are listed.

Predictor	μ Standardized Coefficients	P_{max} Standardized Coefficients
C_{init}	-0.050482	0.154351
$NaNO_{3init}$	-0.628423	0.402856
Timax avg	0.664885	-0.366197
Timin avg	-0.058646	0.281886
Temax avg	-0.876960	0.271945
Temin avg	0.009383	0.277537
PPFD	0.336034	0.295258
Daily Illumination Time	0.421541	0.124203

Tab. 21: Regression standardized coefficients for both outputs: specific growth rate (μ (d^{-1})) and productivity calculated at C_{max} (P_{max} ($gL^{-1}d^{-1}$)).

3.5 Comparison between *Tetradesmus* and *Graesiella*'s outputs

In order to confirm the hypotesis made in the multivariate model's development that considered *Tetradesmus* and *Graesiella* as belonging to a single microalgal strain due to their high similarity, in this paragraph the results obtained running PCA/PLS methods, with the experimental values of each microalga considered singularly, are showed. In both Fig. 78 and Fig. 79 the comparison between *Tetradesmus* and *Graesiella*'s averaged outputps (in terms of μ and P_{max}), during the experiments in which they were cultivated together in parallel, are plotted. The bars represent the Standard Deviations of the replicates for both microalgae, in each experiment, considered separately. The difference is statistically significant, however, there is any difference when data are used separately for PCA/PLS methods.

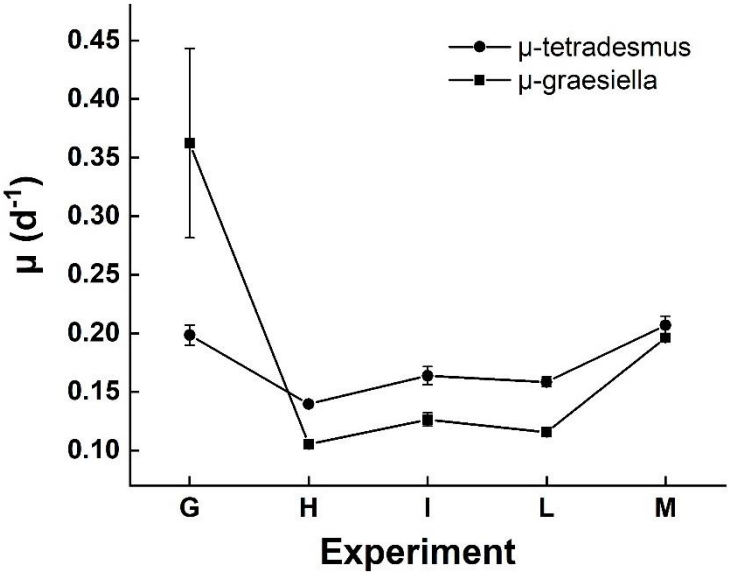

Fig. 78: Comparison between experimental averaged μ values obtained for both *Tetradesmus* and *Graesiella* strains during the experiments in which they were cultivated together in parallel. The bars represent the Standard Deviations of the replicates for both microalgae, in each experiment, considered separately. For each species the replicates' number (n) consist in the number of reactors used the experiment.

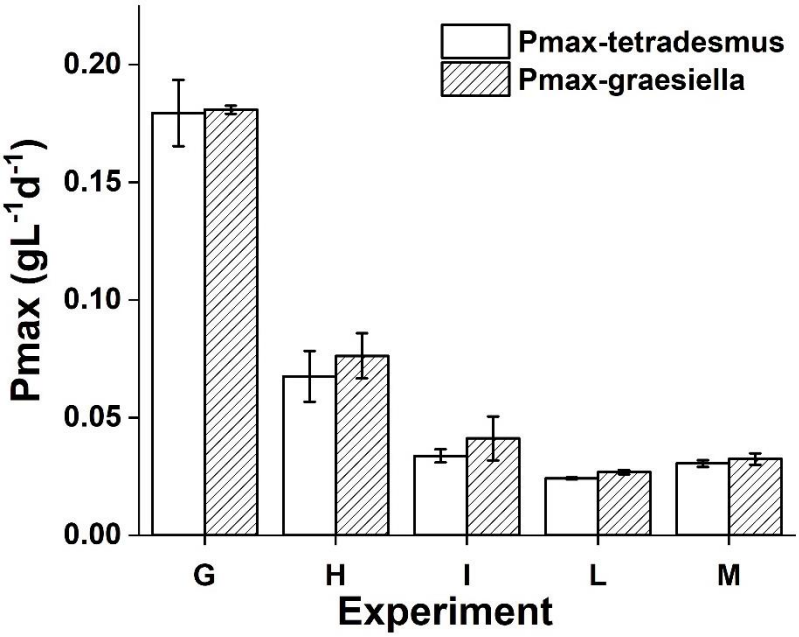

Fig. 79: Experimental averaged P_{max} values obtained for both *Tetradesmus* and *Graesiella* strains during the experiments in which they were cultivated together in parallel. The bars represent the Standard Deviations of the replicates for both microalgae, in each experiment, considered separately. For each species the replicates' number (n) consist in the number of reactors used the experiment.

That is verified in Fig. 80-82 where the results obtained running PCA/PLS methods, with the experimental values of each microalga considered singularly, are shown. All three figures display very similar results, both in the Score and Loading Plot (Fig. 80 and Fig. 81) and in PRESS Plot (Fig. 82).

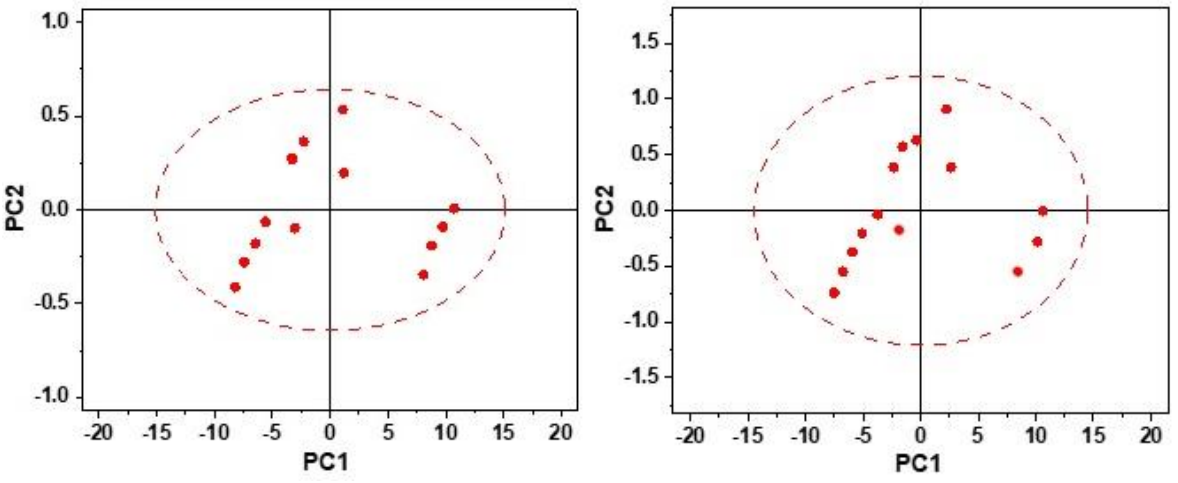

(a) **(b)**

Fig. 80: Score Plot for *Graesiella* (a) and *Tetradesmus* (b) relatively to the first two Principal Components (PC1 and PC2). These results are referred to the experiments (G-M) where both microalgae were cultivated together, showing very similar results in both plots without any outliers. In both plots data are referred to the individual observations collected during the experiments.

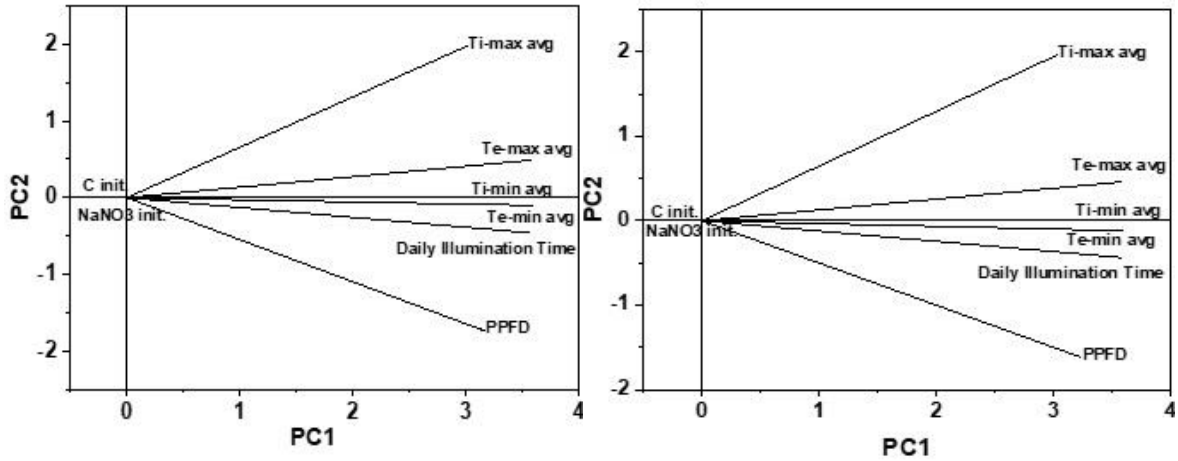

(a) **(b)**

Fig. 81: Loading Plot for Graesiella (a) and Tetradesmus (b) relatively to the first two Principal Components (PC1 and PC2). These results are referred to the experiments (G-M) where both microalgae were cultivated together, showing very similar results in both plots. In both plots, the "Cultivation Conditions" variables ($NaNO_{3init}$ and C_{init}) are nil because in the experiments G-M these variables were not varied.

The PRESS Plot shows that PLS model, for both microalgae, will need 3 predictors to describe most of the variance (95%). This result is different from what is obtained in Fig. 71 because in this case the model was built on data referred only to the experiments where both were cultivated together (Experiments G-M). The same considerations can be applied to the Loading Plots Fig. 81, where the "Cultivation Conditions" variables ($NaNO_{3init}$ and C_{init}) are zero because in the experiments G-M these variables were not varied.

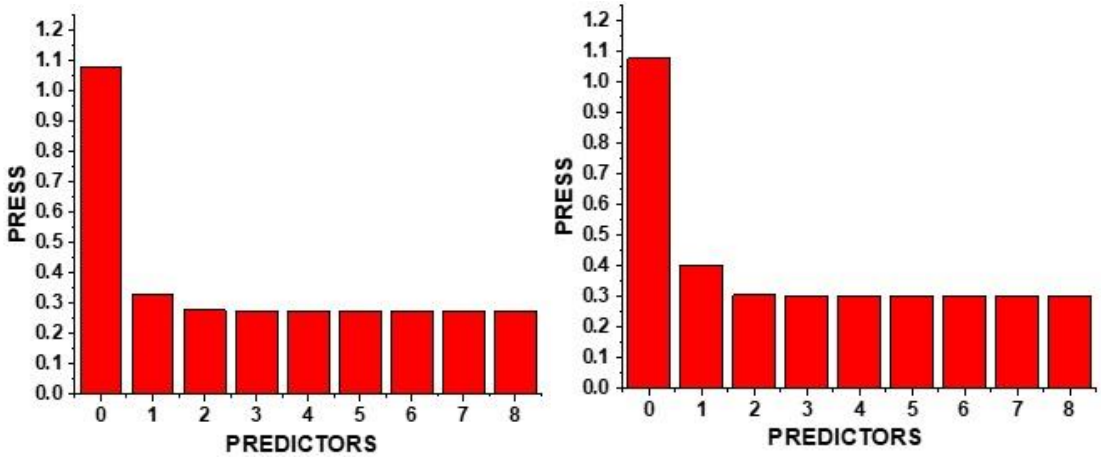

Fig. 82: PRESS Plot for Graesiella (a) and Tetradesmus (b) relatively to the first two Principal Components (PC1 and PC2). These results are referred to the experiments (G-M) where both microalgae were cultivated together, showing very similar results in both plots. The PRESS Plot shows that PLS models, for both microalgae, will need 3 predictors to describe most of the variance (95%).

3.6 Compartmental Model Results

In this paragraph the results obtained from the new developed mathematical model, able to represent in a simple way the accumulation process of metabolites inside microalgae, focusing on the carbon partitioning process between TAG and starch (see subparagraph 1.2.2 and paragraph 2.4), are resumed. In particular the results are divided in subparagraphs, each one is related to the literature work from which data were gathered in order to validate the model. Furthermore, as already explained in the subparagraphs related to the model structure (subparagraph 2.4.2) and to the parameter estimation (subparagraph 2.4.4), the simulated variables are 4 (x, q_n, q_g, q_l) and the estimated and optimized parameters are also 4 ($\boldsymbol{\alpha}$, β, K_I, μ_m). For each variable a plot that shows the difference between the experimental values and the model results is provided. As regards the optimal parameters, a summary table related to each data-set is showed, listing also their confidence intervals and the R-Squared value calculated in order to evaluate the model's goodness of fitting.

3.6.1 Results related to "Breuer et al., 2014" data

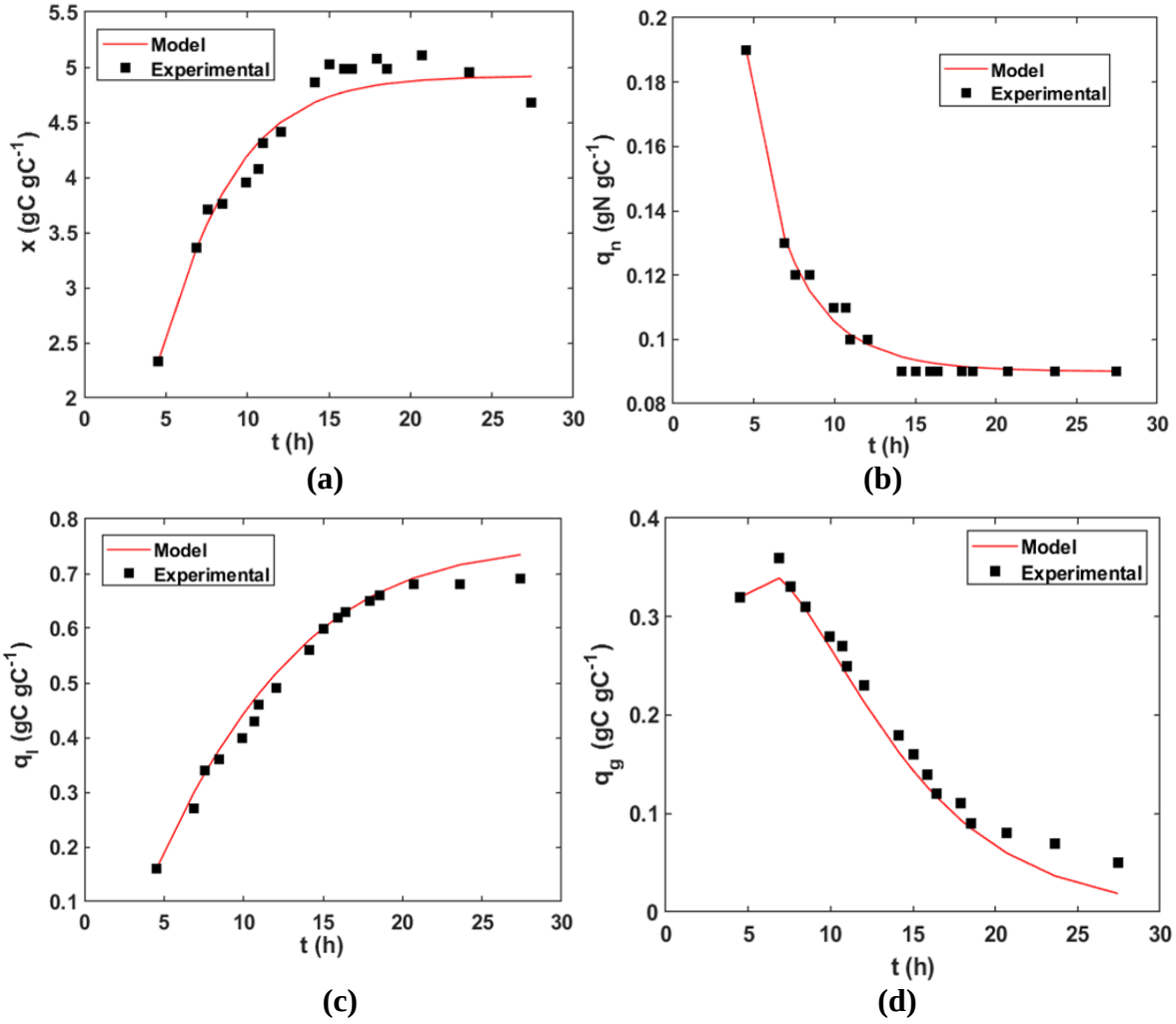

Fig. 83: Model simulation results (solid line) applied to experimental data (squares) gathered from "Breuer et al., 2014" data. The subplots are referred to the 4 model's variables: x (a), q_n (b), q_l (c) and q_g (d). All variables are represented with the unity of measure related to the elemental composition (see subparagraph 2.4.1).

Parameter	Values obtained from the model	Confidence Intervals	R^2
α (g[C] g[C]$^{-1}$)	0.8154	0.7994;0.8314	0.9462
β (g[C] g[C]$^{-1}$)	0.1926	0.1076;0.2776	
μ_m (d^{-1})	0.6762	0.6064;0.7460	
K_I (W m^{-2})	3.4921	3.2403;3.7439	

Tab. 22: Values of the optimal parameters estimated by the developed model with the corresponding confidence intervals and R-squared value.

In all subplots present in Fig. 83 the ability of the new developed model to follow all variables' trends is shown. Furthermore, also the non monotonous behaviour of starch, due

to the carbon partitioning process with TAG (see subparagraph 1.2.2), is represented well by the model, estimating thus with a good accuracy the maximum values reached by q_g. This high level of accuracy is visible also in the results listed in Tab. 22 where a high R^2 is obtained (further details are discussed in the following subparagraph).

3.6.2 Results related to "Breuer et al., 2015" data

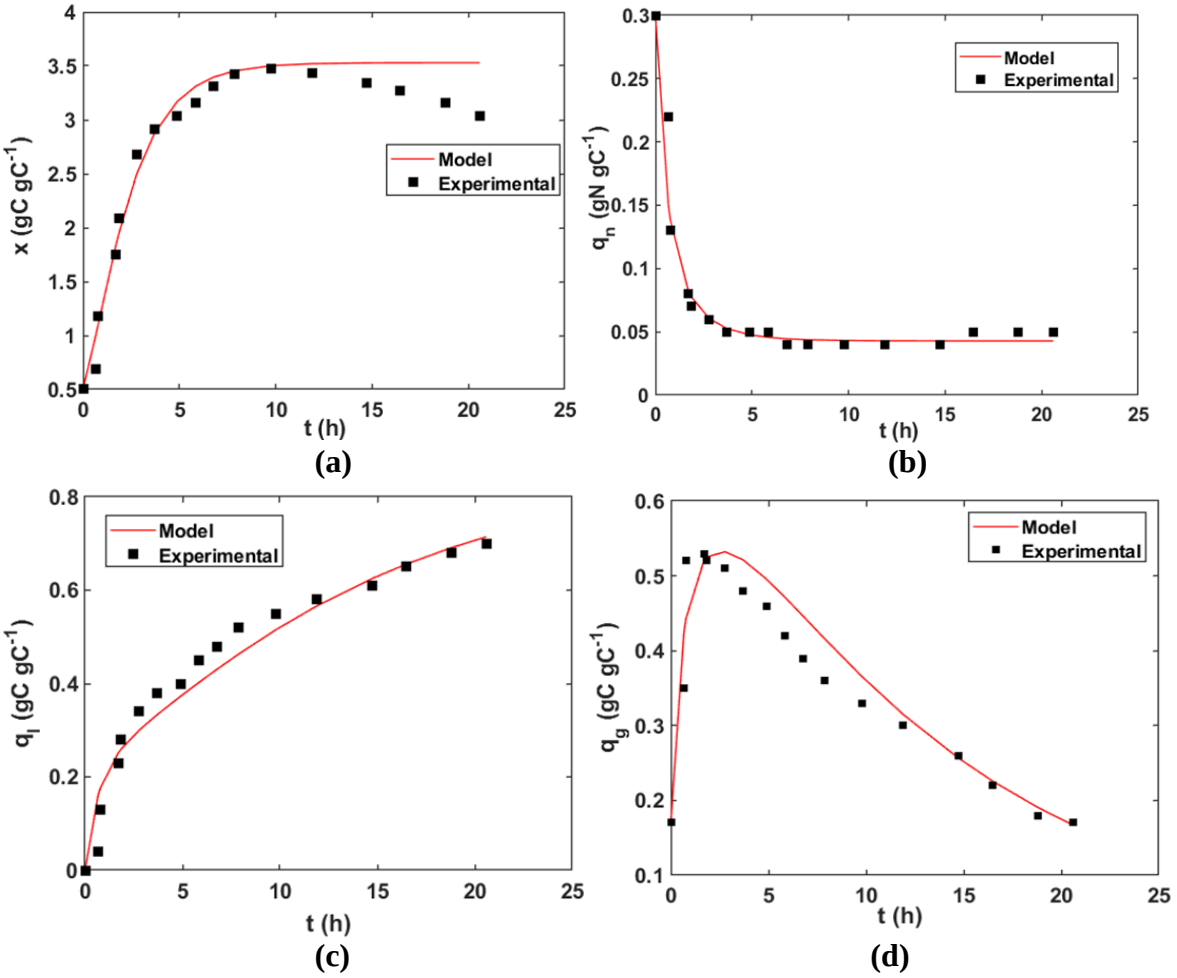

Fig. 84: Model simulation results (solid line) applied to experimental data (squares) gathered from "Breuer et al., 2015" data. The subplots are referred to the 4 model's variables: x (a), q_n (b), q_l (c) and q_g (d). All variables are represented with the unity of measure related to the elemental composition (see subparagraph 2.4.1).

Even in this case, in all subplots present in Fig. 84 the model follows very well the experimental data of each variable. Furthermore, also the starch (q_g) peak is represented with good accuracy. The goodness of fitting can be also seen in the results listed in Tab. 23 where a high R^2 is obtained. In this case, a comparison with the previous results (subparagraph 3.6.1) has to be done since these two data sets come from similar experimental conditions.

Indeed as reported in Tab. 6 for both experiments the same microalga (*Scenedesmus obliquus*) and the same reactor (flat panel photobioreactor), with similar cultivation conditions but different incident light intensity (I_0), were used.

Parameter	Values obtained from the model	Confidence Intervals	R^2
α (g[C] g[C]$^{-1}$)	0.7027	0.6868;0.7185	0.9542
β (g[C] g[C]$^{-1}$)	0.0733	0.0117;0.1349	
μ_m (d^{-1})	2.1141	2.0613;2.1670	
K_I (W m^{-2})	13.3514	13.0082;13.6946	

Tab. 23: Values of the optimal parameters estimated by the developed model with the corresponding confidence intervals and R-squared value.

These differences can be seen both in the plotted variables and the estimated parameters. Indeed higher values for μ_m and K_I are obtained in Tab. 23 compared to those listed in Tab. 22, and this is justified by the higher illumination conditions used in the second work ((Breuer et al., 2015b) respect to the other (Breuer et al., 2014) that caused also an higher specific growth rate (Fig. 83a and Fig. 84a). As regards **α** and β values, they reflect the typical behaviour of the carbon partitioning between starch and lipid during nitrogen starvation, in which the starch is the primary storage compound accumulated with a higher rate (**α**) than TAG (1-**α**). The lower β value obtained in the second case (Tab. 23) represents a slower intercorversion of starch to TAG, compared to that obtained in the previous subparagraph (Tab. 22).

3.6.3 Results related to "Zhu et al., 2014" data

In Fig. 85 the results obtained for the model validation with data from Zhu et. al (Zhu et al., 2014) are resumed. In particular, differently from the previous results (subparagraphs 3.6.1 and 3.6.2) the available data, on which model is developed, are far fewer; these so low data number impacted on the model's results. Indeed, the model describe well the variables' trends but with less accuracy, also in terms of R-squared (Tab. 24). However, the results represent well the carbon partitioning between starch (Fig. 85c) and TAG (Fig. 85d), describing also the presence of the maximum in the starch quota (q_g) trend. As regard the values of the estimated parameters, it can be seen that the value of K_I is lower than those previously obtained due to the lower incident light intesity used (see subparagraph 2.4.1). In fact these values can be compared because, even if in this case the averaged light intensity has been calculated by integration on cylindrical geometry (Eq. 27) and not by a planar geometry (Eq. 26), the reactor used in this experiment had a light path similar (0.025) to the flat panel (0.03) used in Breuer's experiments (subparagraph 3.6.1-3.6.2).

Furthermore, the μ_m is higher than that of Breuer2014 (and lower respect to Breuer2015), even if the light amount is lower; this can be justified by the different microalga used by Zhu et. al (*Chlorella zonfingiensis*).
As regards the carbon partitioning parameters (**α** and β), they are very similar to those of Breuer2014, representing thus similar metabolic pathways.

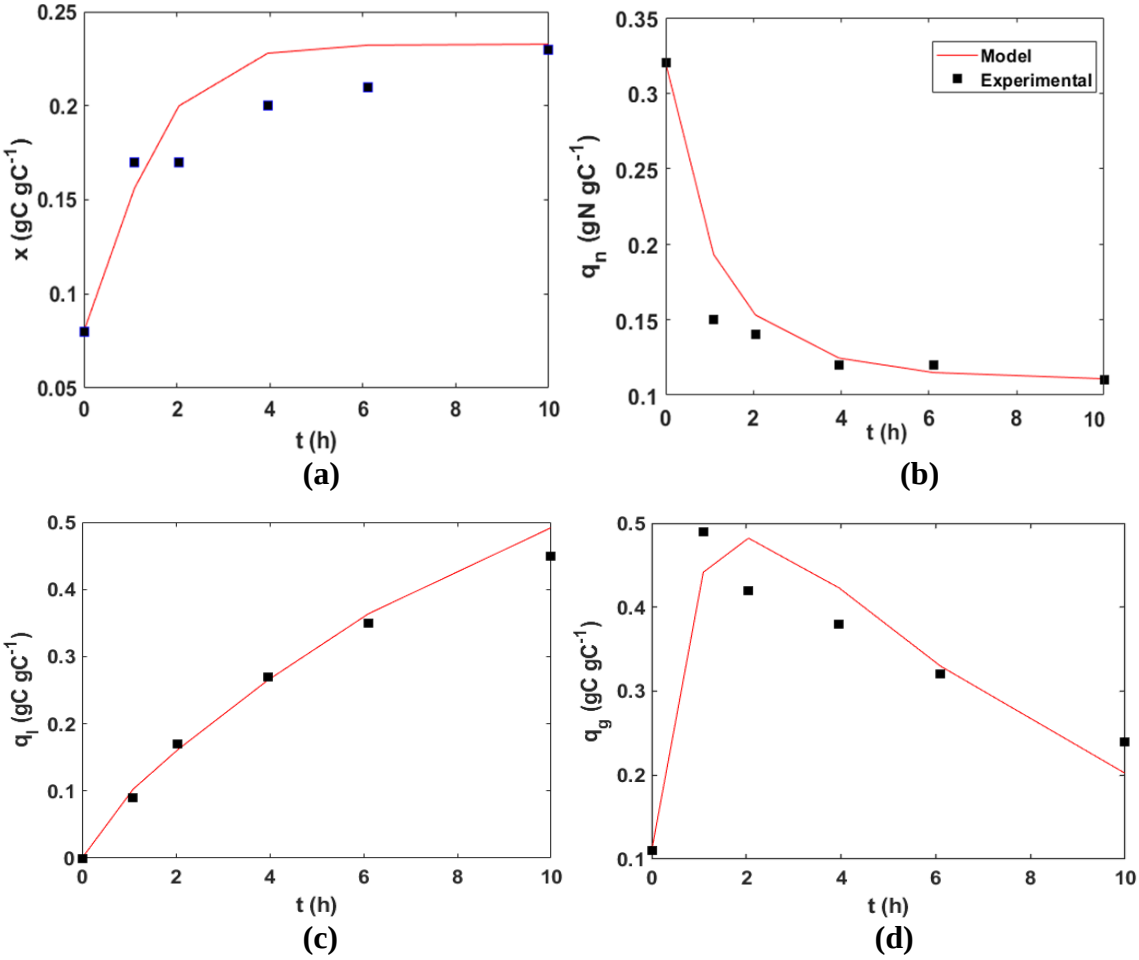

Fig. 85: Model simulation results (solid line) applied to experimental data (squares) gathered from "Zhu et al., 2014" data. The subplots are referred to the 4 model's variables: x (a), q_n (b), q_l (c) and q_g (d). All variables are represented with the unity of measure related to the elemental composition (see subparagraph 2.4.1).

Parameter	Values obtained from the model	Confidence Interval	R^2
α (g[C] g[C]$^{-1}$)	0.8625	0.8473;0.8777	0.9476
β (g[C] g[C]$^{-1}$)	0.1245	0.0356;0.2134	
μ_m (d^{-1})	1.4546	1.4208;1.4884	
K_I (W m^{-2})	1.7998	1.5047;2.0949	

Tab. 24: Values of the optimal parameters estimated by the developed model with the corresponding confidence intervals and R-squared value.

3.6.4 Results related to "Adesanya et al., 2014" data

Finally, the model was applied to Adesanya et al. (Adesanya et al., 2014) data, as can be seen in Fig. 86. In this case, even the number of data on which the model was applied are few, the model is able to follow well the variables' trends with very good accuracy, as visible also in the R-squared value listed in Tab. 25. The only negative aspect is constituted by the failure in reaching the maximum value in the starch quota (Fig. 86d), even if its non monotonous trends is represented.

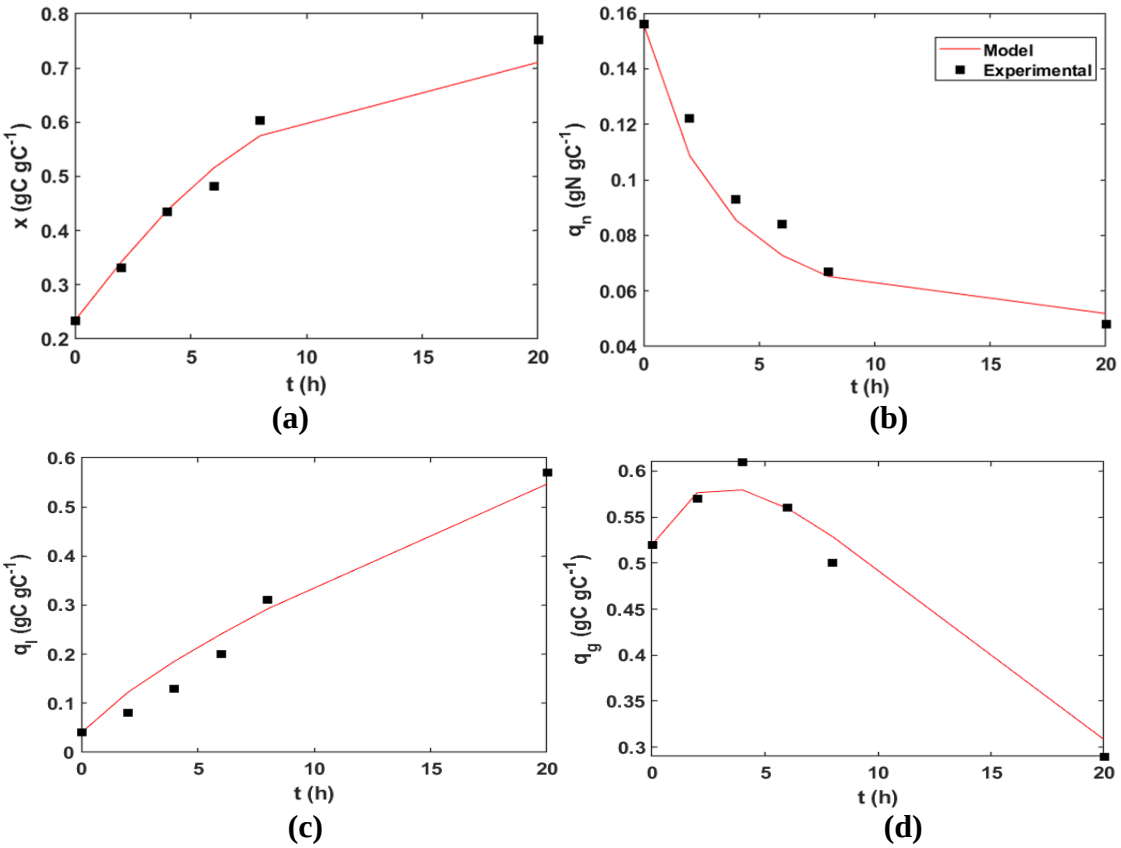

Fig. 86: Model simulation results (solid line) applied to experimental data (squares) gathered from "Adesanya et al., 2014" data. The subplots are referred to the 4 model's variables: x (a), q_n (b), q_l (c) and q_g (d). All variables are represented with the unity of measure related to the elemental composition (see subparagraph 2.4.1).

As regards the optimal parameters, they have unusual values if compared to those obtained in the previous subparagraphs (see subparagraph 3.6.1-3.6.3), first among all the K_I that results higher to Breuer2014 and Zhu even if the incident light intensity used in Adesanya's experiment was the lowest among those listed in Tab. 6.

Parameter	Values obtained from the model	Confidence Interval	R^2
α (g[C] g[C]$^{-1}$)	0.8834	0.8676;0.8991	0.9681
β (g[C] g[C]$^{-1}$)	0.0621	0.0004;0.1234	
μ_m (d^{-1})	0.6374	0.5588;0.7168	
K_I (W m^{-2})	8.5926	8.3149;8.8703	

Tab. 25: Values of the optimal parameters estimated by the developed model with the corresponding confidence intervals and R-squared value.

This problems is caused by the approximate geometry used for the integration of Eq. 24; indeed the experiments of the Adesanya's work were conducted in glass flask (with a culture dept of 30 mm) and not inside a classical photobioreactor. In first approximation, in the cited work, the reactor geometry was considered planar and thus the mean irradiance calculation followed the Eq. 26. These considerations had an impact to the model results, since the reactor geometry is fundamental for μ calculation and also for the 4 parameters' estimation. Consequently, even if the implemented model was able to describe the carbon partitioning process between starch and TAG, the results obtained in this subparagraph cannot be compared to those showed in the previous subparagraphs.

3.6.5 Final considerations on the model

In this subparagraph some additional considerations on the compartemental model have been carried out. In particular, as example the results obtained running the developed model with experimental data obtained from "Bernard et al., 2015" data but with the optimal parameters found in subparagraph 3.6.1, have been reported in Fig. 87. It is visible that the results obtained from the model are not very accurate, because the parameters used were obtained from another experimental data set conducted at different experimental conditions. Indeed, due to the different experimental conditions used in the cited work listed in Tab. 6, the results showed in the previous subparagraphs (3.6.1-3.6.4) were obtained with separated regressions and not with an overall regression of the data set. Furthermore, Fig. 87 was chosen as example because experimental conditions from "Bernard et al., 2015" and "Bernard et al., 2015" were not so different if compared to the other two works. In fact in Fig. 87 the model, even if not accurately, is able to follow the experimental trends, showing also the starch maximum quota, underlining its goodness even in presence of not optimal parameters.

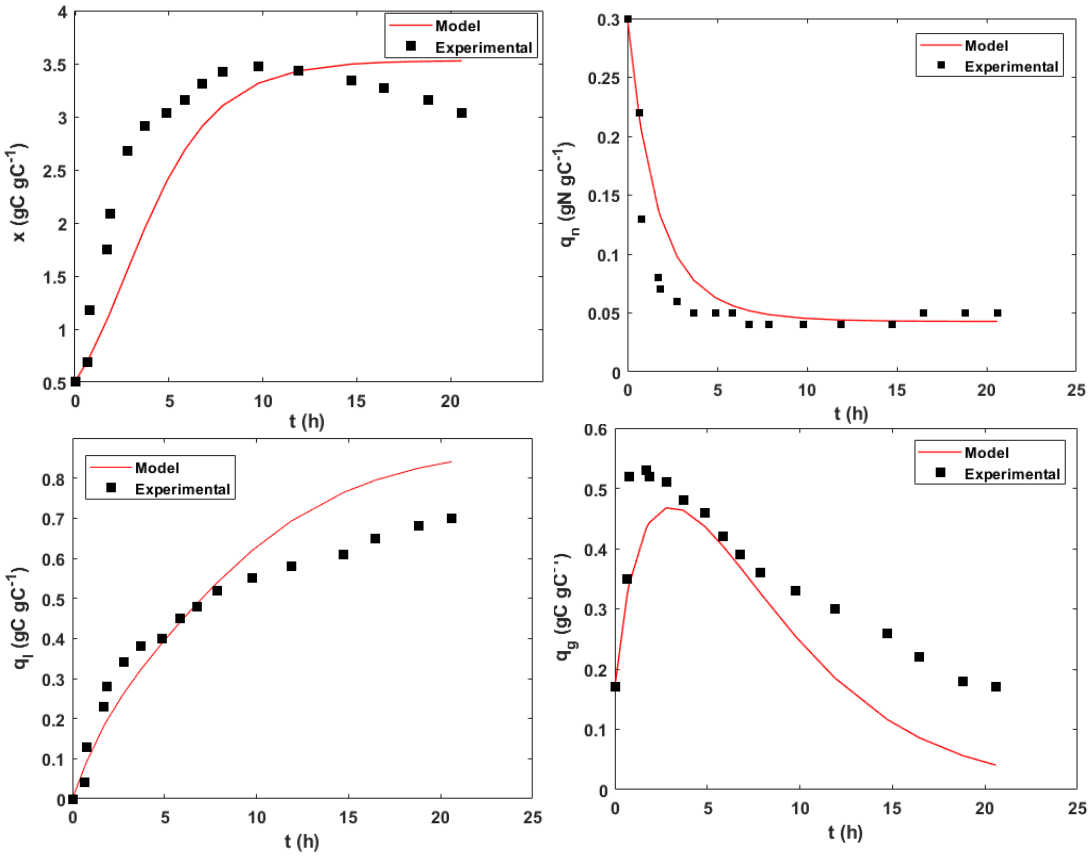

Fig. 87: Model simulation results (solid line) applied to experimental data (squares) gathered from "Bernard et al., 2015" data using the optimized parameters found in subparagraph 3.6.1. The subplots are referred to the 4 model's variables: x (a), qn (b), ql (c) and qg (d). All variables are represented with the unity of measure related to the elemental composition (see subparagraph 2.4.1).

3.7 Supercritical CO_2 modeling results

In this paragraph, the results obtained from the sCO_2 extraction modeling, both in technical and economical point of view are resumed and discussed.

3.7.1 Extraction time

As first step, the extraction time of each component was calculated at specific operative conditions. In these calculations an important assumption was done: for each component the maximum extractable percentage was set to the 85% of its quantity inside the microalgae (Follegatti-romero et al., 2009). This upper limit (based mainly on "oil" extraction) is mainly an operative barrier and it is due to the existence of the mass transport resistances, ever more present with the approach to the complete extraction, that would stretch the extraction time to values too long for any industrial application. In Fig. 88 the maximum extractable percentage (in terms of extraction yield), for the more soluble metabolites in sCO_2, are plotted at T = 60°C, P = 250 bar and SSR = 5 h^{-1} (see the next subparagraphs for the justification of these variables' values). Carotenoids are not present in Fig. 88 as specified in the subparagraph 2.5.2. Also the saturation time, defined as the

time necessary to reach the maximum extractable percentage, was calculated for each component. Even if they are similar, DHA takes longer time to reach its saturation value (370 min) so it was taken as reference. In particular in the subsequent calculations, the desired extraction yields of the others components were determined at the time in which DHA reached the specified yield, assuring thus that also the slower molecule will reach the scheduled yield.

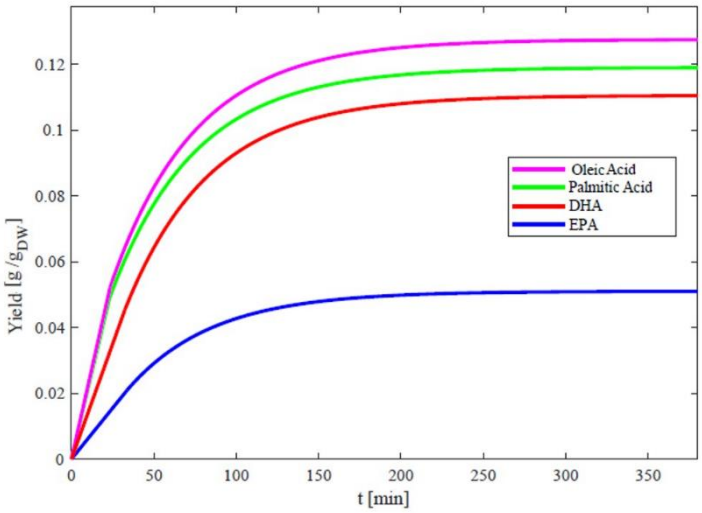

Fig. 88: Target metabolites' yield trend at T = 60 °C,P = 250 bar and SSR = 5 h^{-1}.

3.7.2 Effects of the operative variables on the extraction yield

3.7.2.1 Temperature effects

In this subparagraph, the effects of temperature, pressure and ratio of CO_2 flow rate to microalgal mass (Solvent to Solid Ratio = SSR) on extraction yield are evaluated with the aim of finding the best working conditions that allow also the extraction and separation of carotenoids (residue stream) from fatty acids (extract stream). In Fig. 89 the extraction curves at P = 250 bar, SSR = 5 h^{-1} and different temperatures for palmitic acid are shown.It is visible that with a temperature increase a greater extraction yield is obtained; the same results were achieved for oleic acid (data not shown).

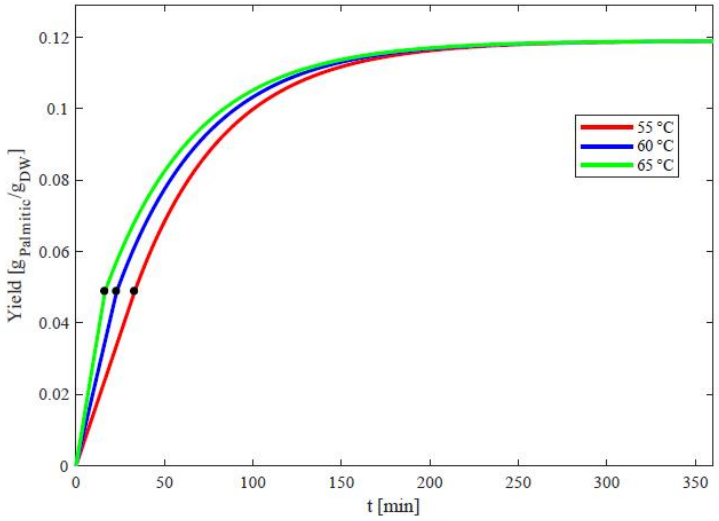

Fig. 89: Palmitic acid's yield in function of time at differenttemperatures.

The temperature range analyzed was 55-65°C because is the best compromise between an improving of the extraction yield and a preservation of bioactive and thermolabile properties of the extracted metabolites. At a first glance the better choice would be to work a T = 65°C because it permits to reach the same extraction yield in a shorter time, caring out more daily cycles with consequent higher productivity, but at this temperature the loss of some properties of the thermosensitive and thermolabile compounds like omega-3 and carotenoids begins (Xu and Howard, 2012). At the same time, lower temperatures than 55°C will lead to lower extraction yield and lower productivity, so T = 60°C was chosen for both molecules. For EPA and DHA the effect of temperature at the same pressure and SSR on the extraction yield has a particular behavior compared to palmitic and oleic acid, underlining the effectiveness of considering metabolites individually (even if the extraction time is about the same for all the analyzed cases). Indeed, it is necessary a magnification in DHA yield trends (Fig. 90) (EPA results are identical, figure not shown) for seeing that to higher temperature corresponds a minor extraction yield at the same time. An explanation for this behavior is found in the cross-over phenomenon.

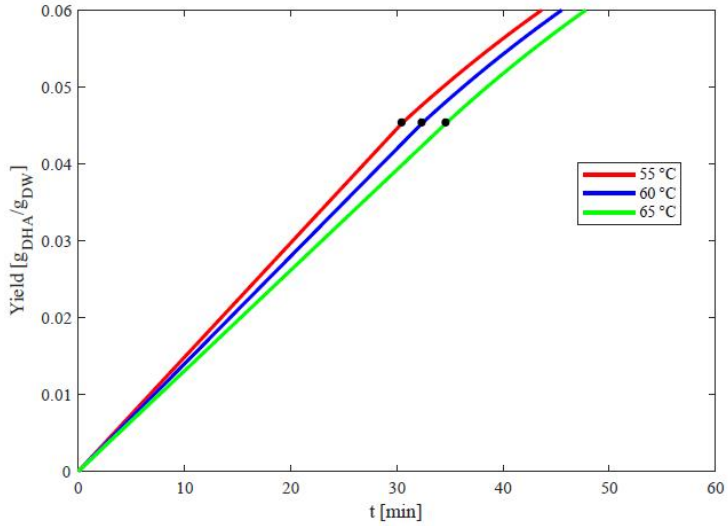

Fig. 90: Magnification of the trend of DHA's yield in functionof time at different temperatures.

Cross-over pressure (P_{co}) is defined as (Erkey, 2011):

- At a $P > P_{co}$ solubility increases with increasing temperature
- At $P = P_{co}$ the temperature hasn't effect on solubility and therefore on yield extraction
- At $P < P_{co}$ solubility decreases with increasing temperature.

In our case, for EPA and DHA the extraction is working under the cross-over pressure. Even if the optimal temperature seems to be 55°C, T = 60°C was chosen also for these two molecules, considering that there isn't a significant difference between two extraction yields.

3.7.2.2 Pressure effects

The same considerations done for temperature were used for pressure analysis. In particular temperature was kept at T = 60°C, SSR = 5 h^{-1} and the pressures range analyzed was 200-300 bar. This range was chosen in order to minimize as much as possible the solubilization of carotenoids into sCO_2 and to increase at same time the fatty acids' extraction yield. In Fig. 91 the pressure's effect on the extraction yield, referred to DHA, is plotted. It is visible that with a pressure increase a greater extraction yield is obtained; this happens also in the case of palmitic acid, oleic acid, EPA and DHA. However, observing the curves in Fig. 91, it is notable that an increase of 50 bar (from 250 to 300) actually involves to limited changes in extraction yield but to higher investment and operating costs. For these reasons P = 250 bar is assumed as optimal pressure.

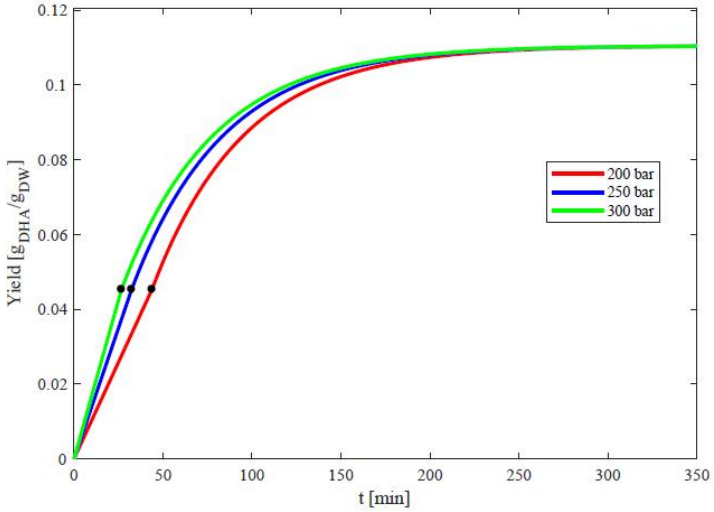

Fig. 91: DHA's yield in function of time at different pressures.

3.7.2.3 Solvent to Solid Ratio (SSR) effects

The study of the effects of the solvent flow rate on the extraction yield is important for two reasons: the first is because the extraction yield is indirectly dependent of it (e.g. Reynolds' number), the latter is due to the industrial importance of knowing the sCO_2 quantity needed to reach the target yield in order to analyze the feasibility of the process, having the sCO_2 flow rate direct impact on the process' economics (being part of the TOTAL OPEX). In this work 360 kg of microalgae was considered as the daily available quantity to process with sCO_2. This value was estimated by combination of literature data (Doucha and Lívanský, 2014) and informations about industrial fermentation plant size (Nutraceutical Business Review, 2018). Different simulations were carried out in order to calculate the number of the daily cycles and consequently the components' amount that can be extracted. In particular in these simulations the Solvent to Solid Ratio (SSR) was changed at these values: 5-10-20-40, always maintaining the pressure at P = 250 bar and the temperature at T = 60°C, finding at each SSR the time needed to reach the maximum extractable percentage (saturation value) of a specific component. Furthermore, considering that the extraction process from microalgae is not continuous but works in cycles, also the duration of each cycle had to be analyzed, depending on the sum of three times:

- The pressurization time (t_p)
- The extraction time (t_e)
- The depressurization time (t_d)

Indicative values of pressurization (1 h) & depressurization (1 h) times were estimated by contacts with extractor's suppliers and cover all the operative steps needed to make in function the extractor's equipments, including: time in which the microalgae is loaded/discharged into/from the extractor, time to place/displace the extractor in/from the correct position, time to turn on/off the compressors and other equipments, time to open/close all the valves, time to collect the extract from the extraction vessel and other additional working times (cleaning, etc.). Therefore, the sum of pressurization and depressurization time had to be added to each extraction time found with the simulations. In this way it was possible to calculate the duration of the single extraction cycle, the number of daily cycles and also the microalgal quantity to be introduced in each cycle. This procedure was applied to the DHA, assumed as the reference component, and the results can be found in Tab. 26. Tab. 26 was chosen in place of a figure in order to increase the clarity of the effects of the solvent flow rate per kg of microalgae (SSR) on both extraction yield and process operability. Indeed, it is shown in Tab. 26 that the same number of daily cycles is reached for each SSR; the reason is because, for a SSR increase, there is also a progressive increase of dead times that don't allow to end entirely any additional cycle within the working day. Also the extracted DHA doesn't change but the sCO_2 flow rate appears to increase together with SSR because the microalgae loaded in each cycle remain the same having always the same number of daily cycles. It is thus convenient to work with a ratio SSR = 5 h^{-1}, indeed this ratio needs a lower CO_2 flow rate

SSR (h^{-1})	Saturation time (h)	Number of cycles	Microalgae cycle (kg)	sCO_2 flow rate (kg/h)	DHA extracted (kg)
5	6.10	3	120	600	39.78
10	5.82	3	120	1200	39.78
20	5.69	3	120	2400	39.78
40	5.62	3	120	4800	39.78

Tab. 26: SSR effects on sCO_2 extraction process.

with the same value of loaded microalgae and especially of extracted DHA. Furthermore, these considerations were related only to DHA; the extracted amount of the other components were found at the DHA saturation time. In our case a daily quantity of fatty acids equal to 147 kg can be extracted, corresponding to the 85% (Follegatti-romero et al., 2009) of their total amount inside the microalgae in that conditions (173 kg).
The composition of the extract and residue streams are summarized in Tab. 27; in particular the not extracted quantity, constituting the residue stream, is equal to 213.19 kg.

	Mass fraction
Component in the extract	
Palmitic acid	0.29
Oleic acid	0.31
EPA	0.13
DHA	0.27
Component in the residue	
Starch	0.29
Protein	0.35
Palmitic Acid	0.03
Oleic Acid	0.03
EPA	0.01
DHA	0.03
Lutein	0.14
Astaxanthin	0.12

Tab. 27: Extract and residue streams' characterization for the extraction conducted until the DHA saturation value.

3.7.3 Effects of the operative variables on the extraction yield

In Fig. 92 the simulated process in Aspen Plus is represented with the corresponding table that sums up the features of each stream; in particular for the first four streams the flow rate values, calculated for the pressurization of the sCO_2 for the make-up, are listed. It is visible that the CO_2 is first compressed with a multistage inter-refrigerated compressor to reach is liquid phase but only with the successive pump (PUMP: T = 37°C and P = 250 bar) and heater (HEATER-1: T = 60°C and P = 250 bar) its supercritical state is achieved; this passage is industrially preferred for the high cost and problems that occur with the gas compression. The supercritical pressure and temperature conditions reached by pump and heater, and also the SSR, are the results of the optimization phase described in the previous subparagraphs. Once reached the supercritical state, the sCO_2 is sent in the extractor where the microalga has been previously loaded and once finished the residence time in the extractor, the sCO_2 comes out from it and drags out the soluble component. The extract stream is then expanded in a valve, allowing to the sCO_2 to return in gaseous state; to ensure that, after the expansion the temperature is kept at the value that it had before the valve with the help of an heater (HEATER-2: T = 60°C and P = 47 bar). After that, this stream is sent in a separator where the components, that in these conditions are not soluble in the CO_2 anymore, are collected on the bottom of the separator while the CO_2 in the gaseous state comes out from the top. This CO_2 is then recycled and reaches the liquid state by a cooler (COOLER-2: T = 10°C and P = 47 bar). This procedure has to be repeated, during each cycle, until the saturation value of the rate determining component (DHA) is reached.

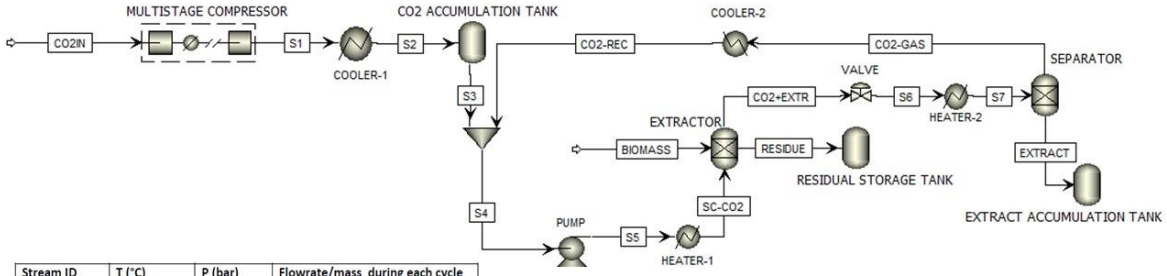

Stream ID	T (°C)	P (bar)	Flowrate/mass during each cycle
CO2IN	25	1	600 kg/h (100 kg/h p for make-up)
S1	115	47	600 kg/h (100 kg/h p for make-up)
S2	10	47	600 kg/h (100 kg/h p for make-up)
S3	10	47	600 kg/h (100 kg/h p for make-up)
S4	10	47	600 kg/h
S5	35	250	600 kg/h
S6	27	47	600 kg/h
S7	60	47	600 kg/h
SC-CO2	60	250	600 kg/h
BIOMASS	25	1	120 kg
RESIDUE	25 (storage)	1 (storage)	71 kg
CO2+EXTRACT	60	250	600 kg/h
EXTRACT	25 (storage)	1 (storage)	49 kg
CO2-GAS	27	47	600 kg/h
CO2-REC	10	47	600 kg/h

Fig. 92: Process scheme with relative mass balance.

The Table present in Fig. 92 is added in order to give informations about the amount of microalgal treated and sCO_2 used during each day of working pilot. The daily process is divided in 3 cycles and in each cycle 120 kg of dry biomass is treated with 600 kg/h of sCO_2 (SSR= $5h^{-1}$). During each cycle the sCO_2 passes continuously through the basket, in

which the dried algae are positioned, and is continuously recycled in its closed loop until the saturation time is reached (about 6 hours). During each cycle the extracted lipids are accumulated in the EXTRACT ACCUMULATION TANK and the residuals remain inside the microalgal matrix. At the end of each cycle it is necessary to depressurize the system in order to offload the residual biomass in the extractor's basket, closing the valve before and after the extractor and opening the extractor, losing thus the sCO_2 contained inside (100 kg for each cycle) that has to be add back at the beginning of each cycle as make-up (100 kg/h as indicated in the modified table in S1, S2 and S3), in order to keep the stream S4 always at 600 kg/h. Indeed, as previously said, sCO_2 extraction works in batch mode and in particular in a closed cycle, except at start-up. These CO_2 of make-up will be accumulated in a refrigerated tank (CO2ACCUMULATION TANK)
placed immediately after the cooler (COOLER-1: T = 10°C and P = 47 bar). At the end of each cycle, during the depressurization phase, the residual biomass is removed from the extractor and placed in a storage tank (RESIDUAL STORAGE TANK) and by opening the shut-off valve located under the separator, the oil precipitates inside an accumulation tank (EXTRACT ACCUMULATION TANK).

3.7.4 Cost analysis

As said in the previous paragraph 2.5, the simulation of the process is necessary to calculate the energy and utilities consumption that, coupled with the design of each equipment, provides tomake an estimation of Operating Expense (OPEX) and Capital Expenditure (CAPEX) that are resumed in this paragraph. For CAPEX evaluation, Direct Costs and Indirect Costs have to be estimated and summed up. Each equipment was designed following our internal procedures and classical engineering equations (Peters et al., 2003).

Direct cost item	Cost (k€)	Indirect cost item	Cost (k€)
Equipments	659.7	Engineering	211.1
Installation	257.3		
Instrumentation	171.5	Construction costs	224.3
Piping	204.5		
Electric systems	65.9	Contractor payment	125.4
Civil works	191.3		
Facilities	362.8	Contingencies	244.1
TOTAL DIRECT COSTS	**1913**	**TOTAL INDIRECT COSTS**	**804.9**
Total CAPEX = Direct Costs + Indirect Costs = 2717.9 k€			

Tab. 28: Total CAPEX of the sCO_2 extraction process.

In particular for vessels, after having calculated the thickness (and therefore the mass) of steel needed for both shell and plates, their costs were evaluated multiplying the weight of the equipment by the unit cost of the material used found in the reference book (Peters et al., 2003). Furthermore, for the most peculiar equipments, as the sCO_2 extractor skid, their cost were estimated from contacts with suppliers. In Tab. 28 the CAPEX of the process is resumed, the other items besides the Equipments were estimated as percentual of the Equipment cost (including freight costs), multiplying each voice for its specific index (or Peters-Timmerhaus Factors (Peters et al., 2003)). In order to estimate OPEX, it was necessary to know the utilities' consumption based on the energy values obtained from the process simulation.

Utility	**Estimated consumption**	**Calculated cost (k€/year)**
Low pressure steam	426.8 (ton/y)	9.5
Cooling water	238.9 (ton/y)	0.003
Chilled water	24617.4 (ton/y)	3.8
Electric energy	43.5 (MWh/y)	2.1
CO_2	109.5 (ton/y)	2.7
TOTAL UTILITIES COSTS		**18.1**
Manpower + Maintenance = 271.8 + 271.8 = 543.6 k€/year		
TOTAL OPEX = Utilities + Manpower + Maintenance = 561.7 k€ /year		

Tab. 29: Utilities' consumption and TOTAL OPEX value for a 7200 h sCO_2 extraction running plant.

Furthermore, knowing the unit costs for each utility, their total cost can be calculated and is reported in Tab. 29. In particular, even if it is not properly an utility, the make-up CO_2 needed to compensate the losses during each cycle, representing an annual cost, is listed in Tab. 29. Considering a CO_2 with 99% purity, its price was estimated (by internal database) to be 0.03 €/kg. The OPEX of the process is showed in Tab. 29, adding to the Total Utilities' Cost two other important items (Manpower and Maintenance) assumed both as 10% of the total CAPEX (271.8 k€/year). The values obtained in Tab. 28 and Tab. 29 give an overview on the costs that the sCO_2 extraction process may require, without considering any integration to another existing plant that may reduce the OPEX (thermal integration, etc.). Furthermore, considering 3 cycles per day with a daily treated biomass equal to 360 kg, the annual (7200 h of running pilot) biomass amout is equal to 108 ton. With this amount it is possible to calculate the **Total Treatment Cost** (TTC= OPEX+CAPEX per kg of treated algal biomass) **equal to 30.36 €/kg**. However these values are preliminary, indeed this part of the thesis' work is focused only on the modeling and optimization of the extraction process, even if they show good financial perspective due to the high market

price of the extracted metabolites. Indeed, the described extraction would be only a part of a larger process that aims to purify the desired extracted products in order to place them on the market as pure components or in mixture (see also paragraph 3.8). In addition to OPEX and CAPEX also a ROI value of the production process would give more accurate informations about the investment's feasibility, but to do that the product's sell price and with it the purification's grade of the metabolites, are required.

3.8 Molecular distillation simulation results

In this paragraph, the results obtained from the simulation of the molecular distillation process, both in technical and economical point of view are resumed and discussed.

3.8.1 Preliminary treatment of the inlet stream

Before showing the results obtained for the molecular distillation purification process, an introduction on the pre-treatments carried out to the stream before the esterification reaction is briefly described here.

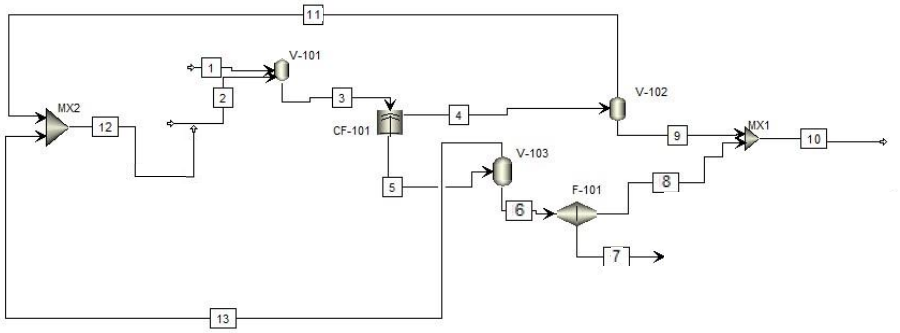

Fig. 93: Process scheme of the pretreatment done on the inlet stream before the esterification

The first operation concerns the extraction of the lipid phase (consisting of fatty acids and carotenoids, residues of the treatment with sCO_2) from the solid fraction consisting of the spent biomass and the starch contained in it in the form of granules (Stream 1). This extraction process is carried out through the use of a polar solvent, ethanol (Stream 2), in a mixture with water (ethanol/water ratio=4:1 by weight) in an agitated tank (V-101 of Fig. 93). The choice of ethanol at this stage of the process is due to the fact that this solvent is subsequently used in the esterification reaction before the molecular distiller. It is well known that the mixture water-ethanol brings to formation of azeotrope with a 95% percentage by volume of ethanol at a temperature of T=78°C and P= 1 bar. This problem is overcome, because the process is carried out at a lower temperature, equal to T=60 °C, and a lower percentage of ethanol (75% v/v). The operating temperature of 60°C is chosen as a precautionary value to avoid structural changes in the starch granule. The liquid/solid ratio (L:S in mass) was determined by literature studies. For biomass not previously treated, a typical value used is 15:1 (Tsibranska et al., 2011) while for ultrasonic or microwave-assisted extractions (to optimize the breaking of the cell wall) typical values of the ratio are 6:1 or 5:1 (Davis et al., 2013; Sepidar et al., 2011).

Since the residue to be treated has already undergone a step of cell wall breaking, it was decided to use an L:S ratio of 6:1, which is equivalent to the use of 1320 kg of solvent. The calculation of the residence time of the biomass-solvent mixture within V-101 was made using a mathematical report from literature (Chan et al., 2014).

$$\ln\left(\frac{C_\infty}{C_\infty - C}\right) = 0.498 + 9.87\frac{D * t}{R^2} \qquad \text{(Eq. 62)}$$

Where:

- C_∞[g L^{-1}] is the solute concentration in the solvent after an infinite time
- C [g L^{-1}] is the solute concentration in the solvent at time t
- t [s] is the extraction time
- D [m^2 s^{-1}] is the solute diffusion coefficient in the solvent
- R [m] is the radius of microalgae considered spherical

The Eq. 62 comes from a simplification of the mass balance in solid particles, in which the resistance to external mass transfer of solvent is neglected, simplifying thus the mathematical treatment of the extraction.
The extraction yield to be reached was fixed at 98% in order to recover most of the fatty acids and carotenoids trapped in the microalgal matrix. With this specification and knowing that R= 5*10^{-6} m and D=1.5*10^{-12} m^2 s^{-1}, an extraction time of about 360 min (6 h) was obtained.
Fig. 94 shows the extraction time [min] necessary to reach the concentration [g L^{-1}] at which the chosen yield is obtained.

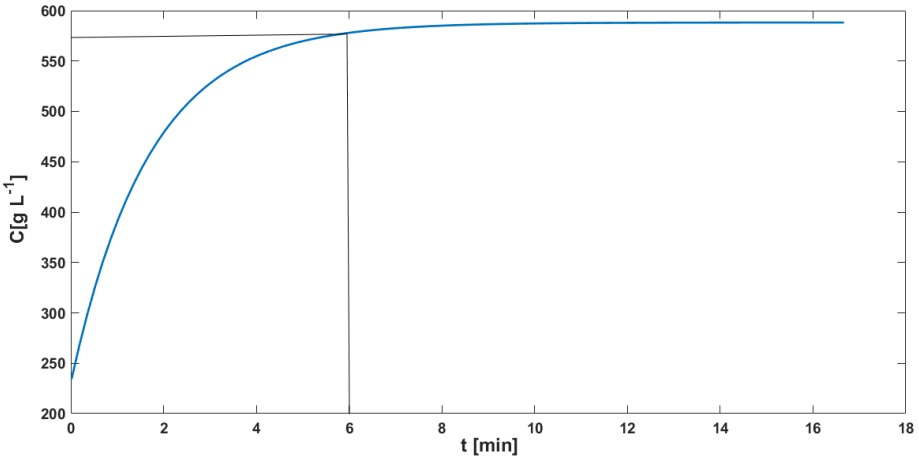

Fig. 94: Trend of the extract concentration versus time

Once the lipidic phase is extracted from the microalgal matrix, the separation between the liquid and the solid phase is realized through the use of a disk centrifuge CF-101. It separates the oily phase, containing most of the solvent, from the solid phase, consisting of the exhausted biomass, the starch and traces of oil and solvent. The oily stream (Stream 4) will go to a later stage where the solvent will be separated from the oil with a flash; while the solid phase (Stream 5) will continue the process not until having separated the solid from traces of oils in the filter F-101. In particular the oily phase stream sent to the purification with molecular distillation is the Stream 10, formed by the sum of extracted oil (carotenoids and traces of fatty acids) collected in both Stream 8 and Stream 9. The

residual biomass containing starch and protein will be sent to further treatments (Stream 7) and the solvent separated in both flashes (V-102 and V-103) is recirculated in the process (Stream 12).

3.8.2 Sizing of CSTR reactor

The sizing of the CSTR reactor was made by integrating Eq. 36 and through a Trial and Error process the optimal compromise between the volume of the reactor and the conversion of oleic acid was found. Through the integration it is possible to know that a volume greater than 3 m^3 does not lead to significant improvements in terms of conversion, as shown in Fig. 95 where the volumes needed to reach a specified conversion are reported. With a volume increase of 7 m^3 and 10 m^3 only a slightly increase of the conversion is reached, obtaining X_{OL} = 0.978 and X_{OL} = 0.982 respectively. Indeed, an increase of 0.012 (from 3 m^3 to 10 m^3) doesn't justify the more than threefold volume increase, involving thus higher Equipment Costs (at least more than twice) and with them higher CAPEX (see subparagraph 3.8.6). For this reasons the CSTR reactor's volume is set to 3 m^3 and, under these conditions, a conversion of about 97% is obtained (at about 15 h), as can be seen from the kinetics shown in Fig. 96.

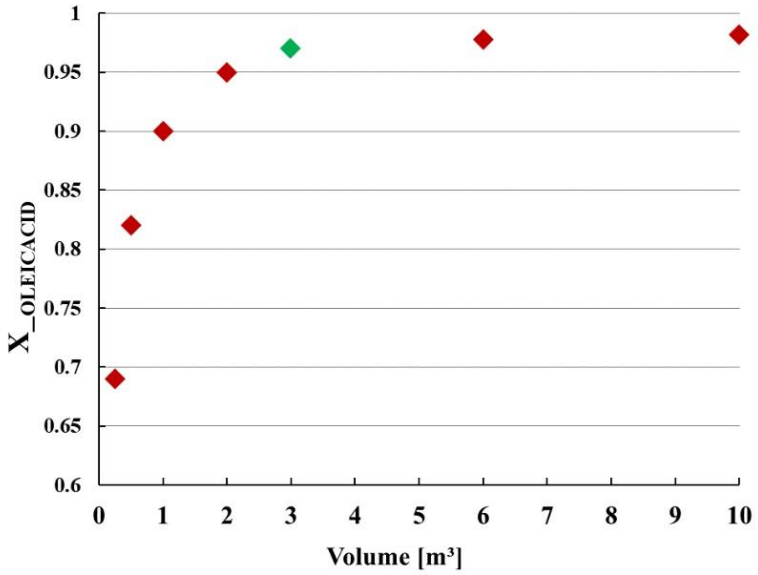

Fig. 95: Oleic acid conversion ($X_{OLEIC\ ACID}$) profile with increased reactor volume.

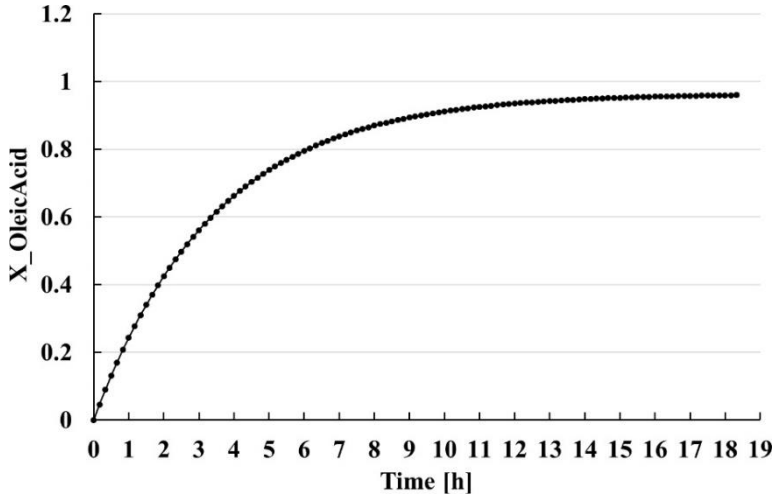

Fig. 96: Oleic acid conversion ($X_{OLEIC\ ACID}$) profile with increased reaction time.

3.8.3 Sizing of water adsorption column

As second step, the sizing of the water adsorption column is made by integration of the Eq. 45. The optimization criterion of minimizing the size of the asdsorption column, allowing also the possibility of working continuously has been described in subparagraph 2.6.3. Regarding the cooling time, a literature value was considered, depending on the regeneration temperature; assuming that this temperature is equal to 200 °C, the cooling time is equal to 1 h (Gabruś et al., 2015). At this point, the optimal dimensions of the water adsorption column calculated are: Length = 1 m and Radius = 0.2. With these dimensions the saturation time of the adsorption column is approximately equal to 4.5 h as shown in Fig. 97, where the water concentration profile over time at the column's outlet section is plotted. The regeneration time is approximately equal to 2.5 h, as shown in Fig. 98 that shows the relationship between the water concentration in the solid phase over the time during the regeneration process. It can be seen, with the dimensions reported and with the sum of cooling time and regeneration time equal to 3.5 h (while the saturation time is equal to 4.5 h), that the system made by two adsorption columns in parallel is able to operate continuously.

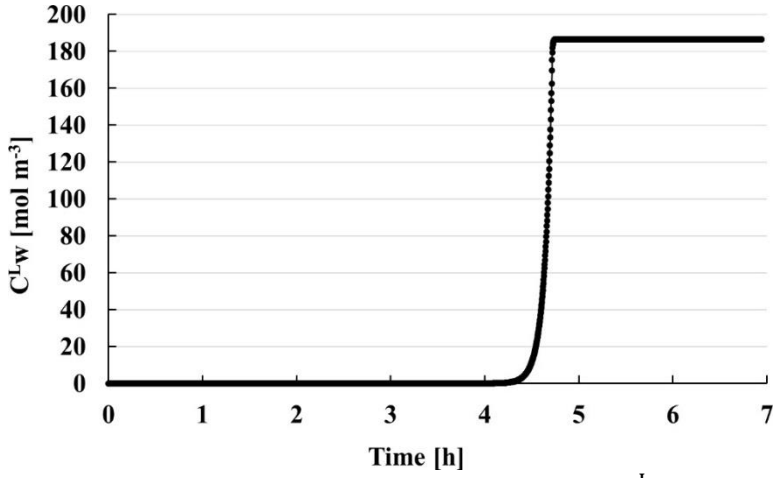

Fig. 97: Concentration profile over the time of water in the liquid phase (C_W^L (mol m^{-3})) at the adsorption column output.

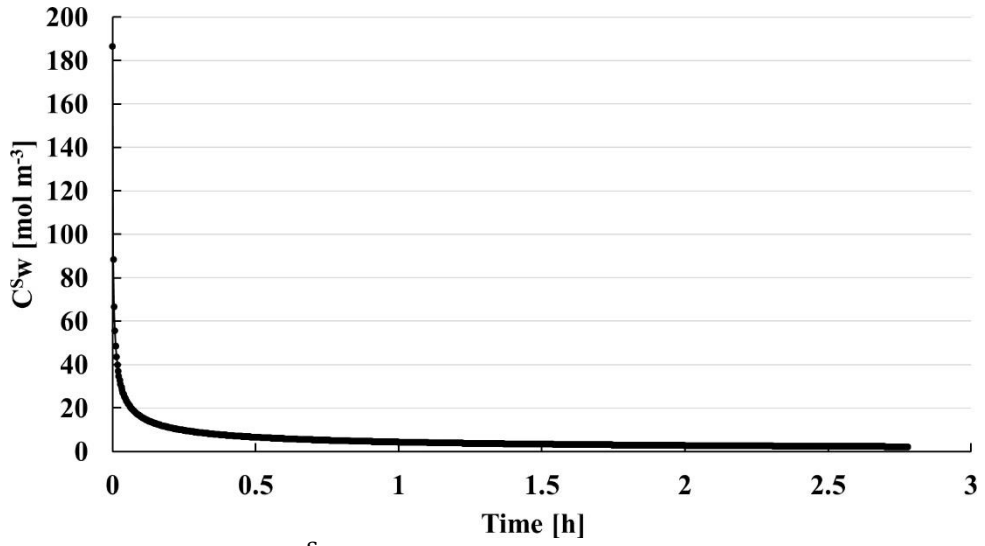

Fig. 98: Water concentration (C^S_W (mol m^{-3})) in the zeolite solid phase over the time during the regeneration process.

3.8.4 Results of RSM analysis

As already mentioned, an RSM analysis was carried out in order to identify the optimal operating conditions to use in the molecular distiller. In order to implement the analysis, N simulations in Aspen Plus were conducted at the operating temperature and pressure conditions (different from the optimal one) reported in Tab. 16. The values of the answers are shown in Tab. 30. Once obtained the y values, it was possible to calculate the regression coefficients bi of both y1 and y2 responses visible in Tab. 31. By implementing the optimization process described in Section 2.4, it was possible to find the optimal operating conditions of temperature and pressure that are: T = 128 °C and P = 0.33 Pa.

Run	X_1	X_2	T [°C]	P [Pa]	y_1	y_2
1	0	0	105	0.55	0.999	0.879
2	0	0	105	0.55	0.999	0.879
3	1	0	150	0.55	0.952	0.993
4	0	1	105	1	0.999	0.812
5	-1	0	60	0.55	0.999	0.606
6	0	-1	105	0.1	0.994	0.973
7	0.71	0.71	137	0.87	0.989	0.977
8	0.71	-0.71	137	0.23	0.959	0.993
9	-0.71	0.71	73.2	0.87	0.999	0.606
10	-0.71	-0.71	73.2	0.23	0.999	0.638

Tab. 30: Answers (y_1, y_2) obtained from the N = 10 simulations in Aspen with the operating conditions as codified variables (X_1, X_2) shown in Tab. 16.

	y_1	y_2
Coefficient β_i	**Value**	**Value**
β_0	0.999	0.878
β_1	-0.021	0.225
β_2	$6.83* 10^{-3}$	-0.049
β_3	-0.023	-0.101
β_4	-0.002	-0.007
β_5	0.015	$7.51*10^{-3}$

Tab. 31: Regression coefficients (b_i) for both y_1 and y_2 responses.

After having obtained the optimal operating conditions for the molecular distiller, the values of the responses deriving from the simulations in Aspen Plus (y_1=0.987 and y_2= 0.983) and from the model (y_1' = 0.975 and y_2' = 0.987) were compared, showing a percentage errors less than 1.5% (δ_1 = 1.2 and δ_1 = 0.4) and affirming the validity and relevance of the model generated by the simulative reality. The RSM analysis also allows to represent graphically the dependence of the responses from the natural variables with the help of response surfaces plots and contour plots. Fig. 99 represents the response surface and the contour plot of the y_1 response; it can be seen that the maximum response (mass fraction of carotenoids in residue stream) occurs at high temperature at minimum pressure. In these conditions, indeed, the lighter components pass completely into the distilled stream with also a little part of the heavier which would diminish its purity.

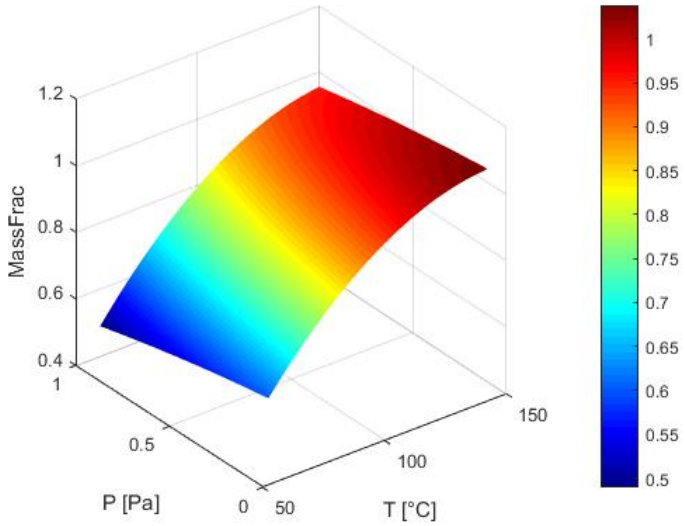

Fig. 99: Response surface of y_1 response showing the dependence of the carotenoids' mass frac in the residue stream from the temperature and pressure of the molecular distiller.

Thereby, the residue current is practically pure in carotenoids in terms of mass fraction but their recovery is not at its maximum value due to the transfer of a little aliquote of them into the distilled. In Fig. 100 is visible that the influence of the pressure is lower than the temperature one, but there is anyway an improvement in the response with a pressure decrease, increasing more and more the vaporization rate of the lighter components.

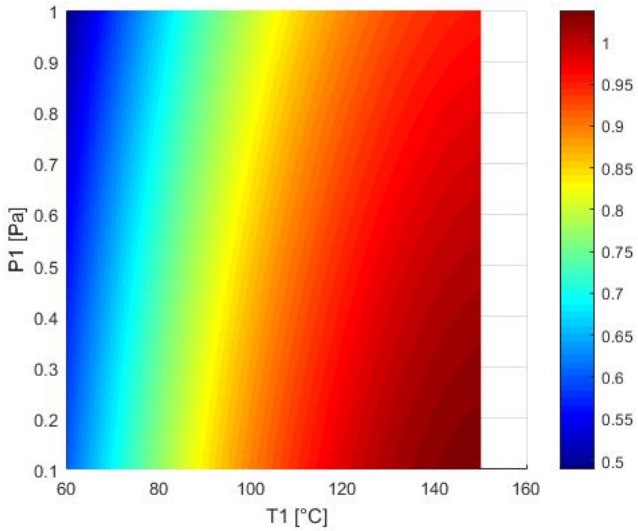

Fig. 100: Contour plot of y_1 response showing the dependence of the carotenoids' mass frac in the residue stream from the temperature and pressure of the molecular distiller.

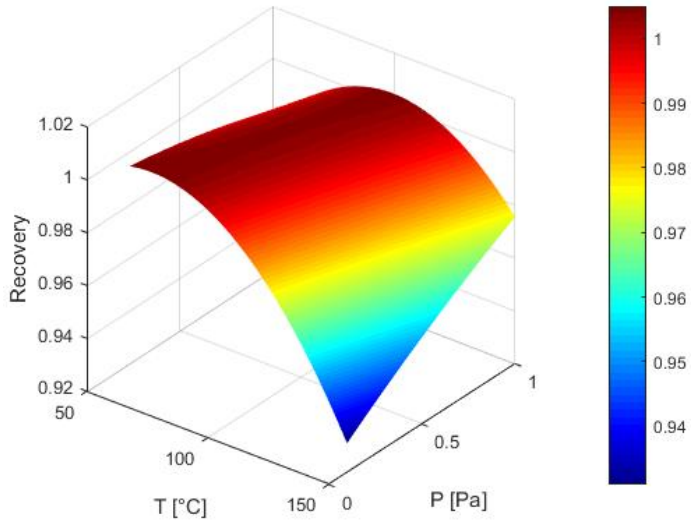

Fig. 101: Response surface of y_2 response showing the dependence of carotenoids' recovery in the residue from the temperature and pressure of the molecular distiller.

The same plots are visible in Fig. 101 and Fig. 102 for the y_2 response. For the opposite reasons of y_1 response, the maximum value of the y_2 response (carotenoids' recovery in the residue stream) occurs at low temperature; in these conditions indeed, the fraction of carotenoids that passes into the distilled stream is minimal, so the entire inlet flow of carotenoids remains in the residue stream.

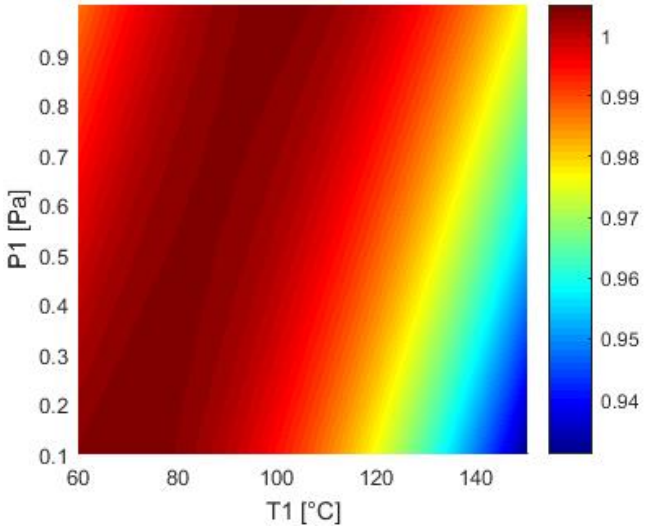

Fig. 102: Contour plot of y_2 response showing the dependence of carotenoids' recovery in the residue from the temperature and pressure of the molecular distiller.

Also in this case the influence of the pressure is lower than the temperature but there is anyway an improvement in the response with a pressure increase, lowering further the carotenoids' vaporization rate. As resulted in both figures, the responses reached their maximum values for diametrically opposite conditions; obviously neither of the two pairs of operating conditions represent an optimal solution for the process. The optimization indeed provides a compromise in maximizing the responses y_1 and y_2, as evidenced by the objective function previously defined in the Eq. 60. At these optimized conditions, the outlet distilled stream is composed mainly by the esterified fatty acids (95% in mass) and by a little fraction (4% in mass) of unesterified fatty acids; on the contrary, the residue stream is composed mainly by carotenoids (98.8% in mass).

3.8.5 Process simulation

In Fig. 103 the simulated process, with the optimized conditions previously defined, is reported with the summary of each stream. In particular the esterification reactor (CSTR) was simulated using RSTOIC model and the output stream is sent to the flash separator (FLASH) where the ethanol + water vapours are treated, after compression, with the adsorption's column (SEP) that separates water from ethanol. Ethanol is recirculated and reused in the reactor and also a MAKE-UP for the reintegration of its losses is considered in the process. For the simulation of the molecular distillation in Aspen a flash vessel was used (MD1), as specified in the previous paragraphs. Furthermore since for passing from 0.01 atm (S18) to 1 atm (S13) (with a pressure ratio of 100) is necessary a multistage inter-refrigerated compressor, in the simulation a series of 5 compressors with 5 condensers were used to represent this equipment. As said previously, this simulation is necessary to calculate the energy and utilities consumption that, coupled with the design of each equipment, provides to make an estimation of Operating Expense (OPEX) and Capital Expenditure (CAPEX) that are reassumed in the next subparagraph.

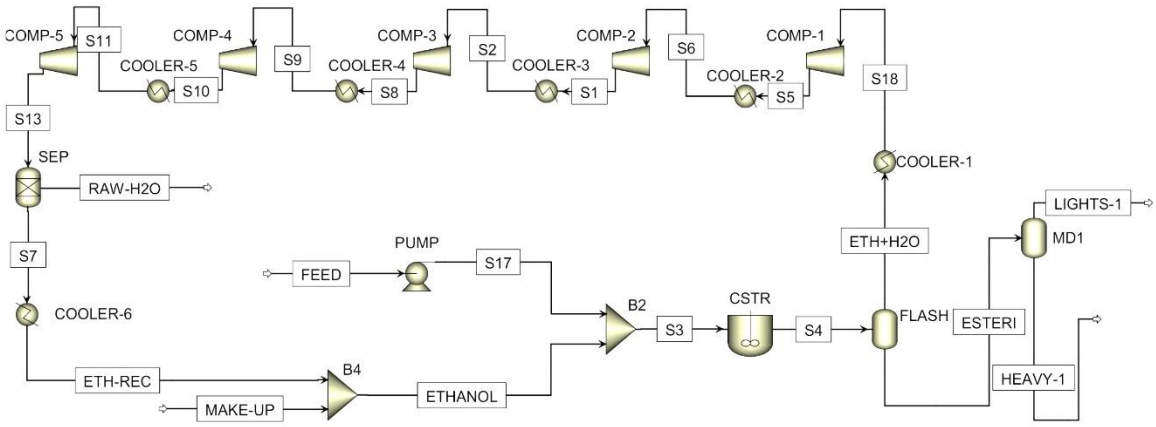

Stream Name	Units	ESTERI	ETH+H2O	ETH-REC	ETHANOL	FEED	HEAVY-1	LIGHTS-1	MAKE-UP	RAW-H2O	S1	S2	
Temperature	°C	80	80	25	25	60	128	128	25	124.6	130	80	
Pressure	bar	0.01	0.01	1	1	0.2	3.3E-06	3.3E-06	1	1	0.065	0.065	
Mass Flows	kg/hr	5.235	19.77	19.5	20.015	5	1.964	3.271	0.479	0.27	19.77	19.77	
Stream Name	Units	S3	S4	S5	S6	S7	S8	S9	S10	S11	S17	S18	S13
Temperature	°C	28.98	60	130	80	125	130	80	130	80	60	80	124.6
Pressure	bar	1	1	0.025	0.025	1	0.17	0.17	0.43	0.43	1	0.01	1
Mass Flows	kg/hr	25.015	25.015	19.77	19.77	19.5	19.77	19.77	19.77	19.77	5	19.77	19.77

Fig. 103: Simulated process scheme with relative streams' summary.

3.8.6 Cost analysis

As has been done for sCO_2 extraction process, also for molecular distillation an estimation of the Operating Expense (OPEX) and Capital Expenditure (CAPEX), using the results of the simulations in terms of energy and utilities' consumption, was done. For CAPEX evaluation, Direct Costs and Indirect Costs have to be estimated and summed up. In particular, after having designed each equipment, following our internal procedures and classical engineering equations (Peters et al., 2003), the Equipment costs (as subset of Direct Costs) were estimated. For the cost calculation of the more standardized equipment (heat exchangers, reactor, pumps, compressors, vessels, etc.) the estimation graphs present in the reference book were used. Indeed, the cost of an heat exchanger was estimated by calculating the required exchange surface and finding inside of the corresponding chart its cost related to the specific material used. This cost was then multiplied by a factor, provided directly in the graph, according to the operating pressure conditions of the exchanger. The same procedure was used for the other equipments; in particular for the adsorption column its cost consists in two contribution: the cost of external shell (as kg of steel), found with the described procedure, and the cost of adsorbent solid (as kg of zeolite 3Å), found by internal database. Lastly, for the most peculiar equipment as the molecular distiller, its cost was estimated from contacts with suppliers. The other costs of CAPEX were estimated as percentual of the Equipment cost (including freight costs), multiplying each voice for its specific index (or Peters-Timmerhaus Factors). On the other hand for OPEX estimation it was necessary to know the utilities' consumption based on the values obtained from the process simulation. Furthermore, knowing the unit cost (Peters et al.,

2003) of each utility, their total cost can be calculated by multiplying it by their consumption. The OPEX value was then calculated adding to the Total Utilities' Cost two other important items (Manpower and Maintenance) assumed both as 10% of the total CAPEX. In Tab. 32 the calculated CAPEX of the process is shown.

Direct cost item	Cost (k€)	Indirect cost item	Cost (k€)
Equipments	451.4	Engineering	163.8
Installation	233.3		
Instrumentation	178.7	Construction costs	203.5
Piping	337.6		
Electric systems	54.6	Contractor payment	109.2
Civil works	89.4		
Facilities	347.5	Contingencies	218.4
TOTAL DIRECT COSTS	**1692.5**	**TOTAL INDIRECT COSTS**	**694.9**
Total CAPEX = Direct Costs + Indirect Costs = 2387.4 k€			

Tab. 32: CAPEX of the molecular distillation process.

Moreover, in Tab. 33 the process OPEX is shown, considering the consumption of each utility for a 7200 h running plant and adding to the Total Utilities' Cost also the costs of Manpower and Maintenance equal to 10% of the total CAPEX (238.74 k€/year). In particular, even if it is not properly an utility, the ethanol for make-up, needed to compensate the losses during each cycle and representing an annual cost, is listed.

Utility	Estimated consumption	Calculated cost (k€/year)
Low pressure steam	87.4 (ton/y)	1.9
Cooling water	2581.6 (ton/y)	0.003
Electric energy	368.5 (MWh/y)	17.8
Ethanol	1.1 (ton/y)	0.9
TOTAL UTILITIES COSTS		**20.63**
Manpower + Maintenance = 238.8 + 238.8 = 477.6 k€/year		
TOTAL OPEX = Utilities + Manpower + Maintenance = 498.23k€/year		

Tab. 33: Utilities' consumption and OPEX value for a 7200 h molecular distillation running plant.

Considering a ethanol with 95% purity, its price was estimated (by internal database) to be 0.76 €/kg. The values obtained in Tab. 32 and Tab. 33 give an overview of the costs

estimated for the designed purification process with molecular distillation. Furthermore, considering the daily treated biomass with sCO_2 equal to 360 kg, the annual (7200 h of running pilot) biomass amout is equal to 108 ton. With this amount it is possible to calculate the **Total Treatment Cost** (TTC= OPEX+CAPEX per kg of treated algal biomass) **equal to 26.72 €/kg**. Notably, further purifications of the omega-3 part of the distilled stream (both in their esterified or unesterified form) are not taken into account because of the possibility to place them directly on the market as mixture and not as pure components; the same considerations have been done for carotenoids. The price of these mixtures, that is very difficult to find because strictly bounded to the composition obtained in this work, would have led to a more accurate economic analysis with a ROI value. Anyhow, this technology is very promising for its fractionation efficiency of heat-labile compounds that have good financial perspective due to their high market price. Indeed, even if it requires several technical attentions for the high vacuum used, the high-added value of the separated molecules makes it an appropriate solution to be combined also with microalgal cultivation and metabolites' extraction in order to realize a complete process.

3.9 MEWLIFE results

3.9.1 Fermenters' design

In this subparagraph the considerations used to design the fermenters, with the corresponding results, are resumed. The first consideration that have to be done and that is bound to all the specifications described below, consists in not having used the classical engineering design equations and definitions due to the presence of several constraints. The main constraint was the dedicated space for pilot installation, having as available heigth max 3.5 m. This 3.8 m had to include the fermentor (planking and heads), its raising from the floor with legs permitting bottom piping connection and the motor group for mixing positioned at its top head. Considering a space of 0.5 m for the raising with legs, 0.5 m for motor group and 0.5 m for motor's maintainance at top head, the residual available height for fermenters' positioning is 2.3 m (H_F). The other important constraint was the volume declared in the project: 3 m^3 of operative volume for each reactor. These two constraint brought to a completely different design from classical fermentors, having a H/D ratio of about 2.5-3. Indeed, after an iterative calculation the internal diameter chosen (D_t) is equal to 1.6 m; adding to that the contribution of the jacket, an external diameter D_e = 1.71 m is obtained. In order to reach the volume declared, it was necessary to design also the bottom heads. Usually the volume present in the bottom head is not considered in the calculation of the operative volume, taking into consideration only the volume between the tangent lines. For the calculation of the head's volume, a spreadsheet in Excel was implemented and is reported in Fig. 104.

Heads' volume calculations			
Reference:	http://www.conrexsteel.com/calculator.php		
Type:	Flanged and Dished Head (F&D)	(< 10 bar)	
Fixed parameters:		inches	mm
	Inside Diameter (ID):	63	1600
	Thickness (T):	0.4	10
	Dished Radius (DR):	63	1600
	Inside Corner Radius (ICR):	6.3	160
	Straight Flange (SF):	1	25
Parameters Obtained:		inches	mm
	Inside Dished Depth (IDD):	12.2	310
	Overall Height (OAH):	13.6	350
	Weight (M_OAH):	476 Pound	216 kg
	Volume:	118US gal	0.45 m3

Fig. 104: Excel spreadsheet developed to estimate the bottom head volume in order to reach an operative volume of 3 m^3 inside each fermenter.

It can be seen that, since the fermentors will be operated at atmospheric pressure, a "Flanged and Dished" is adequate (see Fig. 105).

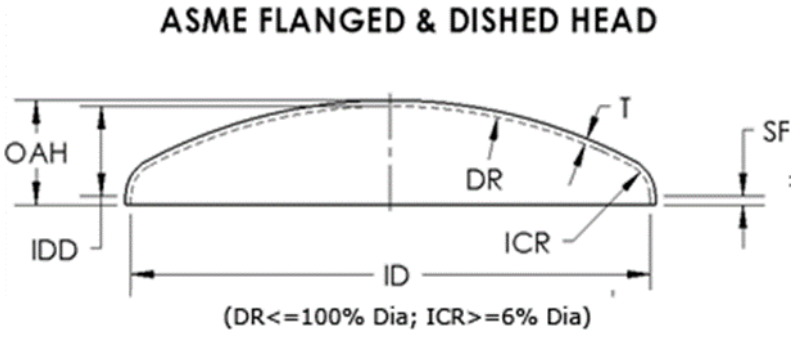

Fig. 105: Flanged and Dished head schematization (http://www.conrexsteel.com/calculator.php).

The volume obtained, after an iterative procedure, is 0.45 m^3 in each bottom head. As a check the operative liquid volume was calculated. Knowing the available fermenter's height equal to H_F=2.3 m and knowing the Overall Height (OAH) for both heads = 2*0.35=0.7 m the cylinder planked height H_C=1.6 m is obtained. Furthermore, knowing the total liquid volume (V_{TOT}) equal to 3.66 m^3, as sum of cylynder planked volume and bottom head volume, the operative volume V_{OP} = 3 m^3 is equal to 0.8*V_{TOT}; this value is acceptable. In Fig. 106 the picture of the fermentors, designed by Bio-P and modified and revised by NextChem and present in the Data-Sheet (DS) sent to vendors, are visible. Along with the dimensions, also the indication of all the required nozzles are reported in Fig. 107 and their position is specified in Fig. 108.

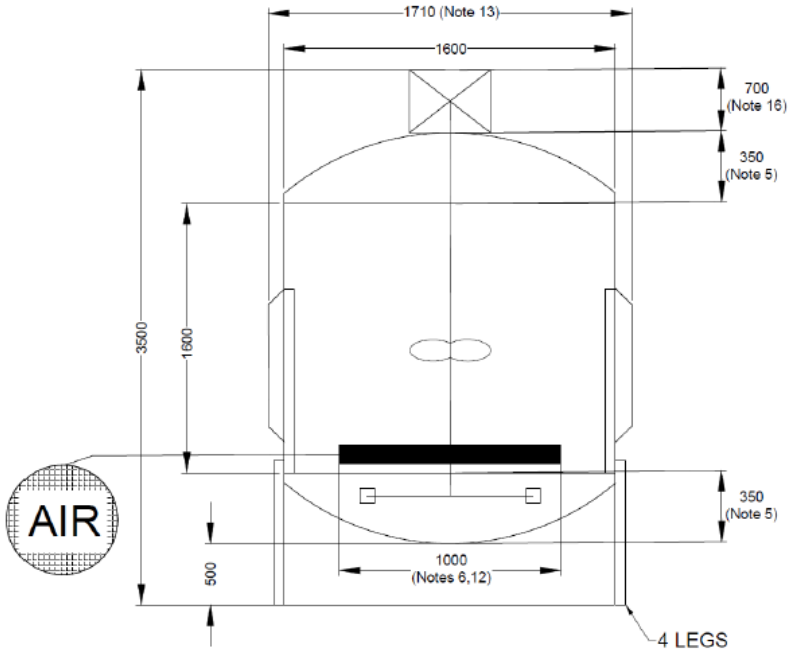

Fig. 106: Fermentor schematization with the relative dimensions.

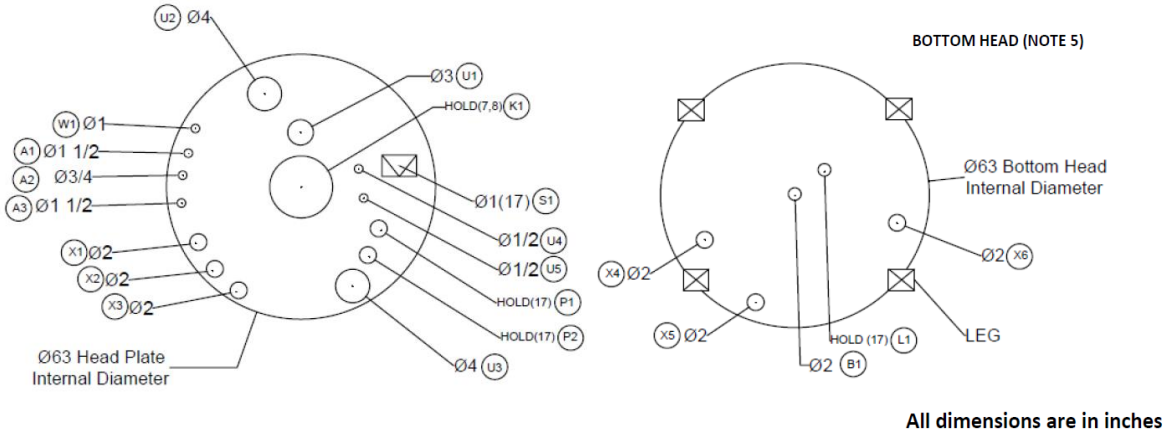

Fig. 107: Fermentor schematization with the nozzles and levels indication.

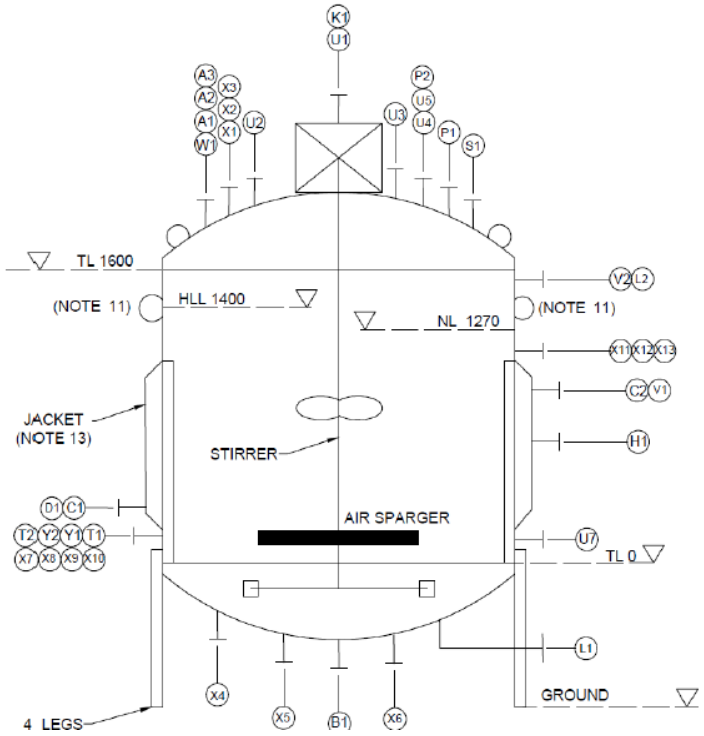

Fig. 108: Bottom and top head nozzles' positioning.

Besides the fermenters, also the internals and the mixing devices were designed. Concerning the baffles (3 baffles are used), considering the ratio usually applied between the baffle diameter (D_b) and the fermentor internal diameter (D_t) equal to 0.09, a D_b = 0.15 m is obtained. Furthermore, also the air sparger was designed and included in fermenters' DS. In order to guarantee the bubbles' rise, the number of holes (N_H) have to be calculated in a way that the holed surface (S_H) is less than the inlet air surface (S_I). In order to guaratee this, it is obtained $N_H < 46$, so N_H=35 is fixed. The diameter of each hole was fixed at 6 mm as compromise between high pressure loss and high bubbles' dimension.

The designed sparger is visible in Fig. 109.

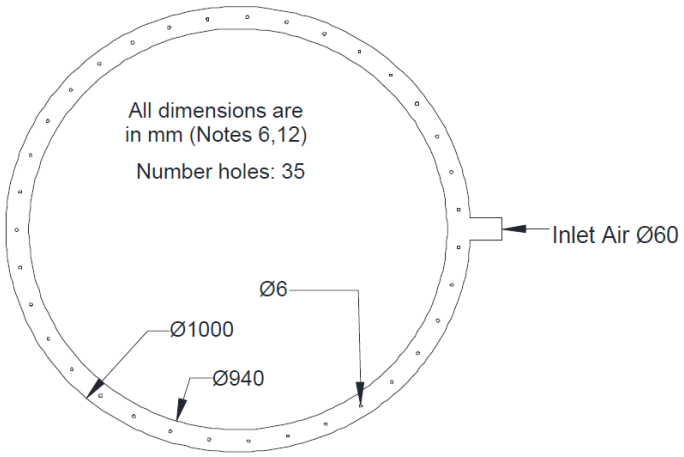

Fig. 109: Sparger schematization with relative dimensions.

As last consideration, the mixing device is described. Differently from typical fermentation process, the configuration and the position of the impellers were designed in order to avoid operative problems occurring in microalgal cultivation. Indeed, usually the impeller is positioned immediately above the sparger, maximazing thus the oxygen dispersion inside the culture medium. In this case, due to the stubby fermentor' configuration, a rushton impeller was positioned below the sparger and near the bottom head in order to avoid any microalgal deposit in the bottom, guaranteeing thus a complete and uniform mixing. The dimension of these impellers were furnished by specialized vendors, able to define the best solution to use.
In conclusion of this section some pictures available to date, showing the designed fermenters just positioned in the Bio-P/Nextchem site, are reported below.

Fig. 110: Detail of the fermenter's sparger designed for the aeration.

In Fig. 110 the detail of the sparger designed and discussed before is reported. It is visible that it is positioned near the bottom head, avoiding any possible microalgal deposit on the bottom. The holes (with a diameter of 6 mm) are not visible because are faced down in order to avoid clogging problems.

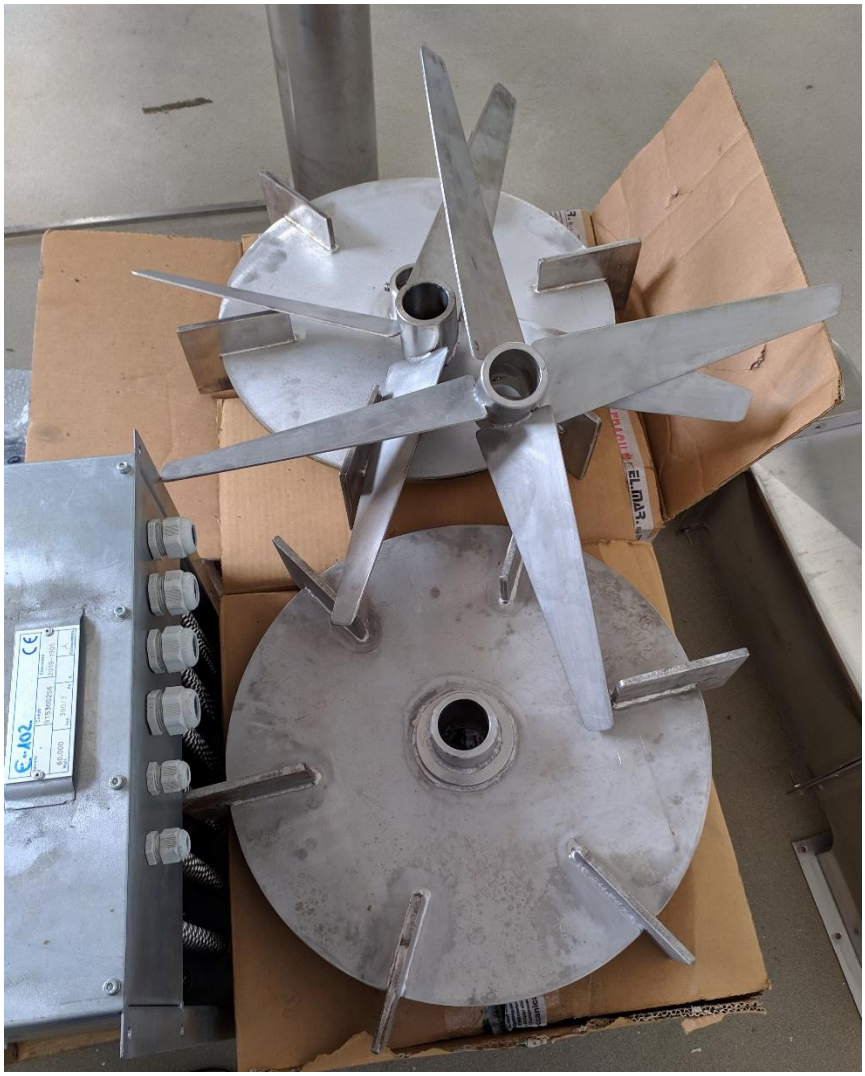

Fig. 111: Detail of the fermenter's impellers designed for colture mixing.

In Fig. 111 the details of the mixing impellers are shown. As anticipated before, the Rushton turbine will positioned under the sparger in order to guarantee a proper mixing in the fermenters' bottom. On the other side, the axial 4 blades hydrofoil impeller will be positioned at the middle of the fermenter's height in order to provide the proper fluidynamic of the microalgal solution.

Fig. 112: Detail of the manufactured fermenter during its development inside the vendor's workshop.

Fig. 113: Fermenter's positioning inside the space dedicated to the indoor pilot plant.

Fig. 114: Detail of the manufactured fermenter designed ad hoc for microalgal heterotrophic cultivation positioned inside the space dedicated to the indoor pilot plant.

In Fig. 112-114 the details of the designed and manufactured fermenters are shown. As previously anticipated, their dimensions and ratio (H/D) doesn't correspond to the typical fermenters configuration due to the constraints described before. In particular, the required noozles (indicated in Fig. 107 and Fig. 108) with their corresponding positions can be seen. It is present also the manhole for the inspection and future cleaning and maintainance. Furthermore, the motor groups are not visible because have to be still installed.

Conclusions

In the present work a study aimed to analyze and model both microalgal growth and production of high added-value metabolites, focusing also on their extraction and purification, has been carried out.

- As regard the outdoor cultivation: a 10 bubble column photobioreactors (PBRs) pilot plant for the cultivation of two microalgae named *Tetradesmus obliquus* and *Graesiella emersonii,* covering a 9 months cultivation period (March 2017-December 2017) has been installed and operated. A preliminary statistical analysis on the outdoor variables (light and temperature) has been done, showing that reactors' position inside the plant has been the only factor that didn't influence the light collected data and confirming the necessity of using two probes for internal/external temperature, considering them as two different input. The best initial conditions to use as sodium nitrate concentration ($NaNO3_{init}$) and inoculm concentration (C_{init}) have been respectively 0.35 g L^{-1} and 0.3 g L^{-1} as compromise between high final concentrations (with long batch's duration) and low final concentrations (with short batch's duration). The best values reached for *Tetradesmus* have been $45*10^6$ cell mL^{-1} (reached in the experiment F: from 20-06-17 to 07-07-17) and $16*10^6$ cell mL^{-1} for *Graesiella* (reached in the experiment G: from 10-07-17 to 27-07-17). Both algae have been cultivated together in the experiments G-M (10-07-17 to 22-02-18), showing high level of replicability between reactors and very similar results for both species that have been considered equivalent.
- The collected data (as microalgal growth rate, outdoor parameters and initial cultivation's conditions) have been used to develop an empirical model for prediction of microalgal growth in photobioreactors at specific outdoor conditions, using Principal Component Analysis (PCA) and Partial Least Squares (PLS) regression method. Model predictions results showed acceptable outcomes for both responses: microalgal specific growth rate (μ) and productivity calculated at the maximum concentration reached at each experiment (P_{max}). Furthermore, the identical results obtained running PCA/PLS methods with the experimental values of each microalga considered singularly, confirmed the hypothesis made in the multivariate model's development to consider *Tetradesmus* and *Graesiella* as belonging to a single microalgal strain. All of these informations could be used as basis for the MEWLIFE European project in which Bio-P has a role as partner. Since this project has as aim the production of microalgal biomass in an integrated phototrophic and

heterotrophic cultivation system using preconcentrated olive oil wastewaters (OMWW) as carbon source, the multivariate model could be applied to phototrophic cultivation validating and reinforcing its predictive power also in a different photobioreactor configuration and estimating both specific growth rate and productivity in a specific outdoor conditions.

- Moving on microalgal metabolism, also a new mathematical model able to simply represent the (high-added value) metabolites' accumulation inside microalgae, focusing on the carbon partitioning process between triacylglycerides (TAG) and starch during nitrogen starvation in phototrophy, has been developed. The model simulated the dynamic of 4 variables related to a phototrophic cultivation during nitrogen starvation (biomass concentration (x), nitrogen intracellular quota (q_n), starch intracellular quota (q_g) and TAG intracellular quota (q_l)), finding with the Simulated Annealing method the best set of parameters ($\boldsymbol{\alpha}$, β, μ_m and K_I) that minimized the Residual Sum of Squares function. Anyhow, even in presence of few data the model gave very good results, with high R-Squared values for each estimated parameter as index of model's goodness of fitting. This model could be applied to heterotrophic section of MEWLIFE project, allowing to know: time needed to reach a fixed output concentration (at a certain glucose/OOMWW and Nitrate concentration as input) but also the estimation of the desidered metabolites quotas, accumulated during nitrogen starved conditions.
- As completion of microalgal process treatment, a study of the downstream processes for the extraction (using supercritical CO_2) and purification of the high added value metabolites (with molecular distillation) has been carried out, developing a feasibility study also from the economical point of view. As regard the extraction modeling, the Broken and Intact Cell Model has been implemented for each component considered singularly, allowing to find the best extraction conditions in terms of operative variables (T = 60°C, P = 250 bar and SSR = 5 h^{-1}). The results obtained from the model have been used to simulate the process, calculating the daily amount ofthe desired products (147 kg of extracted stream and 213.19 kg of residue stream) and estimating also OPEX (561.7 k€/year) and CAPEX (2717.9 k€/year), showing good financial perspective due to the high market price of the extracted metabolites considered as a mixture. Regarding molecular distillation fractionation process of microalgal lipidic products, coming out from sCO_2 extraction step, both esterification and dewatering feed's pretreatments have been analyzed to complete the process, obtaining for the esterification reactor V = 3 m^3 and $X_{OLEIC\ ACID}$ =

97% and for the adsorption column Length = 1 m, Radius = 0.2 m working continously. The optimal operating conditions, obtained from the RSM analysis, has been found at T = 128 °C and P = 0.33 Pa, in which the distilled stream has been composed mainly by the esterified fatty acids (95% in mass) and the residue stream has been constituted mainly by carotenoids (98.8% in mass). These results have been used to simulate the process, in order to estimate OPEX (498.23 k€/year) and CAPEX (2387.4 k€/year), that coupled with the calculation of a ROI value of the production process, could give more accurate informations about the investment's feasibility. Also for these two downstream processes, future experiments should be carried out in order to validate the results obtained from the simulations.

REFERENCES

A. Instrument, 2019. Conversion lux to PPFD [WWW Document]. URL https://www.apogeeinstruments.com

Abbas, K.A., Mohamed, A., Abdulamir, A.S., Abas, H.A., 2008. A review on supercritical fluid extraction as new analytical method. Am. J. Biochem. Biotechnol. 4, 345–353. https://doi.org/10.3844/ajbbsp.2008.345.353

Abiusi, F., Sampietro, G., Marturano, G., Biondi, N., Rodolfi, L., D'Ottavio, M., Tredici, M.R., 2014. Growth, photosynthetic efficiency, and biochemical composition of Tetraselmis suecica F&M-M33 grown with LEDs of different colors. Biotechnol. Bioeng. 111, 956–964. https://doi.org/10.1002/bit.25014

ACEA, 2017. Tap water composition [WWW Document]. URL https://www.gruppo.acea.it/it/acqua/ato-2/mappa-qualita-acqua-acea-ato-2

Acién, F.G., Molina, E., Fernández-Sevilla, J.M., Barbosa, M., Gouveia, L., Sepúlveda, C., Bazaes, J., Arbib, Z., 2017a. Economics of microalgae production. Microalgae-Based Biofuels Bioprod. 485–503. https://doi.org/10.1016/B978-0-08-101023-5.00020-0

Acién, F.G., Molina, E., Reis, A., Torzillo, G., Zittelli, G.C., Sepúlveda, C., Masojídek, J., 2017b. Photobioreactors for the production of microalgae, Microalgae-Based Biofuels and Bioproducts: From Feedstock Cultivation to End-Products. https://doi.org/10.1016/B978-0-08-101023-5.00001-7

Acién Fernández, F.G., García Camacho, F., Chisti, Y., 1999. Photobioreactors: light regime, mass transfer, and scaleup. Prog. Ind. Microbiol. 35, 231–247. https://doi.org/10.1016/S0079-6352(99)80118-0

Acién Fernández, F.G., García Camacho, F., Sánchez Pérez, J.A., Fernández Sevilla, J.M., Molina Grima, E., 1997. A model for light distribution and average solar irradiance inside outdoor tubular photobioreactors for the microalgal mass culture. Biotechnol. Bioeng. 55, 701–714. https://doi.org/10.1002/(SICI)1097-0290(19970905)55:5<701::AID-BIT1>3.0.CO;2-F

Adachi, Y., C.-Y.Lu, B., 1983. Supercritical fluid extraction with carbon dioxide and ethylene. Fluid Phuse Equilibria 14, 240. https://doi.org/https://doi.org/10.1016/0378-3812(83)80120-4

Adamakis, I., Lazaridis, P.A., Terzopoulou, E., Torofias, S., Valari, M., Kalaitzi, P., Rousonikolos, V., Gkoutzikostas, D., Zouboulis, A., 2018. Cultivation , characterization , and properties of Chlorella vulgaris microalgae with different lipid contents and effect on fast pyrolysis oil composition. Environ. Sci. Pollut. Res. 23, 23018–23032.

Adesanya, V.O., Davey, M.P., Scott, S.A., Smith, A.G., 2014. Kinetic modelling of growth and storage molecule production in microalgae under mixotrophic and autotrophic conditions. Bioresour. Technol. https://doi.org/10.1016/j.biortech.2014.01.032

Allen, T.F.H., Koonce, J.F., 1973. Multivariate Approaches to Algal Stratagems and Tactics in Systems Analysis of Phytoplankton. Ecology 54, 1234–1246. https://doi.org/10.2307/1934186

Andrzej Gòrak, Zarko Olujic, 2014. Distillation: Equipment and Processes.

Aranda, D.A.G., Santos, R.T.P., Tapanes, N.C.O., Ramos, A.L.D., Antunes, O.A.C., 2008. Acid-catalyzed homogeneous esterification reaction for biodiesel production from palm fatty acids. Catal. Letters

122, 20–25. https://doi.org/10.1007/s10562-007-9318-z

Ba, D., Boyaci, I.H., 2007. Modeling and optimization i: Usability of response surface methodology. J. Food Eng. 78, 836–845. https://doi.org/10.1016/j.jfoodeng.2005.11.024

Bahadar, A., Khan, M.B., 2013. Progress in energy from microalgae : A review 27, 128–148. https://doi.org/10.1016/j.rser.2013.06.029

Barclay, W., Apt, K., Dong, X.D., 2013. Commercial Production of Microalgae via Fermentation. Handb. Microalgal Cult. Appl. Phycol. Biotechnol. 134–145. https://doi.org/10.1002/9781118567166.ch9

Barkia, I., Saari, N., Manning, S.R., 2019. Microalgae for high-value products towards human health and nutrition. Mar. Drugs 17, 1–29. https://doi.org/10.3390/md17050304

Baroukh, C., Muñoz-tamayo, R., Steyer, J., Bernard, O., 2016. DRUM : A New Framework for Metabolic Modeling under Non-Balanced Growth . Application to the Carbon Metabolism of ... DRUM : A New Framework for Metabolic Modeling under Non-Balanced Growth . Application to the Carbon Metabolism of Unicellular Microalgae 9. https://doi.org/10.1371/journal.pone.0104499

Baroukh, C., Turon, V., Bernard, O., 2017. Dynamic metabolic modeling of heterotrophic and mixotrophic microalgal growth on fermentative wastes. PLoS Comput. Biol. https://doi.org/10.1371/journal.pcbi.1005590

Béchet, Q., Laviale, M., Arsapin, N., Bonnefond, H., Bernard, O., 2017. Modeling the impact of high temperatures on microalgal viability and photosynthetic activity. Biotechnol. Biofuels 10, 1–11. https://doi.org/10.1186/s13068-017-0823-z

Béchet, Q., Shilton, A., Guieysse, B., 2013. Modeling the effects of light and temperature on algae growth: State of the art and critical assessment for productivity prediction during outdoor cultivation. Biotechnol. Adv. https://doi.org/10.1016/j.biotechadv.2013.08.014

Bekirogullari, M., Fragkopoulos, I.S., Pittman, J.K., Theodoropoulos, C., 2017. Production of lipid-based fuels and chemicals from microalgae: An integrated experimental and model-based optimization study. Algal Res. https://doi.org/10.1016/j.algal.2016.12.015

Bernard, O., 2011. Hurdles and challenges for modelling and control of microalgae for CO 2 mitigation and biofuel production, in: Journal of Process Control. https://doi.org/10.1016/j.jprocont.2011.07.012

Bernard, O., Mairet, F., Chachuat, B., 2016. Modelling of microalgae culture systems with applications to control and optimization. Adv. Biochem. Eng. Biotechnol. 153, 59–87. https://doi.org/10.1007/10_2014_287

Bernardi, A., Nikolaou, A., Meneghesso, A., Chachuat, B., Morosinotto, T., Bezzo, F., 2017. Semi-empirical modeling of microalgae photosynthesis in different acclimation states – Application to N. gaditana. J. Biotechnol. 259, 63–72. https://doi.org/10.1016/j.jbiotec.2017.08.002

Bezerra, M.A., Santelli, R.E., Oliveira, E.P., Villar, L.S., Escaleira, L.A., 2008. Response surface methodology (RSM) as a tool for optimization in analytical chemistry. Talanta 76, 965–977. https://doi.org/10.1016/j.talanta.2008.05.019

Bhalamurugan, G.L., Valerie, O., Mark, L., 2018. Valuable bioproducts obtained from microalgal biomass and

their commercial applications: A review. Environ. Eng. Res. 23, 229–241. https://doi.org/10.4491/eer.2017.220

Blanken, W., Postma, P.R., de Winter, L., Wijffels, R.H., Janssen, M., 2016. Predicting microalgae growth. Algal Res. 14, 28–38. https://doi.org/10.1016/j.algal.2015.12.020

Borowitzka, M.A., 2013. High-value products from microalgae-their development and commercialisation. J. Appl. Phycol. 25, 743–756. https://doi.org/10.1007/s10811-013-9983-9

Bosma, R., Miazek, K., Willemsen, S.M., Vermuë, M.H., Wijffels, R.H., 2008. Growth inhibition of Monodus subterraneus by free fatty acids. Biotechnol. Bioeng. 101, 1108–1114. https://doi.org/10.1002/bit.21963

Bosma, R., Zessen, E. van, Reith, J.H., Tramper, J., Wijffels, R.H., 2007. Prediction of Volumetric Productivity of an Outdoor Photobioreactor. Biotechnol. Bioeng. 97, 1108–1120. https://doi.org/10.1002/bit.21319

Bougaran, G., Bernard, O., Sciandra, A., 2010. Modeling continuous cultures of microalgae colimited by nitrogen and phosphorus. J. Theor. Biol. https://doi.org/10.1016/j.jtbi.2010.04.018

Boxwell, M., 2009. The solar electricity handbook [WWW Document]. URL http://www.solarelectricityhandbook.com/

Breuer, G., Jaeger, L. De, Artus, V.P.G., Martens, D.E., Springer, J., Draaisma, R.B., Eggink, G., Wijffels, R.H., Lamers, P.P., 2014. Superior triacylglycerol (TAG) accumulation in starchless mutants of Scenedesmus obliquus : (II) evaluation of TAG yield and productivity in controlled photobioreactors. Biotechnol. Biofuels 7, 1–11. https://doi.org/https://doi.org/10.1186/1754-6834-7-70

Breuer, G., Lamers, P.P., Janssen, M., Wijffels, R.H., Martens, D.E., 2015a. Opportunities to improve the areal oil productivity of microalgae. Bioresour. Technol. 186, 294–302. https://doi.org/10.1016/j.biortech.2015.03.085

Breuer, G., Lamers, P.P., Martens, D.E., Draaisma, R.B., Wijffels, R.H., 2013. Effect of light intensity, pH, and temperature on triacylglycerol (TAG) accumulation induced by nitrogen starvation in Scenedesmus obliquus. Bioresour. Technol. 143, 1–9. https://doi.org/10.1016/j.biortech.2013.05.105

Breuer, G., Lamers, P.P., Martens, D.E., Draaisma, R.B., Wijffels, R.H., 2012. The impact of nitrogen starvation on the dynamics of triacylglycerol accumulation in nine microalgae strains. Bioresour. Technol. 124, 217–226. https://doi.org/10.1016/j.biortech.2012.08.003

Breuer, G., Martens, D.E., Draaisma, R.B., Wijffels, R.H., Lamers, P.P., 2015b. Photosynthetic efficiency and carbon partitioning in nitrogen-starved Scenedesmus obliquus. Algal Res. 9, 254–262. https://doi.org/10.1016/j.algal.2015.03.012

Brunner, G., 1994. Gas Extraction: An Introdution to Fundamentas of Supercritical Fluids and the Application to Separation Process 1 Ed. https://doi.org/DOI 10.1007/978-3-662-07380-3

Camacho-Rodríguez, J., González-Céspedes, A.M., Cerón-García, M.C., Fernández-Sevilla, J.M., Acién-Fernández, F.G., Molina-Grima, E., 2014. A quantitative study of eicosapentaenoic acid (EPA) production by Nannochloropsis gaditana for aquaculture as a function of dilution rate, temperature

and average irradiance. Appl. Microbiol. Biotechnol. 98, 2429–2440. https://doi.org/10.1007/s00253-013-5413-9

Cartens, M., Molina Grima, E., Robles Medina, A., Giménez Giménez, A., Ibánez Gonzalez, J., 1996. Eicosapentaenoic acid (20:5n-3) from the Marine Microalga Phaeodactylum tricornutum. JAOCS, J. Am. Oil Chem. Soc. 73, 1025–1031. https://doi.org/10.1007/BF02523411

Chan, C.H., Yusoff, R., Ngoh, G.C., 2014. Modeling and kinetics study of conventional and assisted batch solvent extraction. Chem. Eng. Res. Des. 92, 1169–1186. https://doi.org/10.1016/j.cherd.2013.10.001

Cheng-Wu, Z., Zmora, O., Kopel, R., Richmond, A., 2001. An industrial-size flat plate glass reactor for mass production of Nannochloropsis sp. (Eustigmatophyceae). Aquaculture 195, 35–49. https://doi.org/10.1016/s0044-8486(00)00533-0

Chew, K.W., Yap, J.Y., Show, P.L., Suan, N.H., Juan, J.C., Ling, T.C., Lee, D.J., Chang, J.S., 2017. Microalgae biorefinery: High value products perspectives. Bioresour. Technol. 229, 53–62. https://doi.org/10.1016/j.biortech.2017.01.006

Chini Zittelli, G., Rodolfi, L., Biondi, N., Tredici, M.R., 2006. Productivity and photosynthetic efficiency of outdoor cultures of Tetraselmis suecica in annular columns. Aquaculture 261, 932–943. https://doi.org/10.1016/j.aquaculture.2006.08.011

Chrastll, J., 1982. Solubility of Solids and Liquids in Supercritical Gases. J. Phys. Chem. 86. https://doi.org/10.1002/0470867833.ch13

Cicci, A., Sed, G., Jessop, P.G., Bravi, M., 2018. Circular extraction: an innovative use of switchable solvents for the biomass biorefinery. Green Chem. https://doi.org/10.1039/C8GC01731J

Cicci, A., Stoller, M., Moroni, M., Bravi, M., 2015. Mass Transfer, Light Pulsing and Hydrodynamic Stress Effects in Photobioreactor Development. Icheap12 12Th Int. Conf. Chem. Process Eng. 43, 235–240. https://doi.org/10.3303/CET1543040

Cunico, L.P., Turner, C., 2017. Supercritical Fluids and Gas-Expanded Liquids, The Application of Green Solvents in Separation Processes. Elsevier Inc. https://doi.org/10.1016/B978-0-12-805297-6.00007-3

Damergi, E., Schwitzguébel, J., Refardt, D., Sharma, S., Holliger, C., Ludwig, C., 2017. Extraction of carotenoids from Chlorella vulgaris using green solvents and syngas production from residual biomass. Algal Res. 25, 488–495. https://doi.org/10.1016/j.algal.2017.05.003

Darvehei, P., Bahri, P.A., Moheimani, N.R., 2017. A model for the effect of light on the growth of microalgae in outdoor condition, Computer Aided Chemical Engineering. Elsevier Masson SAS. https://doi.org/10.1016/B978-0-444-63965-3.50458-X

Davis, R., Biddy, M., Jones, S., 2013. Algal Lipid Extraction and Upgrading to Hydrocarbons Technology Pathway, National Renewable Energy Laboratory.

del Valle, J.M., Aguilera, J.M., 1988. An Improved Equation for Predicting the Solubility of Vegetable Oils in Supercritical CO2. Ind. Eng. Chem. Res. 27, 1551–1553. https://doi.org/10.1021/ie00080a036

Deschênes, J.S., Boudreau, A., Tremblay, R., 2015. Mixotrophic production of microalgae in pilot-scale photobioreactors: Practicability and process considerations. Algal Res.

https://doi.org/10.1016/j.algal.2015.04.015

Desimone, J.M., Desimone, J.M., 2014. Practical Approaches to Green Solvents 799. https://doi.org/10.1126/science.1069622

Di Caprio, F., Altimari, P., Iaquaniello, G., Toro, L., Pagnanelli, F., 2019. Heterotrophic cultivation of T. obliquus under non-axenic conditions by uncoupled supply of nitrogen and glucose. Biochem. Eng. J. 127–136. https://doi.org/10.1016/j.bej.2019.02.020

Di Caprio, F., Altimari, P., Pagnanelli, F., 2017. Effect of Ca^{2+} concentration on Scenedesmus sp. growth in heterotrophic and photoautotrophic cultivation. N. Biotechnol. https://doi.org/10.1016/j.nbt.2017.09.003

Di Caprio, F., Altimari, P., Pagnanelli, F., 2015. Integrated biomass production and biodegradation of olive mill wastewater by cultivation of Scenedesmus sp. Algal Res. 9, 306–311. https://doi.org/10.1016/j.algal.2015.04.007

Di Caprio, F., Visca, A., Altimari, P., Toro, L., Iaquaniello, G., Pagnanelli, F., 2016. Two Stage Process of Microalgae Cultivation for Starch and Carotenoid Production. Chem. Eng. Trans. 49, 415–420. https://doi.org/10.3303/CET1649070

Díaz, M.T., Pérez, C., Sánchez, C.I., Lauzurica, S., Cañeque, V., González, C., Fuente, J.D. La, 2017. Feeding microalgae increases omega 3 fatty acids of fat deposits and muscles in light lambs. J. Food Compos. Anal. 56, 115–123. https://doi.org/10.1016/j.jfca.2016.12.009

Doucha, J., Lívanský, K., 2014. Production of high-density Chlorella culture grown in fermenters. J. Appl. Phycol. 24, 35–43. https://doi.org/10.1007/s10811-010-9643-2

Droop, M.R., 1968. Vitamin B12 and Marine Ecology. IV. The Kinetics of Uptake, Growth and Inhibition in Monochrysis Lutheri. J. mar. biol. Ass. U.K 48, 689–733. https://doi.org/https://doi.org/10.1017/S0025315400019238

Enamala, M.K., Enamala, S., Chavali, M., Donepudi, J., Yadavalli, R., Kolapalli, B., Aradhyula, T.V., Velpuri, J., Kuppam, C., 2018. Production of biofuels from microalgae - A review on cultivation, harvesting, lipid extraction, and numerous applications of microalgae. Renew. Sustain. Energy Rev. 94, 49–68. https://doi.org/10.1016/j.rser.2018.05.012

Environmental Growth Chambers, 2014. Lighting Radiation Conversion [WWW Document]. URL http://www.egc.com/useful_info_lighting.php

Erkey, C., 2011. Supercritical fluids and organometallic compounds: from recovery of trace metals to synthesis of nanostructured materials.

Fachet, M., Flassig, R.J., Rihko-Struckmann, L., Sundmacher, K., 2014. A dynamic growth model of Dunaliella salina: Parameter identification and profile likelihood analysis. Bioresour. Technol. https://doi.org/10.1016/j.biortech.2014.08.124

Ferrell, J., Sarisky-Reed, V., 2010. National algal biofuels technology roadmap. U.S. Dep. Energy.

Figueroa-Torres, G.M., Pittman, J.K., Theodoropoulos, C., 2017. Kinetic modelling of starch and lipid formation during mixotrophic, nutrient-limited microalgal growth. Bioresour. Technol.

https://doi.org/10.1016/j.biortech.2017.05.177

Flassig, R.J., Fachet, M., Höffner, K., Barton, P.I., Sundmacher, K., 2016. Dynamic flux balance modeling to increase the production of high-value compounds in green microalgae. Biotechnol Biofuels 9. https://doi.org/10.1186/s13068-016-0556-4

Follegatti-romero, L.A., Piantino, C.R., Grimaldi, R., Cabral, F.A., 2009. Supercritical CO2 extraction of omega-3 rich oil from Sacha inchi (Plukenetia volubilis L .) seeds 49, 323–329. https://doi.org/10.1016/j.supflu.2009.03.010

Fregolente, P.B.L., Pinto, G.M.F., Wolf-Maciel, M.R., Filho, R.M., 2010. Monoglyceride and Diglyceride Production Through Lipase-Catalyzed Glycerolysis and Molecular Distillation 1879–1887. https://doi.org/10.1007/s12010-009-8822-6

Funazukuri, T., Kong, C.Y., Kagei, S., 2003. Binary diffusion coefficient, partition ratio, and partial molar volume for docosahexaenoic acid, eicosapentaenoic acid and α-linolenic acid at infinite dilution in supercritical carbon dioxide. Fluid Phase Equilib. 206, 163–178. https://doi.org/10.1016/S0378-3812(02)00309-6

Gabruś, E., Nastaj, J., Tabero, P., Aleksandrzak, T., 2015. Experimental studies on 3A and 4A zeolite molecular sieves regeneration in TSA process: Aliphatic alcohols dewatering-water desorption. Chem. Eng. J. 259, 232–242. https://doi.org/10.1016/j.cej.2014.07.108

García Camacho, F., Contreras Gómez, A., Acién Fernández, F.G., Fernández Sevilla, J., Molina Grima, E., 1999. Use of concentric-tube airlift photobioreactors for microalgal outdoor mass cultures. Enzyme Microb. Technol. 24, 164–172. https://doi.org/10.1016/S0141-0229(98)00103-3

Ghazouani, J., Chouaieb, O., Bellagi, A., Thermique, U.R., 2005. Evaluation of the parameters of the Bender equation of state for low acentric factor fluids and carbon dioxide 432, 10–19. https://doi.org/10.1016/j.tca.2004.11.008

Gouveia, L., Veloso, V., Reis, A., Fernandes, H., Novais, J., Empis, J., 1996. Evolution of pigment composition in Chlorella vulgaris. Bioresour. Technol. 57, 157–163. https://doi.org/https://doi.org/10.1016/0960-8524(96)00058-2

Gupta, P.L., Lee, S.M., Choi, H.J., 2015. A mini review: photobioreactors for large scale algal cultivation. World J. Microbiol. Biotechnol. 31, 1409–1417. https://doi.org/10.1007/s11274-015-1892-4

Guschina, I.A., Harwood, J.L., 2009. Algal lipids and effect of the environment on their biochemistry., in: Lipids in Aquatic Ecosystems. pp. 1–24. https://doi.org/10.1007/978-0-387-89366-2

Härdle, W.K., Simar, L., 2015. Applied Multivariate Statistical Analysis, Technometrics. https://doi.org/10.1007/978-3-662-45171-7

Heidaryan, E., Hatami, T., Rahimi, M., Moghadasi, J., 2011. Viscosity of pure carbon dioxide at supercritical region: Measurement and correlation approach. J. Supercrit. Fluids 56, 144–151. https://doi.org/10.1016/j.supflu.2010.12.006

Herrero, M., Cifuentes, A., Iban, E., 2006. Food Chemistry Sub- and supercritical fluid extraction of functional ingredients from different natural sources : Plants , food-by-products , algae and

microalgae A review 98, 136–148. https://doi.org/10.1016/j.foodchem.2005.05.058

Hickman, K.C.D., 1947. COMMERCIAL MOLECULAR DISTILLATION. Ind. Eng. Chem. 39, 686–694.

Ho, S.H., Huang, S.W., Chen, C.Y., Hasunuma, T., Kondo, A., Chang, J.S., 2013. Bioethanol production using carbohydrate-rich microalgae biomass as feedstock. Bioresour. Technol. 135, 191–198. https://doi.org/10.1016/j.biortech.2012.10.015

Huesemann, M., Crowe, B., Waller, P., Chavis, A., Hobbs, S., Edmundson, S., Wigmosta, M., 2016. A validated model to predict microalgae growth in outdoor pond cultures subjected to fluctuating light intensities and water temperatures. Algal Res. 13, 195–206. https://doi.org/10.1016/j.algal.2015.11.008

Jaeger, L. De, Verbeek, R.E.M., Draaisma, R.B., Martens, D.E., Springer, J., Eggink, G., 2014. Superior triacylglycerol (TAG) accumulation in starchless mutants of Scenedesmus obliquus : (I) mutant generation and characterization. Biotechnol. Biofuels 1–11. https://doi.org/https://doi.org/10.1186/1754-6834-7-69

Johnson, X., Alric, J., 2013. Central carbon metabolism and electron transport in chlamydomonas reinhardtii: Metabolic constraints for carbon partitioning between oil and starch. Eukaryot. Cell. https://doi.org/10.1128/EC.00318-12

Kalil, S.J., Maugeri, F., Rodrigues, M.I., 2000. Response surface analysis and simulation as a tool for bioprocess design and optimization. Process Biochem. 35, 539–550. https://doi.org/10.1016/S0032-9592(99)00101-6

Katsuda, T., Arimoto, T., Igarashi, K., Azuma, M., Kato, J., Takakuwa, S., Ooshima, H., 2000. Light intensity distribution in the externally illuminated cylindrical photo-bioreactor and its application to hydrogen production by Rhodobacter capsulatus. Biochem. Eng. J. 5, 157–164. https://doi.org/10.1016/S1369-703X(00)00054-1

Ketenoglu, O., Tekin, A., 2015. Applications of molecular distillation technique in food products. Ital. J. Food Sci. 27, 277–281. https://doi.org/10.14674/1120-1770/ijfs.v269

Khan, M.I., Shin, J.H., Kim, J.D., 2018. The promising future of microalgae : current status , challenges , and optimization of a sustainable and renewable industry for biofuels , feed , and other products. Microb. Cell Fact. 1–21. https://doi.org/10.1186/s12934-018-0879-x

Kim, J., Yoo, G., Lee, H., Lim, J., Kim, K., Kim, C.W., Park, M.S., Yang, J.W., 2013. Methods of downstream processing for the production of biodiesel from microalgae. Biotechnol. Adv. 31, 862–876. https://doi.org/10.1016/j.biotechadv.2013.04.006

Klok, A.J., Verbaanderd, J.A., Lamers, P.P., Martens, D.E., Rinzema, A., Wijffels, R.H., 2013. A model for customising biomass composition in continuous microalgae production. Bioresour. Technol. 146, 89–100. https://doi.org/10.1016/j.biortech.2013.07.039

Komori, S., Takata, K., Yasuhiro, M., 1988. Flow structure and mixing mechanism in an agitated thin-film evaporator. J. Chem. Eng. Japan 98, 639–644. https://doi.org/https://doi.org/10.1252/jcej.21.639

Krzemińska, I., Pawlik-Skowrońska, B., Trzcińska, M., Tys, J., 2014. Influence of photoperiods on the growth

rate and biomass productivity of green microalgae. Bioprocess Biosyst. Eng. 37, 735–741. https://doi.org/10.1007/s00449-013-1044-x

Kumar, A., Guria, C., Chitres, G., Chakraborty, A., Pathak, A.K., 2016. Modelling of microalgal growth and lipid production in Dunaliella tertiolecta using nitrogen-phosphorus-potassium fertilizer medium in sintered disk chromatographic glass bubble column. Bioresour. Technol. https://doi.org/10.1016/j.biortech.2016.07.055

Leitner, W., 2000. Designed to dissolve. Nature 405.

Lemesle, V., Mailleret, L., 2008. A mechanistic investigation of the algae growth "droop" model. Acta Biotheor. 56, 87–102. https://doi.org/10.1007/s10441-008-9031-3

León-Saiki, G.M., Remmers, I.M., Martens, D.E., Lamers, P.P., Wijffels, R.H., van der Veen, D., 2017. The role of starch as transient energy buffer in synchronized microalgal growth in Acutodesmus obliquus. Algal Res. 25, 160–167. https://doi.org/10.1016/j.algal.2017.05.018

Lin, L.P., 1985. Microstructure of Spray-Dried and Freeze-Dried Microalgal Powders. Food MircroStructure 4, 341–348.

Liu, C.P., Lin, L.P., 2005. Morphology and eicosapentaenoic acid production by Monodus subterraneus UTEX 151. Micron 36, 545–550. https://doi.org/10.1016/j.micron.2005.05.001

Liu, Z.Y., Jobson, M., 1999. The Effect of Operating Pressure on Distillation Column Throughput. Comput. Chem. Eng. 23, S831–S834. https://doi.org/10.1016/S0098-1354(99)80204-X

Lutisan, J., Cvengros, J., 1995. Mean free path of molecules on molecular distillation 56, 35–90.

Macìas-Sànchez, M.D., Serrano, C.M., Rodrìguez, M.R., Ossa, E.M. de la, Lubiàn, L.M., Montero, O., 2008. Extraction of carotenoids and chlorophyll from microalgae with supercritical carbon dioxide and ethanol as cosolvent. J. Sep. Sci. 31, 1352–1362. https://doi.org/10.1002/jssc.200700503

Mahadevan, R., Edwards, J.S., Doyle, F.J., 2002. Dynamic Flux Balance Analysis of diauxic growth in Escherichia coli. Biophys. J. 83, 1331–1340. https://doi.org/10.1016/S0006-3495(02)73903-9

Mairet, F., Bernard, O., Masci, P., Lacour, T., Sciandra, A., 2011. Modelling neutral lipid production by the microalga Isochrysis aff. galbana under nitrogen limitation. Bioresour. Technol. https://doi.org/10.1016/j.biortech.2010.06.138

Manjare, S.D., Dhingra, K., 2019. Supercritical fluids in separation and purification: A review. Mater. Sci. Energy Technol. 2, 463–484. https://doi.org/10.1016/j.mset.2019.04.005

March, J., 1992. Advanced Organic Chemistry. https://doi.org/10.1017/CBO9781107415324.004

Markou, G., Nerantzis, E., 2013. Microalgae for high-value compounds and biofuels production: A review with focus on cultivation under stress conditions. Biotechnol. Adv. 31, 1532–1542. https://doi.org/10.1016/j.biotechadv.2013.07.011

Marsullo, M., Mian, A., Ensinas, A.V., Manente, G., Lazzaretto, A., Marechal, F., 2015. Dynamic modeling of the microalgae cultivation phase for energy production in open raceway ponds and flat panel photobioreactors. Front. Energy Res. 3, 1–18. https://doi.org/10.3389/fenrg.2015.00041

Mata, T.M., Martins, A.A., Caetano, N.S., 2010. Microalgae for biodiesel production and other applications:

A review. Renew. Sustain. Energy Rev. 14, 217–232. https://doi.org/10.1016/j.rser.2009.07.020

Mazzelli, A, Buonanno, G., Luzzi, D.M., Cicci, A., Piemonte, V., Iaquaniello, G., 2019. Multi-component extraction process of high added value compounds from microalgae with supercritical CO 2 : A technical and economic study. Chem. Eng. Res. Des. 150, 65–73. https://doi.org/10.1016/j.cherd.2019.07.023

Mazzelli, A., Cicci, A., Caprio, F. Di, Altimari, P., Toro, L., Iaquaniello, G., Pagnanelli, F., 2019a. Multivariate modeling for microalgae growth in outdoor photobioreactors. Algal Res. https://doi.org/10.1016/j.algal.2019.101663

Mazzelli, A., Cicci, A., Franceschini, G., Caprio, F.D., Iaquaniello, G., Altimari, P., Pagnanelli, F., Toro, L., 2018a. Investigation of effects of nutrients and external parameters on kinetic growth of outdoor microalgal cultivation. Chem. Eng. Trans. 64. https://doi.org/10.3303/CET1864116

Mazzelli, A., Cicci, A., Sed, G., Bravi, M., 2018b. Development of a semi-theoretical light radiation and photosynthetic growth model for the optimal exploitation of wastewaters by microalgae. Chem. Eng. Trans. 64. https://doi.org/10.3303/CET1864115

Mazzelli, A., Luzzi, D.M., Buonanno, G., Cicci, A., Piemonte, V., Iaquaniello, G., 2019b. An optimized separation process of microalgal lipidic products by molecular distillation: Techno-economic analysis. Chem. Eng. Sci. 207, 1187–1195. https://doi.org/10.1016/j.ces.2019.07.043

Mendes, R.L., Fernandes, H.L., Coelbo, P., Reis, E.C., Cabral, J.M.S., Anthio, M.N., 1995. Supercritical CO2 , extraction of carotenoids and other lipids from Chlorella vulgaris 53, 99–103. https://doi.org/https://doi.org/10.1016/0308-8146(95)95794-7

Mercer, P., Armenta, R.E., 2011. Developments in oil extraction from microalgae. Eur. J. Lipid Sci. Technol. 113, 539–547. https://doi.org/10.1002/ejlt.201000455

Morales-sa, D., Kyndt, J., Martinez, A., 2014. Heterotrophic growth of microalgae : metabolic aspects. https://doi.org/10.1007/s11274-014-1773-2

Nutraceutical,Business,Review, 2018. Nutraceutical Business Review [WWW Document]. URL https://www.nutraceuticalbusinessreview.com/news/article_page/Allmicroalgae_expands_its_flexible_production_with_fermentation/135426

Ogbonna, J.C., Yada, H., Tanaka, H., 1995. Kinetic study on light-limited batch cultivation of photosynthetic cells. J. Ferment. Bioeng. 80, 259–264. https://doi.org/10.1016/0922-338X(95)90826-L

Olivieri, G., Salatino, P., Marzocchella, A., 2014. Advances in photobioreactors for intensive microalgal production: Configurations, operating strategies and applications. J. Chem. Technol. Biotechnol. https://doi.org/10.1002/jctb.4218

Orth, J.D., Thiele, I., Palsson, B.O., 2010. What is flux balance analysis? Nat. Biotechnol. 28, 245–248. https://doi.org/10.1038/nbt.1614

Pagnanelli, F., Altimari, P., Trabucco, F., Toro, L., 2014. Mixotrophic growth of Chlorella vulgaris and Nannochloropsis oculata: Interaction between glucose and nitrate. J. Chem. Technol. Biotechnol. 89, 652–661. https://doi.org/10.1002/jctb.4179

Panis, G., Carreon, J.R., 2016. Commercial astaxanthin production derived by green alga Haematococcus pluvialis: A microalgae process model and a techno-economic assessment all through production line. Algal Res. 18, 175–190. https://doi.org/10.1016/j.algal.2016.06.007

Patel, A., Matsakas, L., Hrůzová, K., Rova, U., Christakopoulos, P., 2019. Biosynthesis of Nutraceutical Fatty Acids by the Oleaginous Marine Microalgae Phaeodactylum tricornutum Utilizing Hydrolysates from Organosolv-Pretreated Birch and Spruce Biomass. Mar. Drugs 17, 1–17. https://doi.org/10.3390/md17020119

Perez-Garcia, O., Escalante, F.M.E., de-Bashan, L.E., Bashan, Y., 2011. Heterotrophic cultures of microalgae: Metabolism and potential products. Water Res. 45, 11–36. https://doi.org/10.1016/j.watres.2010.08.037

Peters, M., Timmerhaus, K., West, R., 2003. Plant design and economics for chemical engineers.

Pinnarat, T., Savage, P.E., 2010. Noncatalytic esterification of oleic acid in ethanol. J. Supercrit. Fluids 53, 53–59. https://doi.org/10.1016/j.supflu.2010.02.008

Ponce, G.H.S.F., Alves, M., Miranda, J.C.C., Maciel Filho, R., Wolf Maciel, M.R., 2015. Using an internally heat-integrated distillation column for ethanol-water separation for fuel applications. Chem. Eng. Res. Des. 95, 55–63. https://doi.org/10.1016/j.cherd.2015.01.002

Přibyl, P., Cepák, V., Zachleder, V., 2013. Production of lipids and formation and mobilization of lipid bodies in Chlorella vulgaris. J. Appl. Phycol. 25, 545–553. https://doi.org/10.1007/s10811-012-9889-y

Quinn, J., de Winter, L., Bradley, T., 2011. Microalgae bulk growth model with application to industrial scale systems. Bioresour. Technol. 102, 5083–5092. https://doi.org/10.1016/j.biortech.2011.01.019

Raheem, A., Prinsen, P., Vuppaladadiyam, A.K., Zhao, M., Luque, R., 2018. A review on sustainable microalgae based biofuel and bioenergy production: recent developments. https://doi.org/10.1016/j.jclepro.2018.01.125

Rezaei, K.A., Temelli, F., 2000. Using supercritical fluid chromatography to determine diffusion coefficients of lipids in supercritical CO2. J. Supercrit. Fluids 17, 35–44. https://doi.org/https://doi.org/10.1016/S0896-8446(99)00039-X

Ryu, K.H., Sung, M.G., Kim, B., Heo, S., Chang, Y.K., Lee, J.H., 2018. A mathematical model of intracellular behavior of microalgae for predicting growth and intracellular components syntheses under nutrient-replete and -deplete conditions, Biotechnology and Bioengineering. https://doi.org/10.1002/bit.26744

Safi, C., Camy, S., Frances, C., Varela, M.M., Badia, E.C., Pontalier, P., Vaca-garcia, C., 2013. Extraction of lipids and pigments of Chlorella vulgaris by supercritical carbon dioxide : influence of bead milling on extraction performance. https://doi.org/10.1007/s10811-013-0212-3

Sanchez-Camargo, P., Elena, I., Cifuentes, A., Herrero, M., 2017. Bioactives Obtained From Plants , Seaweeds , Microalgae and Food By-Products Using Pressurized Liquid Extraction and Supercritical Fluid Extraction. Compr. Anal. Chem. 76. https://doi.org/10.1016/bs.coac.2017.01.001

Sapkale, G.N., Patil, S.M., Surwase, U.S., Bhatbhage, P.K., 2010. Supercritical Fluid Extraction-A review. Int. J.

Chem. Sci. 8, 729–743. https://doi.org/10.1016/B978-0-12-384947-2.00675-9

Sattler, K., Feindt, H.J., 1995. Thermal Separation Processes: Principles and Design. VCH Verlagsgesellschaft mbH.

Sepidar, S., Zurina Zainal, A., Robiah, Y., Azhari, M., 2011. Solid Liquid Extraction of Jatropha Seeds by Microwave Pretreatment and Ultrasound Assisted Methods. J. Appl. Sci. 11, 2444–2447. https://doi.org/10.3923/jas.2011.2444.2447

Sforza, E., Gris, B., De Farias Silva, C.E., Morosinotto, T., Bertucco, A., 2014. Effects of light on cultivation of scenedesmus obliquus in batch and continuous flat plate photobioreactor. Chem. Eng. Trans. 38, 211–216. https://doi.org/10.3303/CET1438036

Shastri, A.A., Morgan, J.A., 2005. Flux balance analysis of photoautotrophic metabolism. Biotechnol. Prog. 21, 1617–1626. https://doi.org/10.1021/bp050246d

Shi, J., Posada, L.R., Kakuda, Y., Xue, S.J., 2007. Molecular Distillation of Palm Oil Distillates : Evaporation Rates , Relative Volatility , and Distribution Coefficients of Tocotrienols and other Minor Components Molecular Distillation of Palm Oil. Sep. Sci. Technol. 3029–3048. https://doi.org/10.1080/01496390701589024

Simo, M., Sivashanmugam, S., Brown, C.J., Hlavacek, V., 2009. Adsorption/desorption of water and ethanol on 3A zeolite in near-adiabatic fixed bed. Ind. Eng. Chem. Res. 48, 9247–9260. https://doi.org/10.1021/ie900446v

Solimeno, A., Gabriel, F., García, J., 2017. Mechanistic model for design, analysis, operation and control of microalgae cultures: Calibration and application to tubular photobioreactors. Algal Res. https://doi.org/10.1016/j.algal.2016.11.023

Solimeno, A., Samsó, R., Uggetti, E., Sialve, B., Steyer, J.P., Gabarró, A., García, J., 2015. New mechanistic model to simulate microalgae growth. Algal Res. 12, 350–358. https://doi.org/10.1016/j.algal.2015.09.008

Sovová, H., 2005. Mathematical model for supercritical fluid extraction of natural products and extraction curve evaluation 33, 35–52. https://doi.org/10.1016/j.supflu.2004.03.005

Stephan, K., 1992. Heat Transfer in Condensation and Boiling.

Steyer, M.R.J., 2013. Temperature effect on microalgae : a crucial factor for outdoor production 153–164. https://doi.org/10.1007/s11157-013-9310-6

Taher, H., Al-Zuhair, S., Al-Marzouqi, A.H., Haik, Y., Farid, M., 2014. Mass transfer modeling of Scenedesmus sp. lipids extracted by supercritical CO2. Biomass and Bioenergy 70, 530–541. https://doi.org/10.1016/j.biombioe.2014.08.019

Teo, W.K., Ruth van, D.M., 1986. Adsorption of water from aqueous ethanol using 3-Å Molecular Sieves. Ind. Eng. Chem. Process Des. Dev. 25, 17–21. https://doi.org/10.1021/i200032a003

Tiwari, P.K., Samanta, S., Ferreira, J.D., Misra, A.K., 2019. A Mathematical Model for the Effects of Nitrogen and Phosphorus on Algal Blooms 29. https://doi.org/10.1142/S0218127419501293

Tocher, D.R., Betancor, M.B., Sprague, M., Olsen, R.E., Napier, J.A., 2019. Omega-3 Long-Chain

Polyunsaturated Fatty Acids , and Demand 1–20. https://doi.org/10.3390/nu11010089

Treybal R.E., 1980. Mass transfer operation, Cancer Biology and Therapy. https://doi.org/10.4161/cbt.4.3.1637

Tsavalos, A.J., Day, J.G., 1994. Development of media for the mixotrophic/heterotrophic culture of Brachiomonas submarina. J. Appl. Phycol. 6, 431–433. https://doi.org/10.1007/BF02182162

Tsibranska, I., Tylkowski, B., Kochanov, R., Alipieva, K., 2011. Extraction of biologically active compounds from Sideritis ssp. L. Food Bioprod. Process. 89, 273–280. https://doi.org/10.1016/j.fbp.2010.10.004

van Vuuren, S.J., Pieterse, A., 2005. The use of multivariate analysis as a tool to illustrate the influence of environmental variables on phytoplankton composition in the Vaal River, South Africa. African J. Aquat. Sci. 30, 17–28. https://doi.org/10.2989/16085910509503830

Vanrolleghem, P., Borchardt, D., Henze, M., Rauch, W., Reichert, P., Shanahan, P., Somlyódy, L., 2001. River Water Quality Model no. 1 (RWQM1): III. Biochemical submodel selection. Water Sci. Technol. 43, 31–40. https://doi.org/10.2166/wst.2001.0241

Varela, J.C., Pereira, H., Vila, M., León, R., 2015. Production of carotenoids by microalgae: Achievements and challenges. Photosynth. Res. 125, 423–436. https://doi.org/10.1007/s11120-015-0149-2

Wallace, J., Champagne, P., Hall, G., 2016. Multivariate statistical analysis of water chemistry conditions in three wastewater stabilization ponds with algae blooms and pH fluctuations. Water Res. 96, 155–165. https://doi.org/10.1016/j.watres.2016.03.046

Wang, S., Gu, Y., Liu, Q., Yao, Y., Guo, Z., Luo, Z., Cen, K., 2009. Separation of bio-oil by molecular distillation. Fuel Process. Technol. 90, 738–745. https://doi.org/10.1016/j.fuproc.2009.02.005

Wold, S., Esbensen, K., Geladi, P., 1987. Principal component analysis. Chemom. Intell. Lab. Syst. 2, 37–52. https://doi.org/doi:10.1016/0169-7439(87)80084-9.

Wu, X., Merchuk, J.C., 2001. A model integrating fluid dynamics in photosynthesis and photoinhibition processes. Chem. Eng. Sci. 56, 3527–3538. https://doi.org/10.1016/S0009-2509(01)00048-3

Xu, Z., Howard, L.R., 2012. Analysis of Antioxidant-Rich Phytochemicals.

Yamamoto, T., Kim, Y.H., Kim, B.C., Endo, A., Thongprachan, N., Ohmori, T., 2012. Adsorption characteristics of zeolites for dehydration of ethanol: Evaluation of diffusivity of water in porous structure. Chem. Eng. J. 181–182, 443–448. https://doi.org/10.1016/j.cej.2011.11.110

Zeller, M.A., Hunt, R., Jones, A., Sharma, S., 2013. Bioplastics and their thermoplastic blends from Spirulina and Chlorella microalgae. J. Appl. Polym. Sci. 130, 3263–3275. https://doi.org/10.1002/app.39559

Zhu, S., Huang, W., Xu, Jin, Wang, Z., Xu, Jingliang, Yuan, Z., 2014. Metabolic changes of starch and lipid triggered by nitrogen starvation in the microalga Chlorella zofingiensis. Bioresour. Technol. 152, 292–298. https://doi.org/10.1016/j.biortech.2013.10.092